

HYDROCARBON POOL FIRE PERFORMANCE OF FIBER REINFORCED POLYMER  
(FRP) STRENGTHENED AND THERMALLY INSULATED BRIDGE GIRDERS

by

EYOSIAS SOLOMON BENEBERU

Presented to the Faculty of the Graduate School of  
The University of Texas at Arlington in Partial Fulfillment  
of the Requirements  
for the Degree of

DOCTOR OF PHILOSOPHY

THE UNIVERSITY OF TEXAS AT ARLINGTON

DECEMBER 2016

Copyright © by Eyosias Beneberu 2016

All Rights Reserved



## **Acknowledgements**

First and foremost, I would like to thank my God who gave me the passion and the strength to complete this research. From him, through him and to him are all things.

My sincere appreciation goes to my advisor Dr. Nur Yazdani for his continuous support, guidance and mentorship. I am grateful to Dr. Shih-Ho Chao, Dr. Sahadat Hossain, and Dr. Ankur Jain for readily accepting to serve on my dissertation committee as well as for their encouragement and support during my study.

I would like to acknowledge the financial support from Texas Department of Transportation (TxDOT). I also like to thank Walter Fisher III, Sunil Patel and Robert Owens from TxDOT Dallas District for their valuable advice.

I am grateful to Dr. Seyedali Abolmaali, Dr. Khosrow Behbehani and Mr. Jim Crites for helping me find the fire testing center. I would also like to express my gratitude to Chief Randal Rhodes, Chief Brian Mickney, Mr. Rick Reynolds, Mr. Jeff Williams, Mr. Jason Ford, Mr. Chuck Knowles and Ms. Bonnie Barlow for their unceasing support during my work at DFW Airport Fire Training Research Center.

I am thankful to my friends Santosh Timilsnia, Mina Riad, Tariq Al Jaafreh, Yazan Almomani, Natawut Chaiwino, Eric Chavez, Enrique Gonzalez, Alvin Matthew and Sammer Rampurawala for all the help and hard work during the experiment.

I am deeply grateful to my parents and extended family. Last but not least, I would like to thank my beautiful wife, Rahel Demessae, who patiently stood by my side through the entirety of this research.

November 18, 2016

## **Abstract**

### HYDROCARBON POOL FIRE PERFORMANCE OF FIBER REINFORCED POLYMER (FRP) STRENGTHENED AND THERMALLY INSULATED BRIDGES

Eyosias Beneberu, PhD

The University of Texas at Arlington, 2016

Supervising Professor: Nur Yazdani

Highway bridges encounter various extreme load hazards, such as earthquake, flood, blast, collision, wind and fire during their design lives. The effect of accidental, natural or man-made fire on bridges is one of the least investigated which may be due to the assumption that bridge fire has a low probability of occurrence. However, a bridge failure survey showed that fire had caused more bridge collapse in the USA than earthquakes. The main objective of the current research is to study concrete bridges in general, and fiber reinforced polymer (FRP) strengthened bridge girders in particular against fire hazard.

The research is divided into three distinct phases. The first phase involved building the bridge, loading the bridge with the simulated HL-93 live load and finally subjecting it to hydrocarbon fire. The superstructure of the tested bridge comprised of three Texas standard girders, precast deck panels, and cast-in-place deck. One girder was wrapped with carbon fiber reinforced polymer (CFRP), another with CFRP and sprayed with fireproofing and third was a control girder without CFRP or fireproofing. The second phase involved saw cutting the deck, transporting the girders to the CELAB and performing residual strength test. The third phase dealt

with numerical modeling of the test bridge under fire to verify the experimental phase. It was found out that the insulation successfully preserved the integrity of the FRP strengthening, the underlying concrete, and the prestressing strands. On the contrary, the girder without insulation sustained severe damage and lost a significant amount of its flexural load carrying capacity.

## Table of Contents

Acknowledgements .....	iii
Abstract .....	iv
List of Figures.....	x
List of Tables.....	xx
Chapter 1 INTRODUCTION.....	1
1.1 Background.....	1
1.2 Problem Statement.....	5
1.3 Objectives .....	7
1.4 Organization of the Dissertation .....	8
Chapter 2 LITERATURE REVIEW.....	11
2.1 Bridges and Fire Hazard.....	11
2.2 FRP Strengthened Structures and Fire .....	24
2.2.1 Experimental Studies .....	24
2.2.2 Numerical Studies .....	31
2.3 Materials Properties at Elevated Temperatures .....	33
2.3.1 Fiber Reinforced Polymer(FRP).....	35
2.3.2 Concrete.....	40
2.3.3 Prestressing Strands and Mild Reinforcements .....	52
2.3.4 Insulation .....	58
Chapter 3 TEST BRIDGE DESIGN .....	61
3.1 Design of Girders.....	61
3.2 Design of Deck .....	63
3.3 Support Design.....	65
3.4 FRP Design .....	67

3.5 Fireproofing.....	71
3.6 Instrumentation .....	72
Chapter 4 TEST BRIDGE CONSTRUCTION .....	77
4.1 Girders and Precast Deck Panels Fabrication .....	77
4.2 Test Site.....	83
4.3 Test Bridge Construction .....	85
4.3.1 Assembly of Components and Deck Construction.....	87
4.3.2 Installation of FRP .....	96
4.3.3 Installation of Insulation.....	100
Chapter 5 FIRE TEST .....	103
5.1 Test Setup .....	103
5.1.1 Live Loading of the Test Bridge.....	103
5.1.2 Fuel Flow Rate Determination .....	105
5.1.3 Duration of Fire and Location of the Fire Pit .....	107
5.1.4 Determination of safe standing distance .....	107
5.2 Fire Experiment .....	116
5.3 Results and discussions .....	118
5.3.1 Thermal Response .....	120
5.3.1.1 Girder-1 .....	120
5.3.1.2 Girder-2 .....	130
5.3.1.3 Girder-3 .....	137
5.3.1.4 Deck .....	140
5.3.1.5 Bearing Pads.....	144
5.3.2 Visual Inspection and Hardness Test.....	145
5.3.2.1 Girder-1 .....	147

5.3.2.2 Girder-2 .....	151
5.3.2.3 Girder-3 .....	154
5.3.3 Structural Response .....	157
Chapter 6 DEMOLITION OF TEST BRIDGE AND DETERMINATION OF RESIDUAL STRENGTH .....	160
6.1 Demolition of Bridge and Transportation of Specimens to CELAB .....	160
6.2 Casting of Concrete Topping on the Control Girder .....	162
6.3 Residual Strength Test .....	163
6.3.1 Test Setup .....	163
6.3.1.1 Girder-1 strain gauge layout .....	164
6.3.1.2 Girder-2 strain gauge layout .....	166
6.3.1.3 Girder-3 strain gauge layout .....	167
6.3.1.4 Control Girder Strain Gauge Layout .....	168
6.3.2 Compressive Strength of Concrete .....	169
6.3.3 Results and Discussions .....	169
6.3.3.1 Girder-1 .....	169
6.3.3.2 Girder-2 .....	172
6.3.3.3 Girder-3 .....	181
6.3.3.4 Control Girder.....	184
6.3.3.5 Combined Results.....	188
Chapter 7 NUMERICAL MODELING .....	192
7.1 Analysis procedure .....	192
7.1.1 Fire Model.....	192
7.1.2 Heat Transfer and Mechanical Analysis.....	198
7.2 Material properties at elevated temperature.....	200



7.3 Results and discussion .....	205
Chapter 8 CONCLUSIONS AND RECOMMENDATIONS.....	209
8.1 Summary of Findings and Conclusions .....	209
8.2 Future Research .....	212
Appendix A: Shop drawings for girders.....	214
Appendix B: Prestressed concrete panel fabrication details.....	219
Appendix C: Material Properties at Elevated Temperature .....	221
References .....	231
Biographical Information .....	243

## List of Figures

Figure 1-1 Repair/strengthening philosophy (Carolin 2003) .....	2
Figure 1-2 Schematic sketch for variation of elastic modulus ( $E_T$ ) and tensile strength ( $f_T$ ) of adhesive (Borchert and Zilch 2005) .....	3
Figure 1-3 Standard Vs real fire .....	4
Figure 1-4 Hydrocarbon fire damaged SH183 bridge over MacArthur Boulevard (Sika Corporation 2006) .....	5
Figure 1-5 SH183 bridge over Macarthur Boulevard after FRP repair (Sika Corporation) .	6
Figure 2-1 The collapsed Hazel Park Bridge near Detroit, Michigan (Wojdyla 2009) .....	13
Figure 2-2 Collapsed MacArthur Maze Bridge (New York Times 2007).....	14
Figure 2-3 Bill Williams River Bridge fire (Marth et al. 2007) .....	15
Figure 2-4 The collapse of the under-construction Rancho Road Bridge due to accidental fire (Vives et al. 2014) .....	17
Figure 2-5 T-beams testing under ASTM E119 fire (Adelzadeh 2013) .....	26
Figure 2-6 FRP wrapped column before and immediately after fire test (Chowdhury 2009) .....	29
Figure 2-7 Variation of tensile strength of carbon, glass and aramid fibers with temperature (Ahmed 2010) .....	36
Figure 2-8 Variation of thermal conductivity and specific heat as a function of temperature for CFRP laminate (Griffis et al. 1981).....	38
Figure 2-9 Variation of tensile strength of CFRP composite as a function of temperature (Bisby 2003) .....	39
Figure 2-10 Variation of elastic modulus of CFRP composite as a function of temperature (Bisby 2003) .....	39
Figure 2-11 Variation of thermal conductivity of NSC with temperature (Kodur 2014).....	42

Figure 2-12 Variation of specific heat of NSC with temperature (Kodur and Khalid 2011)	43
Figure 2-13 Relative variation of compressive strength of NSC as a function of temperature (Kodur 2014)	44
Figure 2-14 Relative variations of compressive strength of HSC as a function of temperature (Kodur 2014)	45
Figure 2-15 Relative variations of tensile strength of HSC as a function of temperature (Kodur 2014)	46
Figure 2-16 Relative variations of modulus of elasticity of concrete as a function of temperature (Kodur 2014)	46
Figure 2-17 Stress-strain diagram of NSC at elevated temperatures (Kodur 2014)	47
Figure 2-18 Stress-strain diagram of HSC at elevated temperatures (Kodur 2014)	47
Figure 2-19 Variation of coefficient of thermal expansion of NSC with temperature	49
Figure 2-20 Illustration of spalling of concrete due to pressure buildup (Dwaikat 2009)	51
Figure 2-21 Illustration of spalling of concrete due to thermal dilatation (Khalid 2012)	51
Figure 2-22 Variation of thermal conductivity of steel with temperature (Eurocode 3, 2005)	53
Figure 2-23 Variation of specific heat capacity of steel with temperature (Eurocode 3, 2005)	53
Figure 2-24 Variation of Stress-strain curves as a function of temperature for mild reinforcing steel (Eurocode 3, 2005)	54
Figure 2-25 Variation of Stress-strain curves as a function of temperature for prestressing steel (Eurocode 3, 2005 and ASCE 1992)	54
Figure 2-26 Variation of ultimate strength with temperature for mild reinforcement and prestressing steel (Eurocode 3, 2005; ASCE 1992 and PCI 2004)	55

Figure 2-27 Variation of mild reinforcement and prestressing steel yield strength with temperature (Eurocode 3, 2005; ASCE 1992 and PCI 2004).....	56
Figure 2-28 Variation of mild reinforcement and prestressing steel modulus of elasticity with temperature (Eurocode 3, 2005; ASCE 1992) .....	57
Figure 2-29 Variation of mild reinforcement and prestressing steel thermal elongation with temperature (Eurocode 3, 2005; ASCE 1992) .....	58
Figure 2-30 Intumescent coating applied to steel girder (Davidson 2012); (a) before fire exposure; (b) after exposure to fire.....	60
Figure 3-1 PG Super model .....	62
Figure 3-2 Dayton Superior C25 45° adjustable half hanger .....	63
Figure 3-3 Test bridge deck .....	64
Figure 3-4 Reinforcement detail of the deck .....	64
Figure 3-5 Original proposed supporting walls and fuel tanker trailer .....	65
Figure 3-6 Previously tested TX28 Girders .....	66
Figure 3-7 The newly proposed test setup.....	67
Figure 3-8 Labeled girders .....	68
Figure 3-9 Longitudinal FRP layout .....	70
Figure 3-10 U-wraps layout.....	71
Figure 3-11 Fireproofing layout.....	72
Figure 3-12 Locations and labeling of thermocouples on bearing pads and girders .....	76
Figure 4-1 Strands and reinforcements cage .....	78
Figure 4-2 Thermocouple Installed at mid-web of the girder .....	78
Figure 4-3 Concrete casting of girders.....	79
Figure 4-4 Testing to check if the release compressive strength of concrete is attained. 80	
Figure 4-5 (a) Torch cutting of strands (b) Moving girders to the storage area .....	80

Figure 4-6 (a) Thermocouples end after concrete pour;(b) sealed thermocouples & hanger .....	81
Figure 4-7 Prestressed concrete bridge deck panels .....	82
Figure 4-8 The Dallas/Fort Worth International Airport’s Fire Training Research Center (www.dfwairport.com/firetraining/) .....	84
Figure 4-9 Test bridge construction site (map data: © 2016 Google).....	84
Figure 4-10 Test bridge construction schedule.....	86
Figure 4-11 Construction layout and staking survey.....	87
Figure 4-12 Setting of supports and girders.....	90
Figure 4-13 Setting of precast deck panels .....	91
Figure 4-14 Deck forming and concrete pouring .....	95
Figure 4-15 FRP and thermocouple installation .....	100
Figure 4-16 Application of Fireproofing.....	102
Figure 5-1 Arrangement of the design truck load for maximum moment .....	103
Figure 5-2 Loading of zipper barriers.....	104
Figure 5-3 Test bridge loaded with the simulated AAASHTO HL-93 live load .....	104
Figure 5-4 Mock-up fire test .....	105
Figure 5-5 Warping of side of the pan.....	106
Figure 5-6 Welding of additional stiffeners.....	106
Figure 5-7 CFD model computational domain .....	109
Figure 5-8 Direction of wind considered for CFD modeling (map data: © 2016 Google).....	111
Figure 5-9 PyroSim model .....	113
Figure 5-10 Variation of heat flux as a function of distance from the end of the bridge ..	114
Figure 5-11 Thermocouple extension wire.....	115
Figure 5-12 Opening between girders before and after placing the ceramic blanket.....	115

Figure 5-13 Firefighters and Firefighter trucks preparing for the test .....	116
Figure 5-14 Fire test.....	117
Figure 5-15 Uneven distribution of fire due to the wind .....	118
Figure 5-16 Labeling of supports .....	120
Figure 5-17 Temperature vs. time curve measured by thermocouple-1BO .....	121
Figure 5-18 Fire curves from pool fire versus standard fire .....	122
Figure 5-19 Measured temperature at FRP-concrete interface by the rmocouple 1AF & 1BF.....	123
Figure 5-20 Thermocouples under a pile of spalled concrete and charred carbon fibers .....	124
Figure 5-21 Measured temperature at the prestressing strands for Girder-1 (1AR and 1BBR).....	124
Figure 5-22 Girder-1 exposed/broken prestressing strands and exposed shear reinforcements after fire test .....	126
Figure 5-23 Temperature vs. time readings of thermocouple-1AM and thermocouple-1BM .....	127
Figure 5-24 Mid-span temperature vs. time reading of Girder-1 at different depths .....	128
Figure 5-25 Girder-1 after fire test: (a) Chunks of spalled concrete; (b) fuel pan filled with spalled concrete; (c) south elevation view of Girder-1; (d) bottom view of Girder-1.....	129
Figure 5-26 Temperature vs time measured at the FRP-fireproofing interface of Girder-2 .....	130
Figure 5-27 Smoke on the concrete underlying the fireproofing.....	131
Figure 5-28 Cracks on the fireproofing material .....	132
Figure 5-29 Fire temperature vs. temperature at the FRP/fireproofing interface for Girder- 2 .....	133

Figure 5-30 Temperature as a function of time at FRP-concrete interface for Girder-2.	133
Figure 5-31 Measured strand temperature for Girder-2.....	134
Figure 5-32 Measured temperature by Thermocouple-1BBR versus Thermocouple-2BBR .....	135
Figure 5-33 Exposed strands on Girder-2.....	135
Figure 5-34 Temperature vs. time reading of thermocouple-2AM and thermocouple-2BM .....	136
Figure 5-35 Mid-span temperature vs time reading of Girder-2 at different depth .....	136
Figure 5-36 Spalling of concrete on Girder-2.....	137
Figure 5-37 Measured strand temperature for Girder-3.....	138
Figure 5-38 Exposed top reinforcements and strand for Girder-3 .....	139
Figure 5-39 Girder-3 broken prestressing strand.....	139
Figure 5-40 Temperature vs. time reading of thermocouple-3CM.....	140
Figure 5-41 Temperature at the interface between deck and the girder .....	141
Figure 5-42 (a) Bottom of the deck between Girder-1 and Girder-2; (b) Bottom of the deck between Girder-2 and Girder-3 .....	142
Figure 5-43 (a) Overhang portion of the deck on Girder-1 side after the fire; (b) closer look at of the spalled concrete for the overhang portion of the deck on Girder-1 side ...	143
Figure 5-44 Overhang portion of the deck on Girder-3 side after the fire .....	143
Figure 5-45 Measured bearing pads temperatures .....	144
Figure 5-46 Deformation of bearing pad .....	145
Figure 5-47 Colors of concrete at different temperature.....	146
Figure 5-48 Rebound hammer test .....	147
Figure 5-49 Visual inspection of Girder-1 .....	149
Figure 5-50 Hardness testing values of Girder-1 in psi .....	150

Figure 5-51 Visual inspection of Girder-2 .....	152
Figure 5-52 Hardness testing values of Girder-2 in psi .....	153
Figure 5-53 Girder-3 covered with soot .....	154
Figure 5-54 Visual inspection of Girder-3 .....	155
Figure 5-55 Hardness testing values of Girder-3 in psi .....	156
Figure 5-56 Taking elevation measurement .....	157
Figure 5-57 reference point used for measuring the elevation of the mid-span of Girder-1 after the fire .....	158
Figure 5-58 reference point used for measuring the elevation of the mid-span of Girder-2 after the fire .....	158
Figure 5-59 reference point used for measuring the elevation of the mid-span of Girder-3 after the fire .....	159
Figure 6-1 (a) saw-cutting of the deck; (b) lifting of the girder; (c) Girder-1 after saw- cutting .....	160
Figure 6-2 (a) saw-cutting of the overhanging deck; (b) transportation of the girders to UTA CELAB .....	161
Figure 6-3 Control girder: (a) formwork; (b) reinforcement cage; (c) after the concrete pour .....	162
Figure 6-4 Schematic view of the test setup .....	163
Figure 6-5 Girder test setup .....	164
Figure 6-6 Girder-1 strain gauge layout .....	165
Figure 6-7 Installed strain gauges on Girder-1 .....	165
Figure 6-8 Girder-2 strain gauge layout .....	166
Figure 6-9 Strain gauges on (a) FRP; (b) prestressing strand; (c) concrete .....	167
Figure 6-10 Girder-3 strain gauge layout .....	167



Figure 6-11 Surface preparation before installing strain gauges on spalled concrete ...	168
Figure 6-12 Control girder strain gauge layout .....	168
Figure 6-13 Applied load vs mid-span deflection of Girder-1.....	170
Figure 6-14 Displacement profile of Girder-1 at different load levels .....	170
Figure 6-15 Broken prestressing strand.....	171
Figure 6-16 Strain on exposed prestressing strands of Girder-1.....	171
Figure 6-17 Girder-1 concrete strain profiles at different depths .....	172
Figure 6-18 Applied load vs mid-span deflection of Girder-2.....	173
Figure 6-19 First crack on Girder-2 at 110 kips .....	173
Figure 6-20 Deflection along girder length for various load increments of Girder-2.....	174
Figure 6-21 Labelling of U-wraps.....	174
Figure 6-22 Rupture of transverse FRP and debonding of longitudinal FRP .....	175
Figure 6-23 Failure of concrete and FRP in Girder-2 .....	176
Figure 6-24 Strain versus applied load at various points on the longitudinal FRP .....	177
Figure 6-25 Tensile strain in FRP versus length of girder at different load increments..	178
Figure 6-26 Strain versus applied load on U-wraps.....	178
Figure 6-27 Variation of neutral axis depth with load for Girder-2 .....	179
Figure 6-28 Variation of strain with applied load at the extreme concrete compression fiber for Girder-2.....	179
Figure 6-29 Load versus strain at various location on the concrete surface of the bottom flange.....	180
Figure 6-30 Strain on exposed prestressing strands of Girder-2.....	181
Figure 6-31 Applied load vs mid-span deflection of Girder-3.....	182
Figure 6-32 Deflection along girder length for various load increments of Girder-3.....	182
Figure 6-33 Cracks formed during fire and residual strength test .....	183

Figure 6-34 Applied load versus strain at the bottom of Girder-3 .....	183
Figure 6-35 Cracks underneath the strain gauge .....	184
Figure 6-36 Variation of strain with applied load at the extreme concrete compression fiber for Girder-3.....	184
Figure 6-37 Applied load vs mid-span deflection of the control girder.....	185
Figure 6-38 Deflection along girder length for various load increments of the control girder .....	185
Figure 6-39 Variation of neutral axis depth with load for the control girder .....	186
Figure 6-40 Strain versus applied load at the extreme concrete compression fiber for the control girder .....	186
Figure 6-41 Crack pattern of control girder .....	187
Figure 6-42 Applied load versus strain at various location on the bottom of control girder .....	187
Figure 6-43 Applied load versus midspan deflection for all the tested girders .....	189
Figure 6-44 Definition of yield displacement (Park, 1988) .....	190
Figure 7-1 Fire tested bridge Pyrosim model.....	193
Figure 7-2 Half section of Girder-2 considered for modeling .....	193
Figure 7-3 Temperature curve T-6.....	194
Figure 7-4 Temperature versus time curve T-4 .....	194
Figure 7-5 Temperature versus time curve T-5 .....	194
Figure 7-6 Strength reduction factors .....	196
Figure 7-7 Assignment of temperature curves.....	197
Figure 7-8 Temperature versus time curve T-1, T-2 and T-3 .....	197
Figure 7-9 Specific heat capacity and thermal conductivity for concrete.....	200

Figure 7-10 Variation of compressive stress-strain diagram with temperature for the girder concrete .....	201
Figure 7-11 Variation of compressive stress-strain diagram with temperature for the deck concrete .....	202
Figure 7-12 Variation of tensile stress-strain diagram with temperature for the girder concrete .....	202
Figure 7-13 Variation of tensile stress-strain diagram with temperature for the deck concrete .....	202
Figure 7-14 Variation of tensile stress-strain diagram with temperature for prestressing steel.....	203
Figure 7-15 Variation of tensile stress-strain diagram with temperature for mild reinforcement .....	203
Figure 7-16 Thermal Properties of VG insulation (Bisby 2003) .....	204
Figure 7-17 Variation of modulus of elasticity of FRP with temperature.....	204
Figure 7-18 FEM Model .....	206
Figure 7-19 Temperature distributions over the mid-span cross-section: a) t=15 min, (b) t=30 min, (c) t=45 min, (d) t=60 min.....	207
Figure 7-20 Numerical prediction versus experimental result for Girder-2: (a)FRP-concrete interface; (b) Insulation-FRP interface; (c) prestressing strand; (d) mid-height of the web of the girder; (e) deck-girder interface.....	208

## List of Tables

Table 2-1 Examples of bridge fire caused by fuel tanker truck.....	16
Table 2-2 Case studies of numerical modeling of bridges under fire .....	23
Table 2-3 Coefficient of thermal expansion of FRP composites (Mallik 1988) .....	40
Table 3-1 Design summary of girders.....	62
Table 3-2 TXDOT minimum requirements for FRP system to be used in structural strengthening (TXDOT 2015).....	69
Table 3-3 SikaWrap Hex 117C cured laminate design values .....	69
Table 4-1 TxDOT approved precast prestressed manufacturing plant.....	77
Table 4-2 Concrete mix proportions for the girders per cubic yards of concrete.....	79
Table 4-3 Concrete mix proportions for the precast deck panels per cubic yards of concrete .....	82
Table 4-4 Description of bridge construction tasks.....	85
Table 4-5 High early strength (HES) concrete mix design per cubic yards of concrete ...	92
Table 5-1 Consequences of thermal heat flux on human bodies (Zarate et. al 2008) ...	108
Table 5-2 Average wind gust speed and average wind speed history for fire test center for the months of January and February (www.wunderground.com) .....	110
Table 5-3 Compressive strength of concrete used for cast-in-place deck and girders ..	119
Table 5-4 Probable correlation between fire exposed concrete color & temperature (PCI 1989) .....	146
Table 5-5 Mid-span deflection of each girder.....	159
Table 6-1 List of strain gauges for Girder-2 .....	166
Table 6-2 Compressive strength of concrete at the time of residual strength test .....	169
Table 6-3 The strain and the applied load at failure of the broken strands .....	172
Table 6-4 Failure modes of the U-wraps.....	175

Table 6-5 Summarized results of residual strength tests.....	189
Table 6-6 Ductility factor for each girder .....	191
Table 7-1 Reduction factor for compressive strength of concrete (Eurocode 2, 2005b)	195

## **Chapter 1**

### **INTRODUCTION**

#### **1.1 Background**

Most of the U.S. bridges were put in place over 50 years ago; as their service lives are exceeding, many of them are in need of repair or strengthening. Increased traffic load requirements, the use of deicing salts, structural damage from vehicle impact and lack of adequate preventive maintenance contributed to the deterioration of existing bridges. According to ASCE 2013 report card for America's infrastructure, one in nine or 11 % of the nation's bridges are classified as structurally deficient, and 60,971 bridges have posted load restrictions. The federal highway administration (FHWA) estimates that it approximately needs \$76 billion to repair or replace the structurally deficient bridges. Although complete rebuilding is considered by some as the best option, considering the limited budget allocated by the Congress, repair/rehabilitation is far more economical in many cases.

Figure 1-1 shows the various scenarios that call for repair and strengthening of structures. The first scenario is when there is design or construction flaw. These include but not limited to omitting of important reinforcement, using poor quality construction material, improper construction of the design cross-section dimensions, and underestimating the design load. The second scenario is due to structural deficiency as a result of an accident which impairs the ability of the structure to carry the load safely. The third scenario is

when the structure is demanded to carry higher load; for instance, the American Association of State and Highway Transportation Officials (AASHTO) changed the design live load from HS-20 to HL-93.

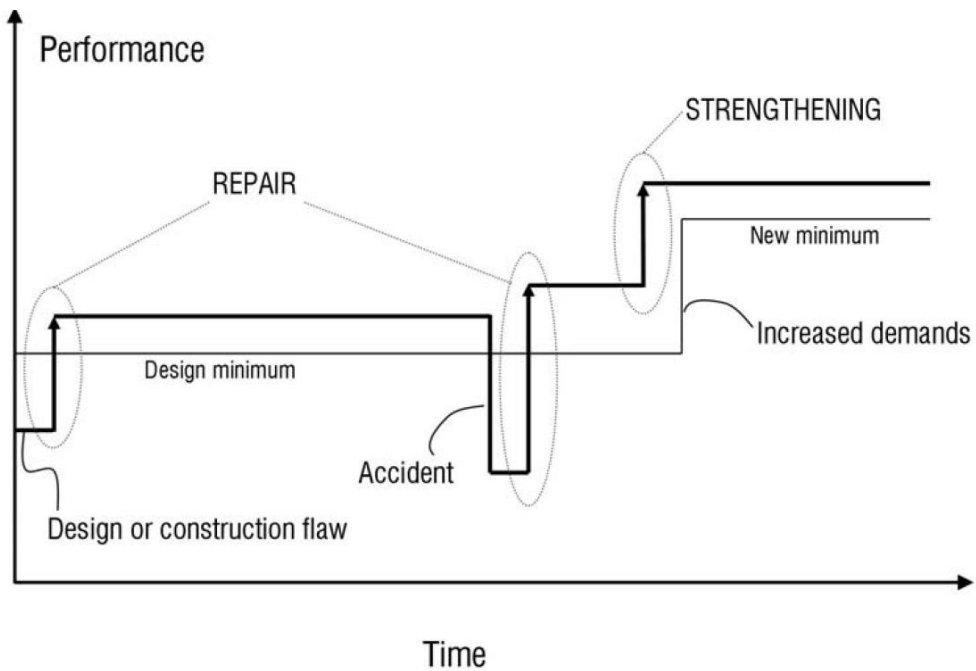


Figure 1-1 Repair/strengthening philosophy (Carolin 2003)

Some of the common methods of structural strengthening are externally bonded steel plates, steel or concrete jacketing, external post-tensioning and externally bonded fiber reinforced polymer (FRP). FRP has an advantage over the other methods. It has high strength-to-weight ratio, excellent corrosion resistance, quick and easy to installation and ease of application in areas where there is limited access. It is capable of substantially enhancing the flexural strength of structural members. Previous research documented that an increase in flexural strength ranging from 10% to 160% can be obtained from FRP strengthening (Meier and Kaiser, 1991; Ritchie et al., 1991; Sharif et al., 1994).

However, FRP suffers from a major drawback of having low fire resistance. The physical and mechanical properties of the resin are influenced by temperature and significantly degrade at a temperature close to and above the glass transition temperature,  $T_g$ , as shown in Figure 1-2. The  $T_g$  is a temperature range over which the resin changes from a glassy state to a viscoelastic state that occurs over a temperature range from 140 to 180°F (ACI 2008). Thus, if a structure retrofitted with FRP is designed for fire resistance rating, ACI 440 (2008) recommends ignoring the load resistance coming from the FRP.

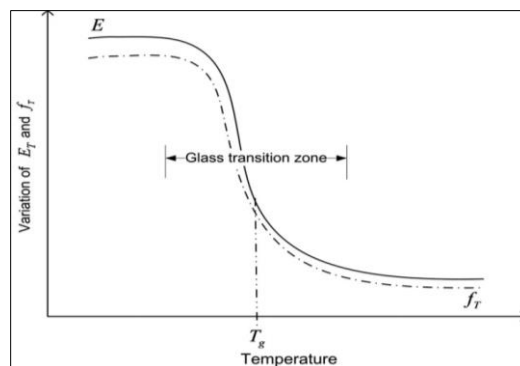


Figure 1-2 Schematic sketch for variation of elastic modulus ( $E_T$ ) and tensile strength ( $f_T$ ) of adhesive (Borchert and Zilch 2005)

Researchers proposed using a layer of insulation to maintain the fire safety of FRP-strengthened member after testing structural components like beams, columns, and slabs using standard fire. However, standard fire protocols, such as ASTM E119 (2014), ISO834 (2000) and CAN/ULC-S101 (2014) were developed for testing of building members not applicable for bridges. The majority of bridge fires are caused by crashing of vehicles and burning of fuels in the vicinity of the bridges, wildfire, and arson. These gasoline fires, also called hydrocarbon fires, are different from standard fires because of the following reasons:



- There is a difference in heating rate, fire intensity and the duration of fire between hydrocarbon and standard fire. Hydrocarbon fire is characterized by high fire intensity which can reach a very high temperature within the first few minutes of exposure.
- Standard fire test involves uniform heating of structural members which does not happen in a real fire scenario.
- Standard fire doesn't consider parameters that govern fire behavior such as variation of fuel load and ventilation.
- As shown in Figure 1-3, real fire has three different stages, the growth phase, fully developed phase and the decay phase. To the contrary, standard fire does not have the decay phase. However, the decay or the cooling phase is an important part of fire behavior due to large plastic strain that may develop in structural elements during heating. On cooling, these unrecoverable strains can produce large tensile forces which consequently leads to failure of connection or other components (Wang et al. 2013).

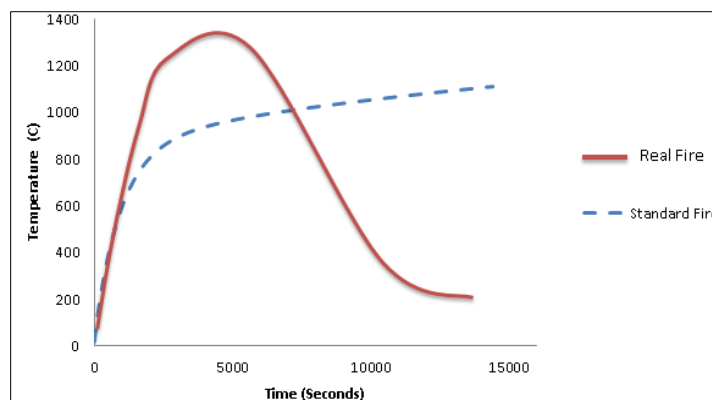


Figure 1-3 Standard Vs real fire

## 1.2 Problem Statement

On the morning of Saturday, May 28, 2005, a 3000-gallon fuel tanker heading east on State Highway 183, Irving, TX, barreled through a guardrail and spiraled off a bridge at about 6:30 am before landing upside down and exploding on MacArthur Boulevard (Sika Corporation 2006). The fire severely burned and cracked the bridge, as shown in Figure 1-4. It took firefighters 30 minutes to extinguish the blaze. After the accident, TXDOT engineers conducted a thorough evaluation and concluded that the damage was extensive and recommended repair. The repair process involved removal of 1000 ft<sup>3</sup> (14.2 m<sup>3</sup>) of delaminated concrete, applying wet spray-applied fiber reinforced mortar and finally strengthening with CFRP. Figure 1-5 shows the bridge after repair.

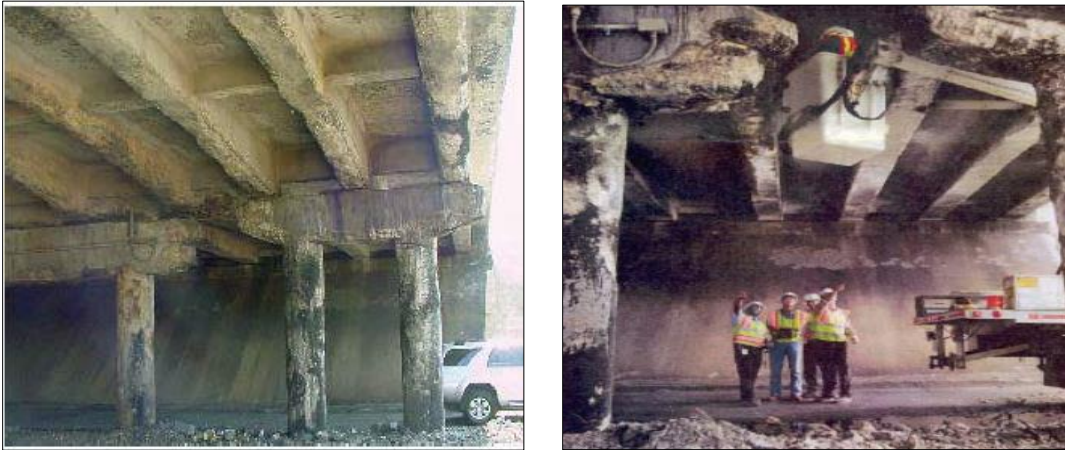


Figure 1-4 Hydrocarbon fire damaged SH183 bridge over MacArthur Boulevard (Sika Corporation 2006)



Figure 1-5 SH183 bridge over Macarthur Boulevard after FRP repair (Sika Corporation)

However, one question remains unanswered after the repair: what if the same type of incident happens (hydrocarbon fire) to the CFRP repaired Macarthur Blvd overpass? It is obvious that the FRP will lose its load resistance once the fire temperature reaches the glass transition temperature of the polymer. To protect the FRP in building strengthening application, the FRP is protected using fireproofing based on the recommendation from standard fire tests. There is no such recommendation when it comes to bridge application since no experimental or numerical work has been done to evaluate the performance of FRP repaired and insulated bridges.

The main impediments to widespread use of FRP on bridges are a lack of knowledge on the structural performance of FRP repaired bridges under fire and lack of tested and proven fireproofing material in the market. The current study proposed a fireproofing material to protect the FRP from hydrocarbon fire and study the performance of FRP strengthened and thermally insulated bridge girders under hydrocarbon fire.

### 1.3 Objectives

While provision for appropriate fire safety measure is a major design requirement in buildings, essentially no structural fire safety provisions for bridges exist. No experimental work has been done to date to study fire hazard in bridges. Looking at the statistics of bridge fire hazards and the substantial increase of petrochemical transport along the nation's vast network of highways, it is high time to conduct adequate research on bridge fire hazard that will lead to the development of structural fire safety provisions for design of new and repaired bridges. And also with the increasing popularity of FRP strengthening of deteriorated concrete bridges, the effect of fire on such repair schemes and adequate measures to make them fireproof need to be studied in depth.

The current research is pioneering in bridging the knowledge gap on the study of bridges in general and FRP- strengthened bridge girders specifically against fire hazard. The research is divided into three distinct phases. The first phase involved building the bridge, loading the bridge with the simulated HL-93 live load and finally subjecting it to hydrocarbon fire. The superstructure of the tested bridge comprised of three TX28 girders, 4" precast deck panels and 4" cast-in-place deck. The first girder was wrapped with carbon fiber reinforced polymer (CFRP), the second girder was wrapped with CFRP and sprayed with fire proofing, and the third girder was neither wrapped with CFRP or sprayed with fireproofing. The second phase involved saw cutting the deck, transporting the girders to the CELAB, concrete casting of control girder and performing residual strength test.

The third phase dealt with numerical modeling of the test bridge under fire to verify the experimental phase.

The research was conducted with the following main objectives:

- Investigate the overall thermal and mechanical response of the tested bridge under fire.
- Evaluate the performance of the proposed fireproofing in protecting the FRP.
- Evaluate the performance of FRP repaired bridge girder under fire.
- Study the effect of fire on the performance of the precast deck panels and cast-in-place deck.
- Evaluate the residual strength of each girder after the fire.
- Correlate the fire test results with the results from non-destructive evaluation and visual observation.
- Providing a benchmark experiment for industry practitioners who are pushing for performance-based design approach.
- Verify the capability of currently available numerical modeling techniques.

#### 1.4 Organization of the Dissertation

This dissertation is organized into eight chapter. The content of each chapter is described as follows.

##### *Chapter 2- Literature Review*

This chapter presents a review of previously conducted experimental and numerical studies on the effect of fire on bridges as well as on FRP strengthened structure members. Review of documented bridge fire incidents across the nation is presented. The thermal and mechanical properties of concrete, mild

reinforcement, prestressing steel, fiber, matrix and composites at elevated temperature is also discussed.

#### *Chapter 3- Test Bridge Design*

The design of the various components of the test bridges and the instrumentation plan are presented. It includes the design of girders, deck, support, FRP and fireproofing.

#### *Chapter 4- Test Bridge Construction*

This chapter discusses the construction of the test bridge and fabrication of the precast components. It also gives an overview of the fire testing center.

#### *Chapter 5- Fire Test*

The preparations made before the fire test are first described. These include live loading of the test bridge, fuel flow rate determination, determination of safe standing distance and determination of the duration of the fire. The results of the fire test are then presented in terms of the thermal and mechanical response of the test bridge.

#### *Chapter 6: Demolition of the Test Bridge and Determination of Residual Strength*

This chapter presents the demolition of the test bridge and transportation of the girders to UTA CELAB. The test setup and the results of the residual strength test of each girder are discussed in detail.

#### *Chapter 7- Numerical modeling*

This chapter discusses the numerical modeling performed to verify the response of the test bridge under fire.

*Chapter 8- Summary, conclusions and recommendations*

The summary of the research conducted is presented. The conclusions drawn from the fire test, residual strength test, and numerical modeling are outlined. Recommendations that need further research are finally discussed.

## **Chapter 2**

### **LITERATURE REVIEW**

#### **2.1 Bridges and Fire Hazard**

Fire is one of the most severe threats to the integrity and safety of bridges. It might be wrongly assumed that the design of new or FRP repaired bridges should not consider fire since bridge fire hazard has a low probability of occurrence. However, data from voluntary bridge failure survey of highway departments (18 respondents, seismic states like California participated in the survey), showed that fire had caused more bridge collapse than earthquake (Wright et al., 2013; Alos-Moya et al. 2014). Another study by Mueller (2015) found that during just the first week of August 2014, nearly ten tanker truck crashes and fires occurred on the country's highway system. Significant attention has been given towards researching the effect of other accidental extreme load events, such as earthquake, wind, flood and vessel collision on bridges, as compared to fire hazards, even though fire hazards in bridges can cause significant economic and public losses. The economic losses have a direct cost of repair or reconstruction and indirect costs involving time and energy loss because of traffic congestion and detours and impacts on the local economy (Gong et al. 2014). Any damage to a bridge in a big metropolitan area will lead to a prolonged lanes closure which will result in significant economic and social impacts to the entire metropolitan area.

Bridges are susceptible to fire due to the constant presence of vehicles and the potential for crashed or overturned vehicles to become fuel sources due to their



flammable content. Vehicles involved in collision also cause a threat to bridges due to the combustion of their contents, including the onboard hydrocarbon fuel and, increasingly common, hybrid batteries (Quiel et al. 2015). Of all these, the most severe damage is caused when big trucks transporting large quantities of combustible cargo, hydrocarbon fuel or other flammable materials involve in a collision around the vicinity of the bridge. The following are some of the fire incidents caused by trucks transporting flammable liquids.

On July 15, 2009, a tanker truck transporting 49.2 m<sup>3</sup> (13,000 gallons) of flammable liquid under a 9-mile road overpass over the I-75 expressway near Hazel Park, Michigan was involved in an accident with another car which resulted in a fire. The bridge comprised of 10 hot-rolled steel girders each spanning 24 m (78'8") and supporting RC slab. The fire generated intense heat reached a temperature as high as 1,100°C and caused the overpass to collapse in about 20 min after the start of the fire as shown Figure 2-1 (Kodur et al. 2013). Luckily, the accident and bridge collapse did not result in any fatalities or significant injury. However, the loss of the bridge cut the main link between the east and west portions of Hazel Park and divided its main business district into two. The bridge replacement and the freeway reconstruction incurred a cost of \$12 million to Michigan department of transportation (High Steel Structures LLC, last accessed June 16, 2016)



Figure 2-1 The collapsed Hazel Park Bridge near Detroit, Michigan (Wojdyla 2009)

Another example is the MacArthur Maze fire collapse. The MacArthur Maze is a collection of seven freeways located to the east of San Francisco-Oakland Bay Bridge in California. On April 29, 2007, a tanker truck hauling 32.6 m<sup>3</sup> (8600 gals) of gasoline on I-80/880 overturned and burst into flame underneath the I-580 expressway which consisted of six plate girders supporting a reinforced concrete deck. Firefighters arrived at the site 14 min after the incident. The temperature from the heat reached 1,110°C. This led to the loss of strength of the steel girders and finally to collapse of the bridge 22 min into the fire as shown in Figure 2-2. The fire caused an estimated \$6 million a day total impact to the bay area (Chuang et al. 2008). The repair involved replacing the 12 longitudinal girders and the single box girder supporting them. The incident cost \$9 million to repair the bridge, and retrofitting took months to finish (Astaneh-Asl et al. 2009).



Figure 2-2 Collapsed MacArthur Maze Bridge (New York Times 2007)

The fire for both the above-cited cases occurred when the trucks were passing underneath the bridge, but the fire could also start due to overturned tanker truck on the top of the bridge deck. One example for such a case is Bill Williams River Bridge fire in Arizona which occurred on July 28, 2006, shown Figure 2-3. The bridge was built in 1967 comprised of fourteen 23.2 m (76 ft) simple spans and two 9.1 m (30 ft) concrete approach slabs. The tanker truck hauling 28.8 m<sup>3</sup> (7600 gals) of diesel, overturned in the middle of the concrete bridge and spilled the fuel which consequently caught fire. The majority of the burning occurred on the bridge deck which lasted about two and half hours. It damaged three spans including the concrete deck and barrier on the top and the pier beam, concrete girders and underside of the deck. Considering the severity of the fire, the bridge survived the collapse, except for the east overhang. The

exterior girders and the deck overhangs were the sections with the most severe localized damage (Kodur et al. 2010).



Figure 2-3 Bill Williams River Bridge fire (Marth et al. 2007)

Table 2-1 shows more examples of bridge fire caused by fuel tanker truck. Unlike other natural hazards, a comprehensive statistical data specific to fires on bridges are not widely available. The author didn't find a database that is specifically dedicated to keeps track of bridges fires occurring in the nations. Fire statistics are collected by the authority of the National Fire Incident Reporting System (NFIRS) managed currently by the Department of Homeland Security (DHS) and its sub-agency the Federal Emergency Management Agency (FEMA). NFIRS publish several annual reports based on the information collected from fire departments from all over the country. But these reports provide little to mention of fires occurring on, below or near bridges (Woodworth 2013).

Table 2-1 Examples of bridge fire caused by fuel tanker truck

<b>Bridge and location</b>	<b>Date</b>	<b>Cause of fire</b>	<b>Bridge material</b>	<b>Damage description</b>
Stop Thirty Road, State Route 386 Nashville, TN, USA	June 20, 2007	A fuel tanker truck rear-ended a loaded dump truck. The tanker erupted into flames beneath the bridge.	Concrete hollow box-beam Bridge	The bridge sustained very little damage, and traffic was reopened after minor repairs
Belle Isle Bridge in NW Expressway, Oklahoma City, OK, USA	January 28, 2006	A truck crashed into the bridge	Concrete deck (precast prestressed I-girders + cast in place reinforced concrete slab)	Concrete girders were slightly damaged by the fire The safety of the bridge was assessed, and the bridge was reopened to traffic
Bridge over the Norwalk River near Ridgefield, CT, USA	July 12, 2005	A tanker truck carrying 30.3 m <sup>3</sup> of gasoline overturned, caught fire and burned out on the bridge	Concrete deck (precast prestressed box girders + cast in place reinforced concrete slab)	The deck was replaced by a new one
I-95 Howard Avenue Overpass in Bridgeport, CT, USA	March 26, 2003	A car struck a truck carrying 30.3 m <sup>3</sup> of heating oil	Composite deck (steel girders + reinforced concrete slab)	Collapse of the southbound lanes and partial collapse of the Northbound lanes
I-20/I-59/I-65 interchange in Birmingham, AL, USA	January 5, 2002	A loaded gasoline tanker crashed	Steel girders	The main span sagged about 3 m (10 feet)
I-80W/I-580E ramp in Emeryville, CA, USA	February 5, 1995	A gasoline tanker crashed	Composite deck (steel girders + reinforced concrete slab)	Deck, guardrail, and some ancillary facilities were damaged

In addition to vehicle collision and burning of hydrocarbon fuel, fire in bridges could also be caused by other potential sources like arson and wildfire. One example is a grass fire that took down a timber bridge near Procupine Plain in Saskatchewan, Canada. On March 25, 2016, a local landowner was trying to burn a grass off walking paths in the area when the fire got out of control and hit

the creosote-soaked posts and consequently led to the complete collapse of the bridge (CBCnews 2016).

Like most hazards, fire on bridges is not predictable. The incidents could happen on old, newly opened or on bridges which are under construction. The severity of the damage it causes depends on the amount of fuel, the location, and properties of fire source, the prevalent wind in the area, response time of firefighter, access to hydrants and type of construction material used. The fire on the under-construction Rancho Road bridge in Hesperia, California which happened on May 6, 2014, is one example of fire on bridges under construction. The fire started when a blowtorch used to cut reinforcement bars ignited a wooden formwork of the bridges. The fire caused a complete collapse of the girders and destroyed the laid-out reinforcement for the deck. The fire is exacerbated by erratic wind gusting up to 35 mph which made it difficult for firefighters to get water on the flames and the limited access to hydrants (Vives et al. 2014).



Figure 2-4 The collapse of the under-construction Rancho Road Bridge due to accidental fire (Vives et al. 2014)

Looking at the cases studies discussed and the various available data calls for measure to be taken to protect these critical infrastructures. While there are various available appropriate fire safety provisions for design of buildings, the risk of bridge fire is largely unaddressed in relevant standards. The only document that tried to address fire safety for bridges is the NFPA 502: Standard for Road, Tunnels, Bridges and Other Limited Access Highways (NFPA 502). The chapter 6 provision for bridges and elevated highways states that “critical structural members shall be protected from collision and high-temperature exposure that can result in dangerous weakening or complete collapse of the bridge or elevated highway”. Even though the standard states that bridges should be protected from “weakening or complete collapse,” it does not provide specific guidelines on how to protect them from a fire which makes it an ambiguous statement. In an attempt to bridge this gap, researchers like Kodur and Naser (2013) developed an approach to determine an importance factor to design bridges for fire hazards. The approach is like the one currently used to determine wind and snow loadings in buildings. They derived the importance factor by assigning weighting factors to key characteristics of bridges, such as geometrical features, material properties, design characteristics, traffic demand, hazard (risk) likelihood, expected environmental damage and economic consequences from the fire accident. Considering these factors, the bridges are categorized into low, medium, high and critical risk grade each with corresponding importance factor. Performance-based design that considers life safety and property protection is the another approach suggested by

researchers (Kodur et al. 2010). But one of the obstacles for moving forward with this approach is the lack of knowledge about bridges response to fire hazard.

A Large number of standard fire tests were conducted to date which are the basis for structural fire safety design guidelines of buildings. However, no experiment has been done in the US or in the world to study the effect of fire on bridges since full-scale fire experiments are not only difficult but also cost-prohibitive. All the studies are entirely numerical which are based on forensic investigation data of past bridge fire events. The numerical modeling involved modeling of the fire and conducting a thermo-mechanical analysis. The fire modeling is normally performed employing a standard fire curve, computational fluid dynamics (CFD) or using analytical calculations. The thermo-mechanical analysis is performed using finite element analysis (FEM) software like ANSYS and ABAQUS.

To simplify the complex modeling of fire, engineers prefers to use standard hydrocarbon fire curve such as in Eurocode-1 (2002) on bridge elements that are believed to be exposed to fire. The equation for the curve is given by:

$$T = 1080(1 - 0.325e^{-0.167t} - 0.675e^{-2.5t}) + T_0 \quad 2-1$$

Where:  $t$  is the time in minutes and  $T_0$  is the ambient temperature.

This approach is performed with the assumption that the surface temperature of the structural element is the same as the fire's temperature time history which avoids the procedures or the need for heat transfer calculation that accounts for the standoff or orientation of the structure to the fire. The standard fire spatial distribution on the bridge must, therefore, be determined by the user. This



method involves a lot of approximation and potentially deliver a conservative prediction of the fire's effect since the applied temperature of the standard hydrocarbon curves are based on an empirical worst-case for fire growth (Quiel et al. 2015). Since standard fire curves don't have a decay phase, they can only be used to determine a time to failure rather than to calculate whether the exposed bridge would survive the duration of the fire event. Paya-Zaforteza and Garlock (2015) studied the response of steel girder bridge to fire by employing the standard fire curve as defined in Eurocode-1(2002) and the fire curve proposed by Stoddard (2004). From the research, it was concluded that restraint to the bridge deck expansion coming from adjacent span should be considered during modeling and it is also found out that the collapse time for girders made of stainless steel is almost twice that of carbon steel.

On the contrary to the simplified hydrocarbon fire curve, a more complex structural fire analysis of bridges in a research or forensics application has been performed using computational fluid dynamics (CFD) software packages, such as the Fire Dynamics Simulator (FDS) developed by the National Institute of Standards and Technology (NIST), to calculate the heat transferred to the bridge elements from the defined fire. Building the CFD model requires defining: (1) a control volume with its boundary conditions which represents the volume where all the analysis will be carried out, (2) a geometry included in the control volume which is submitted to fire load, (3) a mesh or a discretization of the control volume, (4) material properties (conductivity, density, specific heat and emissivity), (5) fire sources, (6) a combustion model. The model will predict the values of variables

such as temperatures, heat fluxes or gas pressures from the fire event. These methods are more robust and generate significant levels of numerical resolution but have their limitations. First, they are computationally expensive and may not be practical in many applications. Second, these models require a large amount of input which most of the time are assumed due to their unavailability on literature. Third, transferring the temperature from the CFD software to the thermo-mechanical analysis is complicated.

Wright et al. (2013) simulated the I-65 bridge fire in Birmingham, Alabama. FDS was used for the fire analysis and Abaqus for the thermo-mechanical analysis. The result obtained under-predicted the bridge damage because of the limited knowledge about the fire event and the simplifications of the model. However, the method was able to reproduce the behavior of the bridge with good accuracy. They also conducted a parametric study to investigate the effect of fire power and fire location on the bridge behavior.

The analytical calculation method is intermediate between the standard fire curve and CFD modeling in terms of its complexity. The method involves determining fire characteristics based on idealized and semi-empirical combustion models. Bennetts and Moinuddin (2009) used this approach to study the effect of fire on structural elements of cable-stayed bridges. They used calculations of the heat release rate for a tanker truck fire on the bridge deck to estimate the magnitude of maximum fire exposure (applied as a surface temperature based on a peak heat flux) experienced by the cables (which were thermally modeled using

layered lumped masses). Table 2-2 depicts the various numerical studies conducted by researchers to evaluate the performance of bridges under fire.

Table 2-2 Case studies of numerical modeling of bridges under fire

Modeling Approach	Authors	Location	Bridge Type	Fire Model	Heat Transfer Model	Structural Model
Hydrocarbon fire and other simplified methods	Dotrepe et al. (2005)	Vivegnis Bridge, Liege, Belgium	Tied steel arch plus concrete deck	Standard hydrocarbon fire curve	Applied temperature time history to "exposed" surfaces of 2-D solid element thermal FE cross-sections	Beam and shell elements for structural FE model of the bridge
	Liu et al. (2015)	MacArthur Maze, Oakland, CA, USA	Steel girders with concrete deck	Standard hydrocarbon fire curve	Applied temperature time history to "exposed" surfaces of 3-D solid element thermal FE model	Solid and shell elements for structural FE model of a single girder and slab
	Kodur et al. (2013)	Hypothetical	Steel girders with concrete deck	Standard hydrocarbon fire curve	Applied temperature time history to "exposed" surfaces of 3-D solid element thermal FE model	Solid and shell elements for structural FE model of a single girder and slab
	Aziz and Kodur (2012)	Hypothetical	Steel girders with concrete deck	Standard hydrocarbon fire curve and two design fires	Applied temperature time history to "exposed" surfaces of 3-D solid element thermal FE model	Solid elements for structural FE model of a single girder and slab
CFD Modeling	Choi (2008)	MacArthur Maze, Oakland, CA, USA	Steel girders with concrete deck	Constant heat release rate per unit area of 250kW/m <sup>2</sup>	Applied temperature time histories based on CFD modeling to 3-D solid FE model	Solid elements for structural FE model of the overpass bridge
	Bajwa et al. (2012)	MacArthur Maze, Oakland, CA, USA	Steel girders with concrete deck	Constant fire temperature of 1100°C	Applied temperature time histories based on CFD modeling to 2-D solid FE model	Solid elements for structural FE model of the overpass bridge
	Alos-Moya et al. (2014)	I-65 Overpass, Birmingham, AL, USA	Steel girders with concrete deck	Several constant heat release rates per unit area that are representative of a burning tanker truck	Applied temperature time histories based on CFD modeling to 3-D solid FE model	Solid elements for structural FE model of the overpass bridge
	Tonicello et al. (2012)	Hans-Wilsdorf Bridge, Geneva, Switzerland	Helical steel arch bridge	Heat release rate time histories for burning vehicles from published sources	Assigned isotherm temperature time histories to finite elements based on CFD modeling	Beam and shell elements for structural FE model of the bridge
Analytical calculation	Astaneh et al. (2009)	MacArthur Maze, Oakland, CA, USA	Steel girders with concrete deck	Constant fire temperature of 1200°C	Analytically calculated heat flux from a "fire bath" solid flame model, applied to 3-D solid element thermal Fe model	Solid element structural FE model of the overpass bridge

## 2.2 FRP Strengthened Structures and Fire

FRP was developed and put to use first by the marine, aerospace, and automotive industries during the 1960s and 1970s (Harris et al. 2003). Using of FRP for civil infrastructure in the USA was started in late 1980 (GangaRao and Vijay 2010). FRP is one of the best choice when it comes to repair and rehabilitation of bridges due to its superior mechanical properties, ease of installation and cost effectiveness. Currently, 24 highway departments in the U.S.A. are using the bridge strengthening technique, and several others states are in the process of adopting it (Mohanamurthy and Yazdani 2015). Despite these advantages, its poor fire performance is one of the impediment for widespread use. Thus, several standard fire tests were conducted over the past two decades to evaluate the performance of FRP-strengthened structural members.

In the following subsections, a review of previously conducted experimental and numerical studies on the fire performance of FRP-strengthened structural members is presented.

### 2.2.1 Experimental Studies

#### **FRP-strengthened reinforced concrete beams**

Various experiments were conducted around the globe to evaluate the performance of FRP-strengthened structural members when subjected to fire. The earliest experiments date back to 1994 (Deuring). Deuring (1994) conducted ISO 834 standard fire tests on six rectangular RC beams with externally bonded carbon fiber reinforced polymer (CFRP) strips and steel plate. The beams were 400 mm x 300 (15.75 in. x 11.81 mm) in cross-section and 5 m (16.4 ft.) in length.

The samples consisted of one un-strengthened RC beam, one beam with adhesively bonded steel plate and four beams strengthened with CFRP strips, out of which two were tested with calcium silicates board insulation of different thickness and the other two without insulation. The test results showed that the insulation system helped to keep the temperature at the interface between the concrete and the FRP low. On the other hand, the FRP-strengthened beam without insulation lost the bond between the FRP and the concrete within 20 minutes.

Fire tests were also conducted on T-beams like the research by Williams et al. (2008) and Adelzadeh (2013). Williams et al. (2008) conducted ASTM E119 standard fire test on two T-beams strengthened with CFRP and protected with commercially available VG insulation system. The test results showed that the beams achieved more than four-hour fire rating under the ASTM E119 criteria. However, the FRP-concrete interface reached the glass transition temperature an hour after fire exposure. Adelzadeh (2013) evaluated the performance of two T-beams strengthened for flexure using CFRP and insulated with spray applied fireproofing under ASTM E119 fire (Figure 2-5). The beams were simultaneously subjected to fire and externally applied load for four hours. It was also found out from this experiment that a fire endurance of more than four hours can be achieved using an appropriate insulation system. But the temperature at the FRP-concrete interface exceeded the glass the transition temperature in less than 30 minutes.



Figure 2-5 T-beams testing under ASTM E119 fire (Adelzadeh 2013)

The performance of FRP strengthened, and insulated beams depend on several factors. This includes the thickness of fireproofing, types of fireproofing, fireproofing layout, anchorage configurations, concrete strength, types of FRP, the fire load ratio (fire load ratio is defined as the ratio of the load sustained during fire exposure to the ultimate load), etc. Blontrock et al. (2000) conducted ISO 834 fire test on CFRP strengthened RC beam by varying several parameters of the insulation scheme including thickness, location, method of bonding and overall length. The test program used ten reinforced concrete beams 300 mm (12 in.) deep, 200 mm (8 in.) wide and spanned 3.15 m (10.3 ft.). Two of the beams were statically loaded to failure; two plain RC beams were loaded to service load level then exposed to fire; the other six RC beams were strengthened with CFRP and protected with insulation. The test result showed that compared to the insulation

scheme that covers the bottom of the beam only, the U-shaped insulation scheme was effective in reducing the temperature of CFRP and the steel which subsequently resulted in small deflection at the end of the test. The research also found that the bond between the CFRP and the concrete degraded significantly once the glass transition temperature is reached. An interesting finding of this study was, insulation applied only within the anchorage zones of the FRP was able to preserve the bond between FRP and concrete up to 38 minutes into the test.

The type of FRP used also have an effect on the performance of FRP repaired beams in fire. Tan and Zhou (2011) evaluated the performance of beams strengthened with Glass and Basalt FRP subjected to an elevated temperature using electrical furnace. Twenty-five specimens comprising of unstrengthened and strengthened beams as well as with and without fireproofing were used for the study. The research result indicated a general decrease in initial stiffness and ultimate strength of the beams with an increase in exposed temperature. The provided insulation system was effective in preserving the structural integrity of Glass FRP when the temperature was less than approximately 700°C. Compared to the Glass FRP strengthened beams, Basalt FRP strengthened beams displayed a smaller deterioration in ultimate strength.

Rein et al. (2007), Barns and Fidell (2006) and Stratford et al. (2009) reported similar studies on the performance of CFRP strengthened beams under standard fire. All of the previously done research involved only reinforced concrete beams. To the author knowledge, no experimental work has been done to date to study the performance of FRP strengthened prestressed concrete girder in fire.



### **FRP-strengthened reinforced concrete slabs**

Compared to the research on FRP-strengthened beams, a relatively small number of experimental researches were conducted on FRP-strengthened concrete slabs. Williams et al. (2005) studied the performance of FRP-strengthened and thermally insulated slabs under ASTM E119 standard fire. Four slabs, each with a dimension of 954 mm (3.13 ft.) in width, 1331 mm (4.37 ft.) in length and 150 mm (5.9 in.) in thickness were used. Two of the four slabs were strengthened and protected with FRP and insulation systems provided by Fyfe Co. LLC, and two were strengthened and protected with systems provided by Degussa Building Systems. Slab 1 and 2 were protected with 19 mm (0.75 in.) and 38 mm (1.5 in.) spray-applied VG fireproofing material. Whereas slab 3 was protected with 38 mm (1.5 in.) MBrace insulation 1 and slab 4 with 38 mm (1.5 in.) MBrace insulation 2. The result of the experiment showed that a 4-h fire endurance rating can be achieved with 38 mm (1.5 in.) of any of the four insulation schemes studied. However, the glass transition temperature was exceeded at 42, 104, 46 and 52 min for slabs 1 through 4, respectively. It is also concluded from the research, providing adequate insulation thickness plays a pivotal role to minimize cracking and preventing delamination of fireproofing material.

Adelzadeh (2013) conducted ASTM E119 fire test on two slabs which were strengthened with CFRP and insulated with Sikacrete-213F. 40 mm and 60 mm thick fireproofing was provided on each slab. As expected, the slab with 60 mm (1.575 in.) thickness of fireproofing had a lower temperature reading compared to the one with 40 mm (2.36 in.) thickness. The glass transition temperature of the

matrix at the FRP-concrete interface was exceeded in less than 30 minutes for both slabs. Similar studies were also conducted by Blontruck et al. (2001) and Kodur et al. (2004).

### **FRP-strengthened reinforced concrete Columns**

Extensive research was performed to study the performance of FRP confined concrete columns at ambient temperature (Pessiki et al., 2001; Lilliston and Jolly, 2000; Xiao and Wu, 2000; Spoelstra and Monti, 1999; Saafi et al., 1999; Toutanji, 1999; Saaman et al., 1998; Karbhari and Gao, 1997, etc). These researchers concluded that FRP confinement of columns increases its axial capacity. Compared to the number of research at ambient temperature, a limited number of studies were conducted at elevated temperature. Figure 2-6 shows a typical standard fire test on CFRP wrapped column.

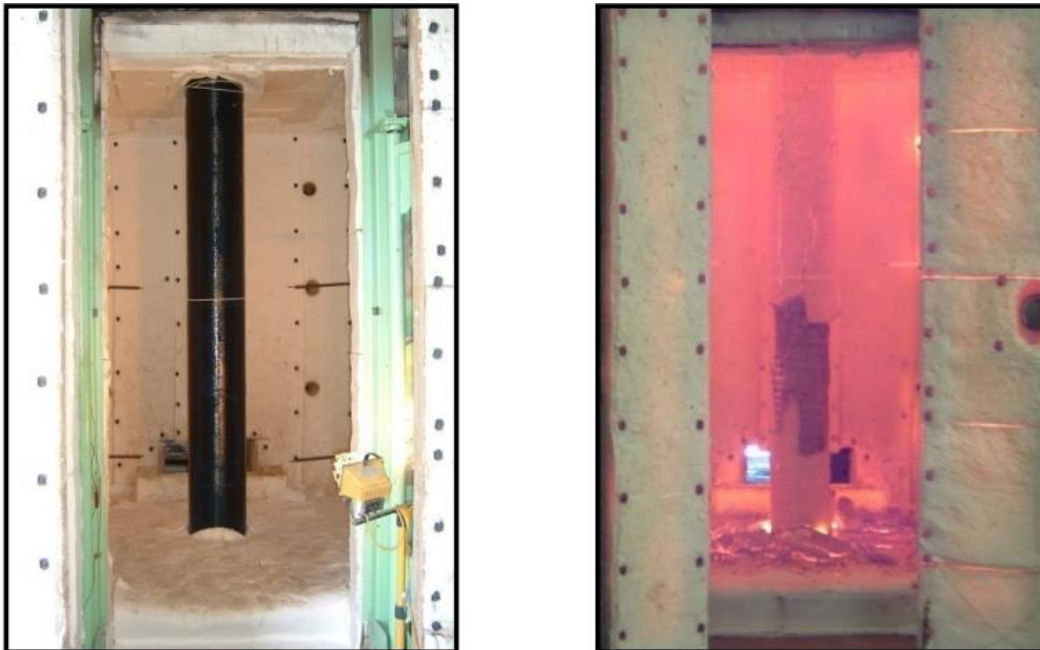


Figure 2-6 FRP wrapped column before and immediately after fire test (Chowdhury 2009)

Bisby et al. (2005) studied the fire endurance of FRP confined concrete columns. The study involved two full-scale circular CFRP-wrapped RC columns and insulated with a fireproofing material. Both columns have a diam of 400 mm (15.75 in.) and an overall height of 3.81 m (12.5 ft.). A single layer of CFRP was applied aiming a 53 % increase in ultimate load capacity. The first column was insulated using 57 mm (2.24 in.) of VG insulation and the second column was protected with 32 mm (1.26 in.) of the same type of insulation. The columns were tested under ASTM E119 fire while simultaneously subjected to a constant sustained axial load of 2515 kN (565.4 kips). Both columns achieved a fire rating of greater than 5 hours according to the ASTM E119 fire criterion. The study also found out that the temperature of the FRP wrap can be kept below 100°C for up to 4 hours provided that it is covered with an adequate thickness of insulation.

Another study by Kodur et al. (2005) evaluated the fire performance FRP strengthened and insulated square reinforced concrete column. Two full-scale square RC columns, one unstrengthened RC column and one FRP-wrapped and insulated RC column, were used for the study. The FRP strengthening involved using three layers of glass FRP (GFRP). The strengthened column is provided with Tyfo VG insulation in combination with Tyfo EI-R paint. Both columns were subjected simultaneously to ASTM E119 fire and sustained concentric axial compressive load. It was found out from the experiment that an FRP strengthened and insulated column was able to achieve a fire endurance rating of 4 hours or more according to the criterion set in CAN/CSA-S101 and ASTM E119 standards.

Visual observation of the insulation during the fire test revealed, it remained intact with only minimal cracking for the duration of the test.

### 2.2.2 Numerical Studies

Full-scale fire test is instrumental in understanding the performance of structural members in fire. However, it is cost prohibitive as well as time-consuming. Hence, developing an effective numerical model is ideally suited to conduct the required study without incurring much cost. Likewise, researchers have made attempts to develop a computer program or used commercially available software to study the performance of FRP-strengthened structural members under fire.

Williams et al. (2008) developed a 2D numerical heat transfer model to predict the temperature at various points within the cross section of the FRP-strengthened and insulated beam. The model involves discretizing the beams into nodal points and then applying thermal equilibrium equation to determine the temperature at each successive time steps using an explicit finite difference formulation. The developed numerical scheme was verified by modeling FRP-strengthened and thermally insulated T-beam subjected to standard fire. Overall, the model provided a reasonable estimate of temperatures at various locations. Hawileh et al. (2009) also developed a numerical model of the same T-beam using commercially available finite element software ANSYS. The model took into consideration variation in thermal and mechanical properties of concrete, steel, and FRP. A non-linear transient thermal-stress analysis was performed to evaluate the thermal and mechanical response of the beam. The temperature predicted by

the numerical model displayed an overall good agreement with the one measured in the experiment.

Liu et al. (2009) developed a two-stage numerical analysis procedure to study the performance of FRP-strengthened and insulated RC beam: a finite-difference heat transfer analysis to predict the temperature fields within the beam, and structural analysis to estimate the load-bearing capacities. The heat transfer analysis used a 2-dimensional explicit finite-difference heat transfer model that discretize the beam cross-section and the supplemental fire insulation into series of rectangular elements. The temperature of each element was then determined by successively applying simple thermal equilibrium equation. After determining the temperature distribution throughout the mid-span cross-section, the flexural capacity of the beam is determined using strain compatibility. The developed numerical scheme was then used by the researchers to conduct parametric studies on the effect of span-to-height ratio, confinement ratio, the thickness of the concrete cover, the thickness of fire insulation and tensile reinforcement ratio on its capacity.

Dai et al. (2014) developed a 3D finite element model using a commercially available software ABAQUS. The model is unique in such a way it considers the bond-slip behavior of FRP-to-concrete and steel-to-concrete interfaces. Previously tested FRP-strengthened and insulated beams by Blontrock et al. (2000), Gao et al. (2010) and Williams et al. (2008) were used to verifying the capability of the proposed numerical scheme. It satisfactorily predicted both the thermal and

mechanical response of flexure-dominated beams. However, the accuracy of the numerical scheme needs to be checked for shear-dominant beams as well.

Numerical models were also developed by researchers to study the heat transfer behavior and load carrying capacity of FRP-confined and thermally insulated columns like Bisby et al. (2005). The proposed procedure used a finite-difference method to get the temperature distribution and strain-equilibrium analysis to determine the axial load carrying capacity. Data available in literature from full-scale fire endurance tests of conventionally reinforced concrete columns were used to check the accuracy of the model. It was found out that the model agreed well with the experimental data obtained from the tests.

### 2.3 Materials Properties at Elevated Temperatures

The thermal and mechanical responses of reinforced or prestressed concrete member subjected to a fire depend on the properties of the constituent materials. These properties include thermal, mechanical, deformation and material-specific characteristics such as spalling of concrete.

The thermal properties are critical in determining the extent of temperature rise and distribution inside the member. These properties include thermal conductivity, specific heat, thermal diffusivity and mass loss. Thermal conductivity is the property of material to conduct heat. Specific heat is the amount of heat per unit mass that is required to change the temperature of a material by one degree. Thermal diffusivity relates thermal conductivity and specific heat capacity. It is the ratio of thermal conductivity to the volumetric specific heat of the material. It is the

parameter that measures the rate of heat transfer from exposed surface to the inner portion of the material.

The extent of strength loss and stiffness deterioration is determined by the inherent mechanical properties of the material. These properties include compressive and tensile strength, modulus of elasticity and stress-strain response of the material.

The mechanical properties together with the deformation properties govern the deflection and the strain response. The deformation properties are thermal expansion, creep of concrete and reinforcement and transient strain in concrete. Thermal expansion is the expansion or shrinkage of a unit length of a material when the temperature is raised by one degree. Creep is a time-dependent plastic deformation of a material. The transient strain which is inherent properties of concrete occurs during the first time heating of concrete, and it is independent of time. It is caused by thermal incompatibilities between the aggregate and the cement paste (Purkiss 2007).

In general, these properties are determined after conducting an exhaustive number of high-temperature material tests. ASCE Manual of Practice No. 78 (1992) and Eurocode 2 (2002) are the two widely accepted sources for high-temperature material properties. The following subsections discuss concrete, mild reinforcement steel, prestressing strand, FRP & insulation material in relation to these properties.

### 2.3.1 Fiber Reinforced Polymer(FRP)

FRP composite is made of continuous fibers embedded in a matrix. The fibers comprised the largest volume fraction and they are the main load carrying component. The matrix is instrumental in transferring load and stress distribution between fibers, providing barriers against adverse environments, protection against mechanical abrasions and keeping the fibers in position (prevent buckling when compressed).

The most common types of fibers are carbon also known as graphite (CFRP), glass (GFRP) and aramid also known as Kevlar (AFRP). Out of the three fiber types, carbon fibers are the most commonly used in civil engineering application because of their high tensile-modulus-to-weight ratio and high tensile-strength-to-weight ratio. Also, carbon fiber is known to perform satisfactorily under fatigue load and moist environment. Carbon fibers have high resistant to higher temperatures with melting temperatures as high as 4000°C and are also considered flame resistance since they burn at very high temperatures (Bourbigot and Flambard 2002). They are chemically inert and are not susceptible to corrosion or oxidation at a temperature below 400°C. Figure 2-7 shows the variation of the tensile strength of carbon, aramid and glass fibers with temperature. It can be observed from the figure that aramid fibers exhibited a pronounced reduction in their tensile strength above 100°C. Glass fiber shows a gradual reduction in strength compared to Aramid fiber. Carbon fibers experience little or no change in their tensile strength up to 1000°C (Rostasy et al. 1992). Fiber types have their



own significant effect on the thermal conductivity of FRP. Compared to glass fiber, carbon fibers have high thermal conductivity (Bisby 2003). Even though it exhibits superiority in terms of stiffness and impact resistance, aramid is the most commonly used fiber due to its high cost (Ahmed 2010).

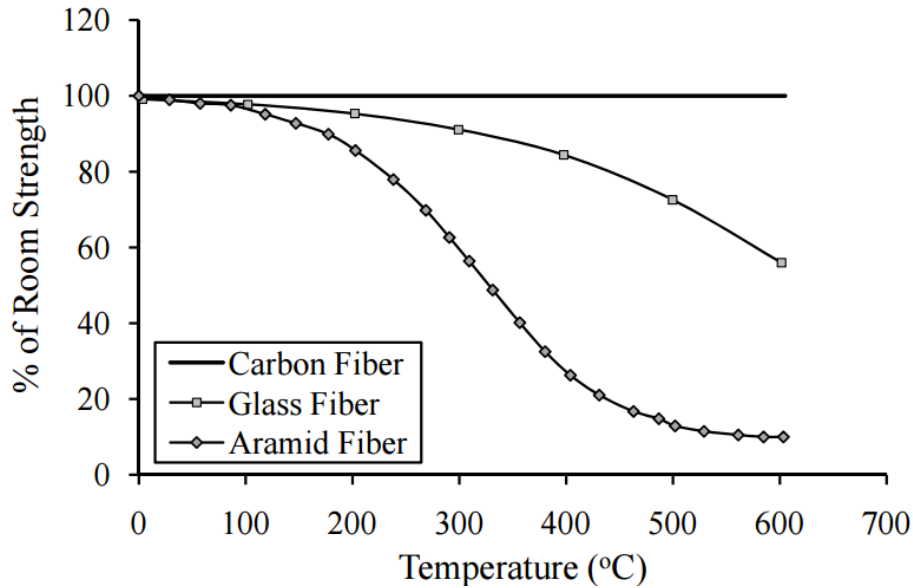


Figure 2-7 Variation of tensile strength of carbon, glass and aramid fibers with temperature (Ahmed 2010)

The matrix acts as a binder for the fiber, and it constitutes a small volume fraction. Polymers are the most widely used matrix material (Gibson 1994). Polymers are categorized being either thermosets (e.g. epoxy, polyester, Phenolic) or thermoplastics (e.g. polyimide, polysulfone etc.). Thermosets form a highly cross linked molecular network which does not melt at high temperature. Whereas, thermoplastics are based on polymer chains which do not cross-link which will make them melt and soften at high temperature, then harden again upon cooling. Thermosets are used for structural application since they are thermally

stable at service temperature, have low creep effect and higher chemical resistance as compared to thermoplastics. One major drawback of the polymer matrix is their low glass transition temperature limit,  $T_g$ . At  $T_g$ , they change from a rigid glass state into a rubber which eventually results in stiffness and strength reduction. Because of this, the fire performance of the FRP-strengthened structural members is primarily dependent on the performance at  $T_g$ . In general, matrix has low thermal conductivity (Mallik 1988).

The thermal and mechanical properties of FRP composites depend on the properties of the matrix, fiber volume fraction, fiber cross-sectional area, fiber orientation in the matrix and method of manufacturing (Bisby 2003). A wide range of FRP products are available in the market. Thus any change in any of these factors influence their property.

### **Thermal Properties of FRP Composites**

In unidirectional FRP composites, the thermal conductivity in the longitudinal direction is controlled by the fiber whereas the thermal conductivity in the transverse direction is controlled by the matrix. Unlike for concrete and steel, relatively little is known about the mechanical and thermal properties of FRP composites at high temperature, particularly for the FRP-polymer combinations used in infrastructure applications.

Griffis et al. (1981) conducted a test on graphite epoxy laminate and suggested the variation of specific heat and thermal conductivity as a function of temperature as shown in Figure 2-8. As it can be observed from the figure, the thermal conductivity decreases with increase in temperature up to 500°C and then

plateau. The specific heat increase steadily at a slower rate up to a temperature of 325°C followed by a spike which then plateaus up to 511°C before it plunges down. It then follows a steady increase at a slower rate with increase in temperature. The plateau observed shows a consumption of additional heat because of thermal degradation of resin.

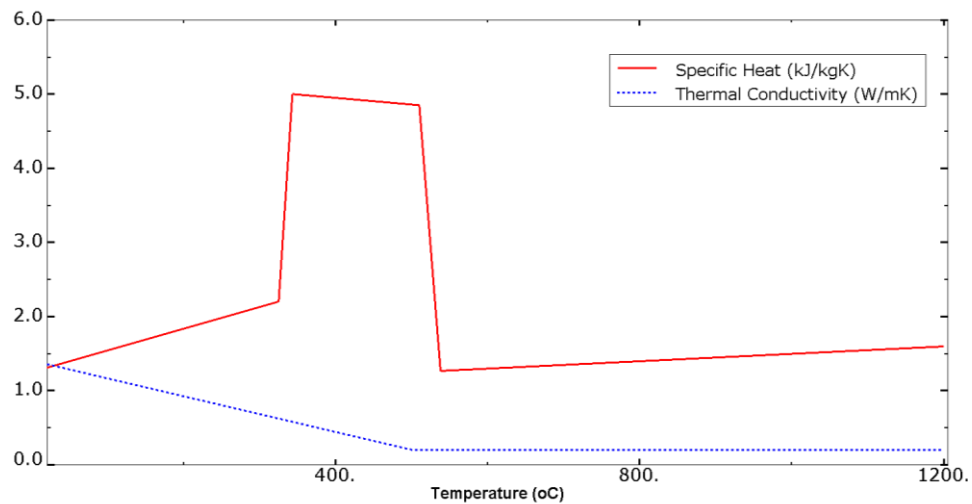


Figure 2-8 Variation of thermal conductivity and specific heat as a function of temperature for CFRP laminate (Griffis et al. 1981)

### **Mechanical Properties of FRP Composites**

In general, the stiffness and the strength of FRP composite decrease with increase in temperature. The elevated temperature has adverse effect on the matrix compared to the fiber as the temperature approaches  $T_g$  (Blontrock et al. 1999).

The variation of mechanical properties of FRP composites with temperature was investigated by various researchers. Bisby (2003) compiled these data and proposed a model that shows the variation of tensile strength and

elastic modulus with temperature. Figure 2-9 and Figure 2-10 shows the collected data and the proposed mode. The proposed model equation is shown in Appendix C.

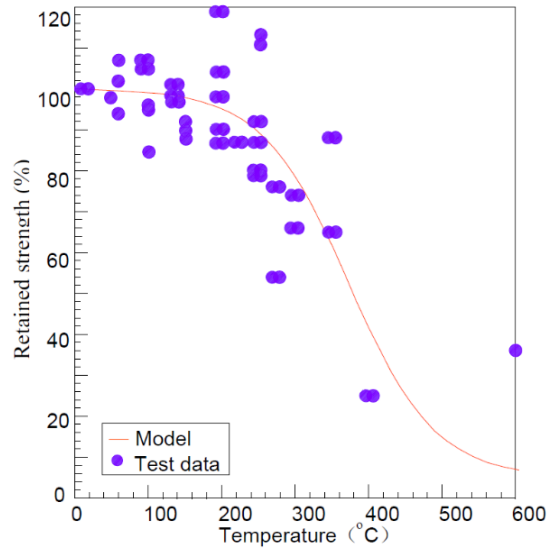


Figure 2-9 Variation of tensile strength of CFRP composite as a function of temperature (Bisby 2003)

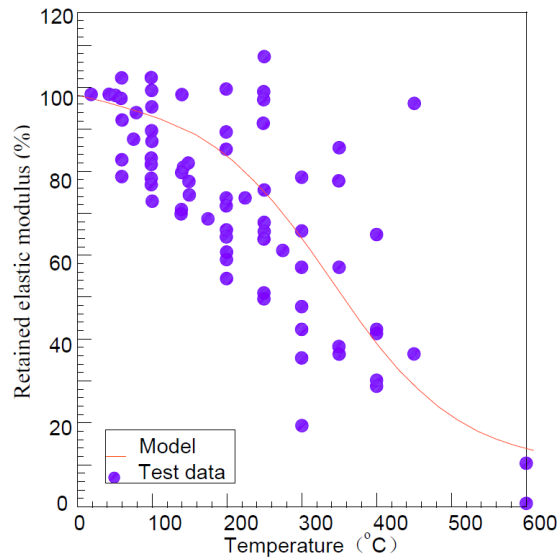


Figure 2-10 Variation of elastic modulus of CFRP composite as a function of temperature (Bisby 2003)

### **Deformation Properties of FRP Composites**

The coefficient of thermal expansion is higher in transverse direction compared to the longitudinal direction. This is due to the presence of the fibers in the later. No literature is available that shows the variation of coefficient of thermal expansion with temperature. Table 2-3 shows the coefficient of thermal expansion of unidirectional composites.

Table 2-3 Coefficient of thermal expansion of FRP composites (Mallik 1988)

FRP Composite	Coefficient of Thermal Expansion ( $\times 10^{-6}/^{\circ}\text{C}$ )	
	Longitudinal Direction	Transverse Direction
Glass/Epoxy	6.3	19.8
Aramid/Epoxy	-3.6	54
High Modulus Carbon/Epoxy	-0.09	27
Ultra-high Modulus Carbon/Epoxy	-1.44	30.6

### **2.3.2 Concrete**

Concrete is available in various forms. Its thermal, mechanical and deformation properties, as well as its tendency to spalling, depend on the composition of the constituent material and its compressive strength. The type of aggregate present creates a variation in thermal properties. The two principal type of aggregates used in normal weight concrete are silicate (siliceous) and carbonate aggregate. The strength of concrete influences its mechanical properties as well as the tendency for spalling. By definition (Kodur 2014), a concrete with

compressive strength in the range of 20 (2.9 ksi) to 50 MPa (7.25 ksi) is classified as normal strength concrete (NSC). Whereas those falling in the range of 50 (7.25 ksi) to 120 MPa (17.4 ksi) are classified as high-strength concrete (HSC).

### **Thermal Properties of Concrete**

The thermal conductivity of concrete is affected by the amount of moisture and the type of aggregate. Specific heat is highly influenced by moisture content, aggregate type and density of concrete (Phan 1996; Harmathy et al. 1973; Kodur and Sultan 1998).

Khalid (2012) compiled previously published experimental data (Shin et al. 2002; Harmathy and Allen 1973; Harmathy 1970; Kodur 1998; Lie and Kodur 1996; Harada 1972) and empirical relationship (EC-2 2004 and ASCE 1992) on the variation of thermal conductivity of NSC with temperature as shown in Figure 2-11. The shaded portion represents the range of values reported by different test programs. As it can be observed from the figure, there is considerable variation in the data which is attributed to moisture content, type of aggregate, test conditions and measurement techniques used in the experiments. In general, the thermal conductivity follows a decreasing trend with rise in temperature. This could be due to variation of the moisture content with increase in temperature (Bazant 1996). The ASCE model provides the thermal conductivity model based on the type of aggregate, whereas the Eurocode model offers an upper and a lower limit. The upper limit was derived from tests on steel/composite structures, while the lower limit is suggested to give more accurate results since it is based on fire tests from a variety of different types of concrete structures (Hatinger 2012).

According to the study by Kodur and Khalid (2011), the thermal conductivity of HSC is higher than NSC. This is attributed to the low water-to-cement ratio and use of different binders in HSC.

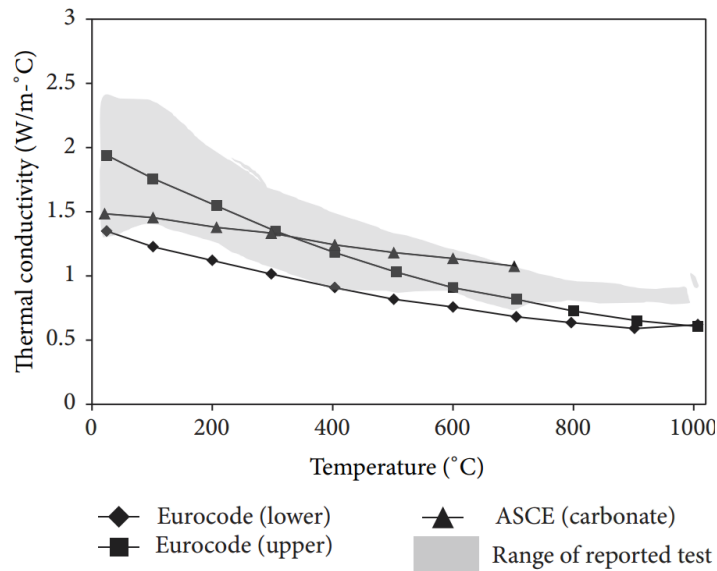


Figure 2-11 Variation of thermal conductivity of NSC with temperature (Kodur 2014)

Kodur and Khalid (2011) compiled previously published data (Harmathy and Allen 1973; Lie 1992; Shin et al. 2002; Eurocode 2004) on the variation of specific heat of NSC with temperature as shown in Figure 2-12. Like it is observed in the thermal conductivity, a considerable variation in the specific heat data is also observed. This is due to moisture content, type of aggregate, test conditions and measurement techniques used in the experiment (Kodur and Sultan 1998; Harmathy and Allen 1973; Eurocode 2004; ASCE 1992). As it can be observed from the figure, the specific heat capacity remains constant up to 400°C, followed by an increase of up to 700°C and then remains constant between 700 and 800°C range. The observed peak in the heat capacity of carbonate aggregate at the

temperature range between 600 and 800°C is due to the endothermic reaction as a result of the decomposition of dolomite. This reaction consumes a large amount of heat which plays a key role in enhancing fire resistance (Ahmed 2010).

According to Kodur and Sultan (2003), HSC has a slightly lower specific heat at the temperature range between 20-800°C compared to NSC.

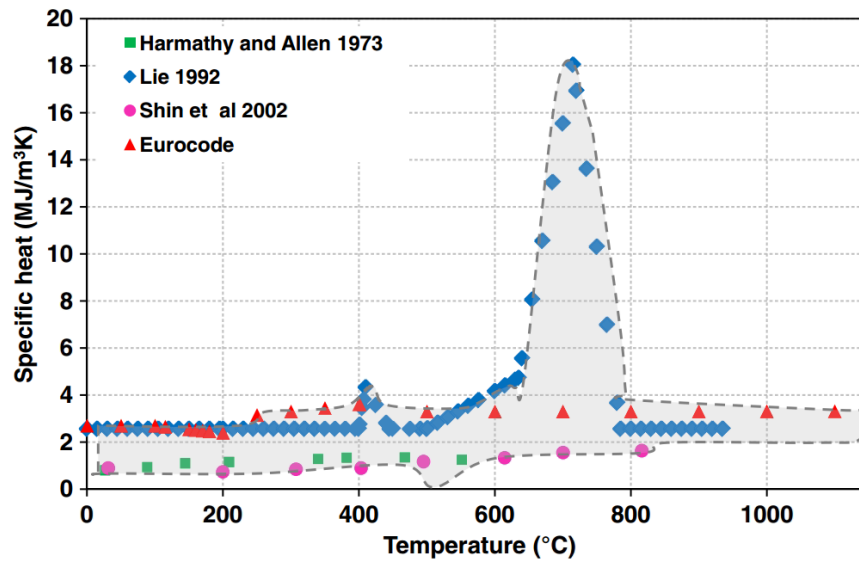


Figure 2-12 Variation of specific heat of NSC with temperature (Kodur and Khalid 2011)

### **Mechanical Properties of Concrete**

Mechanical properties of concrete include tensile strength, compressive strength, modulus of elasticity and stress-stress relationship. Unlike room temperature property measurements, where there are specified specimen sizes as per standards, the high-temperature mechanical properties are usually carried out on a wide range of specimen sizes and loading condition due to lack of test standards for high-temperature testing (Khalid 2012).



Figure 2-13 and Figure 2-14 shows the variation of normalized compressive strength of NSC and HSC respectively, as a function of temperature. It can be observed from Figure 2-12 that the elevated temperature has minimal effect on the compressive strength of NSC up to 400°C. This is due to their highly permeable nature which allows easy diffusion of pore pressure. On the other hand, there is a faster rate of degradation in compressive strength of HSC with the rise in temperature as shown in Figure 2-14. This is due to the compact microstructure of HSC that arises due to the use of binder material like slag and silica fume. The compactness, in turn, makes the concrete highly impermeable, which makes it susceptible to fast strength deterioration and spalling. It is observed from both figures that there is a variation among the data from different tests. This could be due to the difference in heating or loading rates, specimen size and curing, moisture content, age of the specimen and presence of admixture (Kodur 2014).

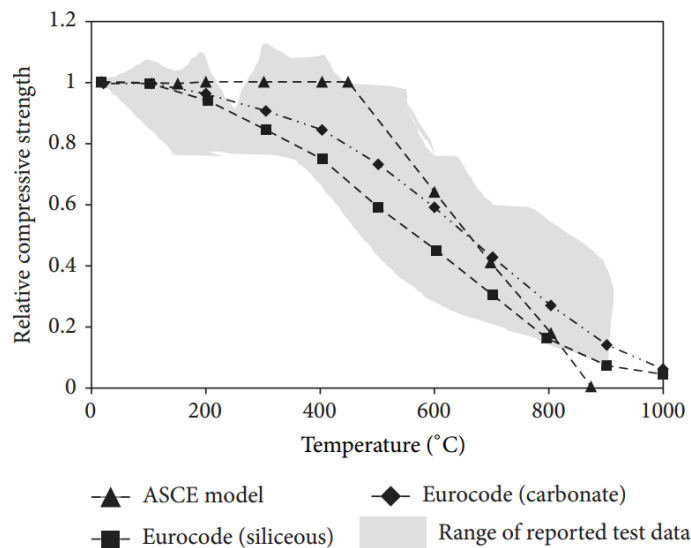


Figure 2-13 Relative variation of compressive strength of NSC as a function of temperature (Kodur 2014)

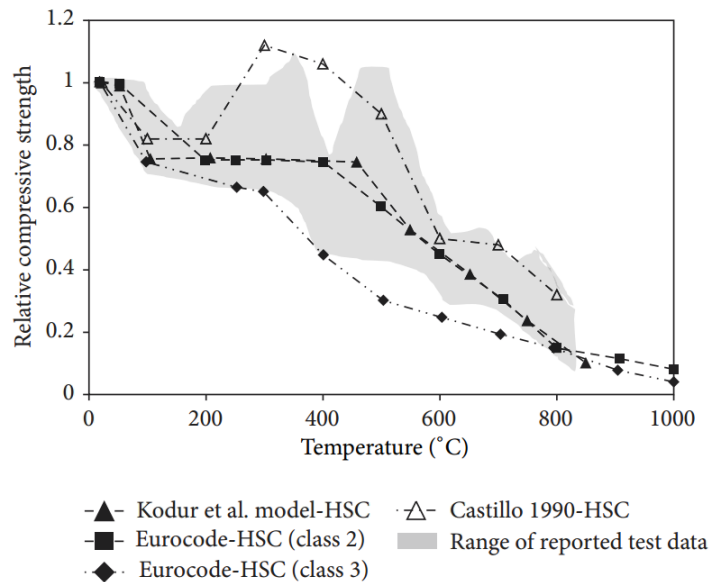


Figure 2-14 Relative variations of compressive strength of HSC as a function of temperature (Kodur 2014)

Figure 2-15 shows the relative variations of the tensile strength of HSC and NSC with temperature (Behond and Ghandehari 2009; Carette et al. 1982; Felicetti et al. 1996; EC-2 2004). As it can be observed from the figure, the tensile strength of concrete decrease with increase in temperature for both HSC and NSC. At 300°C, NSC loses approximately 20% of its tensile strength. Above 300°C, the tensile strength of NSC decreases at a rapid rate. This is due to a more pronounced thermal damage in the form of micro-cracks and reaches to about 20% of its initial strength at 600°C (Kodur 2014). There is also significant variation among the reported data.

The variation of modulus of elasticity of HSC and NSC is shown in Figure 2-16 (Castillo and Durrani, 1990; Phan, 1996; EC-2 2004). The modulus of elasticity of both HSC and NSC shows a decreasing trend with increase in

temperature. As it is observed in the other properties, there is also variation among the reported data.

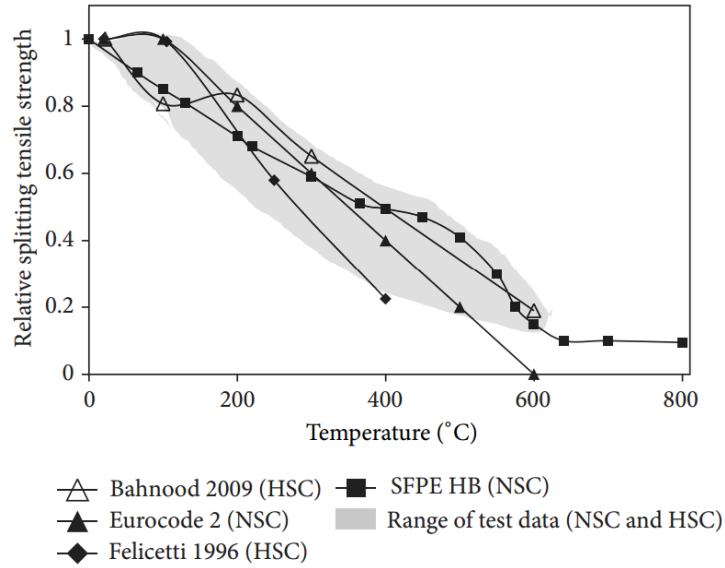


Figure 2-15 Relative variations of tensile strength of HSC as a function of temperature (Kodur 2014)

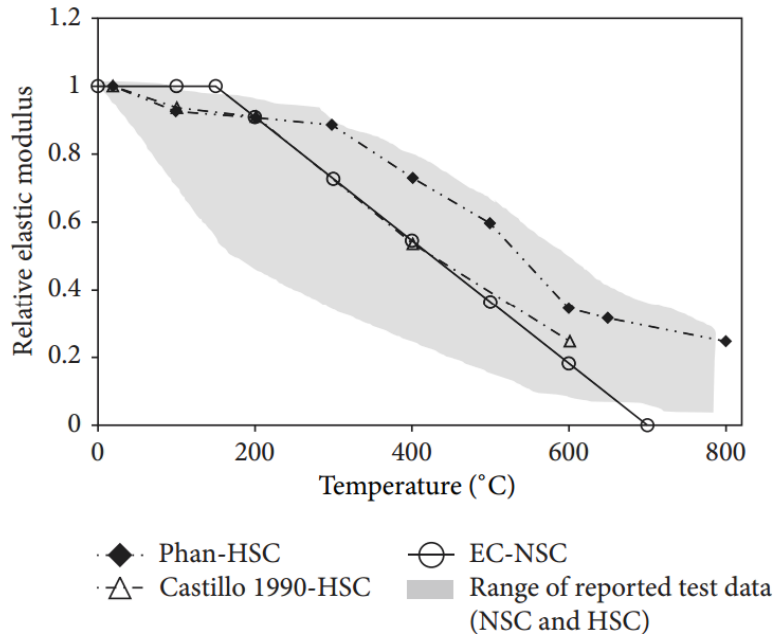


Figure 2-16 Relative variations of modulus of elasticity of concrete as a function of temperature (Kodur 2014)

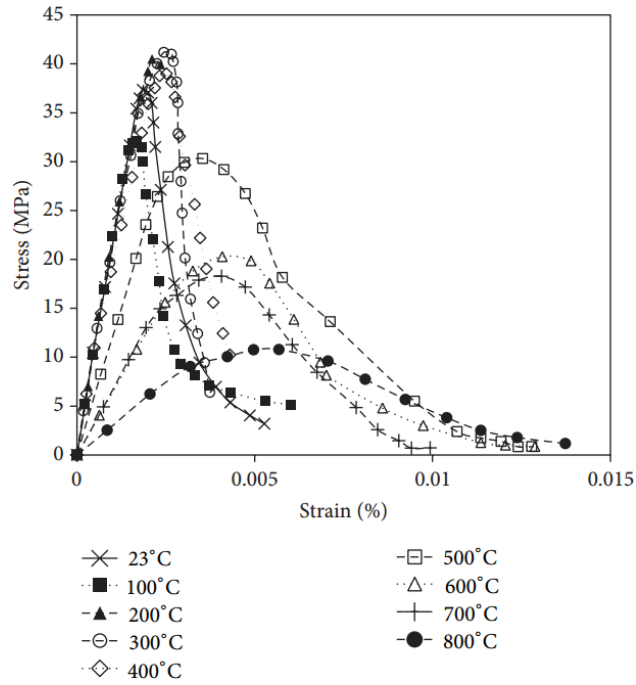


Figure 2-17 Stress-strain diagram of NSC at elevated temperatures (Kodur 2014)

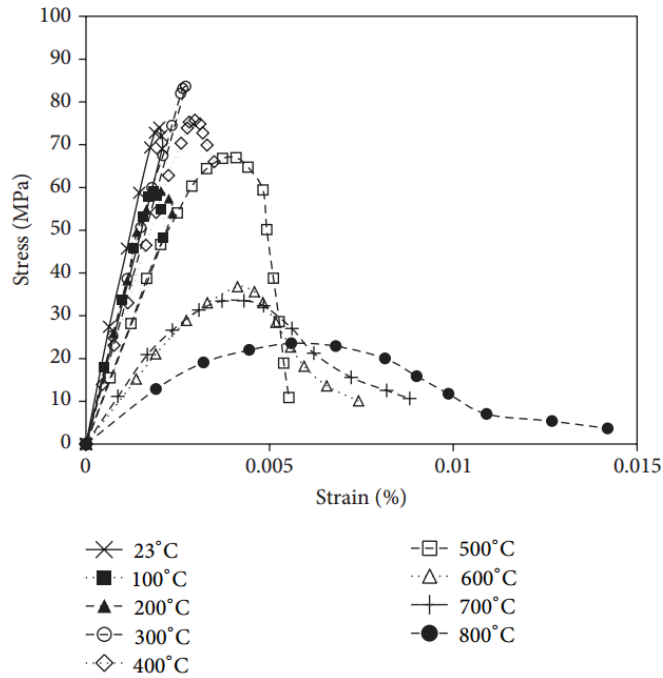


Figure 2-18 Stress-strain diagram of HSC at elevated temperatures (Kodur 2014)

The stress-strain diagram of NSC and HSC are depicted in Figure 2-17 and Figure 2-18 respectively. It is observed from both figures that the peak stress decreases with increase in temperature. To the contrary, the ultimate strain increase with an increase in temperature or increase in temperature leads to an increase in ductility. The strain corresponding to the peak stress increases with a rise in temperature. Compared to NSC, HSC exhibited a brittle response at all temperature ranges.

### **Deformation Properties of Concrete**

Deformation properties of concrete included thermal expansion, creep and transient strains. These properties depend on the type of aggregate used, chemical composition and the chemical and physical reactions in concrete during heating (Schneider 1988).

Figure 2-19 depicts the variation of coefficient of thermal expansion of NSC with temperature (ASCE 1992; EC-2 2004; Kodur et al. 2008; Raut 2011). It is observed from the figure that its values increased approximately up to a temperature of 700°C and then remained constant. According to EC-2 (2004) provision, the coefficient of thermal expansion of concrete with siliceous aggregate is higher compared to the concrete with carbonate aggregate.

Creep is defined as the time-dependent plastic deformation of materials under constant stress level. More specifically, creep is when a material deforms permanently from stress that is less than the yield point. Creep strain is significant at elevated temperature due to rapid movement of moisture. Some of the factors

that affect creep are temperature, stress level, time, loading and mix design of concrete (Dwaikat 2009).

When concrete is exposed to elevated temperature, it induces a complex change in its moisture content and chemical composition of the cement paste. Also, there is also a mismatch in thermal expansion between the cement paste and the aggregate. These changes in chemical composition and mismatch in thermal expansion lead to internal stresses and microcracking which results in a transient strain in concrete (Schneider 1988). Transient strain in concrete develops during its first time heating only (Khoury 2000).

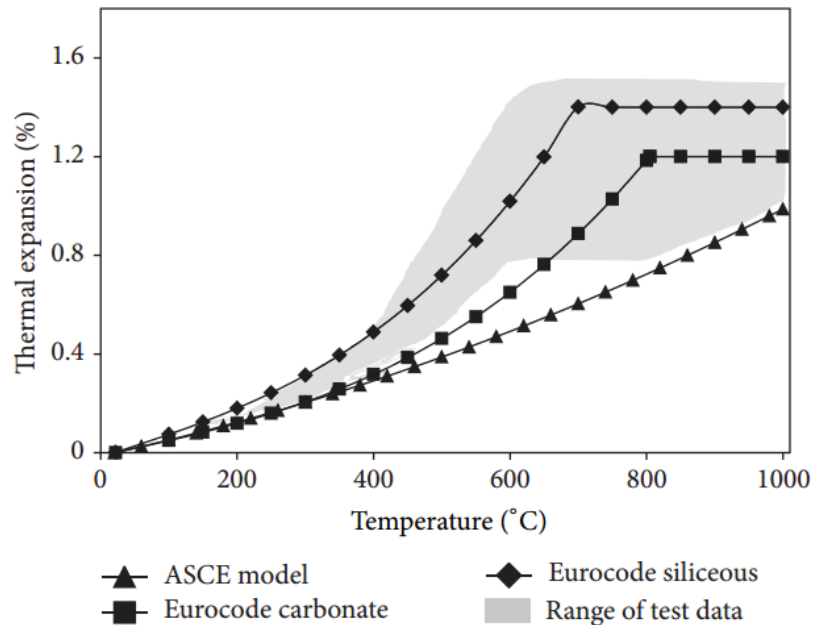


Figure 2-19 Variation of coefficient of thermal expansion of NSC with temperature

There is no direct test to measure transient strain. Transient and creep strain are measured together by measuring total strain and deducting both mechanical and free thermal strain. This lumped measurement is referred to as

transient creep strain. The two most commonly referred guidelines when it comes to concrete properties at elevated temperatures, ASCE 1992 and Eurocode (2004), don't provide a direct relationship either for transient strain or transient creep strain. Rather these effects are included implicitly in their stress-strain relationship by providing an allowance (Khalid 2012).

The constitutive relationships for high temperature creep, and transient strain in concrete were developed by Anderberg and Thelandersson (1976) as shown in equation 2-2 and 2-3.

$$\varepsilon_{cr} = \beta_1 \frac{\sigma}{f_{c,T}} \sqrt{t} e^{d(T-293)} \quad 2-2$$

$$\varepsilon_{tr} = k_2 \frac{\sigma}{f_{c,20}} \varepsilon_{th} \quad 2-3$$

where  $\varepsilon_{cr}$  = creep strain,  $\varepsilon_{tr}$  = transient strain,  $\beta_1 = 6.28 \times 10^{-6} \text{ s}^{-0.5}$ ,  $d = 2.658 \times 10^{-3} \text{ K}^{-1}$ ,  $T$  = concrete temperature ( $^{\circ}\text{K}$ ) at time  $t$  (s),  $f_{c,T}$  = concrete strength at temperature  $T$ ,  $\sigma$  = stress in the concrete at the current temperature,  $k_2$  = a constant ranges between 1.8 and 2.35,  $\varepsilon_{th}$  = thermal strain, and  $f_{c,20}$  = concrete strength at room temperature.

### **Fire-Induced Spalling**

Fire-induced spalling in concrete is explained using two broad theories (Kodur 2000). The first explanation bases the pore-pressure build up that occurs during heating of concrete. The pressure builds up is highest in HSC compared to NSC because of its low permeability and high density. This makes HSC more susceptible to spalling compared to NSC since the extremely high water vapor pressure generated during heating don't have a way out to escape. As it is

illustrated in Figure 2-20, spalling of concrete occurs when the effective pore pressure (effective pore pressure is a product of porosity and pore pressure) exceeds the tensile strength of concrete.

The second explanation is related to restrained thermal dilation close to the heated surface which leads to the development of compressive stress parallel to the heated surface as shown in Figure 2-21. These compressive stresses are released by spalling or brittle fracture of concrete.

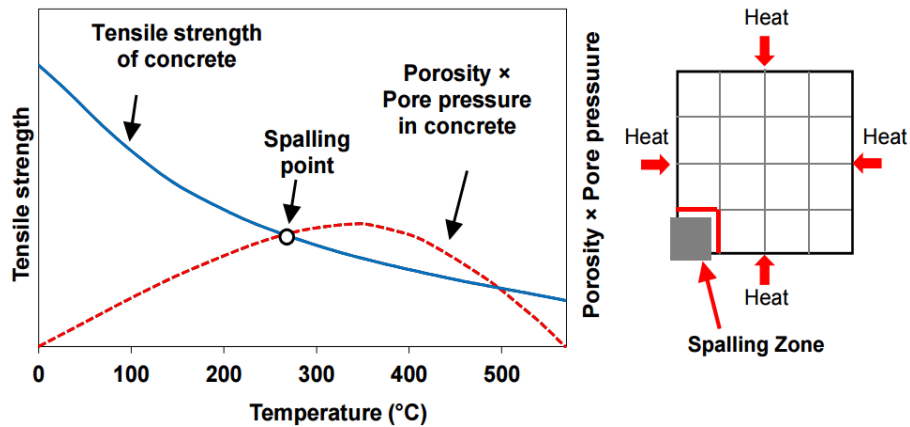


Figure 2-20 Illustration of spalling of concrete due to pressure buildup (Dwaikat 2009)

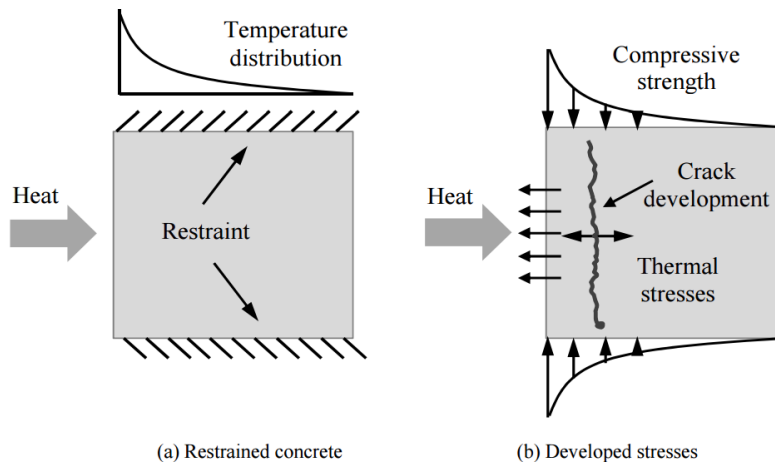


Figure 2-21 Illustration of spalling of concrete due to thermal dilatation (Khalid 2012)



### 2.3.3 Prestressing Strands and Mild Reinforcements

Similar to concrete and FRP; thermal, mechanical and deformation properties have an effect on the response of prestressing steel and mild reinforcement to elevated temperature. There are variations in these properties between mild reinforcement and prestressing strand. Since the former is formed through a hot-rolling process whereas the latter is produced by cold working. The following subsections review these properties in detail.

#### **Thermal Properties**

Compared to most construction materials, all types of steel exhibited high thermal conductivity and low specific heat capacity. At ambient temperature, thermal properties are affected by metallurgical composition, type of reinforcement and temperature. However; under fire condition, temperature is the only variable that has significant effect (Hatinger 2012). In reinforced concrete or prestressed concrete, the mild reinforcement or the prestressing strand area is very small in comparison to overall concrete section. Therefore, the steel has almost no influence on the temperature distribution within the concrete cross section.

Figure 2-22 and Figure 2-23 show the variation of thermal conductivity and specific heat capacity of steel with temperature according to Eurocode (2005). The thermal conductivity decreases linearly with increasing temperature up to 800°C and remains constant after that. The specific heat capacity shows a gradual change for most of the temperature range. However, its values exhibited a spike

at a temperature range between 700-800°C. The apparent sharp rise is due to crystal structural phase change of steel (Wang et al. 2013.)

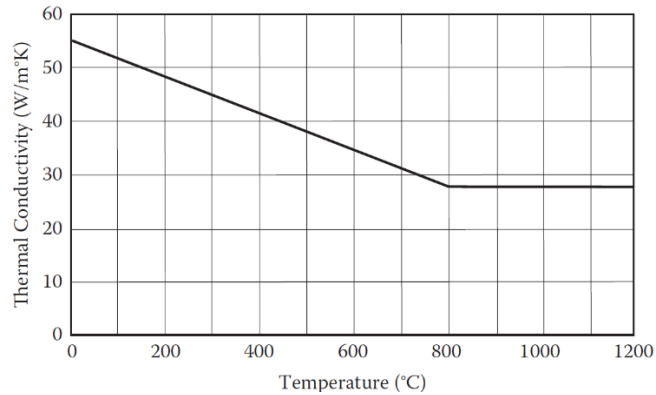


Figure 2-22 Variation of thermal conductivity of steel with temperature (Eurocode 3, 2005)

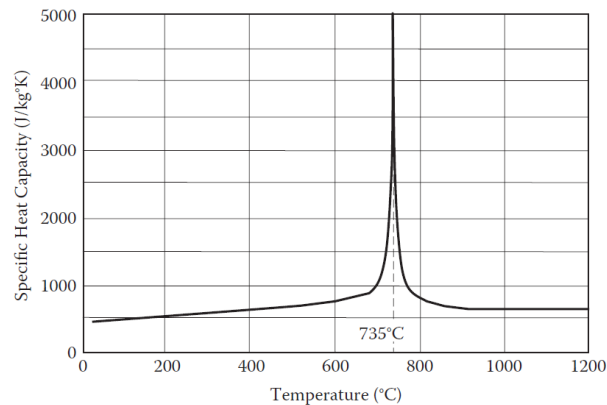


Figure 2-23 Variation of specific heat capacity of steel with temperature (Eurocode 3, 2005)

### **Mechanical Properties**

The mechanical properties of steel that influence the strength and stiffness of mild reinforcement and prestressing steel are yield strength, ultimate strength, modulus of elasticity and stress-strain relationship. These properties are affected by heating rate, strain rate, type of reinforcement and temperature. Prestressing steel are more sensitive to high temperature when compared to mild reinforcement (Hatinger 2012).

When steel is subjected to a fire, a unique stress-strain curve needs to be defined for each rise in temperature. Figure 2-24 and Figure 2-25 shows the stress-strain curve variation at different temperature range for mild-reinforcement and prestressing steel. It is observed from the figures that the strength and stiffness of both prestressing steel and mild reinforcement decrease with temperature. ASCE (1992) provides model only for mild reinforcement.

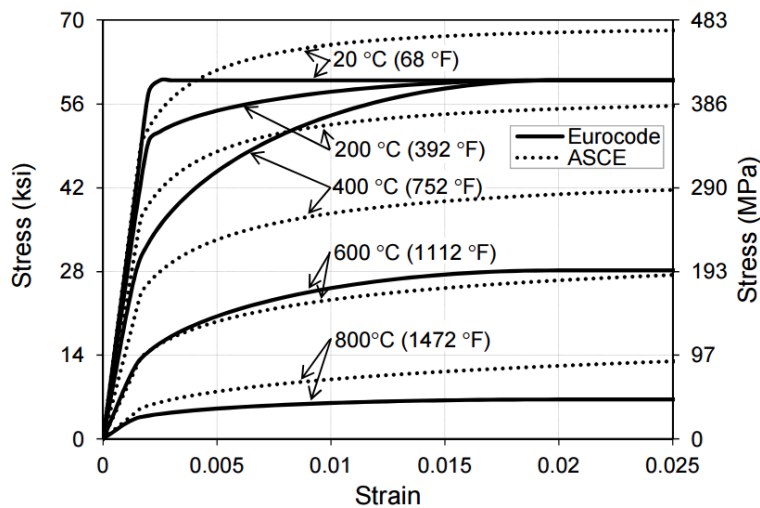


Figure 2-24 Variation of Stress-strain curves as a function of temperature for mild reinforcing steel (Eurocode 3, 2005)

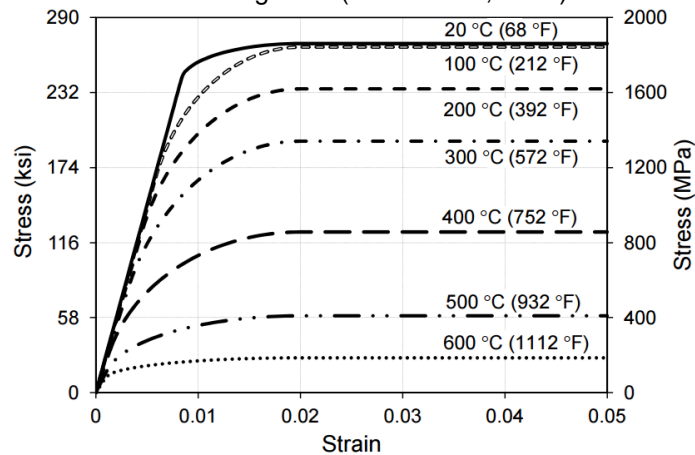


Figure 2-25 Variation of Stress-strain curves as a function of temperature for prestressing steel (Eurocode 3, 2005 and ASCE 1992)

Figure 2-26 depicts the variation of ultimate strength of prestressing steel and mild reinforcement with temperature as per the provision of Eurocode-3 (2004), ASCE (1992) and PCI (2004). Except for the ASCE model, all the curves show an S-shaped ultimate strength degradation curve. According to Eurocode, prestressing steels begin to lose strength at 100°C, whereas mild reinforcements do at 400°C. As per the ASCE model, mild reinforcing steel immediately begins to lose strength linearly until it reaches approximately 20 % of its strength at 900°C and completely degrades once 1000°C is reached. A strong correlation is observed between the ASCE and PCI model.

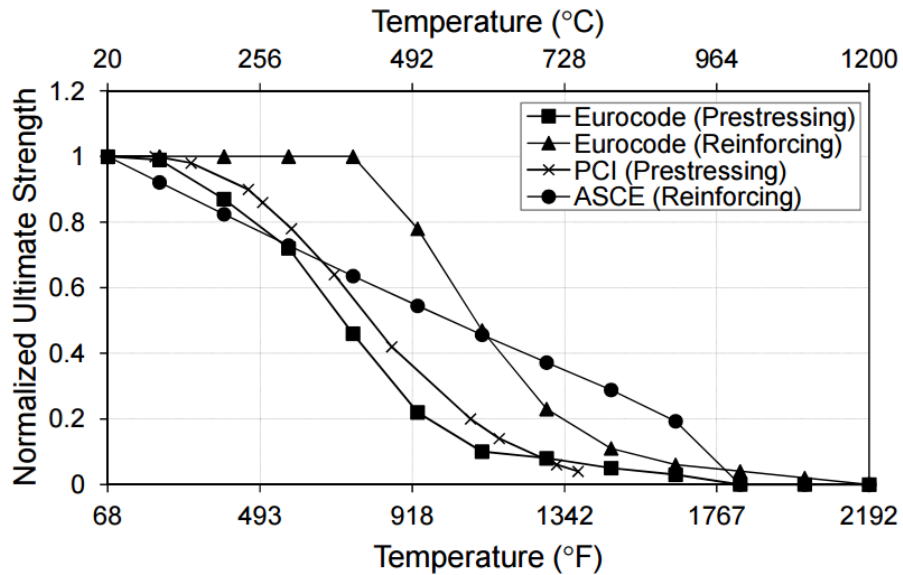


Figure 2-26 Variation of ultimate strength with temperature for mild reinforcement and prestressing steel (Eurocode 3, 2005; ASCE 1992 and PCI 2004)

Figure 2-27 shows the variation of yield strength of prestressing steel and mild reinforcement with temperature as per the provision of Eurocode-3 (2004) and ASCE (1992). It is observed from all of the curves that the yield strength decreases

with increase in temperature. The Eurocode model for mild steel shows a decrease in yield strength above 100°C, to the contrary the ASCE model shows a decrease as soon as the temperature goes above ambient temperature.

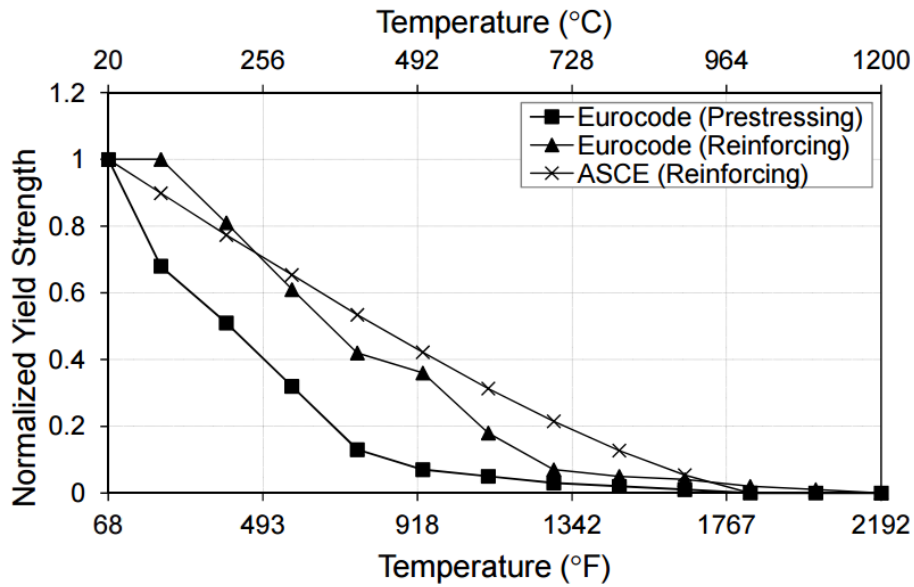


Figure 2-27 Variation of mild reinforcement and prestressing steel yield strength with temperature (Eurocode 3, 2005; ASCE 1992 and PCI 2004)

Figure 2-28 depicts the variation of modulus of elasticity of prestressing steel and mild reinforcement with temperature as per the provision of Eurocode-3 (2004) and ASCE (1992). As expected, the modulus of elasticity exhibits a decreasing trend with a rise in temperature in all of the models. The ASCE model for mild reinforcement begins to show a decrease in yield strength as soon the temperature goes up the ambient temperature, unlike the Eurocode which begins after 100°C temperature. Like the trend observed in Figure 2-26, the Eurocode model exhibited an S-shaped curve.

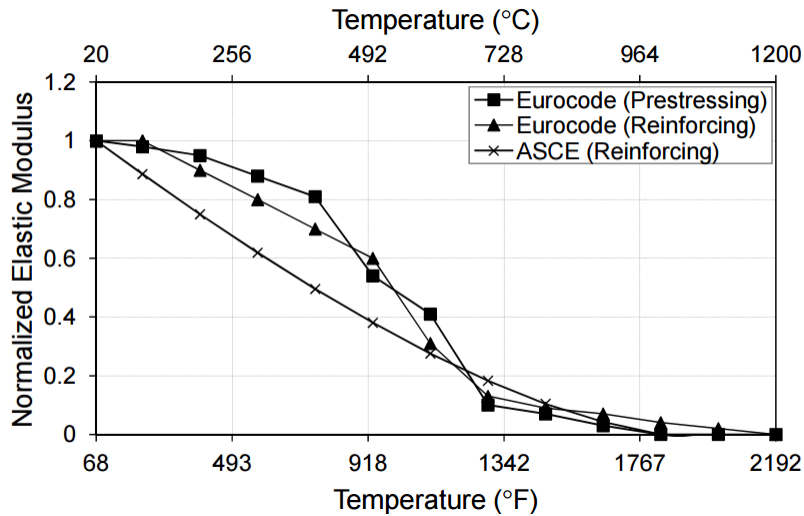


Figure 2-28 Variation of mild reinforcement and prestressing steel modulus of elasticity with temperature (Eurocode 3, 2005; ASCE 1992)

### Deformation Properties

Deformation properties of steel include thermal elongation and creep strain.

Figure 2-29 shows the variation of thermal expansion of prestressing steel and mild reinforcement with temperature (Eurocode 3, 2005; ASCE 1992). Overall, both models depict a linear increase in thermal strain with a rise in temperature. The Eurocode model shows a variation from ASCE model for a temperature range between 800°C and 860°C. The thermal expansion maintains a constant value between this temperature range due to the austenitic transformation of steel, where the crystalline structure of steel transform from ferrite into austenite (Ahmed 2010). It is also observed from the figure that mild reinforcement tends to produce higher strains than that of the prestressing steel.

Creep strain is a plastic strain that results from stress sustained for a longer period. Creep due to high-temperature influence the fire resistance of prestressing

steel, when the temperature exceeds approximately 250°C (Anderberg, 2008). On the other hand, the effect of creep in mild reinforcement will not come into effect until the temperature is around 400°C to 500°C (Elghazouli et. al, 2009). There are few high-temperature material relationships for creep strains in prestressing and reinforcing models in literature, out of which the model proposed by Harmathy (1967) is the most widely accepted and used. To avoid the complexity of predicting creep strain in fire resistance calculations, codes incorporate them implicitly through the stress-strain relationship based on strength and stiffness as a function of temperature (Hatinger 2012).

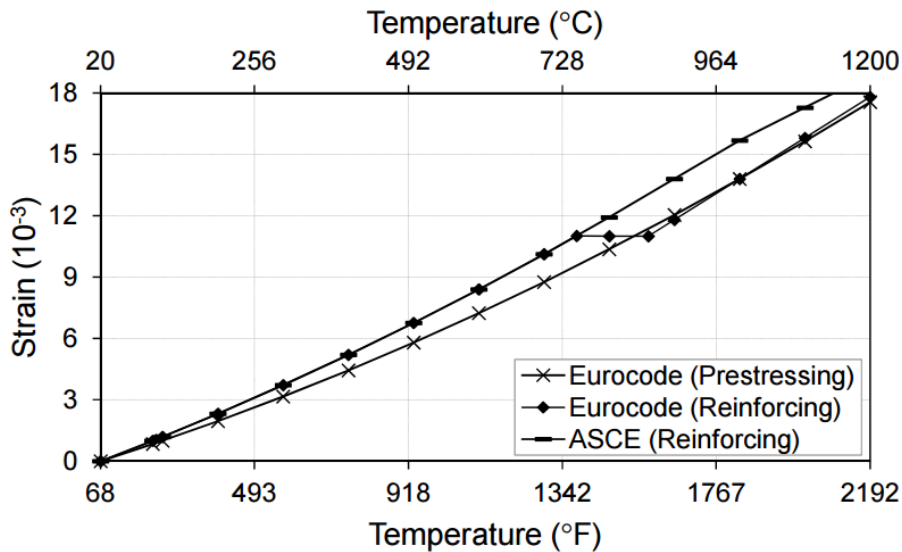


Figure 2-29 Variation of mild reinforcement and prestressing steel thermal elongation with temperature (Eurocode 3, 2005; ASCE 1992)

### 2.3.4 Insulation

Structural systems are protected using either an active or passive fire protection systems. Active fire protection refers to fire suppression systems (e.g.,

water-mist), or monitoring and early-warning systems (e.g., closed-circuit camera networks, traffic control devices). On the other hand, a passive fire protections are insulation materials that can be applied to external faces of structural members. Insulation materials retard the rate of heat flow through their inherent low thermal conductivity and high specific heat capacity properties. The insulation systems are available as spray applied, insulation board and intumescent coatings.

Spray applied protection prevent heat transfer through their low thermal conductivity (0.043-0.078 W/m-K) property and evaporation of entrapped water (Ahmed 2010). There are two major types of spray applied insulation materials. These are cementitious and mineral-fiber. The mineral-fiber mixture combines fibers, mineral binders, air, and water. Whereas, the cementitious coating comprised of lightweight aggregates like vermiculite and a heat-absorbing matrix of gypsum or Portland cement. Compared to other insulation systems, spray applied insulation are cost-effective (Adelzadeh 2013).

Like spray applied insulation, insulation boards provide protection from fire because of their low thermal conductivity and through evaporation of free and chemically bound water which comprises approximately one-fifth of the weight of the board. Calcium silicate, gypsum and vermiculite boards are examples of widely used insulation boards.

Compared to the spray applied and the gypsum board, the intumescent coating is applied in thin layers. When exposed to elevated temperature (usually 200 to 250°C), it swells and produces a charred layer with a very low thermal conductivity as shown in Figure 2-30. In spite of its low thermal conductivity,



intumescent coating usually provides limited fire resistance of 1 hour or less (Adelzadeh 2013). They are typically used for structural steel members.

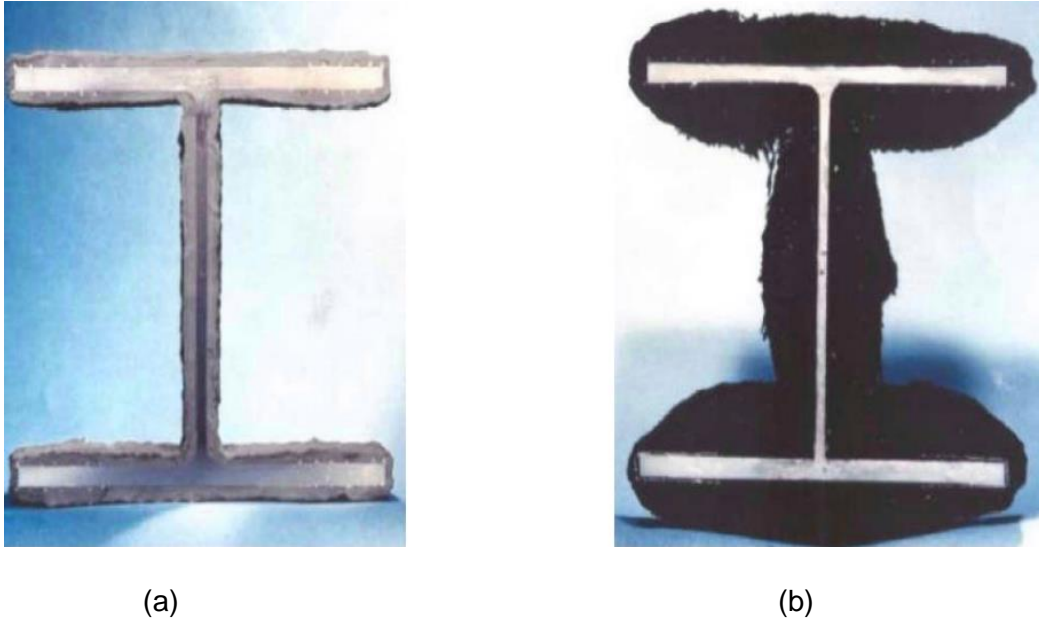


Figure 2-30 Intumescent coating applied to steel girder (Davidson 2012); (a) before fire exposure; (b) after exposure to fire.

Properties of concrete, mild-reinforcement, prestressing steel, FRP and insulation at elevated temperature is presented in Appendix C.

## Chapter 3

### TEST BRIDGE DESIGN

This chapter describes the design consideration and procedures for the various components of the test bridge. Unlike the ASTM E119 standard fire test, there is no specific guideline to date on the size of test specimens and the procedures on how to conduct hydrocarbon pool fire test on bridges. Thus, the components of the test bridge were designed taking into consideration various factors to come up with member sizes.

#### 3.1 Design of Girders

The test bridge superstructure comprised of three Texas standard TX28 girders, each spanning 10.1 m (33 ft.) and spaced at 1.83 m (6 ft.) on center. The 10.1 m (33 ft.) span length was selected taking into consideration the limited space and the lifting capacity of the crane in CELAB. The design considered a Class H concrete with a minimum release strength of 27.58 MPa (4000 psi) and a minimum 28-day compressive strength of 34.47 MPa (5000 psi) as per Texas Department of Transportation (TxDOT) Bridge Design Manual (2013). 12.7 mm (0.5 in.) low-relaxation prestressing strands meeting ASTM A416/A416M (2014) and having specified tensile strength,  $f_{pu}$  of 1861.6 MPa (270 ksi) were used. Grade 60 mild reinforcements meeting ASTM A615 (2014) were also used.

The girders were designed for self-weight, dead load from the deck and AASHTO (2014) HL-93 live load. The geometry of the bridge on PGSuper is shown in Figure 3-1.

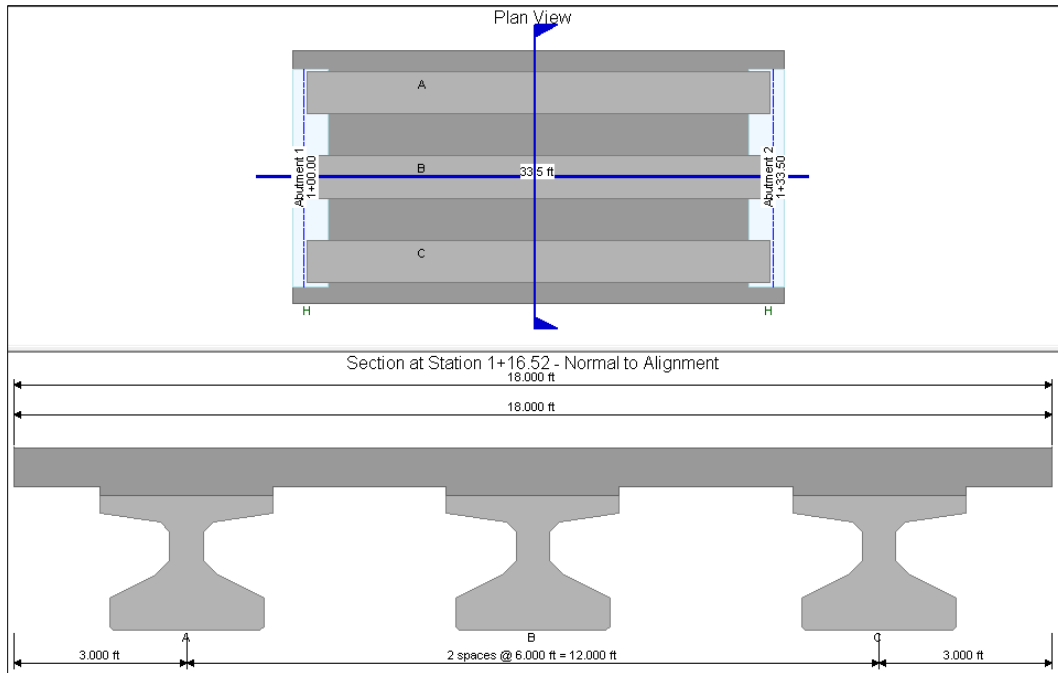


Figure 3-1 PGSuper model

Table 3-1 shows the design summary from PGSuper analysis.

As it can be observed from Table 3-1, the girders were oversized which was caused by a change in the original design. The test bridge was originally designed considering four girders, but TxDOT requested the numbers to be reduced to three. The request for change of plan occurred after the four girders were already fabricated, which made it impossible to optimize the number of strands. The typical shop drawing for the girders is shown in Appendix A.

Table 3-1 Design summary of girders

Girder	No. Of Strands	Mu, kN-m (Kip-ft)	$\Phi$ Mn, kN-m (kip-ft)	Vu, kN (kip)	$\Phi$ Vn, kN (kip)
Interior and Exterior	12	922 (680.06)	1840.3 (1357.3)	474.3 (106.63)	1157.9 (260.30)

The design of the overhang brackets hangers involved determining their optimal spacing that could allow them to carry the load transferred from the formwork safely. The load considered for the design were dead load from the self-weight of the deck and live load from the people working on it. The design yielded a maximum spacing of 1.22 m (48") between hangers, which is approximately nine hangers for each side of the cantilever deck. For this project, Dayton Superior C25 45° adjustable half hanger was used, shown in Figure 3-2.

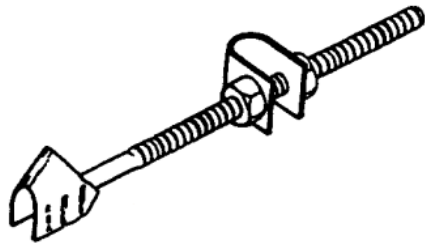


Figure 3-2 Dayton Superior C25 45° adjustable half hanger

### 3.2 Design of Deck

The deck is 9.754 m (32 ft.) long, 5.486 m (18 ft.) wide with 0.914 m (3 ft.) overhang on both sides of the exterior girders and 20.32 cm (8 in.) thick with 5.08 cm (2 in.) and 3.18 cm (1.25 in.) clear cover on the top and the bottom, respectively (Figure 3-3). For the interior bays, the deck comprised of 10.16 cm (4 in.) precast prestressed deck panels and 10.16 cm (4 in.) cast in place concrete, and the overhangs were 20.32 cm (8 in.) thick cast-in-place concrete. The precast prestressed concrete deck panels were made per TxDOT standard detail is shown in Appendix B.

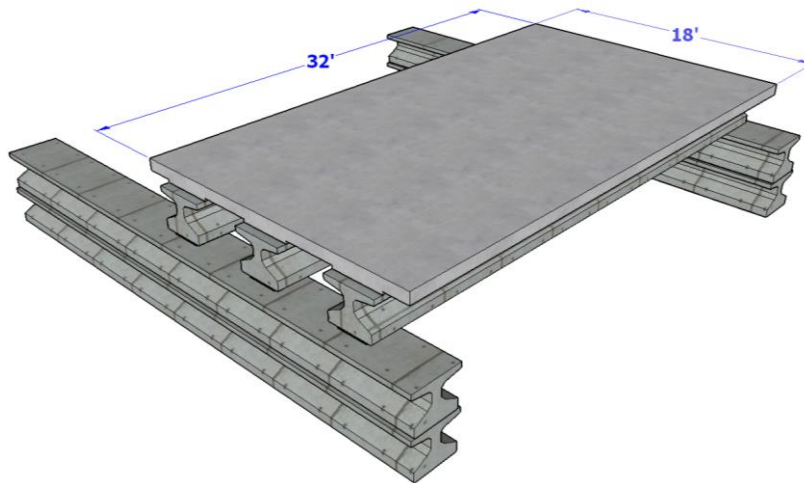


Figure 3-3 Test bridge deck

TxDOT bridge design manual (2013) specify that Class S concrete with  $f'_c = 27.58$  MPa (4.0 ksi) to be used for the construction of concrete deck slabs. However, for this specific project a high early strength (HES) concrete with 72-hours compressive strength of 27.58 MPa (4.0 ksi) was used. Since the 1-month time frame given by the fire test center to build, test and demolish the bridge may not be adequate to attain the required strength of Class S concrete. Using HES helped in achieving the strength earlier than 28 days and allowed early form removal. To attain early strength; water-reducing and accelerating admixture were added into the mix. Grade 60 uncoated reinforcing steel was used. The deck is designed for self-weight, and the expected simulated AASHTO HL-93 live load. Its final reinforcement detail is shown in Figure 3-4.

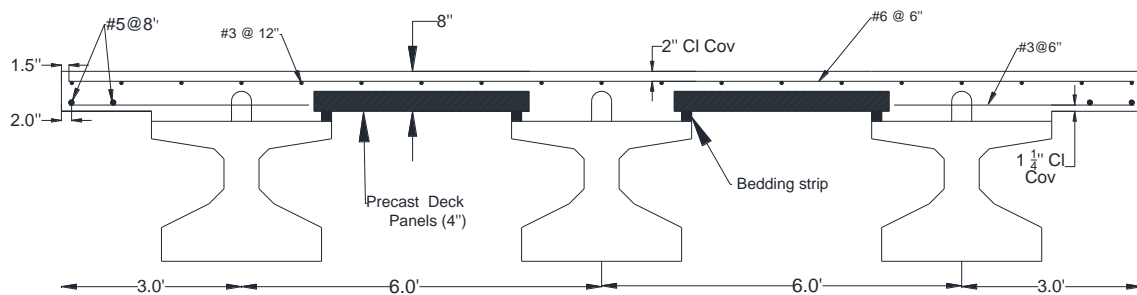


Figure 3-4 Reinforcement detail of the deck

### 3.3 Support Design

AASHTO (2004) requires bridges in urban and rural areas to have a clear height of not less than 4.9 m (16ft.) and 4.3 m (14ft.), respectively. However, most bridges are found in an urban area, so 4.9 m (16 ft.) clearance was considered for design.

The originally proposed research was to build a 4.9 m (16 ft.) height supporting walls and subjecting the bridge to a hydrocarbon fire from fuel in tanker trailer as shown in Figure 3-5. However, this option is not feasible for two reasons. Firstly, building the supporting wall is costly. Second, setting a fire in a fuel confined in a tanker trailer might cause the tanker to explode, which could be hazardous during testing.

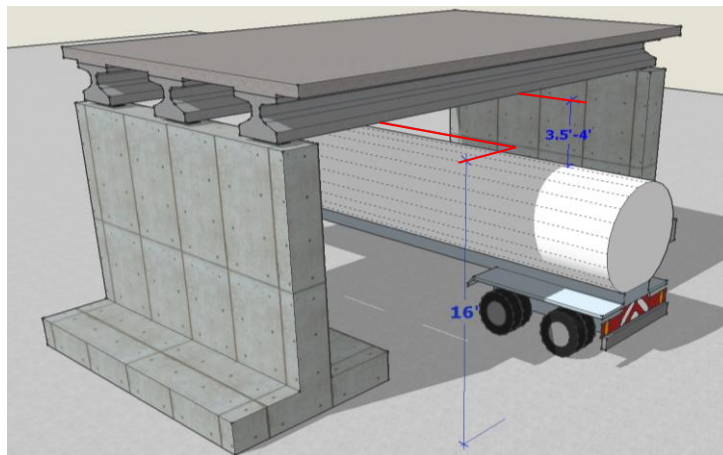


Figure 3-5 Original proposed supporting walls and fuel tanker trailer

The width and height of most fuel carrying tanker trailers range from 2.44 m (8 ft) to 2.59 m (8.5 ft.) and 3.66 m (12 ft) to 4.11 m (13.5 ft.) respectively. When these trailers full of highly flammable fuel pass under a bridge, which satisfies AASHTO (2004) minimum bridge clearance requirement, the gap between the top

of the trailers and the bottom of the bridge girders ranges from 1.07 m (3.5 ft) to 1.22 m (4 ft). If these tanker trailers catch fire, the worst damage is expected to occur from the fire originating from the top of the trailers as it is close to the bottom of the bridge. Hence, it was concluded that instead of building a 16 ft wall, it is ideal and conservative to use supporting walls that satisfy the 1.07 m (3.5 ft) to 1.22 m (4 ft) clearance between the top of the tanker trailer and bottom of the bridges. Fortunately, there were four previously tested TX28 girders, which were not fully damaged, stored in the CELAB as shown in Figure 3-6. After assessing their condition visually and verifying their capacity, a decision was reached to use them. Standard TX28 girders are 0.71 m (28 inches) deep; stacking two of them and placing a 6.35 cm (2.5 inches) bearing pad on the top of them provides a 1.49 m (58.5 inches) clearance between the ground and the bottom of the girder. Instead of using fuel tanker trailer, it was decided to use a 0.305 m (12 inches) deep pan which can be filled up to the top. Considering these dimensions yielded a clearance of 1.19 m (3.83 ft) between the top of the fuel pan to the bottom of girder as shown in Figure 3-7, which is within the range between 1.07 m (3.5 ft) to 1.22 m (4 ft).



Figure 3-6 Previously tested TX28 Girders

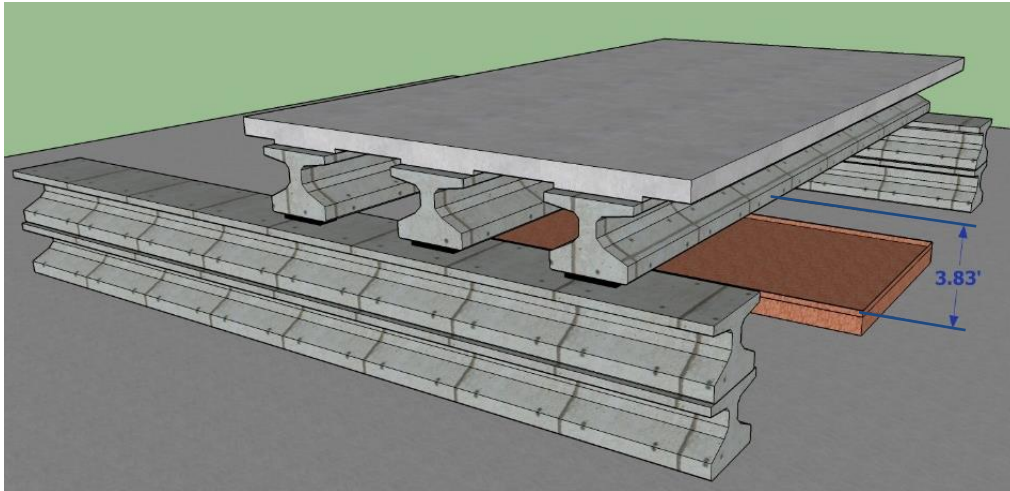


Figure 3-7 The newly proposed test setup

### 3.4 FRP Design

Various documents have been developed in the last two decades that describe FRP strengthening systems and provide guidelines for design assumptions and calculations. These includes:

- NCHRP Report 678, *design of FRP systems for strengthening concrete girders in shear* (Belarbi et al. 2011).
- NCHRP Report 655, *recommended guide specification for the design of externally bonded FRP systems for repair strengthening of concrete bridge elements* (Zureick et al. 2010).
- AASHTO (2013), *guide specifications for design of bonded FRP systems for repair and strengthening of concrete bridge elements*.
- ACI 440.2R-08, *guide for the design and construction of externally bonded FRP systems for strengthening concrete structures*.



Out of these, ACI 440.2R-08 offers a complete coverage of the subject. Thus, the FRP design strictly followed the provision outlined in this document.

The FRP in the current study was provided with the aim of increasing the flexural strength of the girders by approximately 20%. Out of the three girders shown in Figure 3-8, Girder 1 and 2 were strengthened with CFRP whereas girder 3 is unstrengthened.

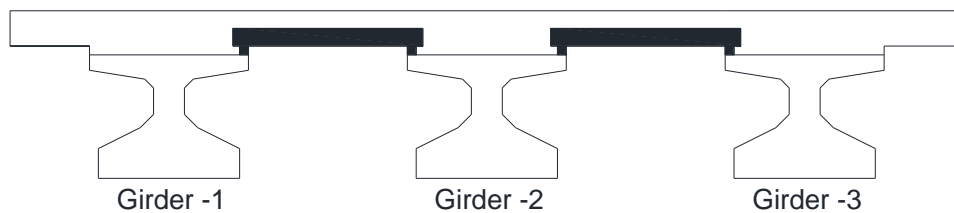


Figure 3-8 Labeled girders

According to TXDOT departmental material specification(DMS) 4700 (TXDOT 2015), FRP system is qualified to be used for structural member strengthening if it satisfies the requirement set forth in Table 2-1. Based on these requirements, the agency has a list of approved producers and their corresponding lists of products (TXDOT 2016). For the current research, Sikawrap Hex 117C, which is among the approved product, was used.

Table 3-2 TXDOT minimum requirements for FRP system to be used in structural strengthening (TXDOT 2015)

Property at Room Temperature (69–73 °F)	Requirement
Ultimate tensile strength in primary fiber direction based on gross-laminate area, Min	689.5 MPa (100 ksi)
Ultimate strain, Min	0.85%
Tensile modulus based on gross-laminate area, Min	55158 MPa (8000 ksi)
Glass transition temperature for FRP and bonding agent, Min	150°F
Fiber volume, Min	30 %
Bond strength to substrate concrete, Min	200 or $(0.065\sqrt{f'c})$ psi
Composite inter-laminar shear strength	44.8 MPa (6.5 ksi)
Coefficient of Thermal Expansion ( $1 \times 10^{-6}$ in./in./°F), Max	3.0

SikaWrap Hex 117C is a unidirectional carbon fiber with cured laminate properties shown in Table 3-3. The manufacturer recommends using Sikadur 300 and Sikadur 330 epoxy with this fiber. Both are a two-component adhesive. The former one is applied on the CFRP, whereas the latter is applied on the concrete surface.

Table 3-3 SikaWrap Hex 117C cured laminate design values

Tensile strength	724 MPa ( $1.05 \times 10^5$ psi)
Modulus of elasticity	56500 MPa ( $8.2 \times 10^6$ psi)
Elongation at break	1.0 %
Thickness	0.51 mm (0.02 in.)

The nominal capacity of unstrengthened girder was 1840.3 kN-m (1357.3 kip-ft). The design calculation yielded that providing three layers of CFRP increase the capacity to 2238 kN-m (1650.7 kip-ft), which is a 22% increase. Figure 3-9 shows the layout for the longitudinal FRP.

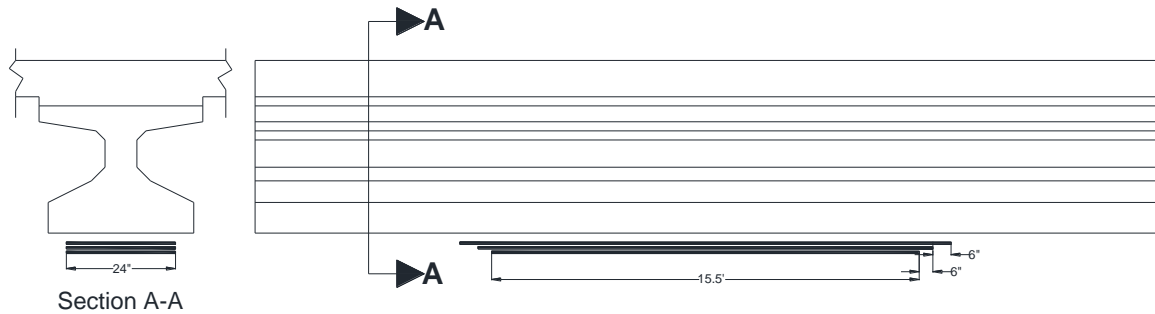
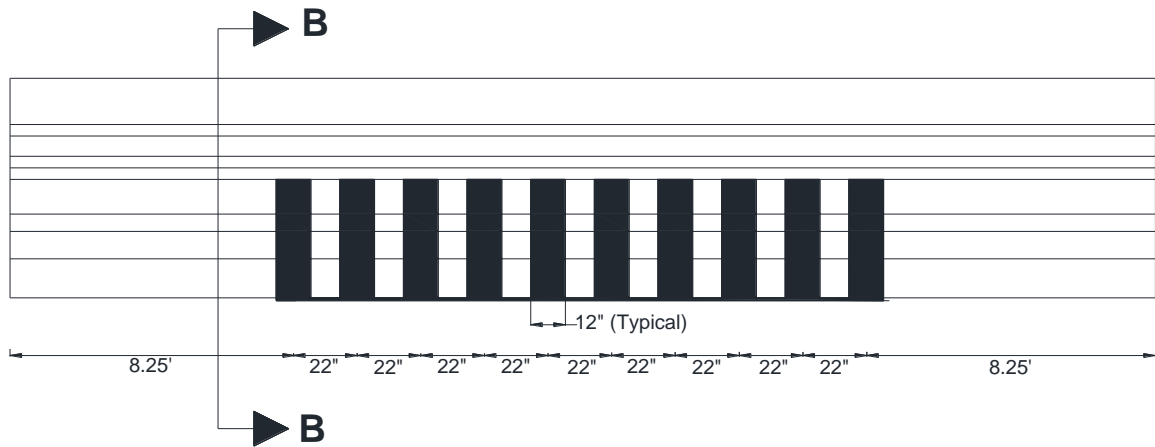
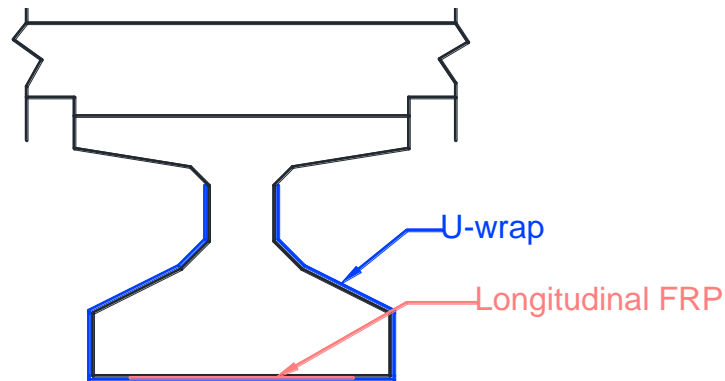


Figure 3-9 Longitudinal FRP layout

According to ACI 440.2R-08, provision of transverse clamping U-wraps along the length of longitudinal FRP has been observed to result in increased FRP strain at debonding. In addition, a typical TxDOT repair detail for prestressed concrete girders using CFRP requires providing 0.3048 m (12 inches) wide U-wraps at 0.6096 m (24 inches) maximum spacing (Yang et al. 2011). For the current study, U-wraps at 0.5588 m (22 inches) spacing were used as shown in Figure 3-10.





Section B-B

Figure 3-10 U-wraps layout

### 3.5 Fireproofing

To provide fire protection over the FRP, Sikacrete-213F was used as insulation. Sikacrete-213F is a cement based, dry mix fire protection mortar for wet sprayed application. It contains phyllosilicate aggregates which are highly effective in resisting fire. The manufacturer previously conducted standard fire tests on beams and columns strengthened with Sikawrap 103C fabric and CarboDur plates and protected with Sikacrete-213F. From these tests, it was found out that a fire rating up to four hours can be achieved with 40 mm (1.57 in.) thickness of insulation. Likewise, for the current study a 40 mm (1.57 in) of Sikacrete-213F was used as shown in Figure 3-11. Out of the two FRP strengthened girders, only Girder-2 was provided with Sikacrete-213F. The fireproofing was applied 152.4 mm (6 in.) and 71mm (2 in.) past the termination points of the longitudinal and transverse FRP, respectively. This helps to prevent the CFRP from direct heat exposure and consequently prevent premature debonding.

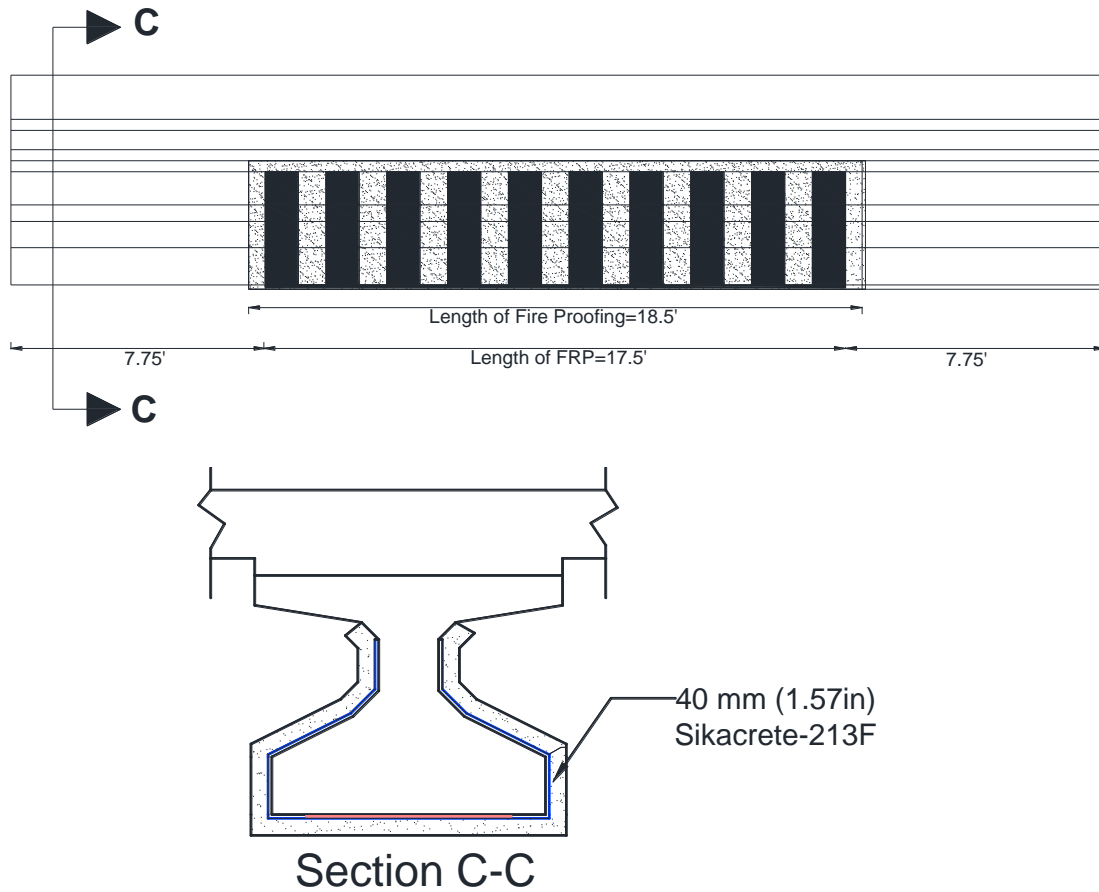
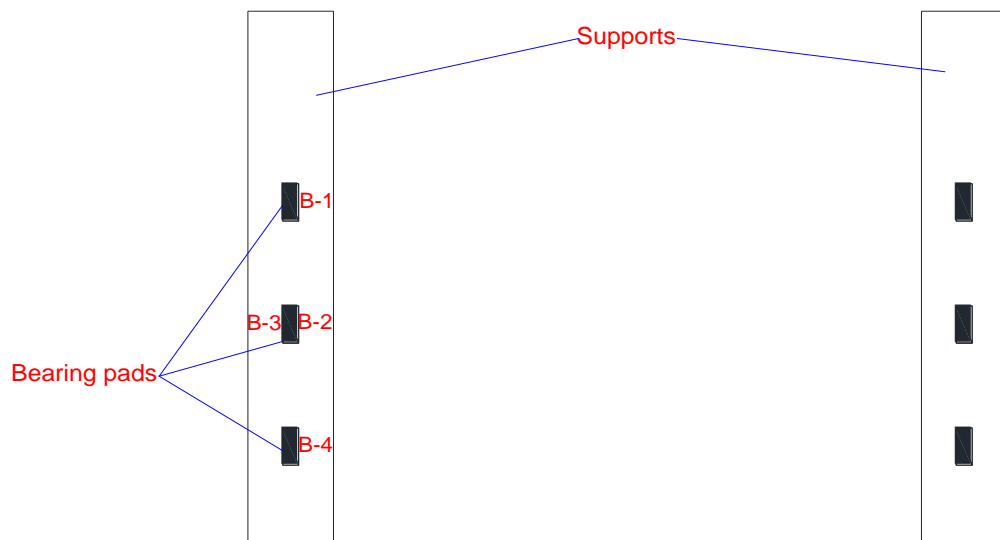


Figure 3-11 Fireproofing layout

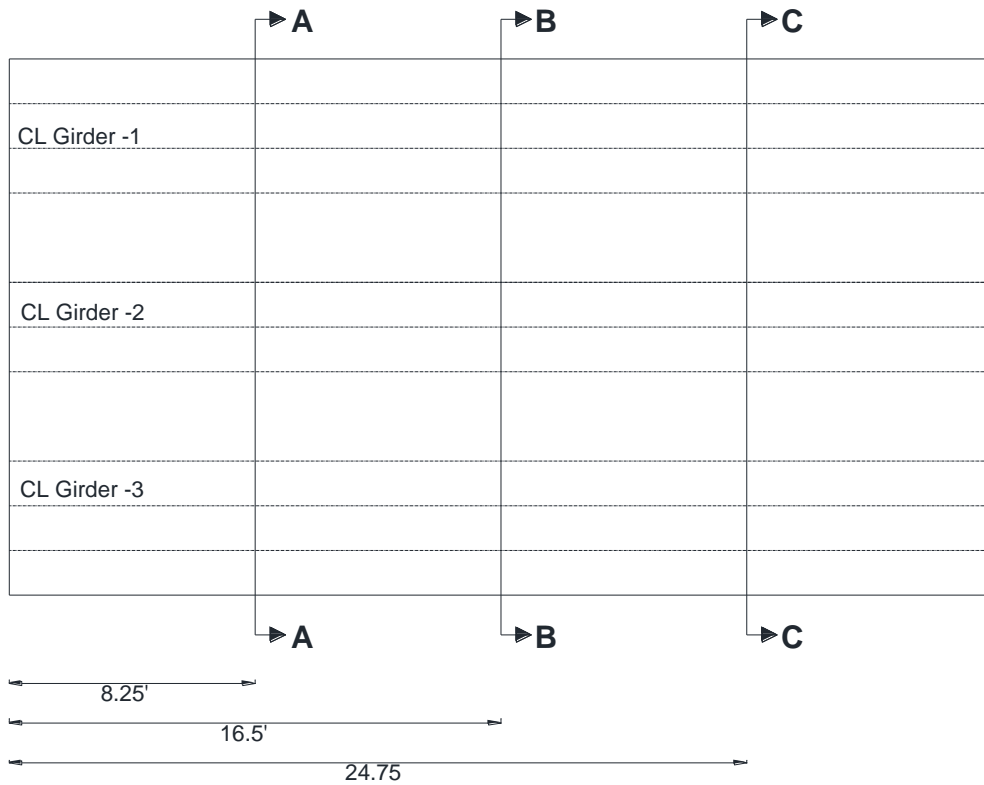
### 3.6 Instrumentation

The girders and the bearing pads were instrumented to measure temperature progression with time. A total of 36 Type-K Inconel sheathed thermocouples were installed on prestressing strands, at various depth in concrete, FRP-concrete interface, insulation-FRP interface, on the exposed surface of the girders and bearing pads. Figure 3-12 shows the locations and the labeling of thermocouples on bearing pads and girders.

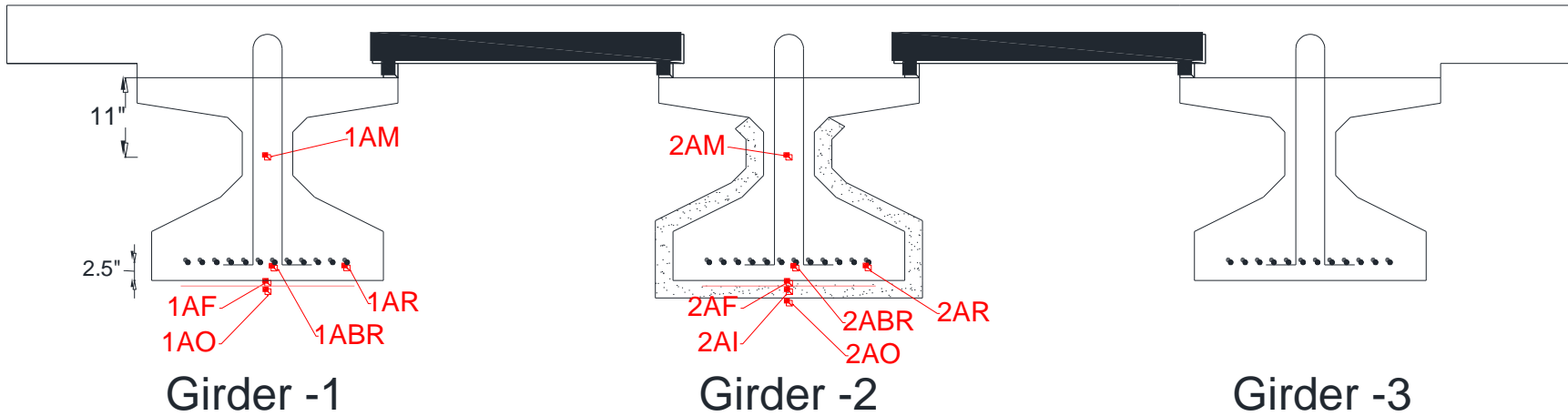
An extensive search was conducted to find an LVDT that can withstand such a high temperature; however, it was unsuccessful. After consulting with manufacturers and industry practitioner, robotic total station and laser scanner were proposed for displacement measurement. The proposed method involved measuring the elevations of various points on the girder at regular time interval. The deflection is then calculated by taking the difference between successive elevation readings as the fire progress.



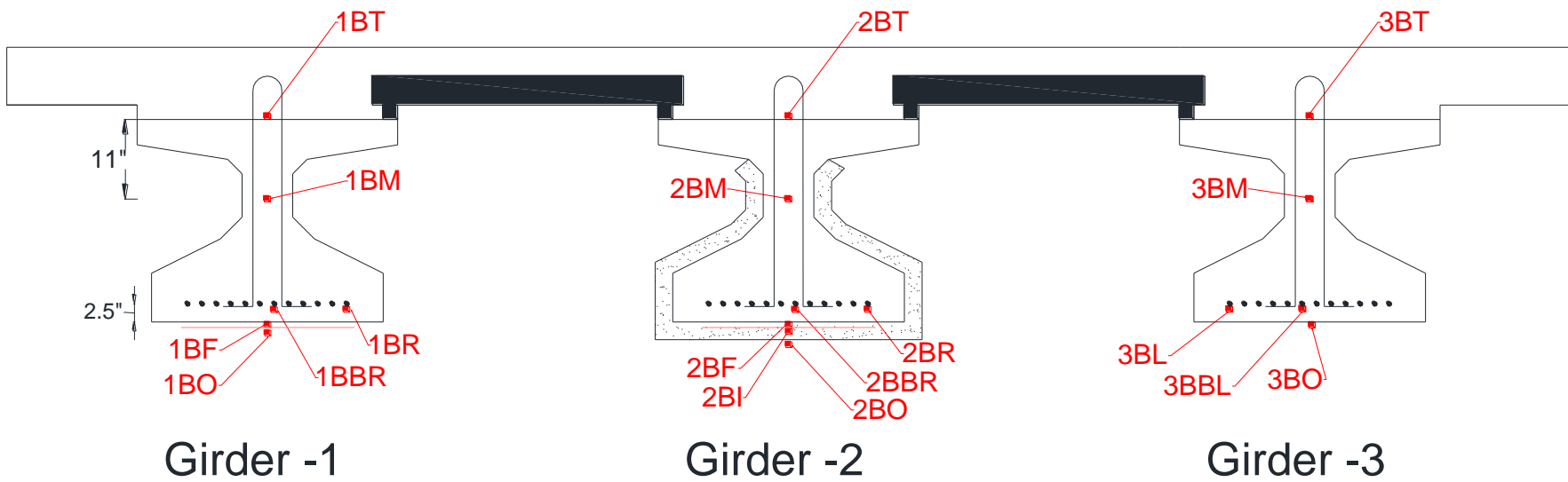
Thermocouples on bearing pads



Plan



### Section A-A



### Section B-B



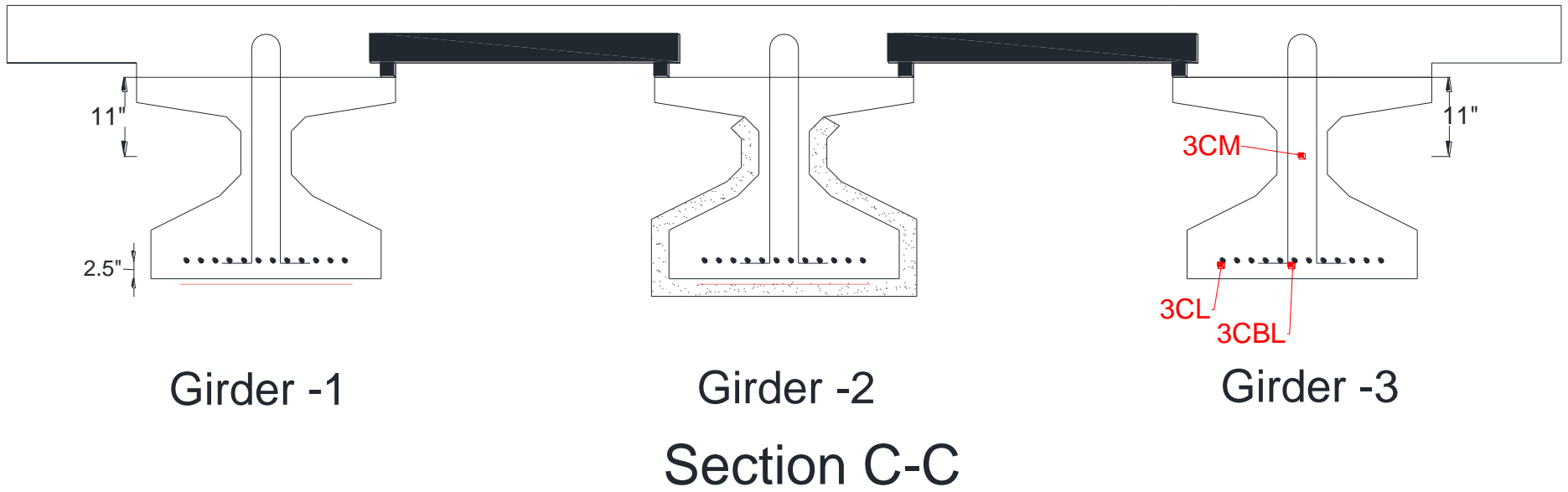


Figure 3-12 Locations and labeling of thermocouples on bearing pads and girders

## Chapter 4

### TEST BRIDGE CONSTRUCTION

#### 4.1 Girders and Precast Deck Panels Fabrication

TxDOT has a list of approved fabrication plants that produce prestressed members. The plants are divided into major and minor member prestressed manufacturing plants. Minor prestressed members include pile, bridge deck panels, and sound wall panels; whereas major prestressed members include all other prestressed member not listed as minor prestressed members (TxDOT 2014). Table 4-1 shows the lists of these approved plants.

Table 4-1 TxDOT approved precast prestressed manufacturing plant

<b>Major Prestressed Member Fabrication Plants (Multi-Project)</b>		
<b>Producer Code</b>	<b>Fabricator</b>	<b>Location</b>
99725	Bexar Concrete Works I, Ltd.	San Antonio, TX
99693	Flexicore of Texas, Inc.	Houston, TX
99716	Heldenfels Enterprises, Inc.	San Marcos, TX
99701	Texas Concrete Partners, L.P., Victoria Division (formerly Texas Concrete Company)	Victoria, TX
99723	Texas Concrete Partners, L.P., Waco Division (formerly Texas Prestressed Concrete, Inc.)	Waco, TX
99437	Valley Prestressed Products, Inc.	Eagle Lake, TX
98324	Zachry Odebrecht Parkway Builder	Houston, TX
<b>Minor Prestressed Member Fabrication Plants (Multi-Project)</b>		
<b>Producer Code</b>	<b>Fabricator</b>	<b>Location</b>
99714	Austin Prestressed Company	Austin, TX
99725	Bexar Concrete Works I, Ltd.	San Antonio, TX
98283	Castillo Prestress	Belen, NM
99693	Flexicore of Texas, Inc.	Houston, TX
99704	Heldenfels Enterprises, Inc.	Corpus Christi, TX
99716	Heldenfels Enterprises, Inc.	San Marcos, TX

The TX28 girders were fabricated by Texas Concrete Partners located in Elm Mott, TX on February 19, 2015. The casting bed was first cleaned and then the prestressing strands were drawn and stressed. All the mild reinforcements and welded wire mesh were then placed as shown in Figure 4-1.



Figure 4-1 Strands and reinforcements cage

A total of 18 Type-K thermocouples were installed at different depths and sections of each girder (Figure 4-2).

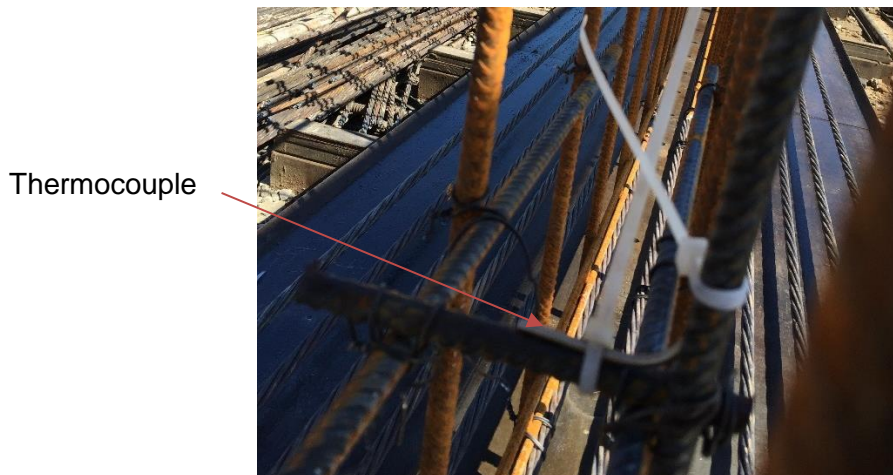


Figure 4-2 Thermocouple Installed at mid-web of the girder

The formwork was closed and then class H concrete as specified in the design was poured as shown in Figure 4-3. The mix design proportion for class H concrete is shown in Table 4-2. 10 concrete cylinder samples were made during the concrete pouring, which were later tested in the lab according to ASTM C39/C39M (2014) to check their compressive strength.



Figure 4-3 Concrete casting of girders

Table 4-2 Concrete mix proportions for the girders per cubic yards of concrete

<b>Components</b>	<b>Weight</b>
Type III cement	255.83 kg (564 lb)
Fly Ash-Class F	85.28 kg (188 lb)
Coarse aggregates	762.49 kg (1681 lb)
Fine aggregates	640.47 kg (1412 lb)
Admixture:	
7700 (Water reducing admixture)	1.7 kg (60 oz.)
100XR	0.113 kg (4 oz.)
Water	102.51 kg (226 lb)

On the following day, two of the concrete samples was tested to check if the release compressive strength was attained (Figure 4-4). A compressive strength of 29 MPa (4214.0 psi) and 28 MPa (4060 psi) was obtained, which was more than the required release strength of 27.58 MPa (4000 psi). The prestressing strands were released, and the girders were then transferred to their designated storage area (Figure 4-5).



Figure 4-4 Testing to check if the release compressive strength of concrete is attained.



(a)

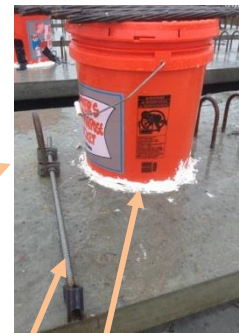
(b)

Figure 4-5 (a) Torch cutting of strands (b) Moving girders to the storage area

The connectors of the thermocouples are prone to corrosion. Since the girders were kept outside for a long time, they were protected from the adverse environment by epoxy sealing them inside a bucket as shown in Figure 4-6. The overhang brackets were also installed as shown in Figure 4-6.



(a)



Hanger      Waterproof epoxy

(b)

Figure 4-6 (a) Thermocouples end after concrete pour;(b) sealed thermocouples & hanger

The precast prestressed concrete panels were fabricated by Austin PreStress Partners located in Austin, TX. Class H concrete with mix design proportion shown in Table 4-3 was used.

Table 4-3 Concrete mix proportions for the precast deck panels per cubic yards of concrete

<b>Components</b>	<b>Weight</b>
Type III cement	191.87 kg (423 lb)
Fly Ash-Class F	63.96 kg (141 lb)
Coarse aggregates	839.15 kg (1850 lb)
Fine aggregates	613.71 kg (1353 lb)
Admixture:	
Viscocrete 2100 (Water reducing admixture)	1.11 kg (39 oz.)
Plastiment	0.17 kg (6 oz.)
Water	97.52 kg (215 lb)

The panels were manufactured according to the specification of TxDOT shown in Appendix B. For the current research projects, eight-1.092 m by 2.44 m (3'7" by 8') panels, which were already fabricated and stored in the yard, were procured (Figure 4-7).



Figure 4-7 Prestressed concrete bridge deck panels

## 4.2 Test Site

To the author knowledge, no attempt has been made in the nations or in the world to perform a full-scale hydrocarbon pool fire test on a bridge. This is due to primarily cost, the lack of research facilities and safety and environmental concerns during testing. Likewise, one of the challenges of undertaking this research project was finding a test site that has adequate space for construction and also equipped with all the facilities for fuel source and fire safety. A lot of options were explored in Texas and out of state. But all of the options were either cost prohibitive or have safety or environmental concerns. After a lot of failed attempt, the research team was able to secure a test site at the Dallas/Fort Worth International Airport's Fire Training Research Center (FTRC). The center is selected for the following reason: 1) it is located at short driving distance from UTA; 2) it has a permit to burn propane and E-III fuel; 3) The center house a firefighting station; 4) It has adequate land for construction and to provide safe standing distance during the fire test.

The Dallas/Fort Worth International Airport's Fire Training Research Center (FTRC), which is referred to as fire test center on this report, is located in the Southwest corner of the Dallas/Fort Worth International Airport (Figure 4-8). The center is equipped with state of the art technology to provide aircraft rescue firefighting and structural fire training.





Figure 4-8 The Dallas/Fort Worth International Airport's Fire Training Research Center

[\(www.dfwairport.com/firetraining/\)](http://www.dfwairport.com/firetraining/)

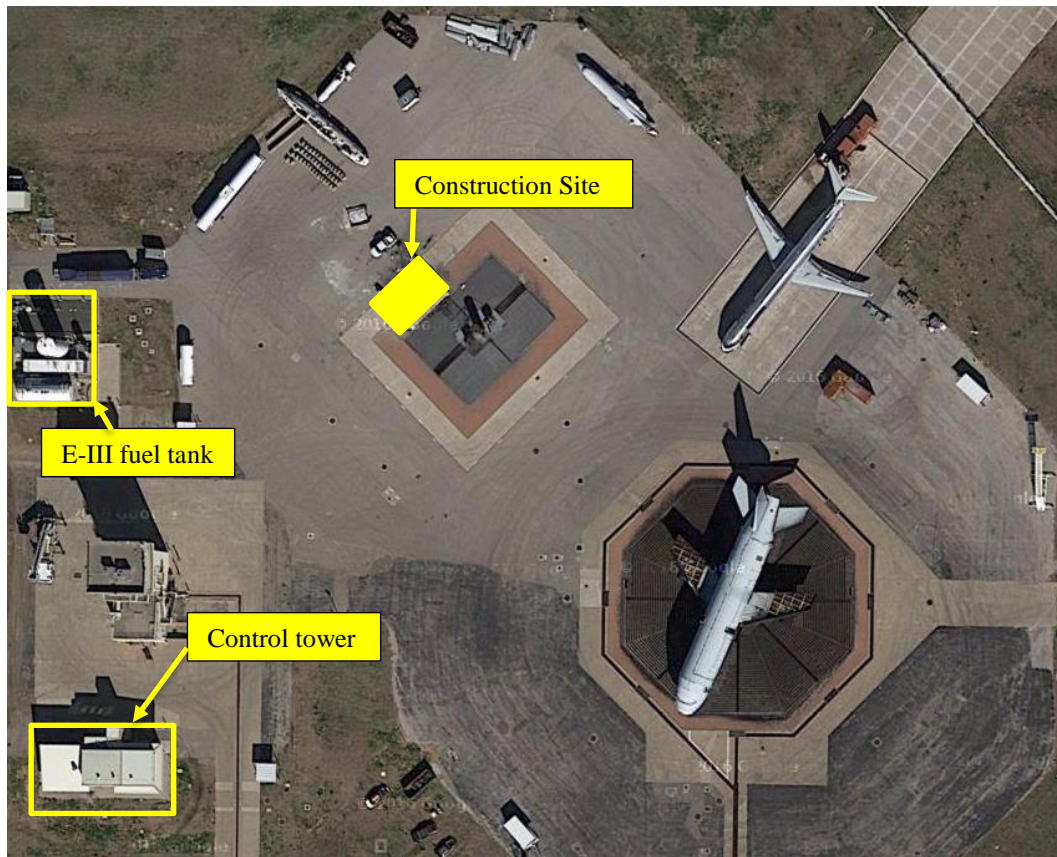


Figure 4-9 Test bridge construction site (map data: © 2016 Google)

Figure 4-9 shows the location of the test bridge construction site. The particular location was selected for two reasons. The first reason was its proximity to fuel source (E-III fuel tank). Second, it was this side of the facility which won't be needed for training purpose for the time frame the research team needed to build, test and demolish the test bridge.

### 4.3 Test Bridge Construction

A total of 32 days were used to construct, test and demolish the experimental bridge. Table 4-4 and Figure 4-10 show the list of tasks and their corresponding durations respectively. On the subsections to follow the details of each task will be described.

Table 4-4 Description of bridge construction tasks

<b>Task</b>	<b>Descriptions</b>
Task 1	Construction layout and staking survey
Task 2	Mobilization of construction materials and equipment
Task 3	Setting of supports and girders
Task 4	Setting of precast deck panels
Task 5	Deck forming and placing of reinforcement
Task 6	Deck concrete pour
Task 7	Sandblasting of girders
Task 8	FRP installation
Task 9	Fireproofing installation
Task 10	removal of deck formwork
Task 11	Loading the bridge with zipper barriers
Task 12	Preparation for the fire test
Task 13	Fire experiment
Task 14	NDE tests and visual observation
Task 15	Demolition and site clearing

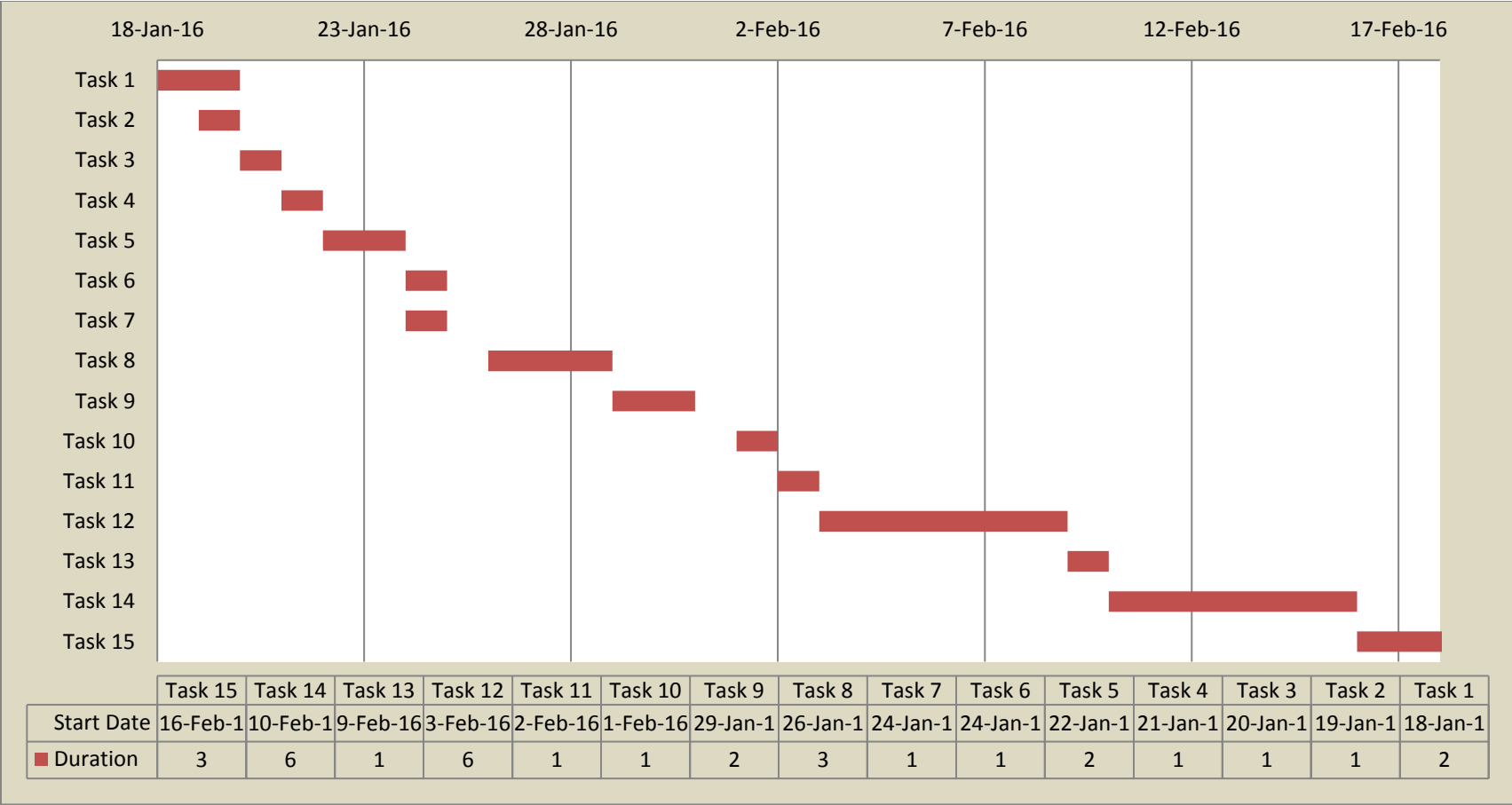


Figure 4-10 Test bridge construction schedule

### 4.3.1 Assembly of Components and Deck Construction

The first two days activities involved performing site layout survey to locate the exact position of the support girders (Figure 4-11), leveling the ground and mobilization of construction materials and equipment.



Figure 4-11 Construction layout and staking survey

#### **Setting of Supports and Girders**

The supports were transported to the fire test center (Figure 4-12 (a)). They were then placed on their marked position after cutting off the lifting hooks and grinding any surface irregularity (Figure 4-12 (b) and (c)). Six-228.6 mm x 533.4mm (9”X21”) bearing pads were placed on the top of the support at their respective marked position. Finally, the three girders were placed on the top of the bearing pads (Figure 4-12 (d) and (e)).



(a) Transportation of the support girders from CELAB to the fire test center



(b) Cutting off the lifting hooks and grinding surface irregularities



(C) Setting of the support girders to the ground



(d) Setting of the girders on the support



(e) Supports and girders after placement

Figure 4-12 Setting of supports and girders

### **Setting of Precast Deck Panels**

A layer of epoxy was spread on the edge of the girders first (Figure 4-13(a)). The bedding strips were then attached on the top (Figure 4-13(b)). The precast deck panels were finally placed after allowing the epoxy to cure (Figure 4-13(c)).



(a) Spreading of epoxy on the edge of the girder



(b) Placing of bedding strip



(c) Placing of precast deck panels

Figure 4-13 Setting of precast deck panels



### **Deck Forming and Concrete Pouring**

The deck forming began by hanging the overhang brackets on the hangers using dowel bars at 1.22 m (4ft.) spacing (Figure 4-14 (a)). A 19.05 mm (¾”) thick plywood was nailed on the top of the 50.8 mmx101.6mm (2”X4”) lumbers which were screwed to the top of the hangers (Figure 4-14 (b)). The longitudinal and transverse reinforcements were then placed per the spacing and the clear concrete cover specified in the design (Figure 4-14 (c)). TxDOT approved high early strength (HES) concrete was then poured using a concrete pump (Figure 4-14 (d), (e) and (f)). The mix design for the concrete is shown in Table 4-5. After allowing the concrete to cure for seven days, the formwork was removed.

Table 4-5 High early strength (HES) concrete mix design per cubic yards of concrete

<b>Components</b>	<b>Weight</b>
Cement	319.78 kg (705 lb)
Fly Ash-Class F	0
Coarse aggregates	839.15 kg (1850 lb)
Fine aggregates:	
Concrete sand	127.46 kg (281 lb)
Bridgeport sand	379.66 kg (837 lb)
Admixture:	
Type A(MRWR)	1.4 kg (49.4 oz.)
Type C (NC)	3.62 kg (127.6 oz.)
AEA	0.06 kg (2.1 oz.)
Water	121.11 kg (267 lb)



(a) Installation of hangers



(b) Forming of the overhang portion of the deck



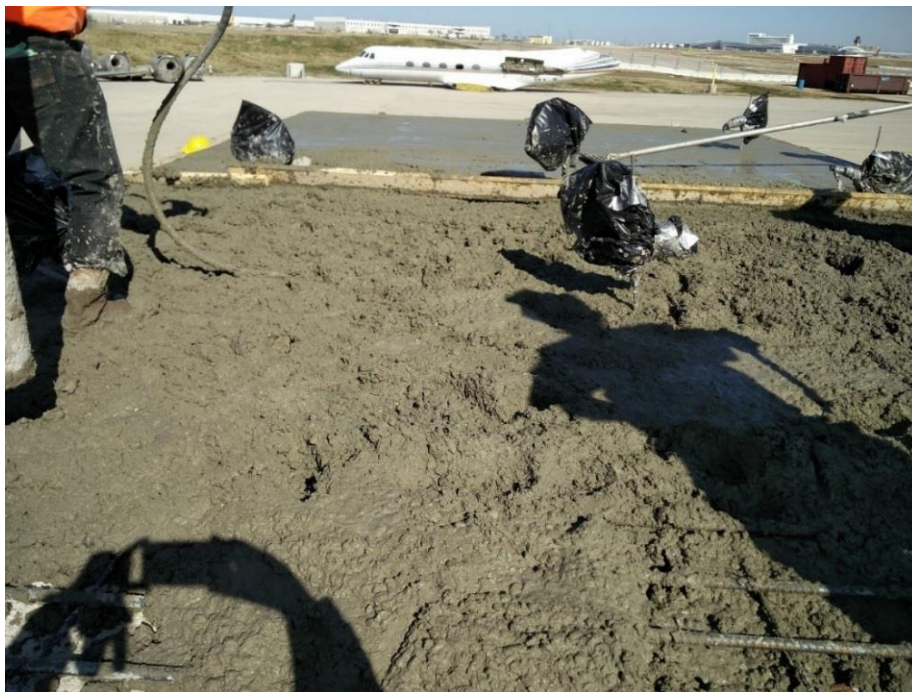
(c) Deck reinforcement



(d) Concrete pump



(e) Deck concrete pour



(f) Concrete pouring and finishing

Figure 4-14 Deck forming and concrete pouring

### 4.3.2 Installation of FRP

Even though the FRP installation procedures are straightforward, previously conducted studies showed that even a minor deviation from the prescribed procedures could dramatically affect the final performance of the whole system. These effects include but not limited to premature delamination at the concrete/FRP interface. In most of the FRP applications, the FRP bond to the concrete is critical. If the concrete surface is not properly prepared prior wrapping, the FRP may not adhere adequately to the concrete surface.

ACI 440.2R (2008) requires that where the FRP wrap around corners, the corners should be rounded to a minimum of 13 mm (0.5 in.) radius to prevent stress concentrations in the FRP systems and voids between the FRP and the concrete. As shown in Figure 4-15(a) the chamfers of the girders in all the areas where the transverse FRP wrap around were rounded to a radius more than specified in ACI 440.2R (2008).

Both ACI 440 (2008) and the FRP manufacturer requires the substrate surface, where the FRP adheres, to be a concrete surface profile 3 (CSP 3) as specified by the International Concrete Repair Institute (ICRI). ICRI's guideline specifies nine distinct surface profiles ranging from CSP 1 which is nearly flat to CSP 9 which is very rough (Figure 4-15 (b)). The FRP industry uses grinding or sandblasting to get the required surface profile. For the current study, both methods of surface preparation were tried and it was found out that sandblasting

(Figure 4-15 (e)) gives a surface profiles that is close to CSP-3 compared to grinding (Figure 4-15 (d)).

After sandblasting the surface (Figure 4-15 (b)), a groove was cut on the bottom flange of the girder to attach the thermocouple at the interface between the FRP and the concrete (Figure 4-15 (f)). Sikadur 31 was used to bury the thermocouple inside the groove (Figure 4-15 (g)).

A blower is then used to remove any dust or loose material from the concrete surface ((Figure 4-15 (i)). Sikadur 31 was used to patch any voids or honeycombs on the surface of the concrete ((Figure 4-15 (j)). While the Sikadur 31 was still tacky, Sikadur 330 was applied on the surface of the girder ((Figure 4-15 (k)). The CFRP was then saturated with Sikadur 300 (Figure 4-15 (l)) and attached to the concrete substrate. Figure 4-15 (m) and (n) shows the longitudinal and transverse FRP applied on both girder-1 and girder-2.

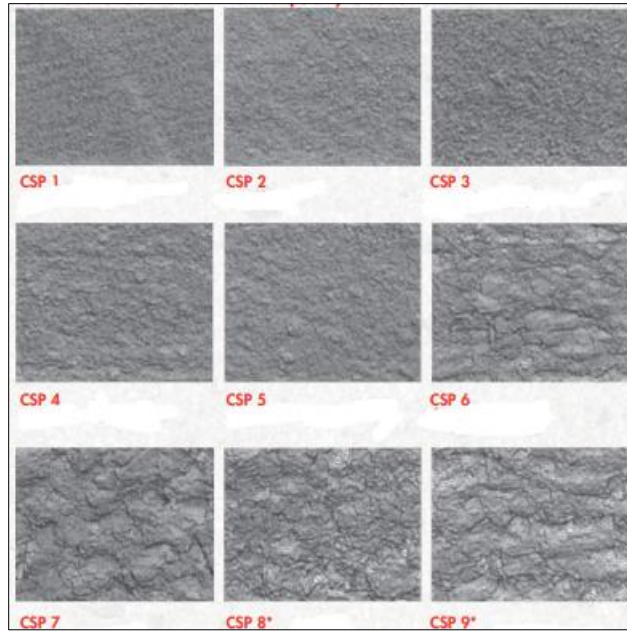


Before grinding



After grinding

(a) Girder chamfer before and after grinding



(b) ICRI concrete surface profiles (CSP)



(c) Sandblasting unit (left) and operation (right)



(d) Concrete surface prep using grinder (e) Concrete surface prep using sandblasting



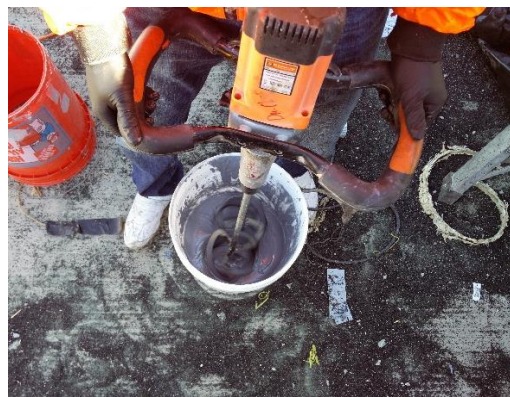
(f) Groove cutting



(g) Installed thermocouple



(h) Pressurized dust removal



(i) Mixing of Sikadur-330



(j) Patching of voids using Sikadur 30



(k) Applying Sikadur-330 on the concrete





(l) Saturating the CFRP with Sikadur 300



(m) Longitudinal FRP with Thermocouples installed at the Interface between the fire proofing and the FRP



(n) Transverse FRP

Figure 4-15 FRP and thermocouple installation

#### 4.3.3 Installation of Insulation

The fireproofing installation comprised of applying of Sikadure-300 on the concrete surface (Figure 4-16(a)) followed by spraying of sand to enhance the FRP-insulation bond (Figure 4-16(b)). The fireproofing material, which is the Sikacrete-213F, was then mixed with the appropriate amount of water as specified in the product data sheet and spray applied on the girder (Figure 4-16(c)). It was

sprayed in two layers. Since applying the whole 40 mm (1.57 in.) thickness caused debonding of the mortar (Figure 4-16(d)).

The test site is located in an area where there is no wind barrier, which created a challenge during application. Despite the wind, a fairly uniform thickness of fireproofing was provided. The product data sheet or the manufacturer didn't specify what curing method should be used. Thus, cracks were observed in some areas few days after the application.



(a) Application of Sikadur 300



(b) sprayed sand



(c) spraying unit(left) and mixing of Sikacrete-213F (right)



(d) spray applying of fireproofing

Figure 4-16 Application of Fireproofing

## Chapter 5

### FIRE TEST

#### 5.1 Test Setup

The following subsections discuss the preparation made before the fire test.

##### 5.1.1 Live Loading of the Test Bridge

During a fire event, it is a common standard practice to shut down bridges from any traffic. But if there is a disabled vehicle, the bridge will be subjected to a combined live load and fire. For the current study, the fire test was conducted assuming there will be a vehicle on the bridge deck during such event, to observe the performance under the worst case scenario.

Bridges are designed for a maximum of design truck plus design lane load or design tandem plus design lane load (AASHTO 2014). The total width of the experimental bridge was 5.486 m (18 ft.), which ideally made it capable of accommodating only one traffic lane. A moving load analysis showed that a design truck with the arrangement shown in Figure 5-1 yields the maximum moment on the girders. According to the analysis result, the 35.585 kN (8 kip) front wheel load is out of the span limit of the bridge.

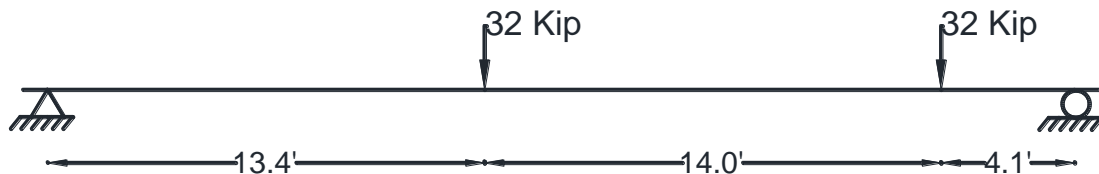


Figure 5-1 Arrangement of the design truck load for maximum moment

During the fire test, the design truck load was simulated by loading the test bridge with blocks of zipper barriers. Each barrier weighs approximately 6178.6 kN (1389 lb). 22 of them were stacked together at the location of each wheel to yield the wheel reaction (Figure 5-2). The barriers were lined across the width of the bridge deck to provide an approximately equal distribution of load among the three girders per their tributary area (Figure 5-3).



Figure 5-2 Loading of zipper barriers



Figure 5-3 Test bridge loaded with the simulated AAASHTO HL-93 live load

### 5.1.2 Fuel Flow Rate Determination

A pan with dimensions of 3.048 m (10 ft.) width, 6.096 m (20 ft.) in length and 0.3048 m (1 ft.) in depth was used as a fire pit. It was made by welding steel plates of thickness 9.525 mm (3/8 in.). Pipes were fitted to the pan to supply the fuel at a constant controlled rate.

Before the actual experiment, a mock-up fire test was performed. The test was conducted with the aim of determining the fuel flow rate that gives a consistent fire without spilling excessive fuel. And, to evaluate the performance of the fire pit under prolonged fire exposure. Figure 5-4 shows the mock-up fire test in progress.



Figure 5-4 Mock-up fire test

One concern before the test was whether the pan could survive the heat without buckling or warping. To curb this, the pan was filled with water to a depth of approximately of 0.254 m (10 in.) before starting the fire as a means to cool

down. The fire was then started and observation was made for 5 minutes by varying the fuel flow rate. It was found out that 20 gallons per minute were the optimum flow rate. After putting off the fire, the pan showed warping, as shown in Figure 5-5. As a remedy, more stiffeners were welded as shown in Figure 5-6.



Figure 5-5 Warping of side of the pan



Figure 5-6 Welding of additional stiffeners

### 5.1.3 Duration of Fire and Location of the Fire Pit

In actual bridge fire; the volume of fuel, type of fuel, response time of the fire department, time to extinguish the fire, location of the incident (rural or urban area), total surface area of the spill and many other factors determines the extent of damage to the bridge. From previously documented incidents, the volume of fuel can be as low as 11.35 m<sup>3</sup> (3000 gals) (Sika Corporation 2006) and as high as 37.5 m<sup>3</sup> (9900 gallons) (Alos-Moya et al. 2014). The time to extinguish the fire could be as low as 30 minutes (Sika Corporation 2006) and as high as 2 hours (SFGATE 2007). Considering these variables, the test bridge was subjected to 1.0-hour fire.

The maximum moment of the test bridge is at its mid-span. Hence, the fuel pan was placed at this location to see the maximum effect of the fire on the flexural strength of the girders.

### 5.1.4 Determination of safe standing distance

One of the concern before the fire test was the safe standing distance while collecting the test data without sustaining any burn. The human body by its nature can withstand a certain threshold limit of heat flux without sustaining injury. Zarate et al. (2008) tabulated ranges of heat fluxes and their effects on human bodies as shown in Table 5-1. According to this study, a human body is safe without requiring special protection as long as the heat flux doesn't exceed 1.4 kW/m<sup>2</sup>.



Table 5-1 Consequences of thermal heat flux on human bodies (Zarate et. al 2008)

<b>Heat flux (kW/m<sup>2</sup>)</b>	<b>Effects on a human body</b>
1.4	Harmless for persons without any special protection
1.7	Minimum required to cause pain
2.1	Minimum required to cause pain after 60 s
4.0	Causes pain after an exposure of 20 s (first-degree burns)
4.7	Causes pain in 15–20 s and burns after 30 s
7.0	Maximum tolerable value for firefighters completely covered protected by special Nomex protective clothes

For the current study, three different methods were considered to determine the safe standing distance: empirical equation method, CFD analysis and recommendation from an expert who has done open pool fire experiment previously.

Sudheer et al. (2013) conducted open pool fire experiments to determine the safe standing distance. From the experiment, it was found out that the fire safety distance for a 4 m x4 m (13.11 ft. X 13.11 ft.) open diesel fire is around eight times the length/width of the fire. Even though the current study used E-III fuel, the recommendation from this study was used to get an idea. The fire pit used for the current study was rectangular with total surface are of 18.58 m<sup>2</sup> (200 ft<sup>2</sup>). Converting this area to an equivalent square dimension yields a fire pit with a dimension of 4.31 m x 4.31 m (14.14 ft. x 14.14 ft.). Eight times 4.31 m (14.14 ft.)

yielded 34.48 m (113.0 ft.) safe standing distance from the center of the fire or 29.47 m (96.62 ft.) from the end of the bridge. This empirical formula didn't take into consideration the variation of wind speed or obstructions.

The second approach was to develop a CFD model that takes into consideration the variation of wind. The model was developed on PyroSim software. PyroSim is a graphical user interface for the Fire Dynamics Simulator (FDS) software. Building FDS model requires defining: a computational domain with all its boundary conditions, the geometry of the structure, mesh or discretization of the computational domain, material properties, fire source and combustion model. The computational domain shown in Figure 5-7 was considered for the analysis. The dimensions were wide enough to represent the volume affected by the fire adequately but small enough to run the analysis in a reasonable amount of computational time.

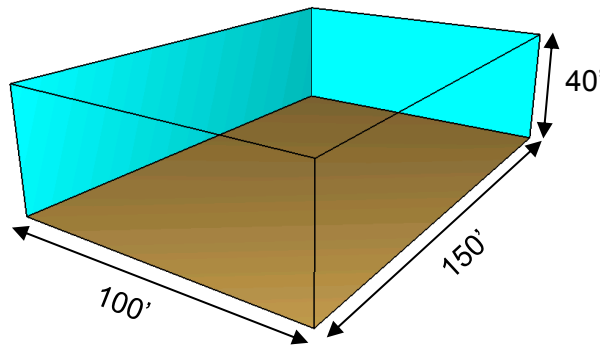


Figure 5-7 CFD model computational domain

The past 15-years average wind speed and average wind gust speed data of the fire test center for the months of January and February were collected from [www.wunderground.com](http://www.wunderground.com), shown in Table 5-2. The average of the 15-years

average wind gust speed and average wind speed was 25.7 mph and 10.8 mph, respectively. 25.7 mph wind speed was then considered for the CFD model, assuming worst case scenario. Figure 5-8 shows the location of the proposed data recording station during the fire test. Northeast wind has the maximum effect on the proposed data recording station, hence a 25.7 mph northeast wind was considered in the CFD modeling.

Table 5-2 Average wind gust speed and average wind speed history for fire test center for the months of January and February (www.wunderground.com)

Year	Average wind gust speed (mph)		Average wind speed (mph)	
	January	February	January	February
2000	26	27	10	10
2001	24	25	9	11
2002	24	25	11	10
2003	26	27	10	12
2004	25	24	10	10
2005	25	25	10	9
2006	26	28	12	11
2007	25	26	10	12
2008	28	27	12	12
2009	26	26	11	14
2010	25	24	9	10
2011	24	27	8	13
2012	27	24	11	11
2013	24	26	10	12
2014	27	27	13	12
2015	26	27	10	11

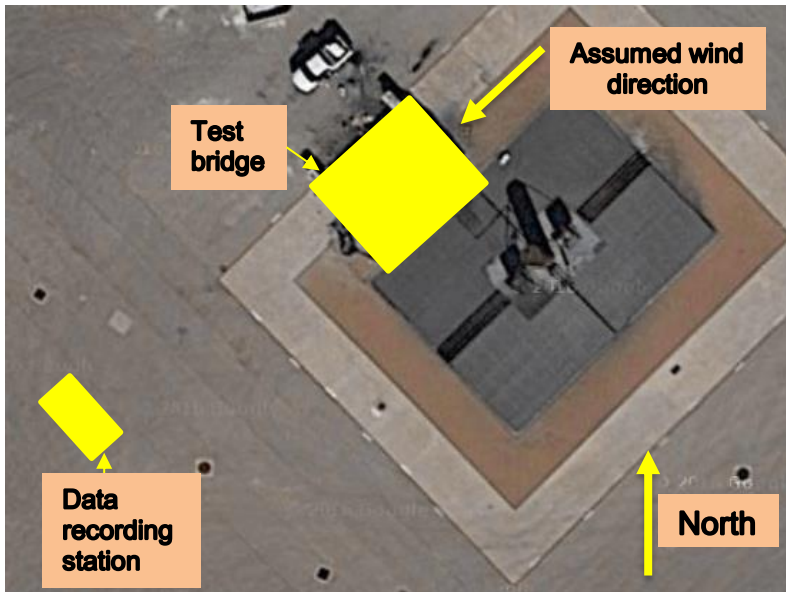


Figure 5-8 Direction of wind considered for CFD modeling (map data: © 2016 Google)

To define the fire load, PyroSim requires the heat release rate per unit area (HRRPUA). The heat release rate of a pool fire is calculated using equation (5-1), specified in chapter 26 of SFPE handbook of fire protection engineering (2016).

$$\dot{q} = \Delta h_c \dot{m}'' (1 - e^{-k\beta D}) A \quad 5-1$$

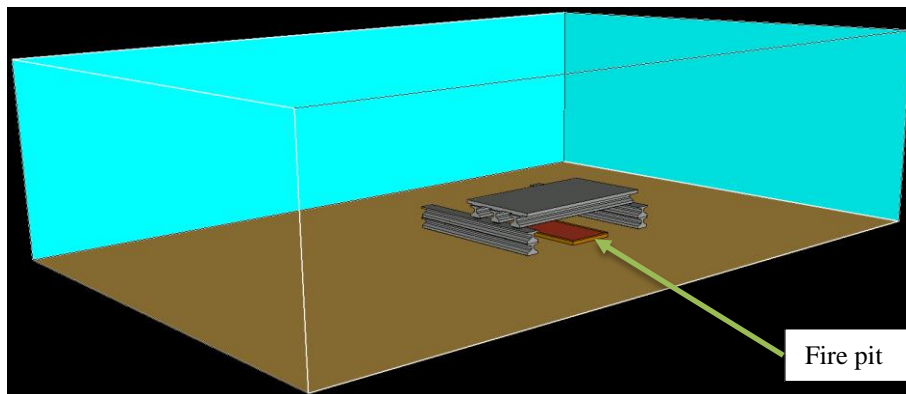
Where:  $\dot{q}$  is the heat release rate of the pool;  $\Delta h_c$  is the effective heat of combustion of the fuel;  $\dot{m}''$  is mass burning rate of fuel per unit surface area;  $k\beta$  is the empirical constant;  $D$  is the diam of the pool fire and  $A$  is the surface area of the pool fire.

But  $\dot{m}''$ ,  $\Delta h_c$  and  $k\beta$  are not available for the E-III fuel. The author checked all the sources that were believed to have these parameters including the manufacturer, but it was unsuccessful. As an alternative to E-III, it was decided to

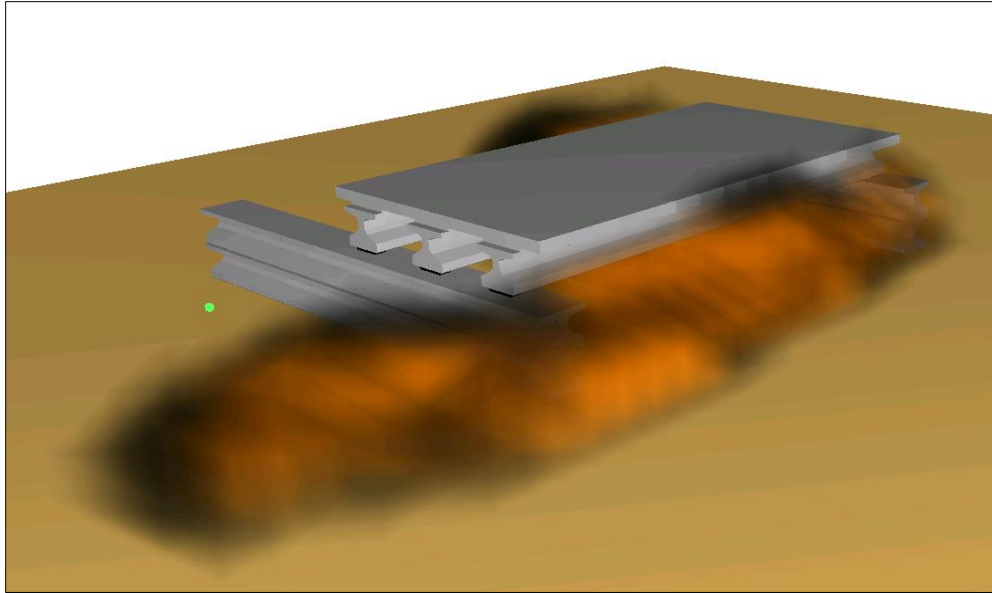
use gasoline as fuel since its thermomechanical properties are readily available on Table 26.21 of the SFPE hand book of fire protection engineering (2016).

The fire pit (pan) has a total surface area of  $18.605 \text{ m}^2$  ( $200 \text{ ft}^2$ ). Hence, the heat release rate per unit area (HRRPUA) of the fire is  $2400 \text{ kW/m}^2$  ( $211.33 \text{ Btu/ft}^2$ ). The HRRUPA curve inputted to PyroSim increases linearly from 0 to the maximum value of  $2400 \text{ kW/m}^2$  ( $211.33 \text{ Btu/ft}^2$ ) in 20 secs and remain constant for 3580 seconds (59 mins and 40 secs).

The test bridge and the fire pit were modeled inside the computational domain, shown in Figure 5-9. The maximum total heat flux at distance of 3.048 m (10'), 9.144 m (30'), 15.24 m (50'), 18.288 m (60') and 22.86 m (75') from the support were recorded during the analysis for each time step. As expected, the heat flux decreases moving away from the support as shown in Figure 5-10. It can be observed from this figure, the heat flux at a distance of 22.86 m (75') is approximately zero, which is well below the threshold limit a human body can endure without sustaining any injury. This is less than the distance predicted by the empirical equation.

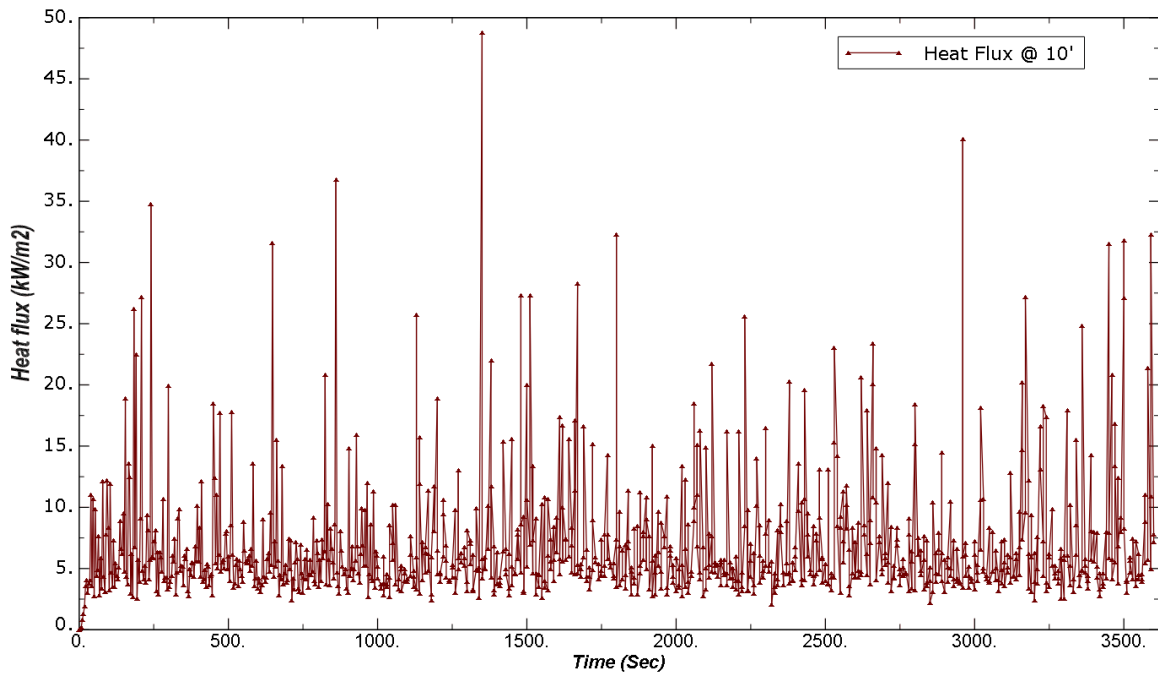


(a) Test bridge inside the computational domain



(b) Fire from gasoline four mins after the start of the fire

Figure 5-9 PyroSim model



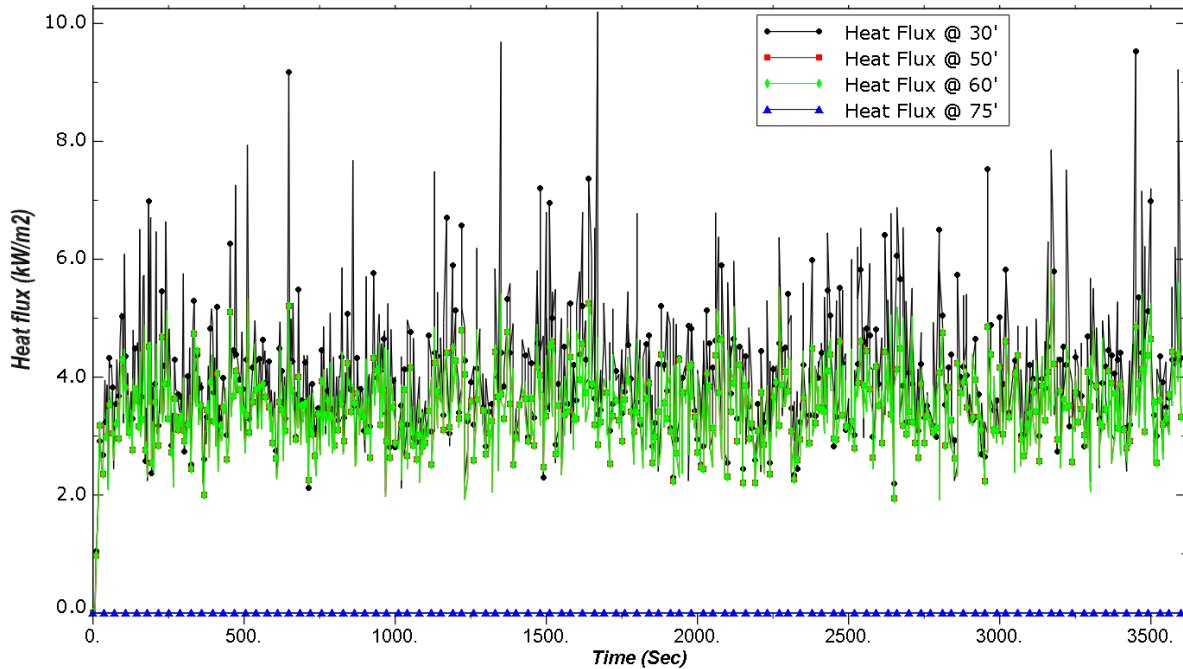


Figure 5-10 Variation of heat flux as a function of distance from the end of the bridge

In addition to the empirical equation and the CFD analysis, experts who have extensive experience on open pool fire experiments were consulted. It was finally decided to take the data reading at 22.86 m (75 ft.) from the end of the bridge.

Using a very high temperature rated extension wire for the whole 22.86 m (75 ft.) was cost prohibitive. Hence, after consulting the result from the CFD analysis, two types of extension wires were used. The first 10.668 m (35 ft.) of the extension wire was 1204°C rated 20-gauge wire with high-temperature ceramic fiber insulation. The remaining 12.192 m (40 ft.) was 700°C rated 20-gauge wire with high-temperature fiberglass insulation (Figure 5-11).



Figure 5-11 Thermocouple extension wire

As an additional precaution, ceramic fiber blanket which is rated for 1400°C temperature was used to cover the opening between the girders to stop the flame from projecting towards the data recording station as shown in Figure 5-12.



(a) Opening between girders before placing the ceramic blanket



(b) Opening between girders after placing the ceramic blanket

Figure 5-12 Opening between girders before and after placing the ceramic blanket



## 5.2 Fire Experiment

### **Before starting the fire**

One of the challenges of conducting open pool fire experiment is wind since it is the determining factor in getting a uniform fire distribution. The research team selected the date of the experiment to be on a non/minimal wind day after watching the weather forecast on an hourly basis. As a matter of fact, the test date was postponed two times due to windy weather.

Before starting the fire; students, TxDOT officials, and other invited people were notified not to trespass the designated watching area to make sure everyone's safety. Two firefighter trucks and nine firefighters were at the scene to control any unforeseen events during the test (Figure 5-13).



Figure 5-13 Firefighters and Firefighter trucks preparing for the test

The coordinates and the elevation of various points on the bridges were taken using 3D laser scanner and a robotic total station.

### **During the fire test**

The pan was filled with water to a depth of 0.254 m (10") first followed by the E-III fuel. The fire was then started.

It was a calm and a non-windy at the beginning of the test as it can be observed from the even distribution of the flame shown in Figure 5-14. But few minutes past the start of the fire, a southeast wind came and disrupted the even distribution of the fire as shown in Figure 5-15. The wind persisted until the end of the test. The test was conducted for an hour burning 4.32 m<sup>3</sup> (1140 gallons) of E-III fuel.



Figure 5-14 Fire test



Figure 5-15 Uneven distribution of fire due to the wind

A continuous popcorn like explosion and an intermittent loud explosion from the spalling of the concrete were heard throughout the fire test. At approximately six mins after the start of the fire, the longitudinal FRP from Girder 1 was observed debonding and falling on the ground.

### 5.3 Results and discussions

The following subsections discuss the response of the bridge to the pool fire considering various parameters. These include the thermal and mechanical response, results of visual inspections and results of surface hardness test.

The thermal and mechanical response of the test bridge to the fire depend on the compressive strength of the concrete at the time of the experiment. Table 5-3 shows the cast-in-place deck and the girders concrete compressive strength during the fire experiment. The compressive strength of the precast deck panels

was not available. However, the precast deck panels were made of Class H concrete, which is the same class of concrete used for fabricating of the girders. Hence, the concrete used for the precast panels is expected to show the same level of gain in strength with time like the concrete used for the girders.

The concrete used for the cast-in-place deck fell into the normal strength concrete (NSC) category. Whereas, the concrete used for the girders and the precast deck panels are in high-strength concrete (HSC) group.

Table 5-3 Compressive strength of concrete used for cast-in-place deck and girders

<b>Component</b>	<b>Compressive strength MPa (psi)</b>
Deck	39.1 MPa (5666 psi)
Girders	75.5 MPa (10952 psi)

The current report used support-1 and support-2 as a reference points when explaining the results of the test (Figure 5-16). Support -1 refers to the end of the bridge with less fire; on the contrary, support-2 refers to the end where there was more fire due to the prevalent wind during the test. The current elevation view shown in Figure 5-16 is referred as the South elevation view and the view on the opposite side is referred as North elevation view. The thermocouples were installed at quarter, half and three-quarter of the span length measured from support-1 as shown in Figure 3-12.



Figure 5-16 Labeling of supports

### 5.3.1 Thermal Response

During a standard fire test of structural members, it is a common phenomenon to observe a steady increase in temperature readings with time. On the contrary to this, the temperature readings for the current study showed erratic variation due to the prevalent wind.

While the fire test was in progress, data from the installed thermocouples were recorded. The following sections discuss the thermal response of each component of the test bridge.

#### 5.3.1.1 Girder-1

Girder-1 sustained the most severe damage compared to the other two girders. Figure 5-17 depict the temperature vs. time reading from thermocouple-1BO, installed on the outside surface of Girder-1 at Section B-B (Figure 3-12). As it can be observed from the graph, the temperature from the fire reached as high

as 1131°C. During the growth phase, the fire peaked to a temperature of 876°C within 41 secs after starting the test. The temperature plunged down by 800°C in three minutes during the decay phase. The temperature from the fire goes up and down erratically due to the prevalent wind. A temperature difference of up to 640°C was observed among temperature reading taken within a 1-minute interval. This sudden rise and falling, as well as, the erratic variations of temperature caused thermal shock which eventually contributed to cracking and spalling of concrete.

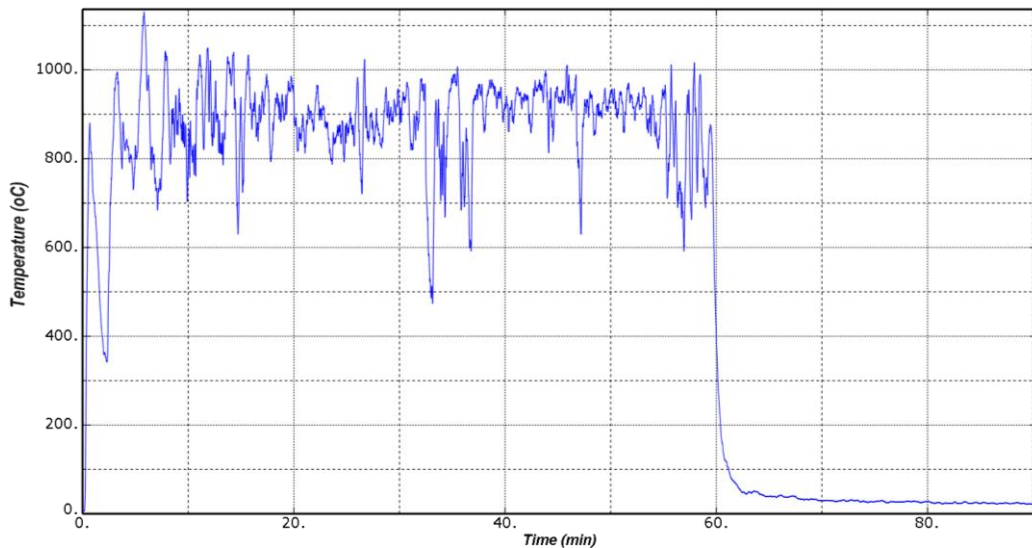


Figure 5-17 Temperature vs. time curve measured by thermocouple-1BO

Figure 5-18 compare the temperature versus time readings of thermocouple-1BO with two of the most commonly used standard fire curves i.e. ASTM E119 and ISO 834. Both standard curves peak to a high temperature at a very slow rate compared to the pool fire. There is also no erratic variation of temperature in the standard fire curves since the tests are performed under

controlled condition. The temperature readings from the pool fire are more than the standard fire curves for most of the duration.

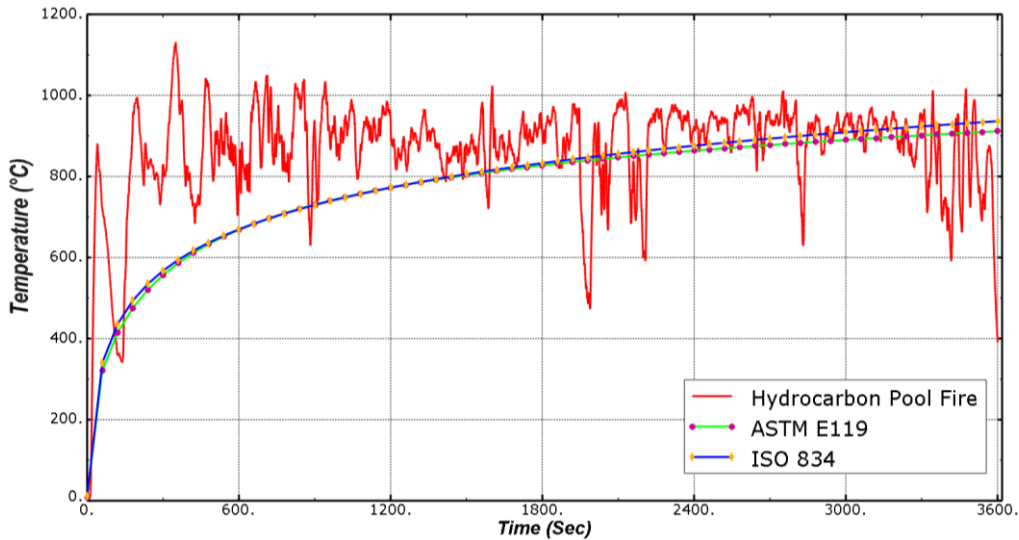


Figure 5-18 Fire curves from pool fire versus standard fire

The temperature measured at the FRP-concrete interface is a good indicator to evaluate the performance of the bond between FRP and concrete. The resin used for the current study has a glass transition temperature,  $T_g$ , of  $60^{\circ}\text{C}$ . Figure 5-19 depicts the temperature measured by thermocouple-1AF and thermocouple-1BF at this interface. The reading from both thermocouples showed that  $T_g$  was exceeded early on the test; 41 secs and 168 secs after the test began for thermocouple-1BF and thermocouple-1AF, respectively. Thermocouple-1AF took relatively longer time to reach  $T_g$  compared to thermocouple-1BF because of uneven distribution of fire. After approximately six mins into the test, the FRP was observed debonding and falling on the ground. Later on the test, charred carbon fibers were found spreading on the ground as shown in Figure 5-20.

After the test had been completed, both thermocouple-1AF and thermocouple-1BF were found on the ground under a pile of spalled concrete as shown in Figure 5-20. In addition to the wind, this resulted in a series of spike followed by falling of temperature reading for both thermocouples as observed in Figure 5-19.

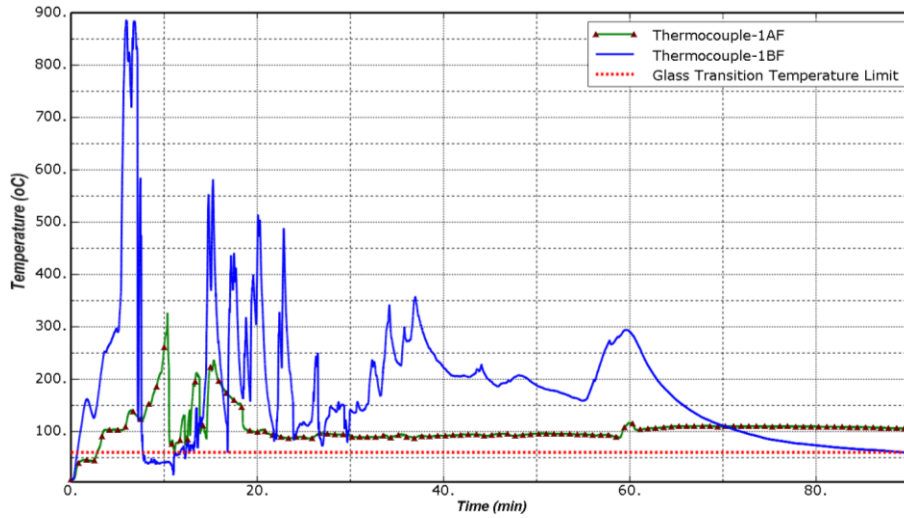


Figure 5-19 Measured temperature at FRP-concrete interface by the rmocouple 1AF & 1BF





Figure 5-20 Thermocouples under a pile of spalled concrete and charred carbon fibers

Figure 5-21 shows the temperature versus time curve for the prestressed strands. The temperature reading from thermocouple-1AR is lower than the reading from thermocouple-1BBR since the former was exposed to less fire. It is also observed from the graph that the temperature reading from thermocouple-1AR kept on increasing for approximately 20 minutes after the fire was extinguished. This is due to conduction of heat from the hot region. On the contrary, the temperature reading from thermocouple-1BBR went down as soon as the fire was extinguished since it was located in the high-temperature region. The temperature reached as high as 205°C and 473°C for thermocouple-1AR and thermocouple-1BBR, respectively. At a temperature of 473°C, prestressing strands are known to lose approximately 70 % of their strength (Eurocode-2, 2004).

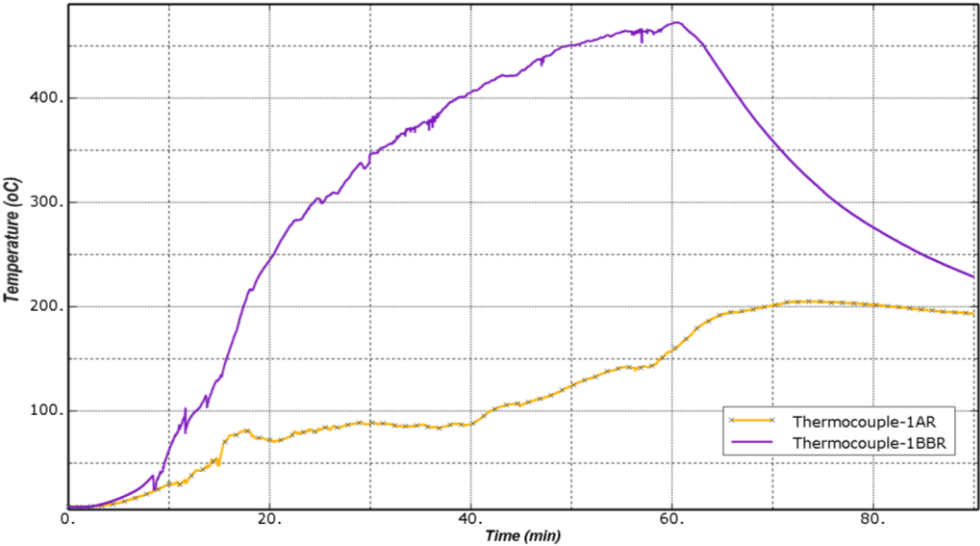
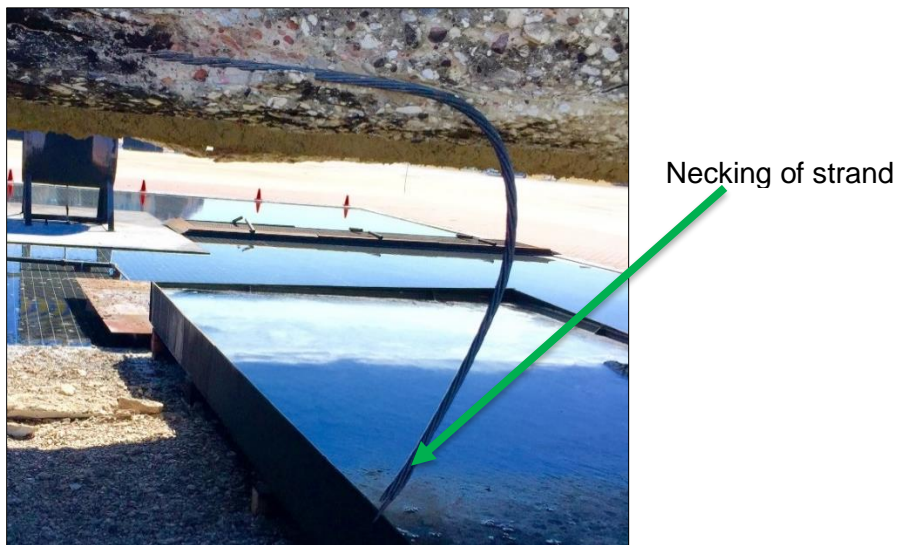


Figure 5-21 Measured temperature at the prestressing strands for Girder-1 (1AR and 1BBR)

It was visually observed that two prestressing strands were broken at 3.63 m (11.9') and 3.99 m (13.1') from support-2 as shown in Figure 5-22 (a). One of the strands lost the concrete cover for approximately 3.35 m (11') of its length (Figure 5-22 (a)). The remaining strands had concrete which barely covers them. Six of the shear reinforcements, which were placed at a distance of 2.957 m (9.7ft.) from support-2, had a partial loss of concrete cover as shown in Figure 5-22 (c).



(a) Broken and exposed prestressing strands



(b) Necking of prestressing strand



(c) Exposed shear reinforcements

Figure 5-22 Girder-1 exposed/broken prestressing strands and exposed shear reinforcements after fire test

Figure 5-23 show the temperature measured as a function of time by thermocouples-1AM and thermocouple-1BM inside the web of Girder-1. As expected, the temperature measured by later was higher than the former for most of the duration of the fire. Compared to the other thermocouple installed on Girder-1, these two thermocouples took a longer time to cool down after the fire was extinguished. Temperature readings from thermocouple-1AM and thermocouple-1BM kept on increasing for approximately 55 min and 44 min respectively after extinguishing the fire, before starting to go down.

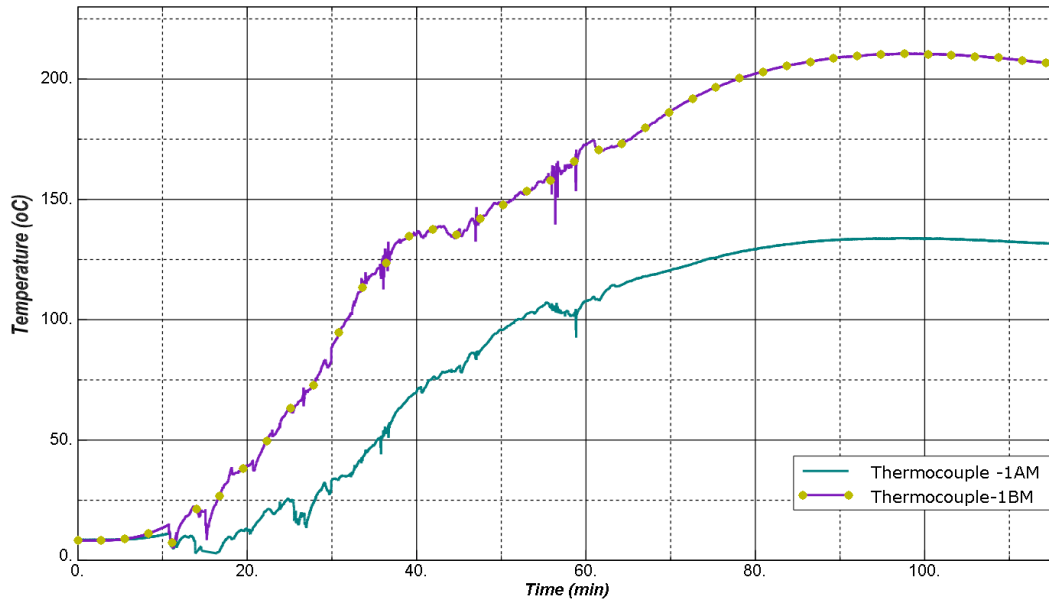


Figure 5-23 Temperature vs. time readings of thermocouple-1AM and thermocouple-1BM

Figure 5-24 shows the progression of the fire across the cross section of the girder at its mid-span. It is observed from the figure that the measured temperature in concrete decrease with increasing depth from the bottom of the surface. This is attributed to the low thermal conductivity and high thermal capacity of concrete, which plays a key role in slowing down heat penetration to the inner layers of concrete. It is a common phenomenon in standard fire tests to observe a temperature plateau at about 100°C from the readings of the thermocouples placed inside the concrete (Hou et al., 2015; Dwikat and Kodur 2009). This is due to evaporation of free water in concrete which occur around 100°C. However, no temperature plateau was observed in current study at this temperature. This could be due to spalling/cracking of the concrete in the vicinity of the thermocouples or the migration of moisture to the inner portions of concrete sections.

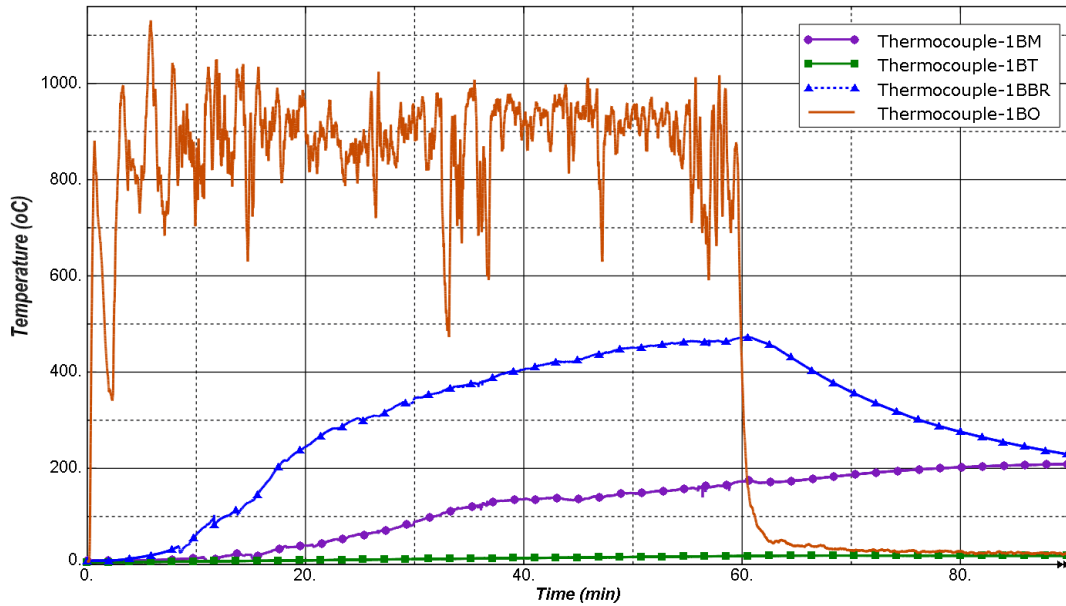


Figure 5-24 Mid-span temperature vs. time reading of Girder-1 at different depths

Severe spalling of concrete was observed on Girder-1. It lost approximately 25 % of concrete. High strength concrete (HSC) is known to be more prone to spalling than normal strength concrete (NSC) because of its low permeability and low water-cement ratio. During fire, the low permeability of HSC increases the buildup in pressure in the girders. When this pressure exceeds the tensile strength of concrete, chunks of concrete fall off from the surface (Figure 5-25 (a)). Inspecting the color of spalled of concrete revealed that most of the big chunks were spalled off at the early stages of the fire. The fuel pan was filled with spalled off concrete ranging from small pieces to big chunks as big as 0.914 m (3 ft.) (Figure 5-25 (b)). Concrete spalling and cracking sound continued to be observed and heard even after the fire was put out.



(a)



(b)



(c)



(d)

Figure 5-25 Girder-1 after fire test: (a) Chunks of spalled concrete; (b) fuel pan filled with spalled concrete; (c) south elevation view of Girder-1; (d) bottom view of Girder-1

### 5.3.1.2 Girder-2

The two thermocouples placed on the exterior surface of the fireproofing give out a bad reading. However, the values of the surface hardness and the results of visual inspections of the concrete not protected by the insulation revealed that the severity of the fire on Girder-1 and Girder-2 were similar. These results are discussed in section 5.3.2.2. Also, during the fire test, the same intensity of fire was observed on both Girder-1 and Girder-2.

Figure 5-26 shows the temperature measured at the FRP-insulation interface. From the graph, it is observed that the temperature was constant for the first 4 minutes and then sharply increased to 71°C in approximately 13 min and stayed steadily fluctuating between 60°C and 80°C till the fire was extinguished. The sharp rise in temperature was due to the ingress of smoke through the cracks observed on the surface of the insulation. Inspection of the concrete underneath the fireproofing around the vicinity of thermocouple-2BI revealed smoke on the concrete surface (Figure 5-27).

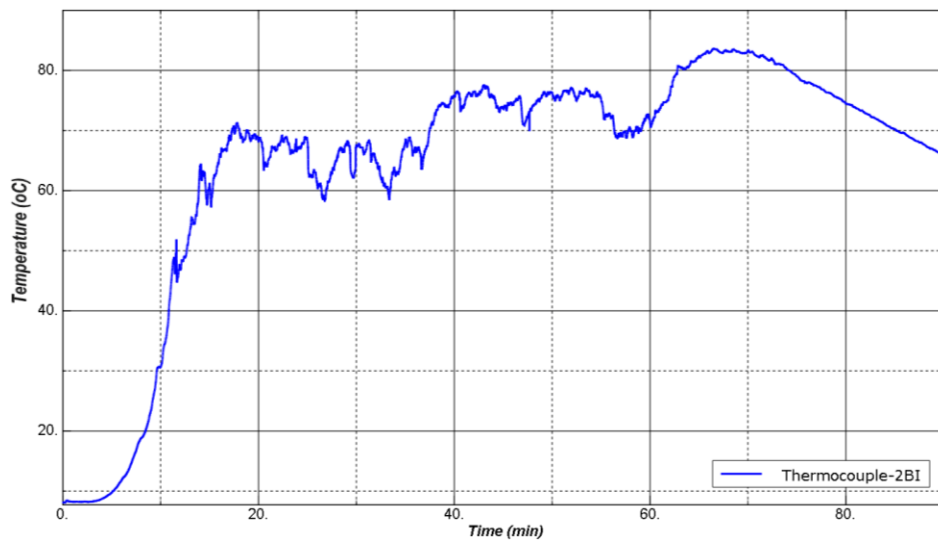


Figure 5-26 Temperature vs time measured at the FRP-fireproofing interface of Girder-2



Smoke on the  
concrete surface

Figure 5-27 Smoke on the concrete underlying the fireproofing

Minor cracks were detected on the surface of the fireproofing before the fire test. These cracks got wider and longer after the fire test (Figure 5-28(a)). This could be due to thermally-induced shrinkage. Cracks were also observed emanating around the perimeter where the insulation terminates. In addition to the thermally induced shrinkage, this could be due to the stress created by the spalling of adjacent concrete.





(a) Cracks on the surface of the insulation



(b) Cracks emanating from termination point of fireproof

Figure 5-28 Cracks on the fireproofing material

Despite the cracks, the insulation was successful in lowering the temperature at the FRP-fireproofing interface by a significant amount. As it can be seen from Figure 5-29, the temperature of the fire was as high as 1131°C and the maximum temperature at the FRP-insulation interface was 83°C. This is a reduction of 1048°C. No spalling or separation of fireproofing from the surface of the FRP or the concrete was observed.

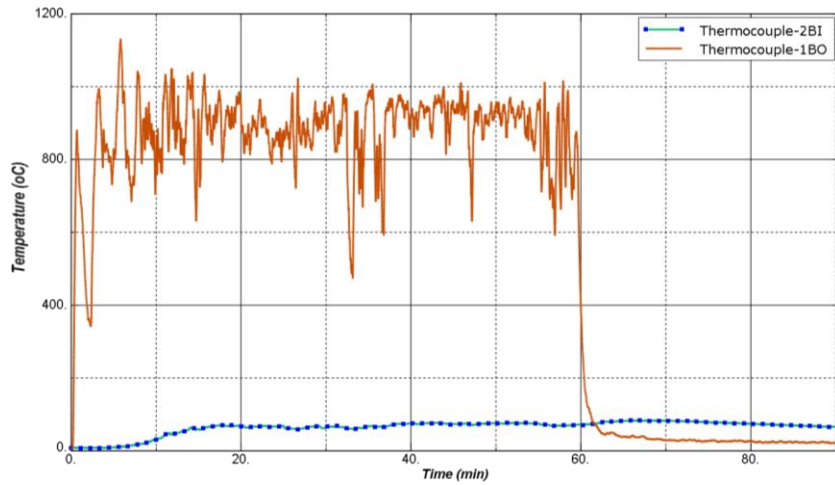


Figure 5-29 Fire temperature vs. temperature at the FRP/fireproofing interface for Girder-2

Figure 5-30 shows the temperature as a function of time at the FRP-concrete interface of Girder-2. As it can be observed from the graph, the insulation was successful in keeping the temperature at the FRP-concrete interface below the glass transition temperature,  $T_g$ . After the fire test had been completed, inspection of the FRP-concrete bond was also conducted by removing the insulation at various locations. It was found out that the bond between the FRP and the concrete remained intact.

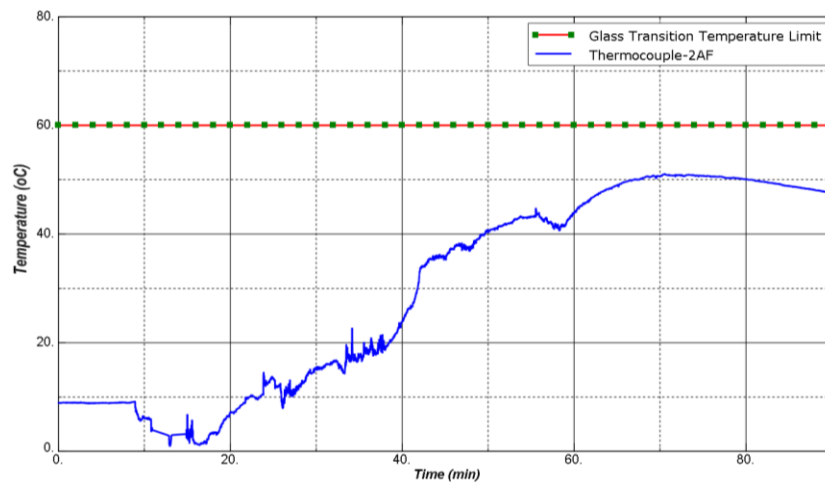


Figure 5-30 Temperature as a function of time at FRP-concrete interface for Girder-2

The fireproofing not only protected the FRP but it also insulated the prestressing strands and the concrete. Figure 5-31 shows the temperature vs. time measurements at three different locations of the prestressing strands of Girder-2. The maximum temperature measured was 48°C. Prestressing strand are known to retain 100 % of their strength up to a temperature of 100°C (Eurocode-2, 2004).

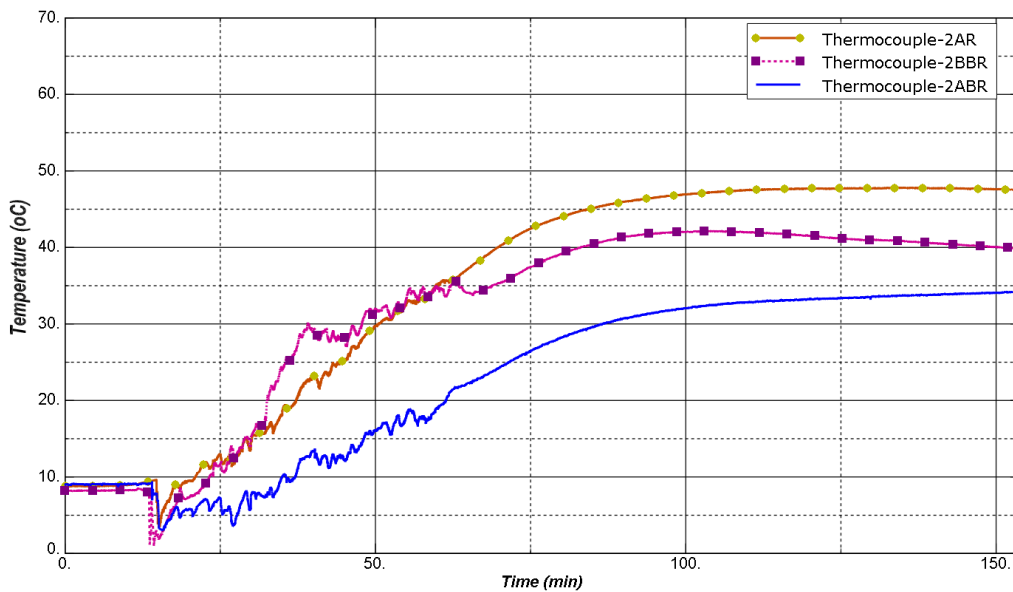


Figure 5-31 Measured strand temperature for Girder-2

Figure 5-32 compare the temperature measured by thermocouple-1BBR and thermocouple-2BBR. These thermocouples were installed at the mid-span of Girder-1 and Girder-2, respectively. The maximum temperature measured by thermocouple-1BBR and thermocouple-2BBR was 473°C and 48°C respectively. The lower temperature in the latter was due to the presence of the fireproofing. The fireproofing played an important role in lowering the temperature and protecting the concrete covering the prestressing strand from spalling. Outside the

area where there was no fireproofing, six prestressing strands were exposed as shown Figure 5-33.

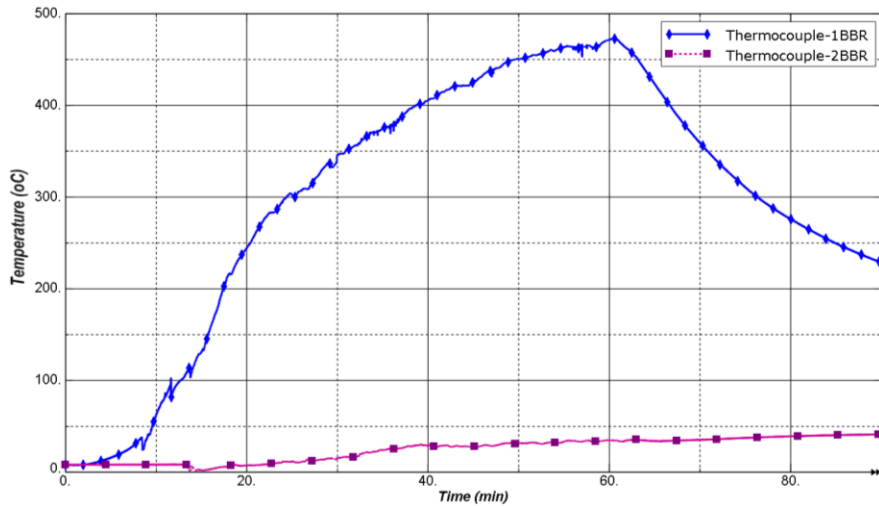


Figure 5-32 Measured temperature by Thermocouple-1BBR versus Thermocouple-2BBR



Figure 5-33 Exposed strands on Girder-2

Figure 5-34 show the temperature measured as a function of time by thermocouple-2AM and thermocouple-2BM inside the web of Girder-1. The temperature readings from these thermocouples were small as well due to the insulating effect of the fireproofing. Even though it is at a slow rate, their temperature reading kept on increasing after the fire was extinguished.

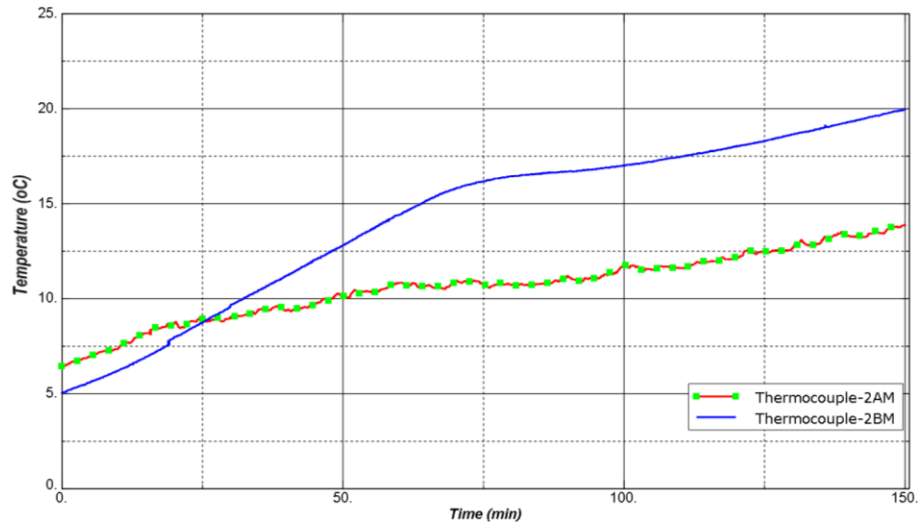


Figure 5-34 Temperature vs. time reading of thermocouple-2AM and thermocouple-2BM

Figure 5-35 shows the progression of the fire across the cross section of the girder at its mid-span. Like Girder-1, It is observed from the figure that the measured temperature in concrete decrease with increasing depth from the bottom of the surface.

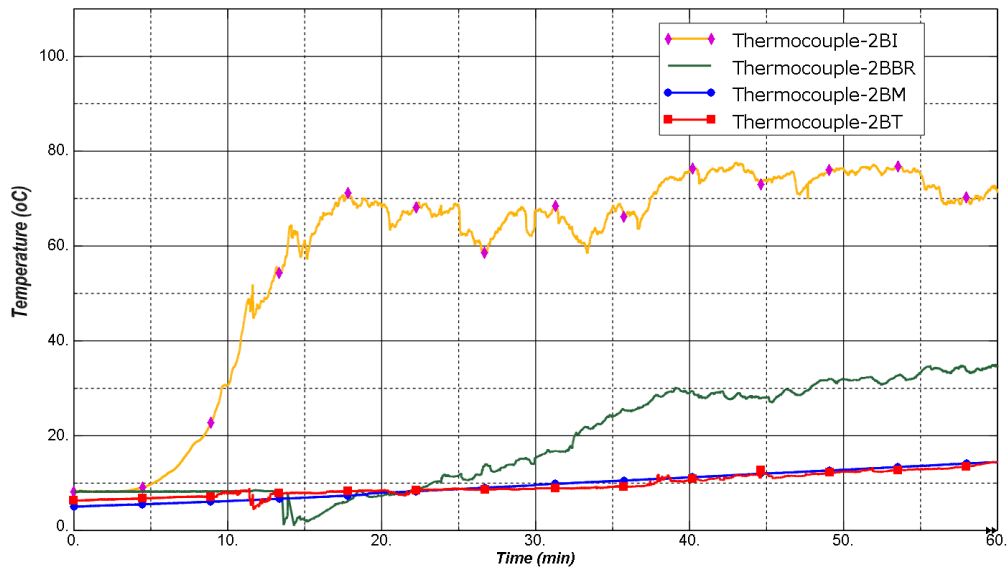


Figure 5-35 Mid-span temperature vs time reading of Girder-2 at different depth

The insulation covered approximately 42% of the fire-exposed surface of Girder-2. As a result, majority of the concrete exposed to the severe fire was protected from spalling. Areas which were not protected with the fire proofing exhibited a moderate level of spalling as shown in Figure 5-36.



Figure 5-36 Spalling of concrete on Girder-2.

#### 5.3.1.3 Girder-3

The thermocouple installed on the exterior surface of Girder-3 failed to give a good reading. However, the data from the other thermocouples and the results of the visual inspections and the surface hardness values revealed that the intensity of the fire on Girder-3 was minimal compared to Girder-1 and Girder-2. It was also witnessed during the fire test; the fire was concentrated on Girder-1 and Girder-2 for most of the duration of the test.

Figure 5-37 show temperature as a function of time for the prestressing strands. The maximum measured temperature was 40°C. Prestressing Strand retains 100 % of their strength at a temperature of this magnitude.

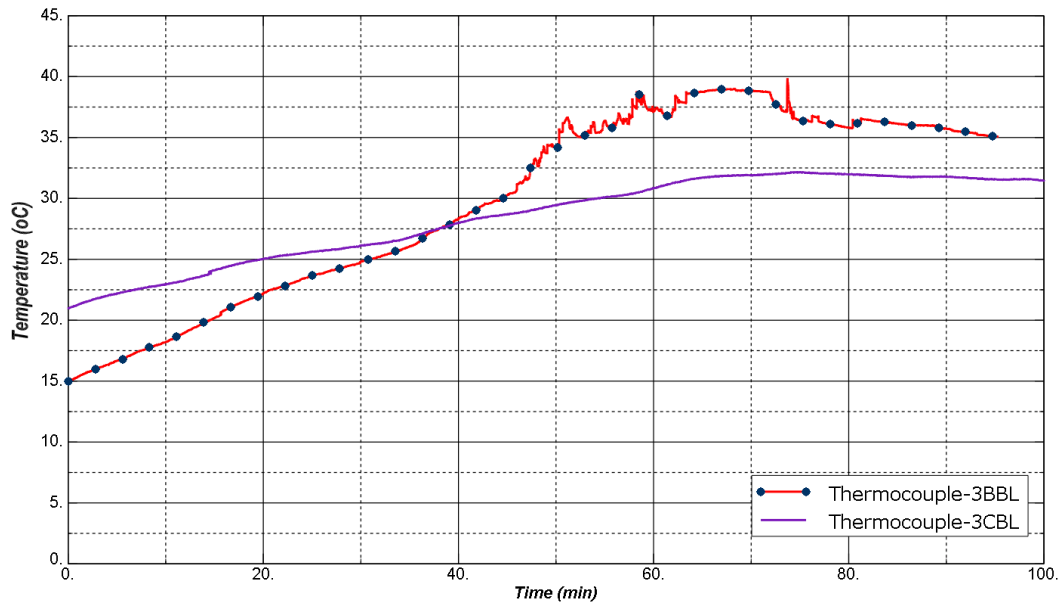


Figure 5-37 Measured strand temperature for Girder-3

Inspection of the girder after the fire test showed that three top reinforcements lost their concrete cover as shown in Figure 5-38. Two of them were exposed for 2.74 m (9ft.) and the third one for approximately 0.914 m (3 ft.). A 7.01 m (23 ft.) long full-depth longitudinal crack was also observed on the bottom flange. The crack could be caused by thermal gradient on this section of the girder. Minimal spalling of concrete was observed on the north elevation and no spalling on the south elevation. Other than these, all the prestressing strands and reinforcements were still under the concrete.

However, the next day after the fire test, it was found out that the strand along the longitudinal crack was broken (Figure 5-39(b)). Big chunks of concrete were observed hanging on the broken strand and laying on the fuel pan (Figure 5-39(a)). The breaking of the prestressing strand could be due to the weight of the concrete hanging on the strand after cracking.



Figure 5-38 Exposed top reinforcements and strand for Girder-3



(a) Concrete hanging on the broken strand      (b) broken strand

Figure 5-39 Girder-3 broken prestressing strand



Figure 5-40 shows the temperature reading from thermocouple installed in the middle of the web at three-quarter span length from support-1. As it can be seen from the figure, the temperature readings are very low. The low temperature reading inside the girder has the potential to create thermal gradient when the exterior surface is subjected to high temperature intermittently. And the thermal gradient eventually causes cracking.

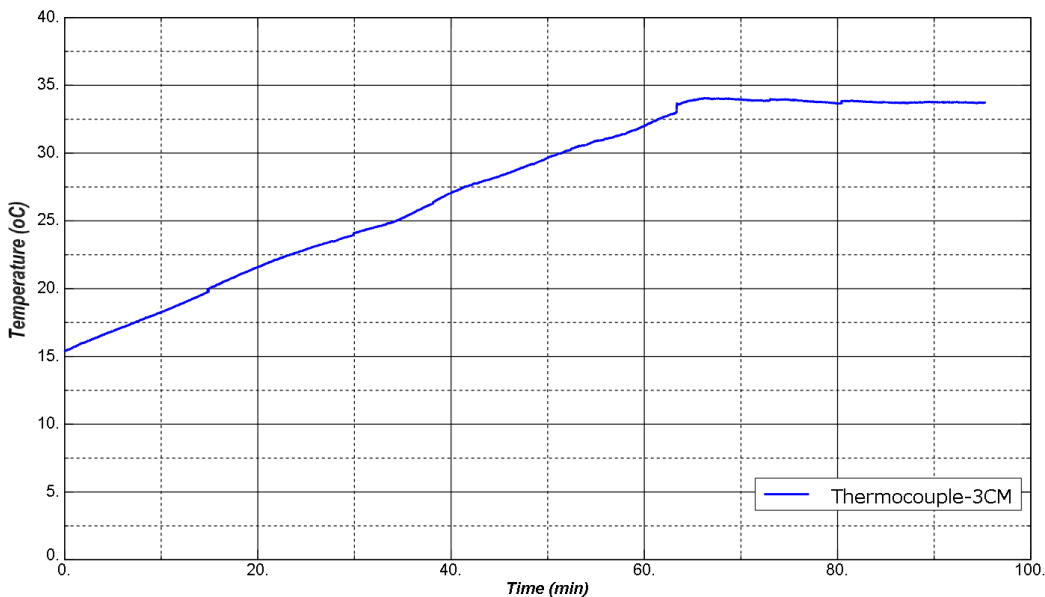


Figure 5-40 Temperature vs. time reading of thermocouple-3CM

#### 5.3.1.4 Deck

Figure 5-41 shows the temperature as a function of time at the deck-girder interface for Girder-1 and Girder-2. The temperature at this interface is a determining factor that could affect the composite action between the two. However, the temperature readings from both thermocouple were minimal, which didn't have the potential to affect the bond between the girder and deck adversely.

This was due to the low thermal conductivity and high thermal capacity of concrete, which played a key role in slowing down the heat penetration to the top of the deck.

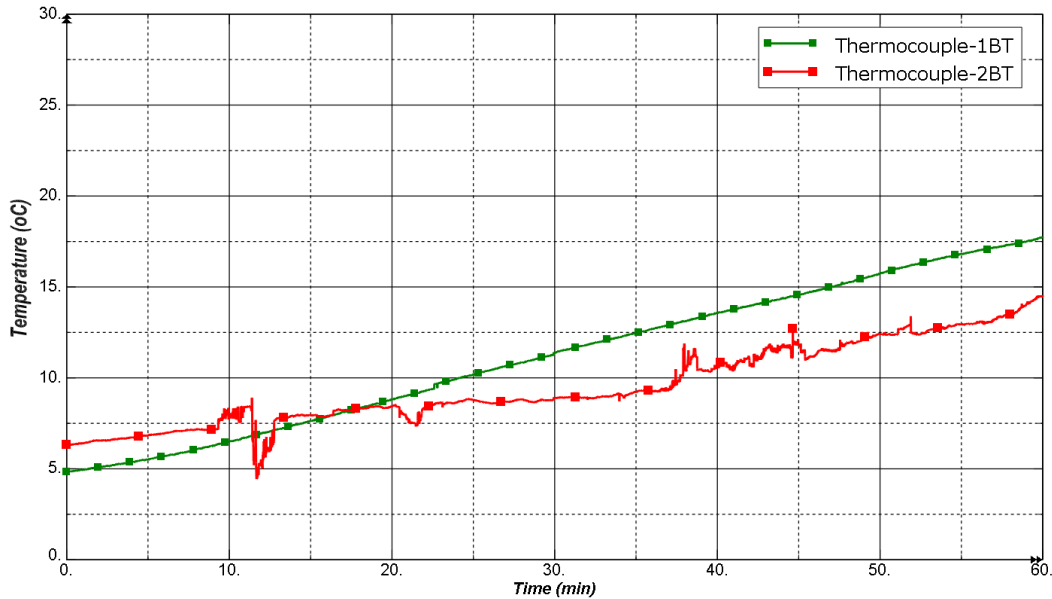


Figure 5-41 Temperature at the interface between deck and the girder

Figure 5-42 (a) and (b) shows the bottom of the deck between Girder-1 and Girder 2 and between Girder-2 and Girder-3 respectively after the fire. It is observed from the figure that majority of the precast deck panels sustained severe spalling of concrete. The spalling ranges from 50.8 mm (2 in.), which is the clear cover for the prestressing strand, to 101.6 mm (4 in.), which is the thickness of the precast deck panels. The degree of spalling was more severe for the deck between Girder-1 and Girder-2 compared to the deck between Girder-2 and Girder-3. This was due to the most intense fire in the former.



(a)

(b)

Figure 5-42 (a) Bottom of the deck between Girder-1 and Girder-2; (b) Bottom of the deck between Girder-2 and Girder-3

The cantilever portion of the deck on Girder-1 side (Figure 5-43) sustained more severe damage compared to the cantilever deck on Gider-3 side (Figure 5-44). The majority of Gider-3 side was covered with soot. Only small portion of it sustained minor spalling. The cantilever deck on Girder-1 side lost an average of 38.1 mm (1.5") deep concrete for approximately 7.93 m (26 ft.) of its span length.

A more severe damage was observed in the precast deck panels compared to the cast in place deck. Since the former was made of high strength concrete (HSC) and the later from normal strength concrete (NSC). Despite the severe spalling on the bottom, the top of the deck showed no sign of crack or distress.

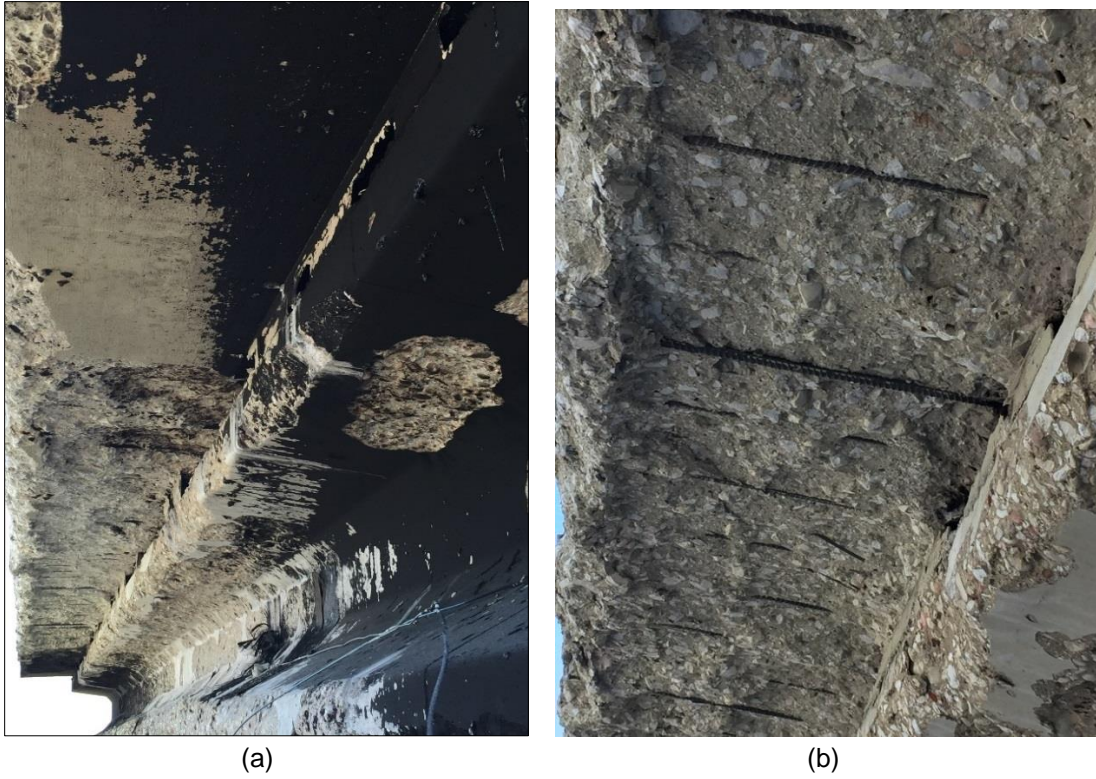


Figure 5-43 (a) Overhang portion of the deck on Girder-1 side after the fire; (b) closer look at of the spalled concrete for the overhang portion of the deck on Girder-1 side



Figure 5-44 Overhang portion of the deck on Girder-3 side after the fire

### 5.3.1.5 Bearing Pads

Out of the six bearing pads, 3 of them located on support-1 were instrumented with thermocouples as shown in Figure 3-12. The readings from these thermocouples are shown in Figure 5-45. Even though they are placed on the surface of the bearing pads, their readings were lower than the reading from the thermocouple installed on the exterior surface of Girder-1. This is due to the shielding effect of support and the girders.

Only bearing pad B-1 showed a visible deformation after the fire test (Figure 5-43). Hardness test, shear modulus test, compression test, adhesion strength test, tensile test, and elongation test were conducted on these bearing pads to study the effect of the fire on their performance. The discussion of these test results and the overall performance of the bearing pads is out of the scope of the current study.

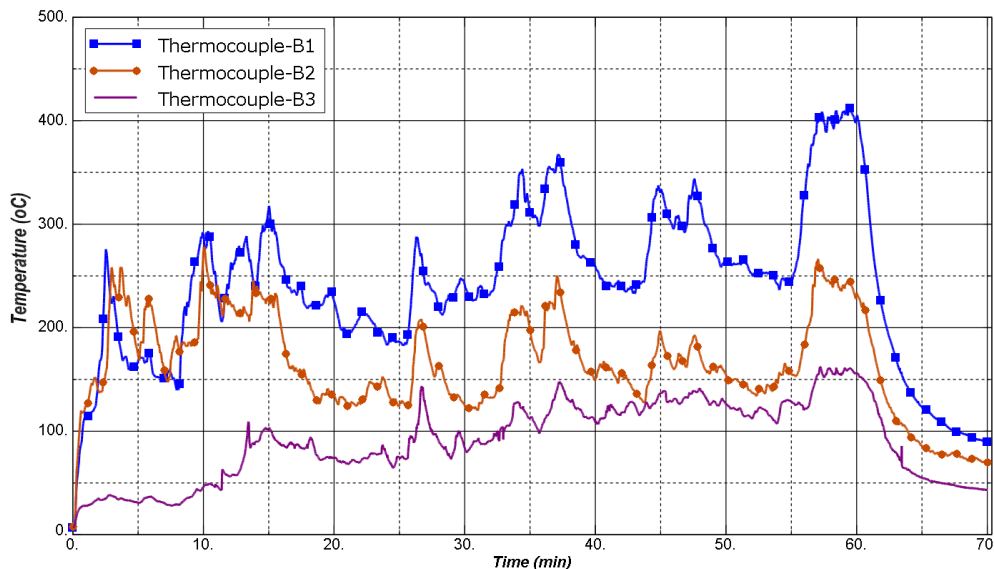


Figure 5-45 Measured bearing pads temperatures



Figure 5-46 Deformation of bearing pad

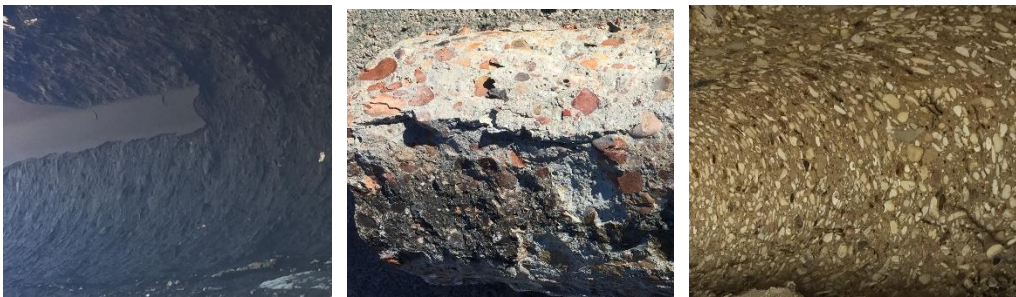
### 5.3.2 Visual Inspection and Hardness Test

It is evident that the prevalent wind during an open pool fire test causes temperature variation. This variation calls installing a large number of thermocouples at different sections of the bridge components. However, the high cost of thermocouples and extension wires made it impractical to install as many thermocouples as needed. To understand the thermal state on locations where there was no thermocouple, visual inspection, and Schmidt hammer hardness testing was employed.

Visual inspection was used to correlated the color of the concrete surface with the maximum temperature it experienced. Table 5-4 shows the probable correlation between fire exposed concrete color and temperature. Figure 5-47 shows how each of these colors was displayed on the concrete surface after the fire test.

Table 5-4 Probable correlation between fire exposed concrete color & temperature (PCI 1989)

<b>Color</b>	<b>Probable maximum temperature (°C)</b>
No discoloration	Less than 316
Pink/Red	316-593
Whitish-grey	Greater than 593
Buff (light tan)	Greater than 927



(a) Soot

(b) Red

(c) Buff (light tan)

Figure 5-47 Colors of concrete at different temperature

The surface hardness of the concrete was determined using Schmidt hammer or rebound hammer test (Figure 5-48). By comparing the values of the surface hardness of the fire tested girders with that of control girder, it is possible to correlate the severity of the fire with the surface hardness at different locations. The higher the hardness, the less severe the fire was at the location under consideration and vice versa. The control girder, which was not subjected to fire, had an average surface hardness of 9000 psi. Readings were taken at 49 different locations on each girder. The results are reported for each girder considering the three different fire exposed sides i.e. elevation view of the north side, elevation view of the south side and bottom flange.



(a) Surface preparation



(b) Taking reading

Figure 5-48 Rebound hammer test

#### 5.3.2.1 Girder-1

Figure 5-49 shows the results of the visual inspections of Girder-1. The majority of the section of the bottom flange and the elevation view on the south side exhibited the tan color which implied an extremely severe fire. These sections were characterized by severe spalling of concrete, exposed strand/reinforcement and broken prestressing stands. The sections around the supports were covered with soot. Majority of the concrete in these areas was sound except some cover delamination.

The rebound hammer test results agree well with the visual observation. The visual inspection revealed that the fire was more severe on the south elevation view of Girder-1 compared to the north elevation. The rebound hammer test result showed the same trend as shown in Figure 5-50. The values of the surface hardness are very small compared to the reading from the control girder (9000psi)



around the areas that showed tan color, whereas, those regions covered with soot resulted in high surface hardness readings as expected. Areas that displayed pink/red aggregate color also displayed a reduced surface hardness value compared to the areas covered with soot. For any section under consideration, it is observed that the value of surface hardness of the web is always more than the reading of the top and bottom flange. This is due to the shadowing effect of the top and bottom flange.

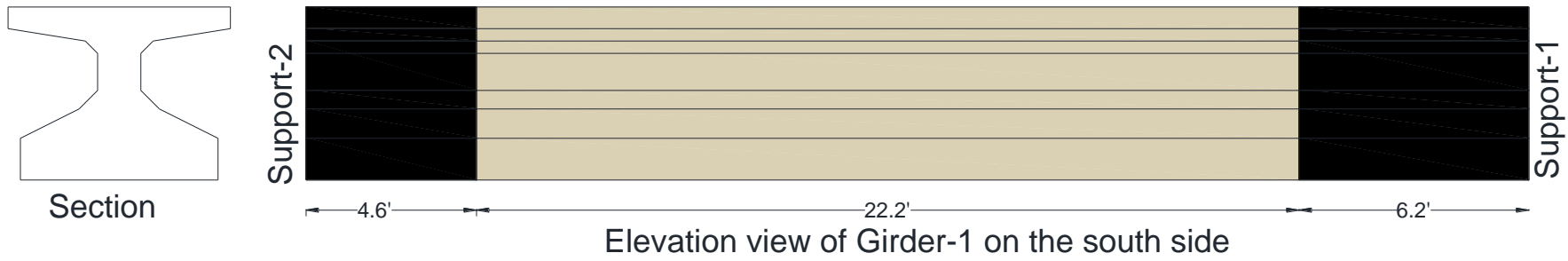
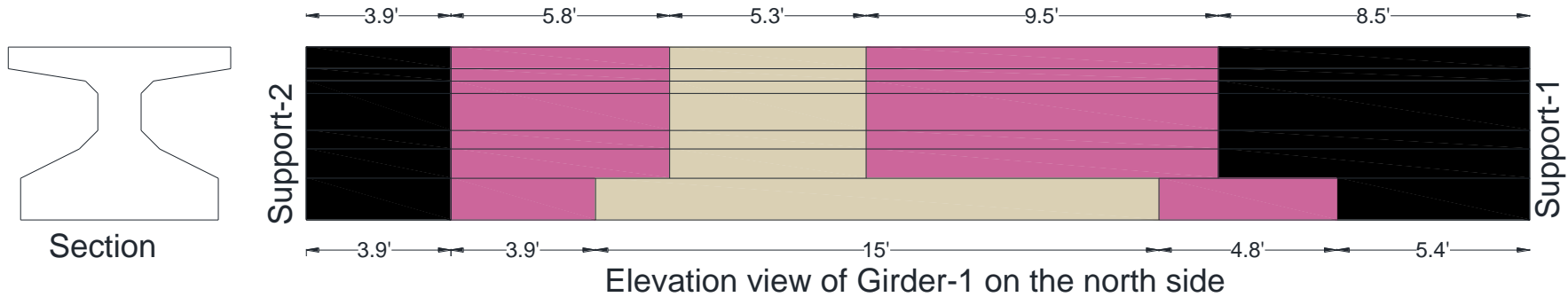
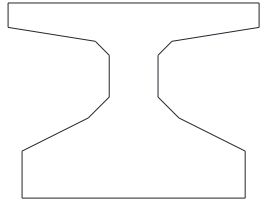
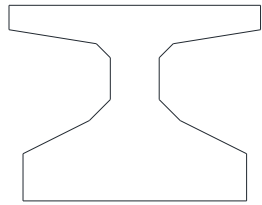
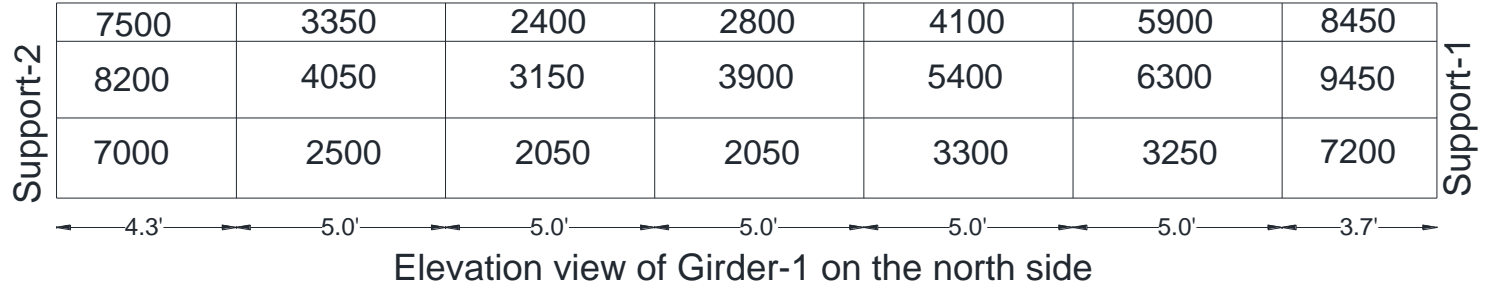


Figure 5-49 Visual inspection of Girder-1



Section



Section

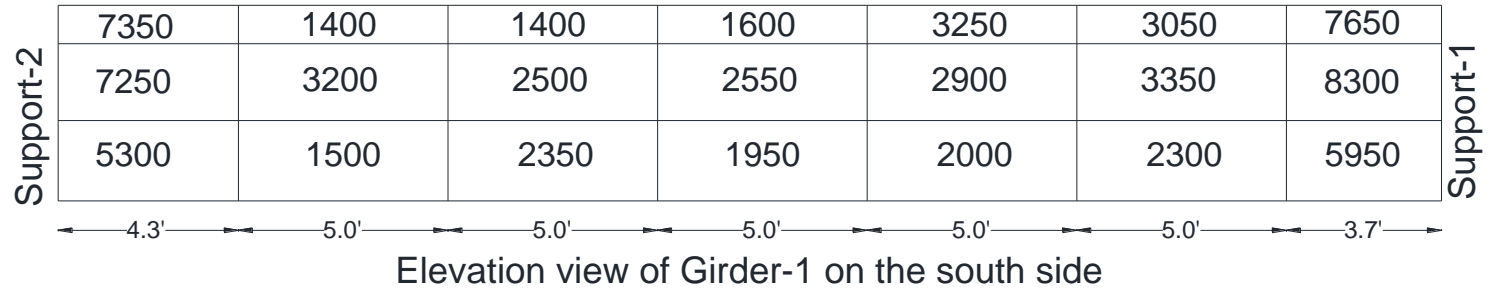


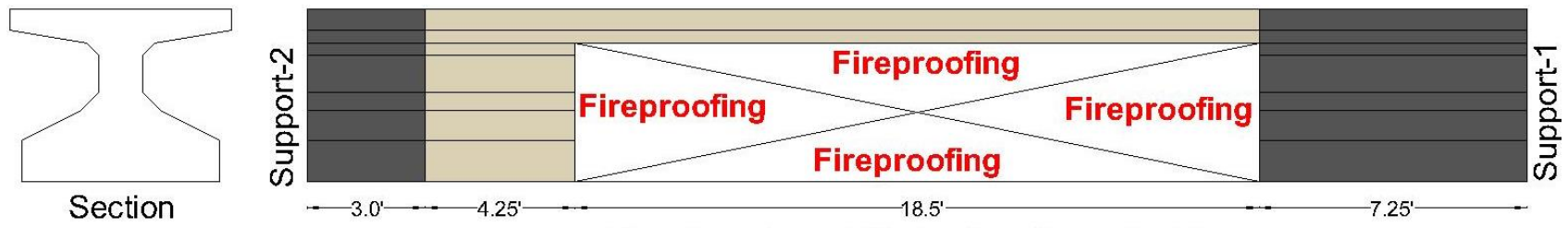
Figure 5-50 Hardness testing values of Girder-1 in psi

### 5.3.2.2 Girder-2

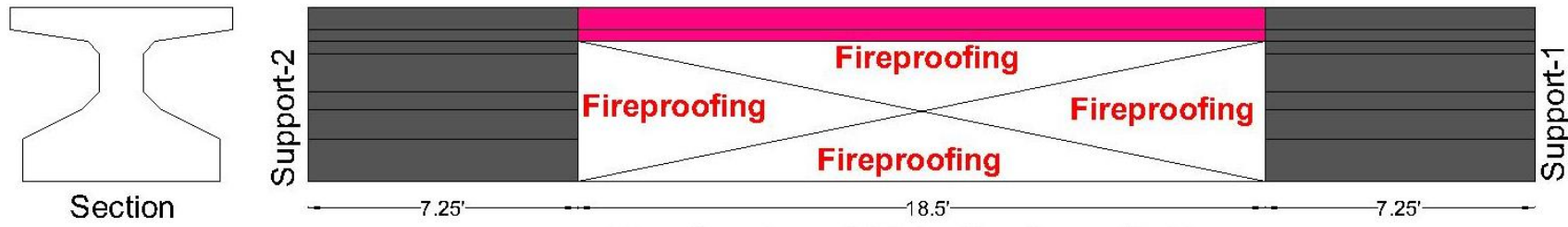
Figure 5-51 display mapping of the visual inspection of Girder-2. The majority of area exposed to the highest intensity of fire was protected by the fireproofing. However, most of the area (not covered with insulation) in the elevation view of the north side displayed the light tan color which implied an extremely severe fire. The top flange on the elevation view on the south side exhibited a mixture of pink/red and whitish-grey color. Part of the area covered with soot sustained a moderate damage; even though the exact color of the concrete was not identified due to the presence of the soot.

The rebound hammer test result agrees well with the visual inspection. The hardness values are very small on the north side elevation due to high temperature. The values are relatively higher on the south side elevation because of the wind. The smaller values are localized on the concrete around the perimeter of the fireproofing material. This suggests that most of the fire was concentrated around the fireproofing.

Comparing the visual inspection mapping and the hardness test result, both Girder-1 and Girder-2 displayed a similar trend. It was also observed during the fire test, most of the fire was concentrated on Girder-1 and Girder-2. Hence, it can be concluded that both girders sustained the same intensity of fire.



Elevation view of Girder-2 on the north side



Elevation view of Girder-2 on the north side

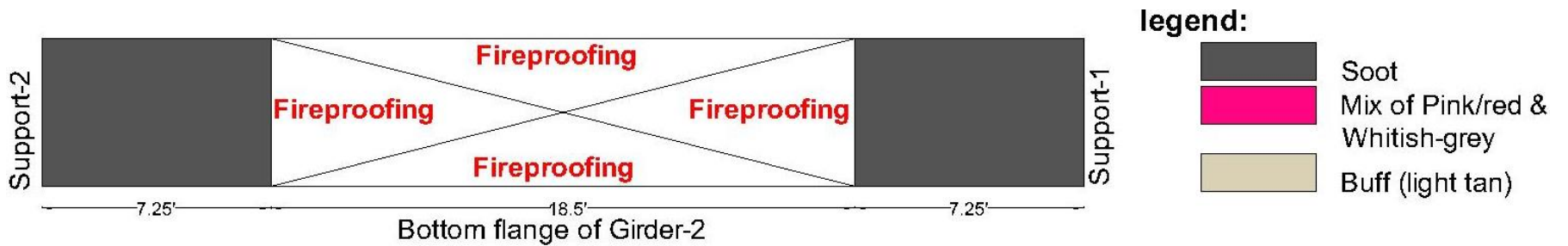


Figure 5-51 Visual inspection of Girder-2

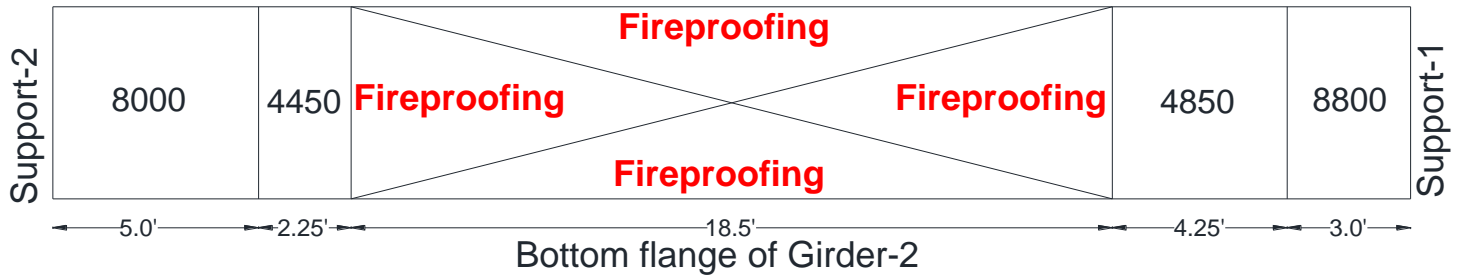
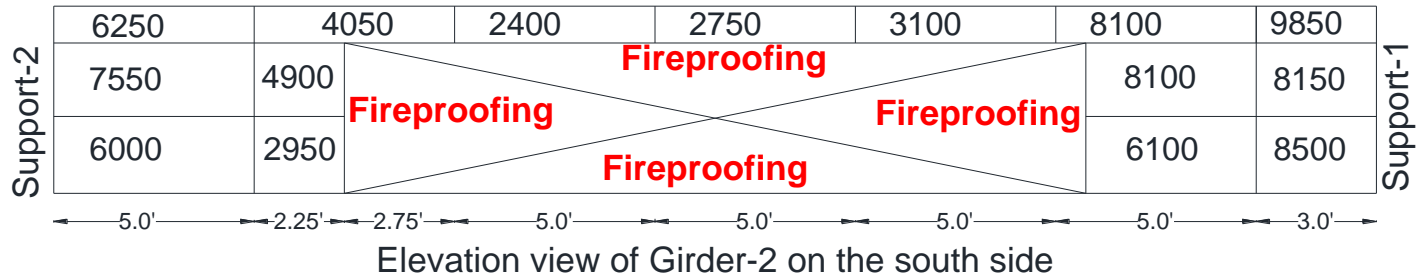
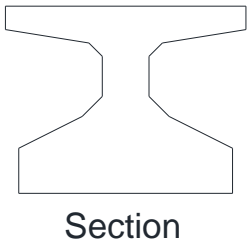
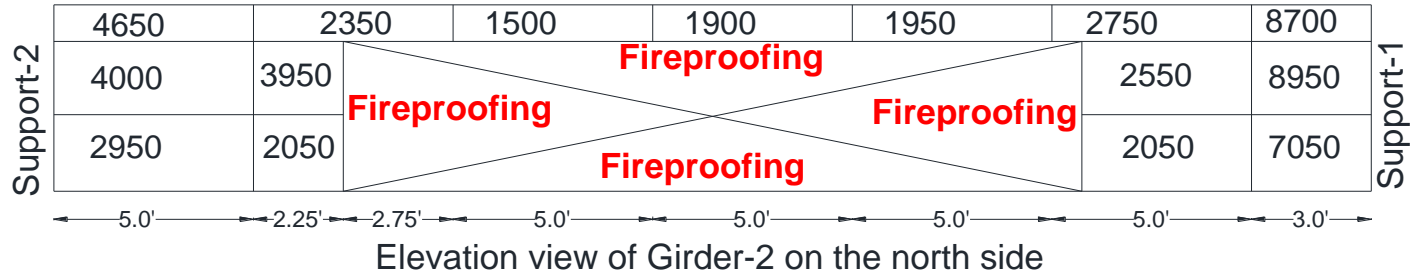
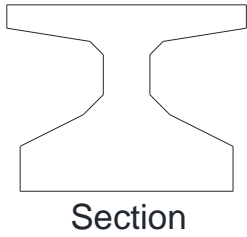


Figure 5-52 Hardness testing values of Girder-2 in psi

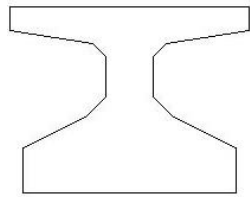
### 5.3.2.3 Girder-3

Figure 5-54 and Figure 5-55 shows the visual inspection and rebound hammer test result respectively for Girder-3. Both results showed that Girder-3 sustained minimal damage compared to Girder-1 and Girder-2 due to uneven distribution of fire from the prevalent wind.

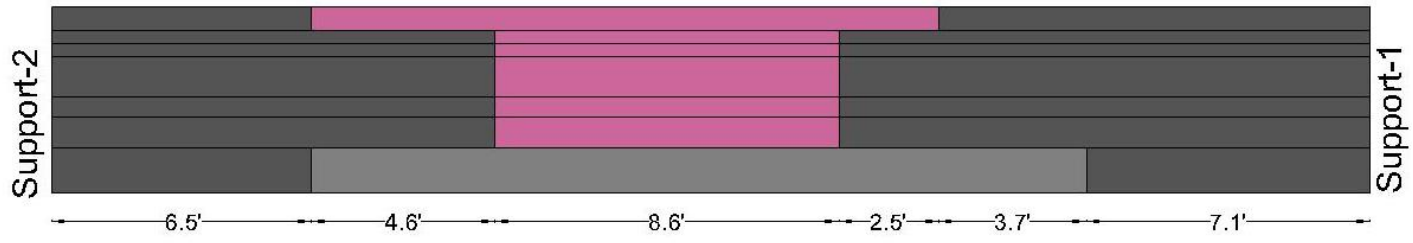
Majority of the girder surface was covered with soot which is an indication less intense fire. The south elevation was entirely covered with soot as shown in Figure 5-53, which agrees well with the high magnitude of surface hardness values. The section which displayed pinkish color and whitish-grey color were the one with lower values of surface hardness values. It was also in these areas where broken strand and exposed reinforcements were observed.



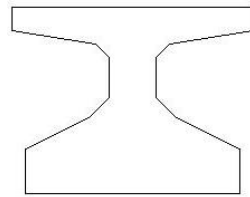
Figure 5-53 Girder-3 covered with soot



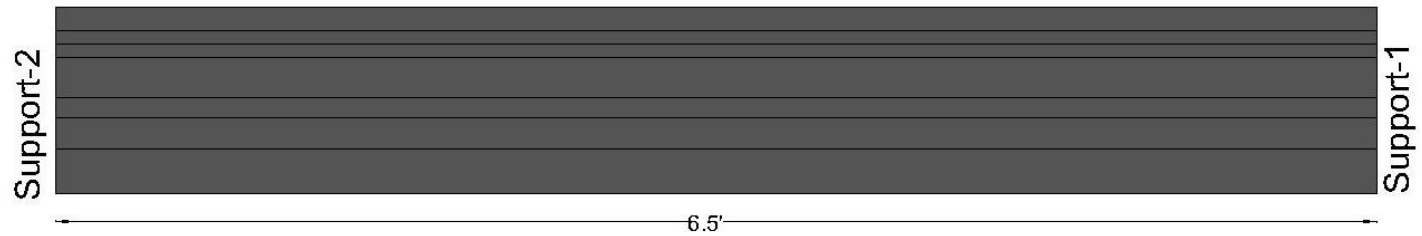
Section



Elevation view of Girder-3 on the north side



Section



Elevation view of Girder-3 on the south side



Bottom flange of Girder-3

**Legend:**




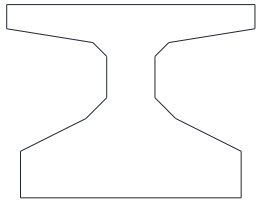
-  Soot
-  Pink/red
-  Whitish-grey

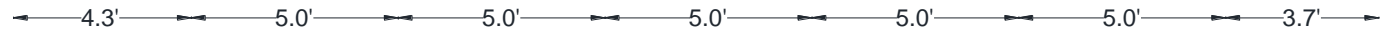
Figure 5-54 Visual inspection of Girder-3



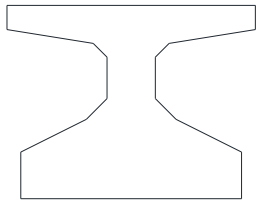


Section

Support-2	6700	5000	4250	5150	5200	6800	9750	Support-1
	6550	5850	4850	4250	5000	7300	8500	
	4150	2950	3650	2600	5000	3150	4900	

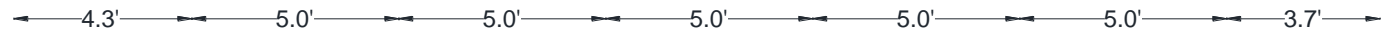


Elevation view of Girder-3 on the north side



Section

Support-2	7900	6300	5550	8600	8350	8250	9350	Support-1
	7600	7500	6250	8650	8750	8650	8850	
	7900	6100	5100	7950	7000	7450	9600	



Elevation view of Girder-3 on the south side

Support-2	6050	1700	2350	3300	5250	5450	9350	Support-1

Bottom flange of Girder-3

Figure 5-55 Hardness testing values of Girder-3 in psi

### 5.3.3 Structural Response

The structural response of the girders can be gauged through their deflection progression with fire exposure time. Unlike other experiments conducted at ambient temperature, the current experiment was performed at a high temperature which made it impossible to find a displacement measuring LVDT. The current study proposed robotic total station and laser scanner to curb this challenge (Figure 5-56).

However, the laser scanner was not successful in reading the coordinates and the elevation of points on the girders due to the obstruction from the smoke. As a result, the displacement as a function of time for each girder was not obtained. Rather the total displacement of each girder was found by taking the difference in elevation of the mid-span before and after the fire.



Figure 5-56 Taking elevation measurement

The reference point on Girder-1, where the mid-span elevation was measured before the fire, was not found after the fire because of the spalled concrete. To get the elevation of the same point after the fire, first, the elevation of the exposed strand at the same location was measured

(Figure 5-57). Adding 63.5 mm (2.5 in.) of concrete cover to this elevation yielded the post-fire elevation of the reference point.

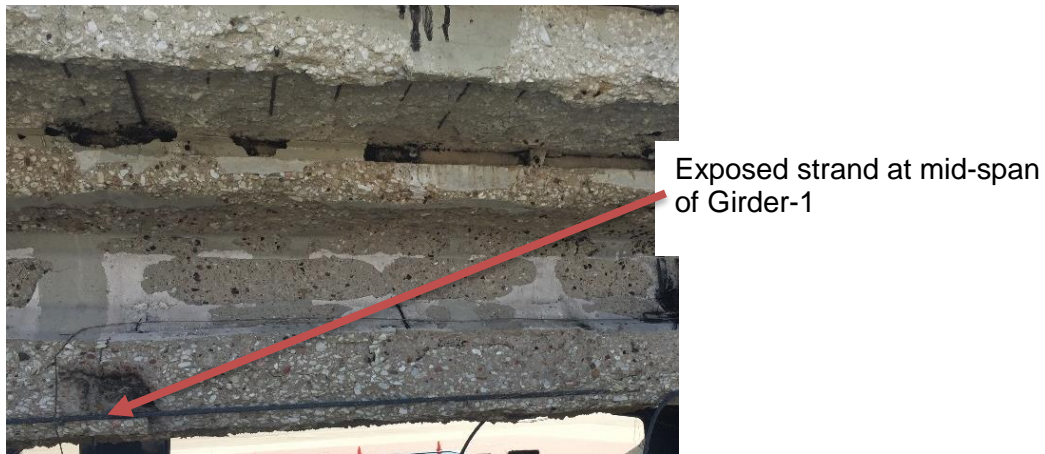


Figure 5-57 reference point used for measuring the elevation of the mid-span of Girder-1 after the fire

No spalling of fireproofing was observed on Girder-2 after the fire test. Hence, the same reference point was used when measuring the before and after the fire elevation (Figure 5-58).

But these measurements didn't take into account the shrinkage of the fireproofing if any.



Figure 5-58 reference point used for measuring the elevation of the mid-span of Girder-2 after the fire

Because of the relatively low intensity of the fire on the bottom of Girder-3, some portion of its concrete surface at the mid-span didn't sustain any form of spalling (Figure 5-59). Hence, the elevation before and after the fire was taken at the same reference point.

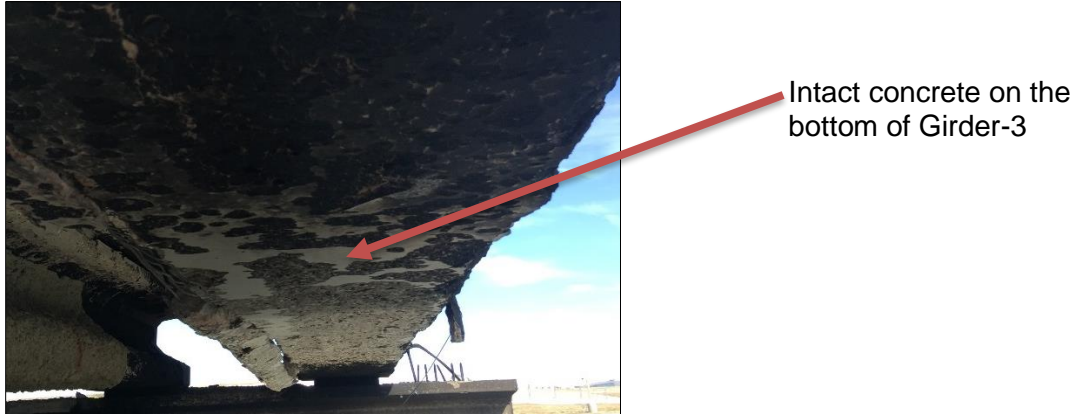


Figure 5-59 reference point used for measuring the elevation of the mid-span of Girder-3 after the fire

Table 5-5 shows the calculated mid-span deflection of each girder by taking the difference between the before and after the fire exposure elevation of the reference points. Out of the three girders, Girder-1 experienced the most severe damage. Its largest mid-span deflection reflects that. Even though Girder-2 was subjected to the same intensity of fire as Girder-1, it experienced less deflection. This is mainly due to the beneficial effect of the insulation material in protecting the FRP from debonding, the concrete from spalling and in slowing down the rise in temperature of prestressing strands. The deflection of Girder-3 is the smallest. Since most of the fire was concentrated on Girder-1 and Girder-2.

Table 5-5 Mid-span deflection of each girder

<b>Girder</b>	<b>Elevation before fire m (ft.)</b>	<b>Elevation after fire m (ft.)</b>	<b>Deflection mm (in.)</b>
Girder-1	173.4760 (569.147)	173.4580 (569.088)	18.00 (0.708)
Girder-2	173.4675 (569.119)	173.4580 (569.088)	9.50 (0.372)
Girder-3	173.4672 (569.118)	173.4614 (569.099)	5.80 (0.228)

## Chapter 6

### DEMOLITION OF TEST BRIDGE AND DETERMINATION OF RESIDUAL STRENGTH

#### 6.1 Demolition of Bridge and Transportation of Specimens to CELAB

After completing the fire test and the post-fire evaluation; the next tasks were to remove the zipper barriers, saw cut the deck and transport the specimens to the CELAB to conduct residual strength tests. The deck was saw cut at the center line between the girders to get a T-beam cross section as shown in Figure 6-1.

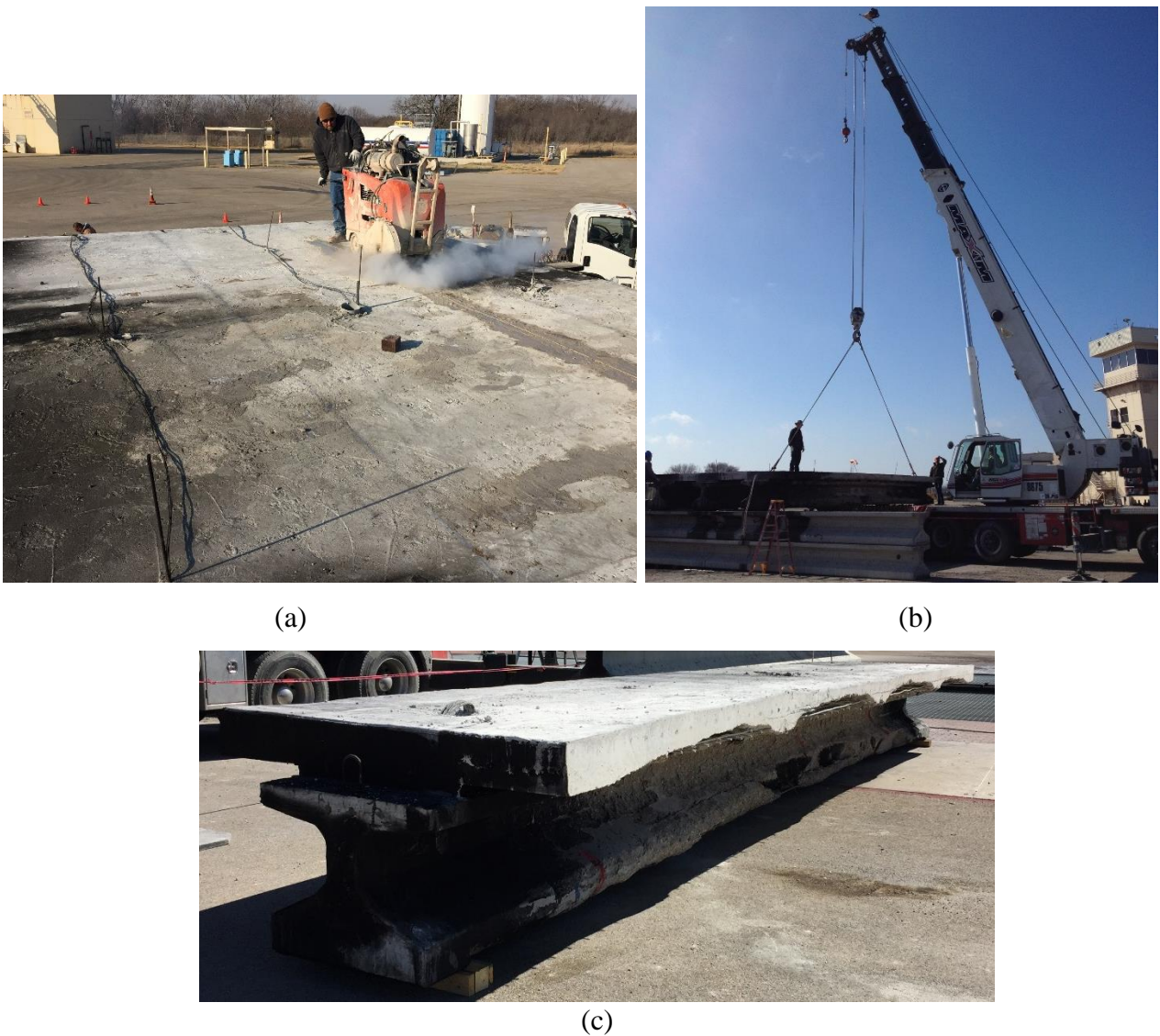


Figure 6-1 (a) saw-cutting of the deck; (b) lifting of the girder; (c) Girder-1 after saw-cutting

However, the weight of the T-beam was more than the lifting capacity of the crane at the CELAB. Thus, the overhanging section of the deck from each girder was sawn cut as shown Figure 6-2(a). The girders were then transported to UTA CELAB (Figure 6-2(b)).



(a)



(b)

Figure 6-2 (a) saw-cutting of the overhanging deck; (b) transportation of the girders to UTA CELAB

## 6.2 Casting of Concrete Topping on the Control Girder

A girder which was not subjected to fire was stored at the CELAB to serve as a control. To make it identical with the fire tested girders, a 254 mm (10 in.) concrete topping was poured on the top of the flange. The control girder was first formed (Figure 6-3(a)), and then reinforcement cage made from #6 rebar at 152.4 mm (6 in.) transversely and #3 rebar at 304.8 mm (12 in.) longitudinally were tied (Figure 6-3(b)). A 254 mm (10 in.) thick concrete was finally poured on the top of the flange to make it identical to fire subjected girders (Figure 6-3(c)). A high early strength concrete (HES), which is the same type of mix used for the test bridge deck, was used.



(a)



(b)



(c)

Figure 6-3 Control girder: (a) formwork; (b) reinforcement cage; (c) after the concrete pour

## 6.3 Residual Strength Test

### 6.3.1 Test Setup

A three-point bending test was performed on each girder to determine their residual strength. The girders were loaded by a hydraulic cylinder mounted on steel frame placed at their mid-span. The load from the hydraulic jack is measured by the load cell and then distributed to the top of the girder by the stacked plates and W12x72 wide flange section. Each girder was supported by a 228.6 mm (9 in.) wide steel plates that rested on a free rod to simulate a roller support at one end and restrained rod to simulate a hinged support on the other end. Each rod was supported by concrete blocks measuring 914.4 mm (3 ft.) in length, 609.6 mm (2 ft.) in width and 609.6 mm (2 ft.) in height. Figure 6-4 and Figure 6-5 show the schematic and the actual test setup respectively of the experiment.

The displacement of the girders during the experiment was monitored by LVDT placed at the support, quarter span, mid-span and three-quarter span. One LVDT was placed at each location except the mid-span where two LVDTs were used.

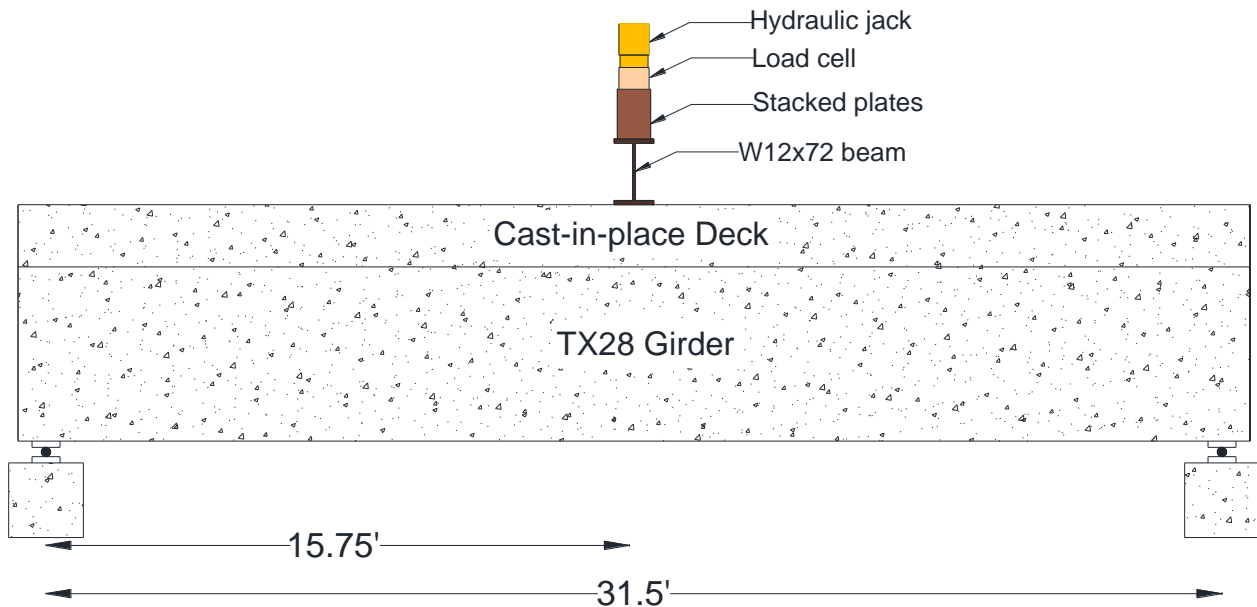


Figure 6-4 Schematic view of the test setup



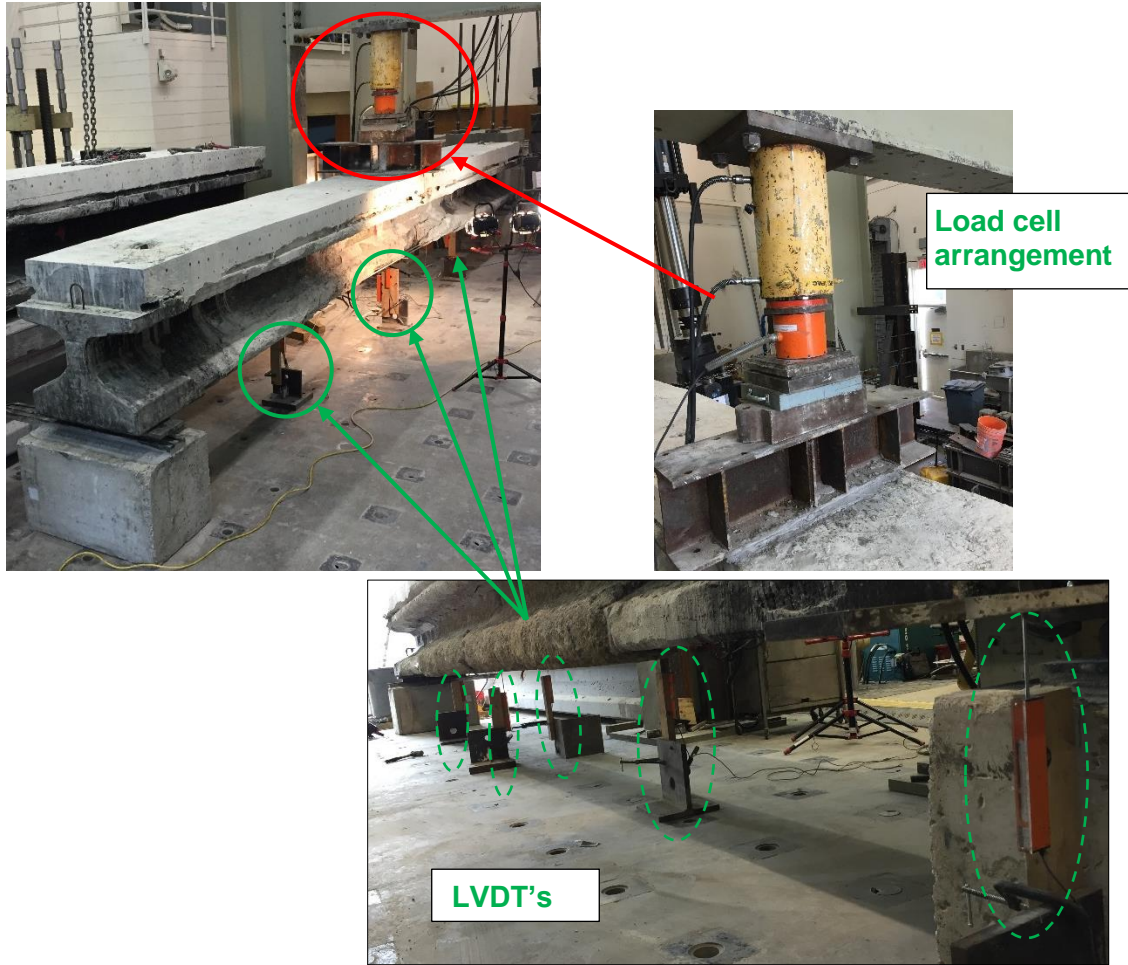


Figure 6-5 Girder test setup

The strain in the concrete, FRP, and exposed prestressing strands were measured using PL-60-11, UFL-5-11 and YHFLA-2 strain gauges, respectively. All of the strain gauges have 120  $\Omega$  electrical resistance.

### 6.3.1.1 Girder-1 strain gauge layout

No strain gauge was installed on the bottom flange of Girder-1 since most of the concrete was spalled off. The only strain gauges on the concrete surface were G1-1, G1-2 and G1-3 which were installed on the top of the deck, top flange of the girder and on the middle of the web of the girder. Out of the ten strands which survived the fire, six of them lost their concrete cover. Thus, they were instrumented with strain gauges. Figure 6-6 and Figure 6-7 shows the strain gauge layout and the installed strain gauges on Girder-1, respectively.

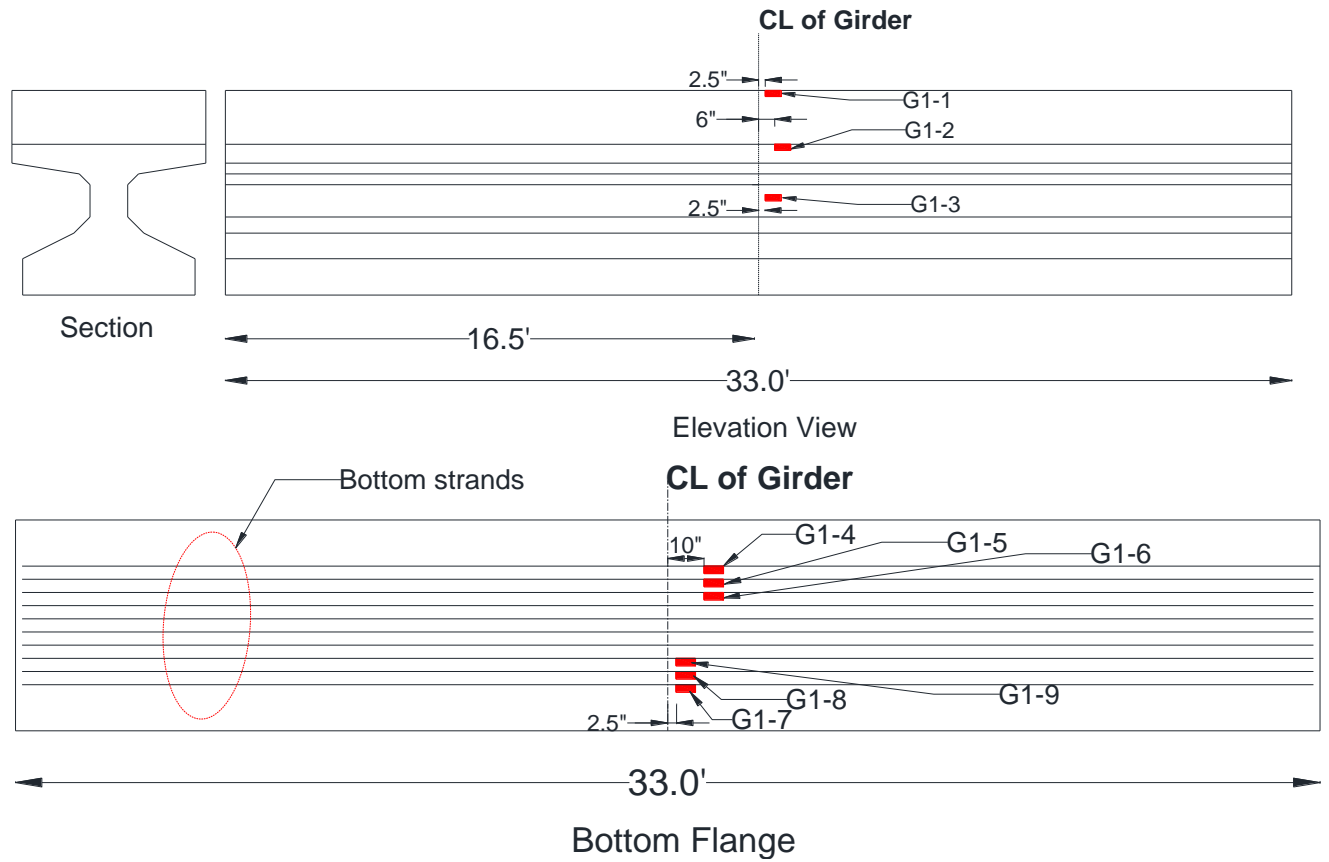


Figure 6-6 Girder-1 strain gauge layout

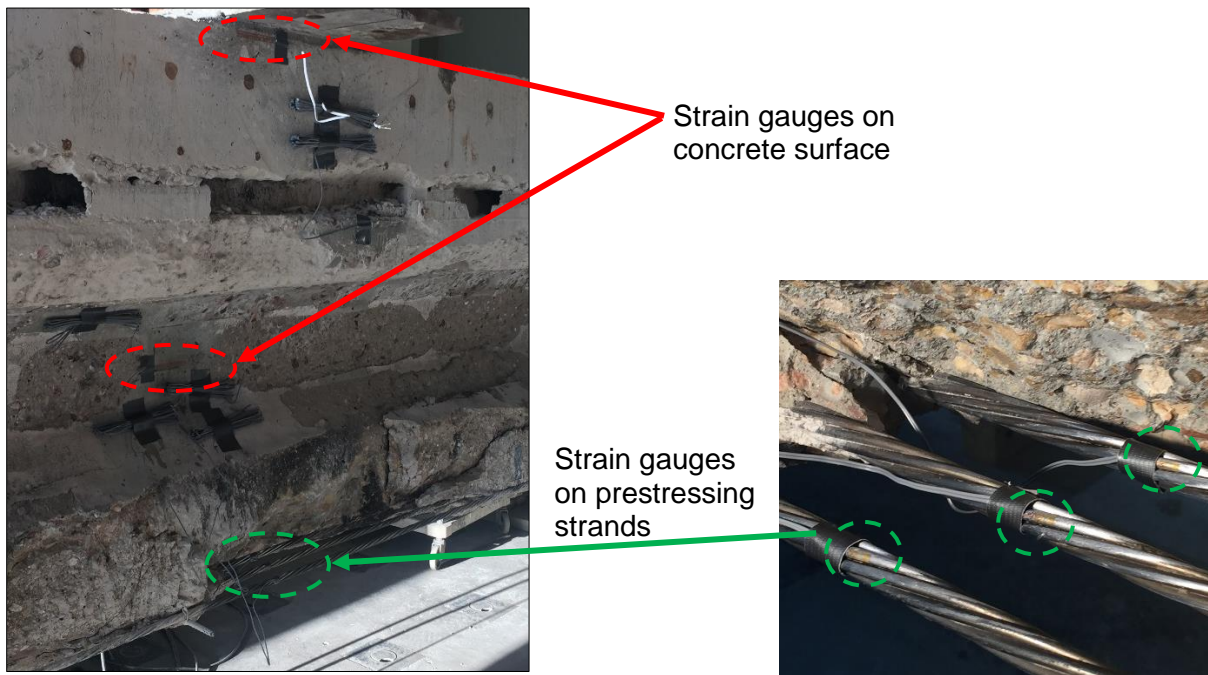


Figure 6-7 Installed strain gauges on Girder-1

### 6.3.1.2 Girder-2 strain gauge layout

A total of 23 strain gauges were installed at different locations on the concrete surface, exposed strands, longitudinal FRP and transverse FRP (U-wraps) as shown in Figure 6-8 and Figure 6-9. Table 6-1 shows the list of strain gauges, categorizing them based on the surface they were installed. The strain gauges on the concrete, longitudinal FRP and prestressing strands were oriented in the longitudinal direction. Whereas, those on the U-wraps were oriented in transverse direction.

Table 6-1 List of strain gauges for Girder-2

Surface	Names of strain gauges
Concrete	G2-7, G2-8, G2-9, G2-10, G2-12, G2-15, G2-18, G2-20, G2-23, G2-25
Longitudinal FRP	G2-11, G2-14, G2-17, G2-19, G2-22
Transverse FRP	G2-13, G2-16, G2-21, G2-24
Prestressing strands	G2-26, G2-27, G2-28, G2-29

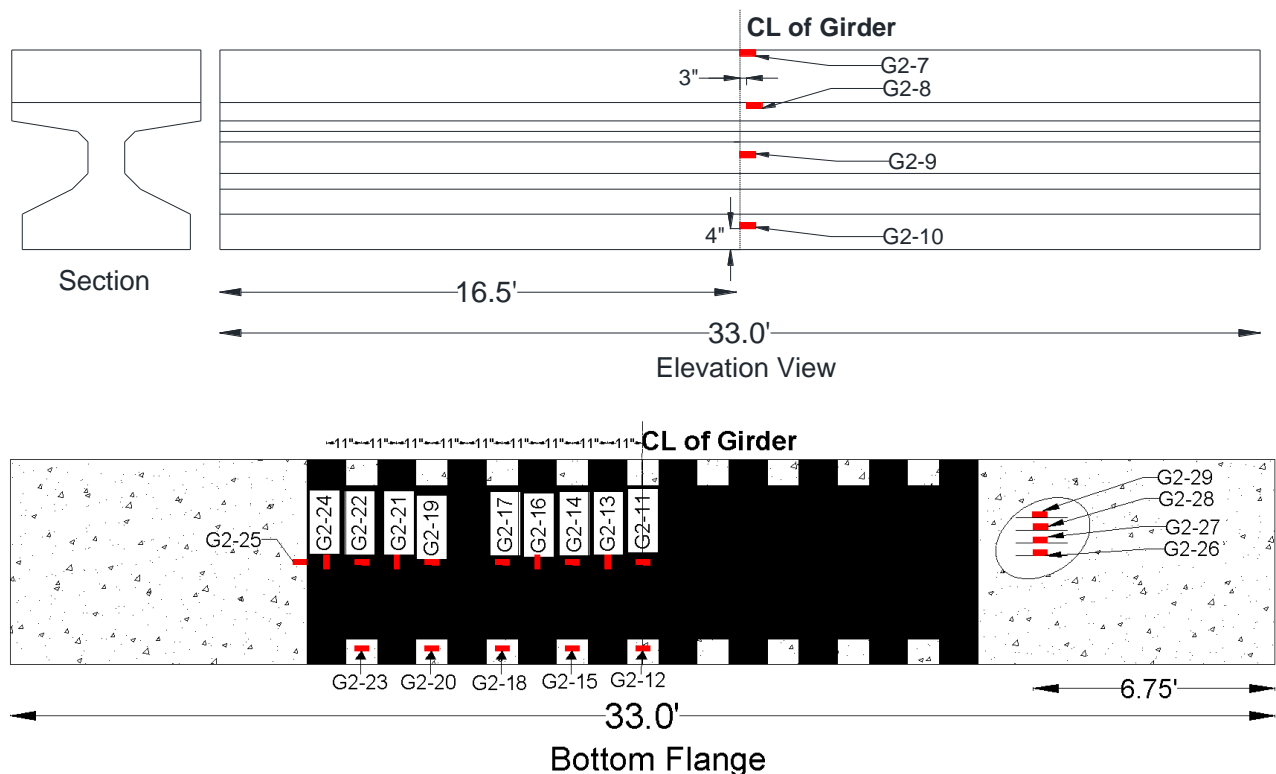


Figure 6-8 Girder-2 strain gauge layout



(a) (b) (c)

Figure 6-9 Strain gauges on (a) FRP; (b) prestressing strand; (c) concrete

### 6.3.1.3 Girder-3 strain gauge layout

The bottom flange of Girder-3 had sustained minor spalling. To install the strain gauges, first the loose concrete was chipped off with the hammer (Figure 6-11 (a)) and then leveled with a grinder to remove any surface irregularities. The evenness of the surface was checked using a spirit level (Figure 6-11 (b)). An epoxy was then applied to the surface to patch any hairline crack. After allowing the epoxy to dry, the surface was rubbed using a fine grit sandpaper (Figure 6-11 (c)). The surface was finally cleaned with acetone before installing the strain gauge (Figure 6-11 (d)). Figure 6-10 shows the strain gauge layout for Girder-3.

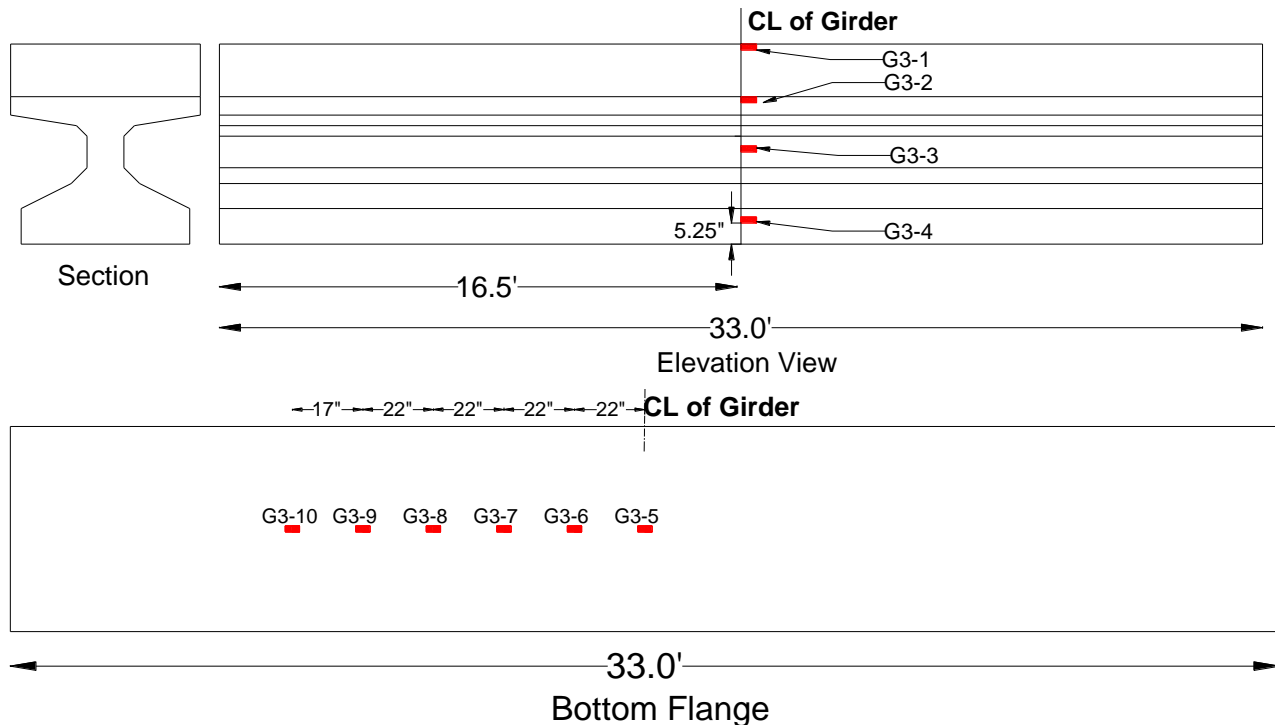


Figure 6-10 Girder-3 strain gauge layout

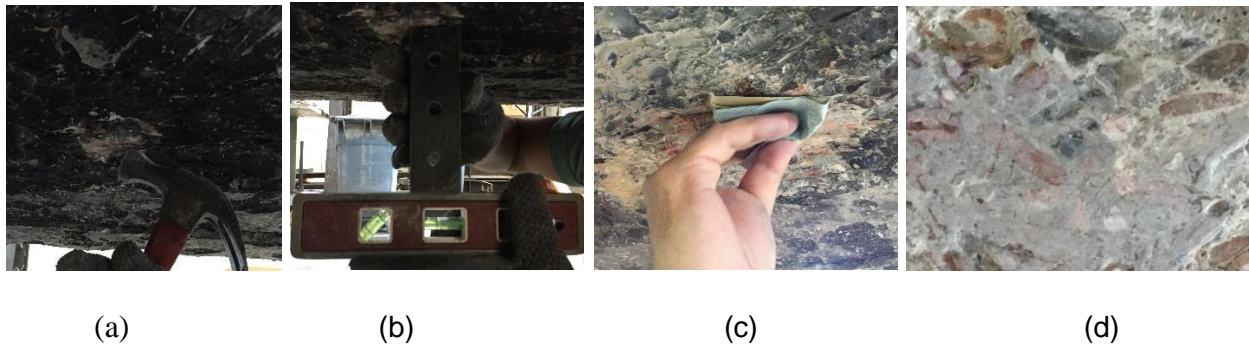


Figure 6-11 Surface preparation before installing strain gauges on spalled concrete

### 6.3.1.4 Control Girder Strain Gauge Layout

Figure 6-12 shows the strain gauge layout for the control girder.

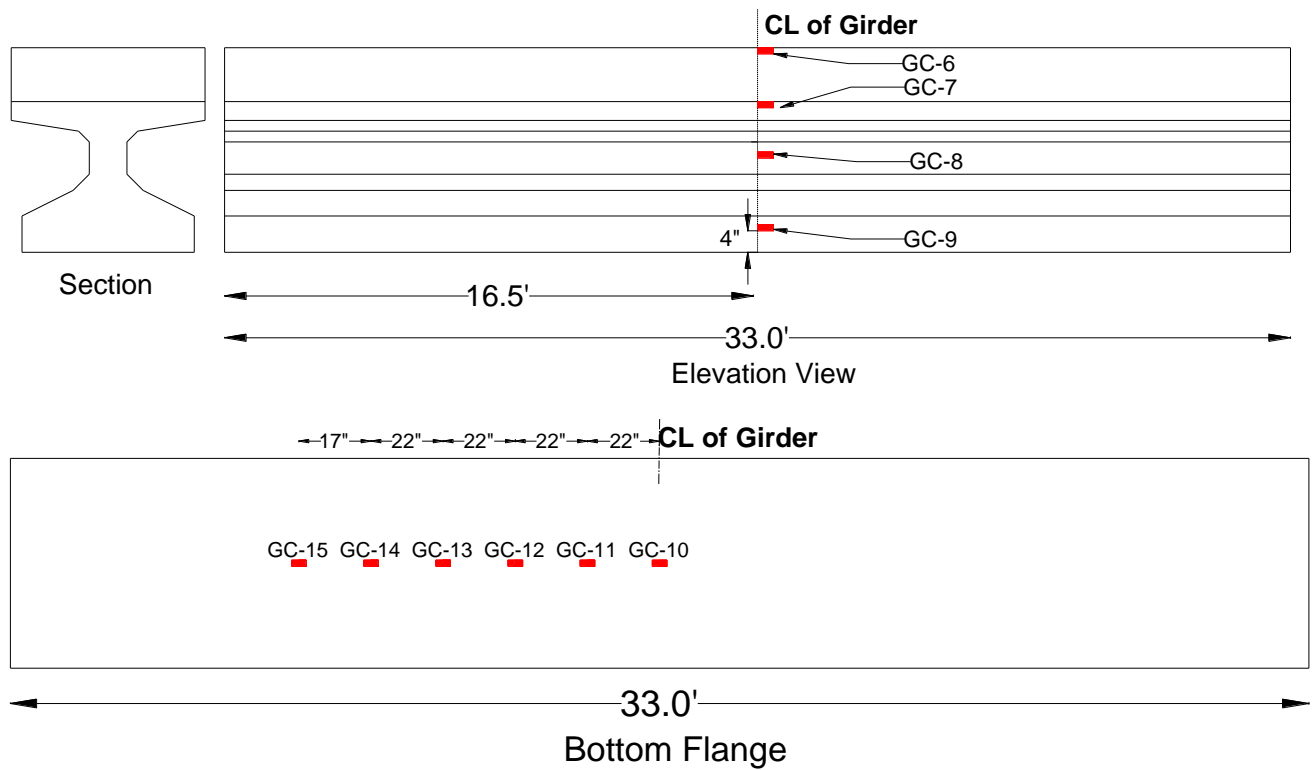


Figure 6-12 Control girder strain gauge layout

### 6.3.2 Compressive Strength of Concrete

Table 2-1 shows the compressive strength of concrete used for casting the deck, girders and the topping of the control girder. The topping of the control girder was poured 38 days after the deck. Thus, it had a lower compressive strength compared to the concrete used for the deck at the time the residual strength test was performed. Both were not poured simultaneously due to a tight project completion schedule that required completing the fire test in a short period.

Table 6-2 Compressive strength of concrete at the time of residual strength test

<b>Component</b>	<b>Compressive strength MPa (psi)</b>
Deck	46.16 MPa (6695 psi)
Control girder topping	27.89 MPa (4030 psi)
Girders	78.45 MPa (11378 psi)

### 6.3.3 Results and Discussions

The following sections discuss the results of the residual strength test.

#### 6.3.3.1 Girder-1

Figure 6-13 shows the applied load versus midspan deflection of Girder-1. It is observed from the figure that the curve behaves in a linear elastic manner up to a load of 135 kN (30 kips). However, the first visible crack was observed late on the test at a load of 333.62 kN (75 kips), since most of the concrete on the bottom flange was spalled off. It then exhibited a decrease in flexural stiffness. The curve showed large drops in the applied load twice before failure. This was due to the breaking of prestressing strands. The girder failed at a load of 399.10 kN (89.70 kips) when the mid-span deflection was 66.04 mm (2.6 inches). This corresponds to an applied moment of 957.96 kN-m (706.55 kip-ft). The calculated nominal flexural capacity of fire unaffected girder according to ACI440 (2008) is 2412.7 kN-m (1779.5 kip-ft). The fire caused the girder to lose 60.3 % of its flexural strength. Figure 6-14 shows the deflected shape profile of the girder at a different

range of loads. Since the applied load was symmetrical, the deflected shape exhibited symmetry at quarter and three-quarter span length.

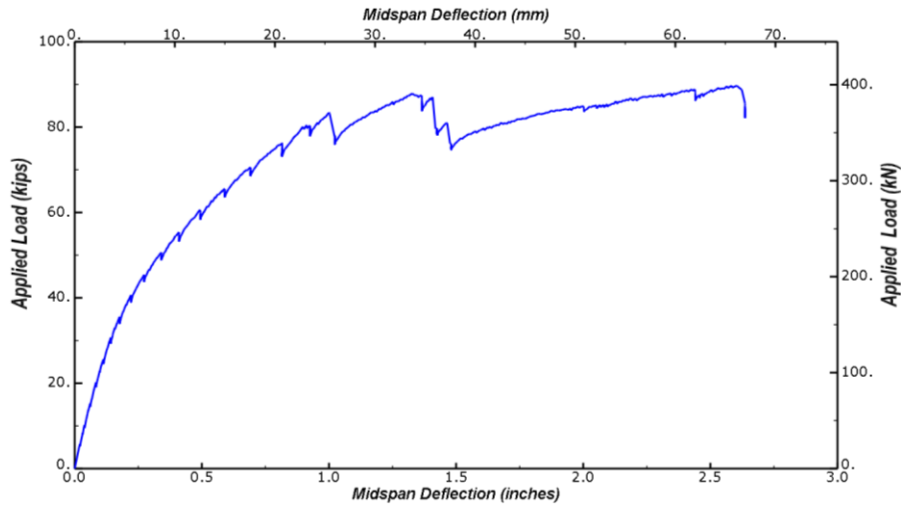


Figure 6-13 Applied load vs mid-span deflection of Girder-1

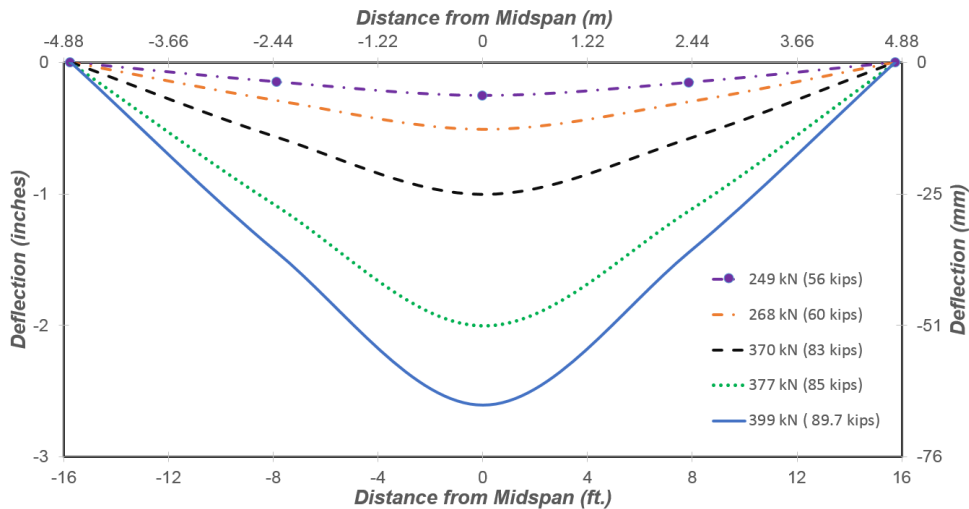


Figure 6-14 Displacement profile of Girder-1 at different load levels

Figure 6-16 shows the strain measured in each of the instrumented strands as a function of the applied load. Out of the ten prestressing strands that survived the fire, 3 of them were broken during the residual strength test (Figure 6-15). Table 6-3 shows the strain and the corresponding applied load at failure for each of the strand. As it can be observed from the table, they were broken at different strain and applied load level. This was due to the difference in temperature experienced by each strand. G1-7 exhibited the lowest failure load and the highest

strain. From this it can be deduced that out of the six instrumented strand, G1-7 was subjected to the highest temperature. It is also observed from the figure that the strain profile follows a similar pattern like the applied load versus the mid-span deflection curve.



Figure 6-15 Broken prestressing strand

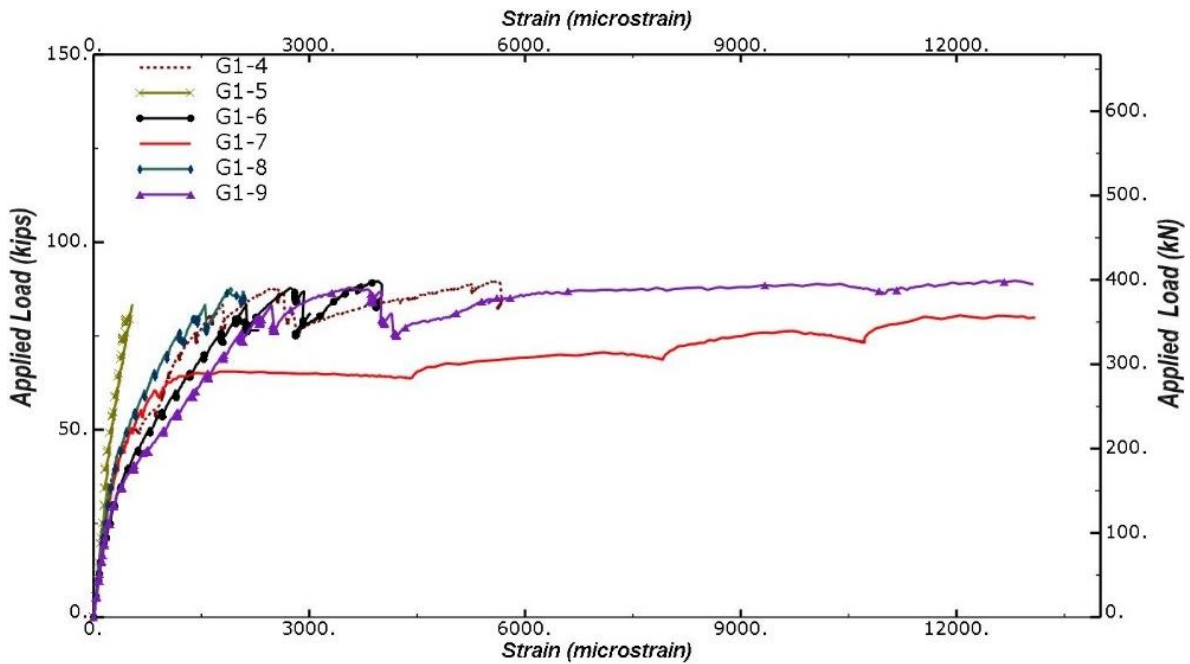


Figure 6-16 Strain on exposed prestressing strands of Girder-1



Table 6-3 The strain and the applied load at failure of the broken strands

Strain gauge	Failure load kN (kips)	Failure strain ( $\mu\epsilon$ )
G1-5	371.0 (83.4)	539
G1-7	355.2 (79.9)	13094
G1-8	387 (87)	2077

Figure 6-17 shows the applied load versus strain of the concrete surface at different depths. The maximum strain attained by the extreme top compression fiber at failure was 1199  $\mu\epsilon$ , which was less than the maximum usable strain assumed during flexural design. The reading of strain gauge G1-3 decreased after an applied load of 197.70 kN (44.4 kips). This was attributed to the presence of a crack.

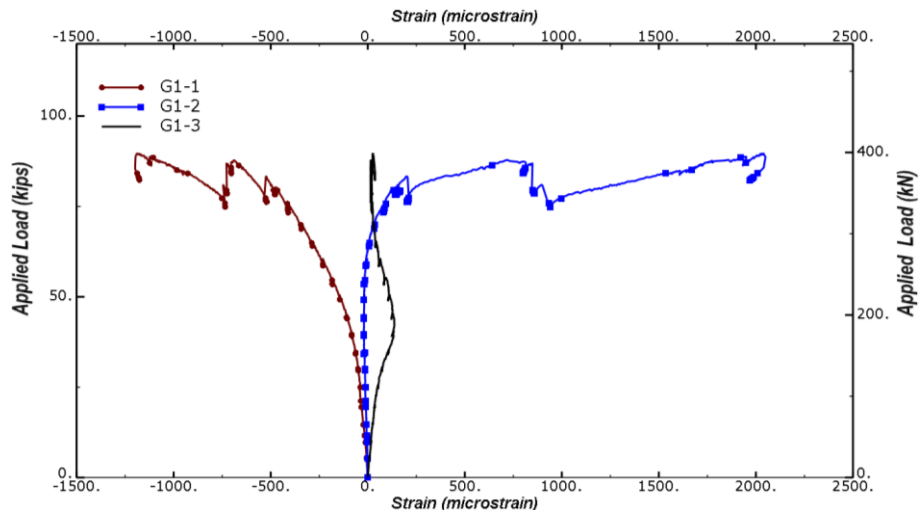


Figure 6-17 Girder-1 concrete strain profiles at different depths

### 6.3.3.2 Girder-2

Figure 6-18 shows the applied load versus deflection of Girder-2. The curve behaved in a linear elastic manner up to a load of 489.3 kN (110 kips) and then showed a decrease in stiffness. The first crack was also observed at an applied load of 489.3 kN (110 kips) on the bottom flange as shown in Figure 6-19. The calculated cracking moment as per AASHTO's (2014) guideline is

1237.90 kN-m (913.3 kip-ft), which corresponds to an applied load of 516 kN (116 kips). The equation over-predicted the cracking load by 5%. The girder failed at a load of 994.80 kN (223.63 kips) when the mid-span deflection was 60.45 mm (2.38 inches). This corresponds to an applied moment of 2387.7 kN-m (1761.1 kip-ft). It's calculated nominal flexural capacity per the provision of ACI440 (2008) was 2412.7 kN-m (1779.5 kip-ft). The theoretically predicted capacity deviated from the actual test result by only 1%. Figure 6-20 shows the deflected shape profile of the girder at various load levels.

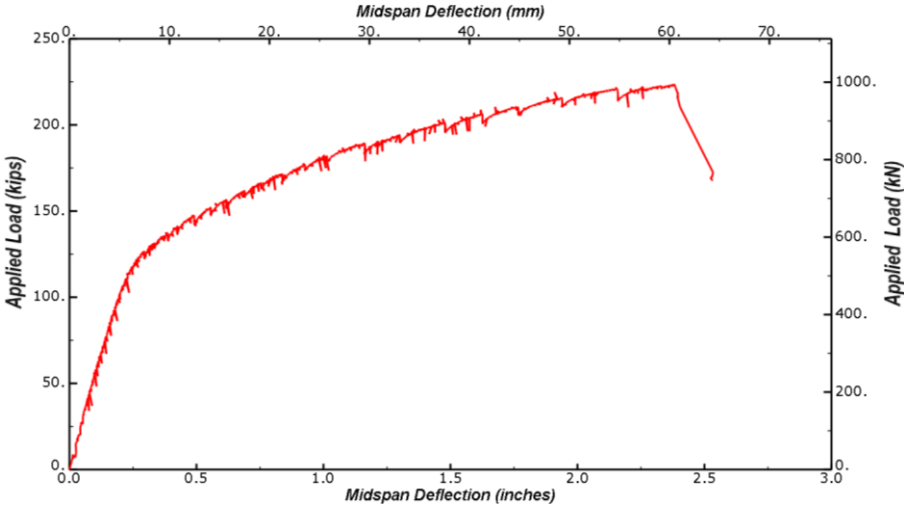


Figure 6-18 Applied load vs mid-span deflection of Girder-2



Figure 6-19 First crack on Girder-2 at 110 kips

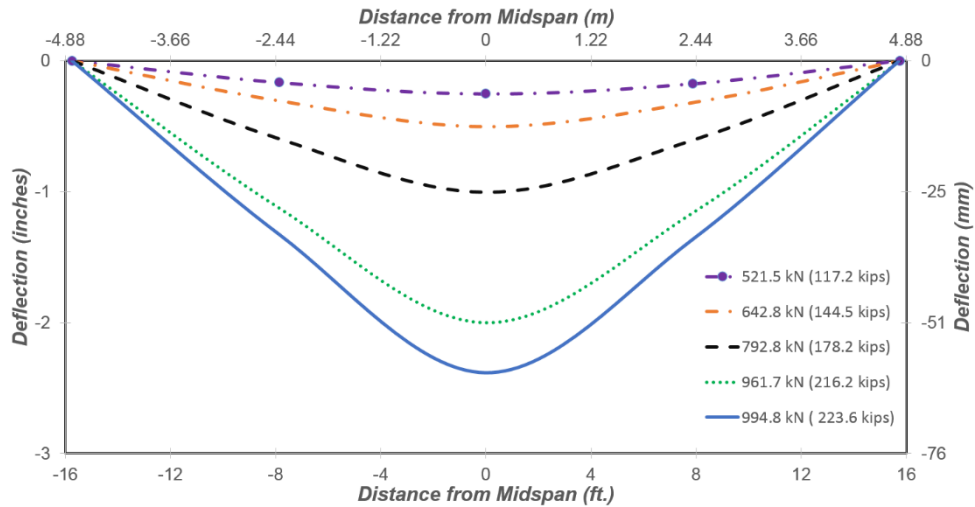


Figure 6-20 Deflection along girder length for various load increments of Girder-2

At a load of 188 kips, a small section of U5 was observed debonding on the side of the bottom flange. U6 also exhibited debonding on the side of the bottom flange at a load of 205 kips. At the failure load, U1, U2, U3, U4 and U5 ruptured followed by the debonding of the longitudinal FRP. The rupture occurred in the bottom of the bottom flange, where the U-wraps transition from the longitudinal FRP to the concrete surface as shown in Figure 6-22. Each U-wrap was inspected to evaluate their failure mechanism. Table 6-4 shows the failure mode of each U-wrap. The debonding of the longitudinal FRP was induced by the flexural crack which occurred at mid-span (Figure 6-23(a)). The debonding then progressed through the cement matrix which eventually lead to failure. Small chunks of concrete were also observed on the surface of the debonded FRP as shown in Figure 6-23(c). No inter-laminar debonding was observed either between the layers of the longitudinal FRP or between the transverse FRP and the longitudinal FRP.

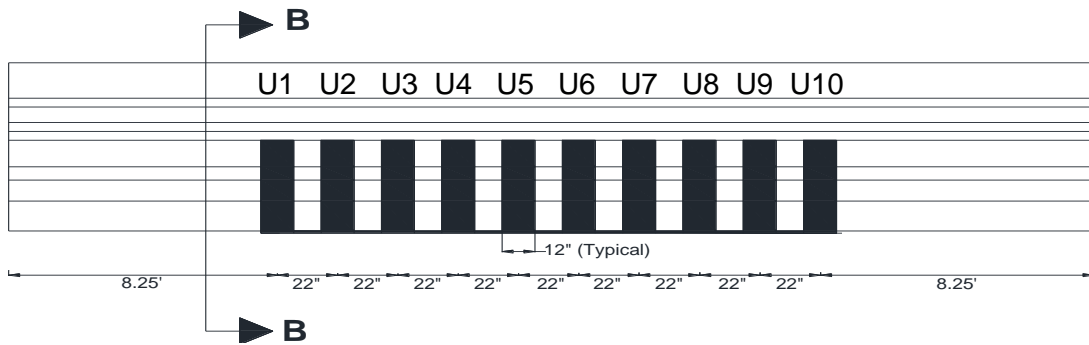


Figure 6-21 Labelling of U-wraps

Table 6-4 Failure modes of the U-wraps

U-wrap	Failure Mode
U1	ruptured
U2	ruptured
U3	ruptured
U4	ruptured
U5	ruptured
U6	debonded from the bottom of the bottom flange and the web
U7	debonded from the bottom of the bottom flange and the web
U8	No rupture/debonding
U9	debonding observed on a small area on the web and the sides of the bottom flange
U10	debonding observed on a small area on the web and the sides of the bottom flange

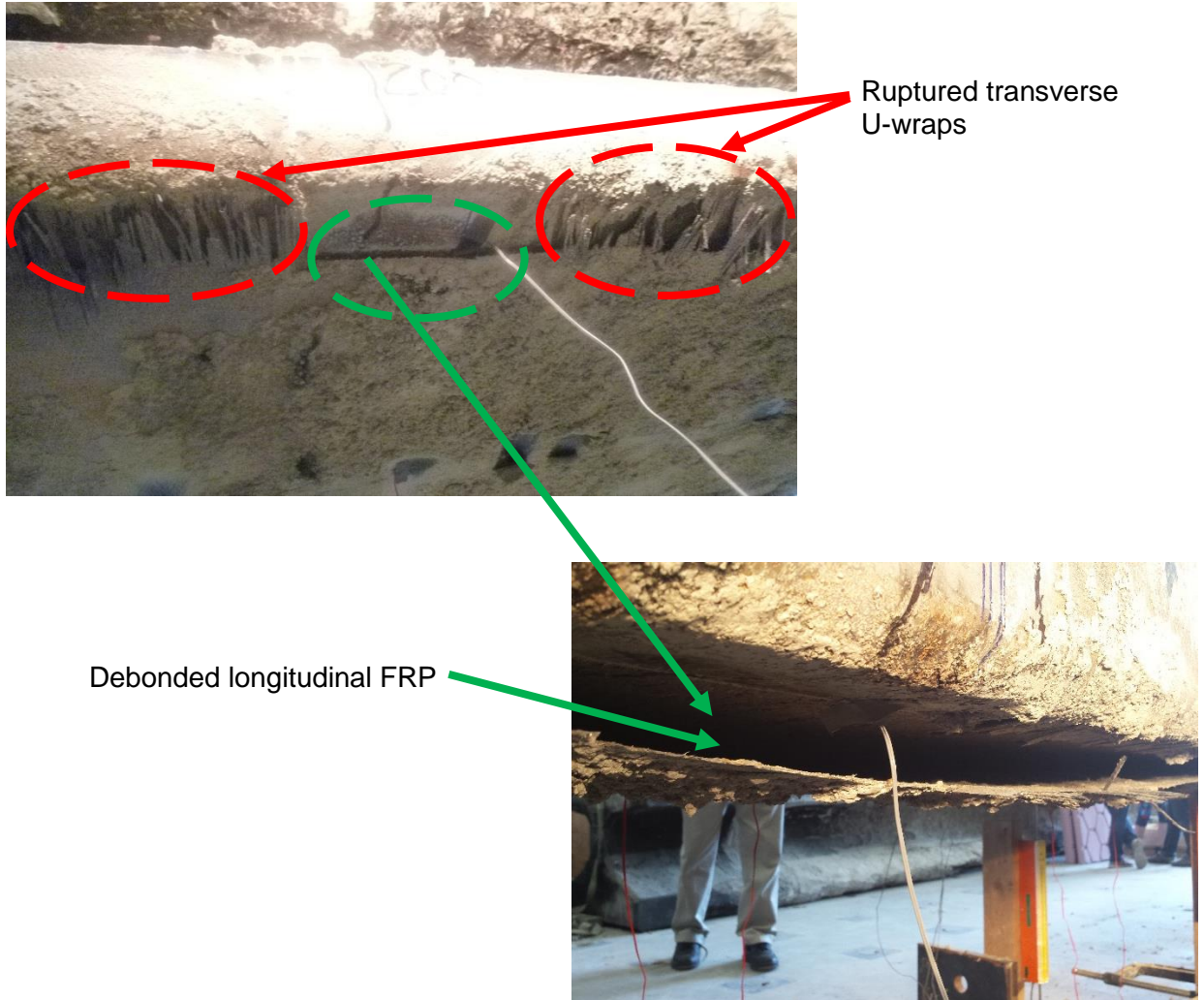
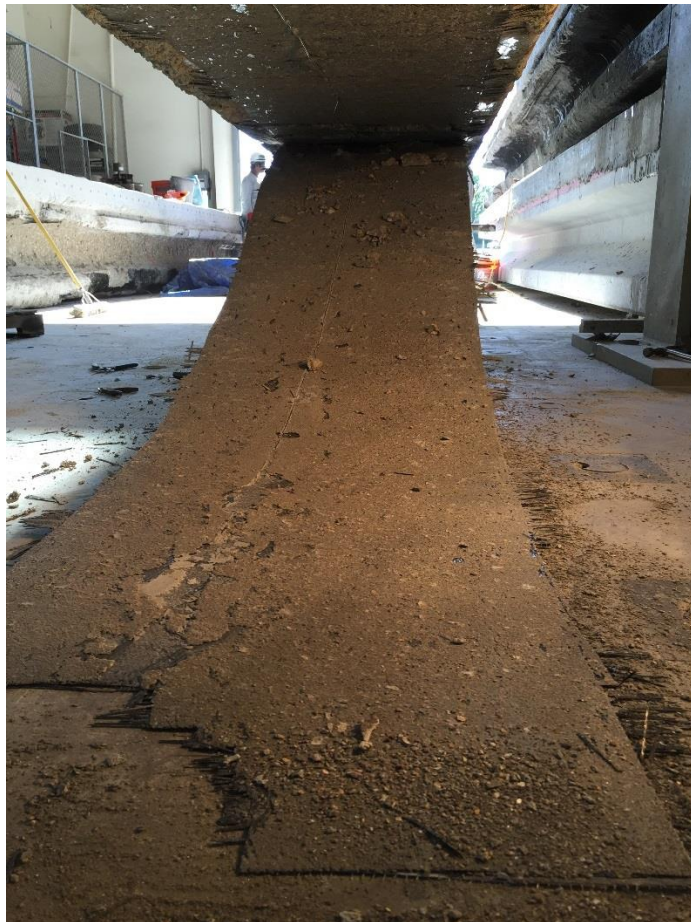


Figure 6-22 Rupture of transverse FRP and debonding of longitudinal FRP



(a) Cracks on the bottom flange at mid-span

(b) small chunks of concrete on the debonded FRP



(c) Debonded longitudinal FRP

Figure 6-23 Failure of concrete and FRP in Girder-2

Figure 6-24 shows the applied load versus strain measured at various locations on the longitudinal FRP. It is observed from the figure that the maximum tensile strain was measured at the mid-span (G2-11) and the smallest strain close to the termination point of the FRP (G2-22). The maximum tensile measured at ultimate load was 8100  $\mu\epsilon$ . To prevent crack-induced debonding, ACI 440 (2008) recommends the effective strain in the FRP to be less than  $\epsilon_{fd}$  given by equation 6-1. The strain value calculated using this equation is 9000  $\mu\epsilon$ . The actual debonding strain deviated from the theoretical value by 11%. The manufacturer reported strain at failure for cured laminate FRP is 10,000  $\mu\epsilon$ . The flexural induced crack at mid-span prevented the FRP from utilizing its full strain capacity.

$$\epsilon_{fd} = 0.083 \sqrt{\frac{f'_c}{nE_f t_f}} \leq 0.9\epsilon_{fu} \quad 6-1$$

Where:  $\epsilon_{fd}$  is the debonding strain,  $f'_c$  is the specified compressive strength of concrete,  $n$  is the number of plies of FRP,  $E_f$  is the tensile modulus of elasticity of FRP and  $t_f$  is the nominal thickness of one ply of FRP.

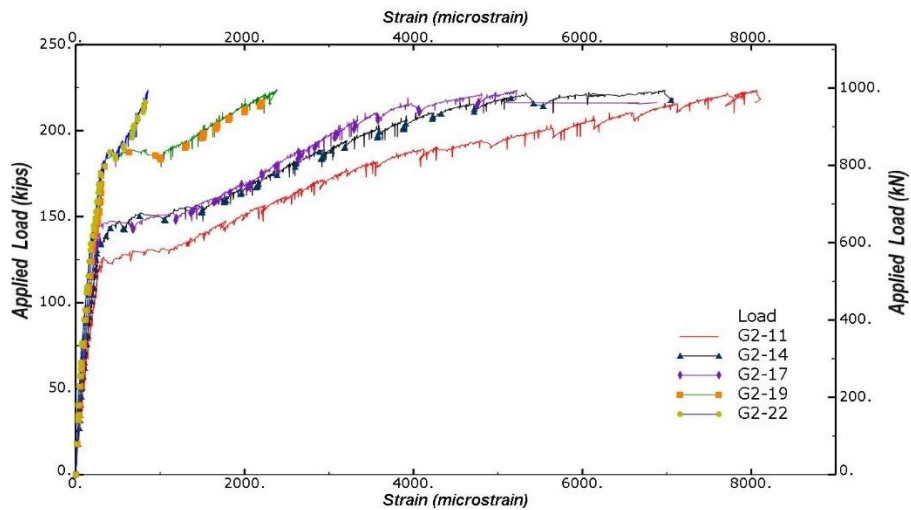


Figure 6-24 Strain versus applied load at various points on the longitudinal FRP

Figure 6-25 depicts the strain profile of the longitudinal FRP from the mid-span to its termination point at various load increments. It can be observed from the figure that the value of

the tensile strain was approximately constant in all the strain gauges until the cracking load. After cracking, the strain at the mid-span kept on increasing at a higher rate compared to the strain at the termination point.

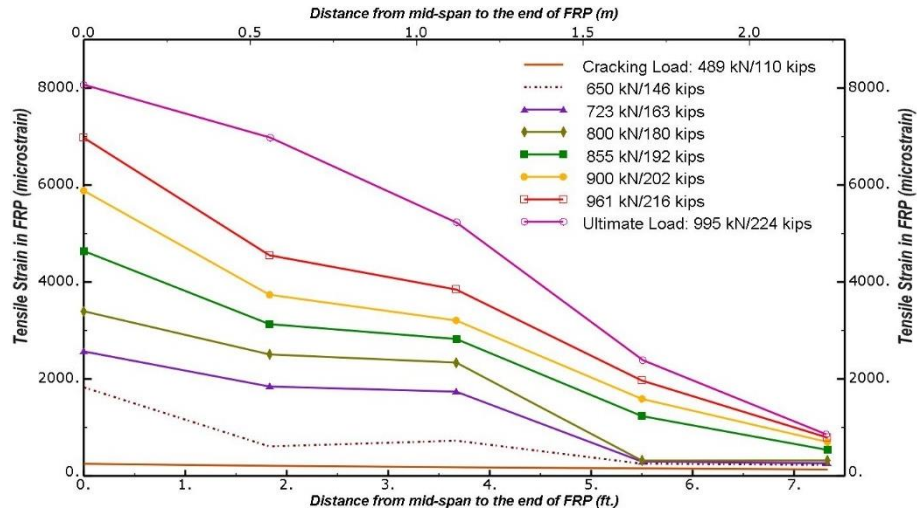


Figure 6-25 Tensile strain in FRP versus length of girder at different load increments

The strain readings from the strain gauges installed on the U-wraps is shown in Figure 6-26. Most of the gauges gave relatively a consistent reading till the cracking load. After the cracking load, they showed erratic variations which are not shown in the figure. All the readings have a negative value which is attributed to the Poisson's effect.

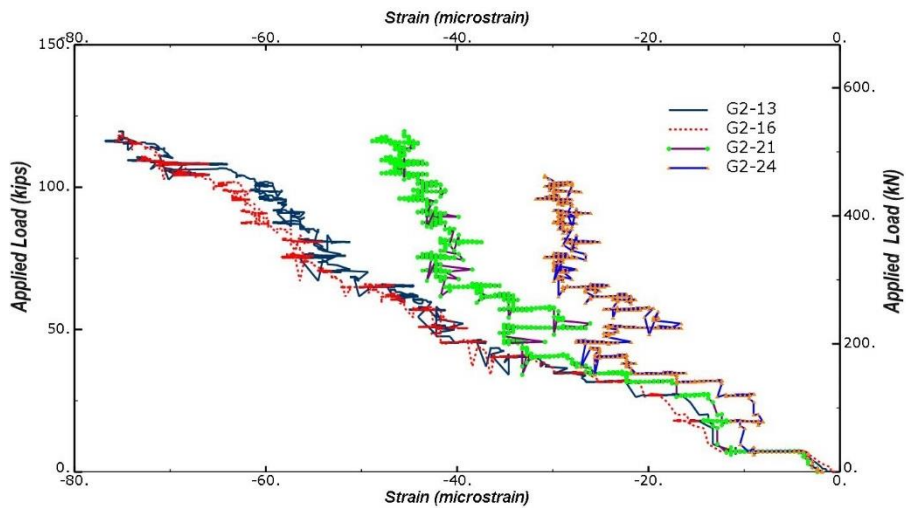


Figure 6-26 Strain versus applied load on U-wraps

Figure 6-27 shows the approximate variation of the depth of the neutral axis with an increase in the applied load for the mid-span cross section. The neutral axis is calculated using the reading from strain gauges G2-7, G2-8, G2-11, and G2-12. As it can be observed from the figure, the neutral axis stays relatively at the same depth before cracking. It then moved up and stabilized.

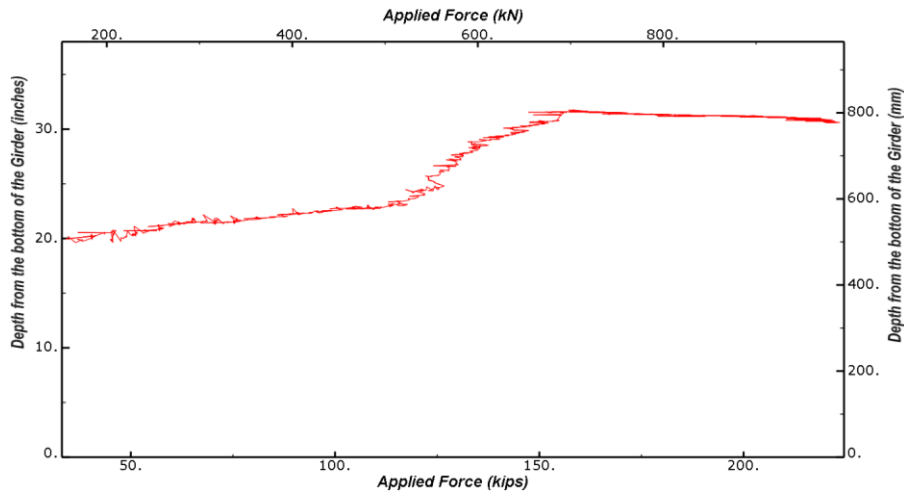


Figure 6-27 Variation of neutral axis depth with load for Girder-2

Figure 6-28 shows the variation of strain in the extreme compression fiber of concrete with the applied load. The maximum strain recorded was 1514  $\mu\epsilon$ .

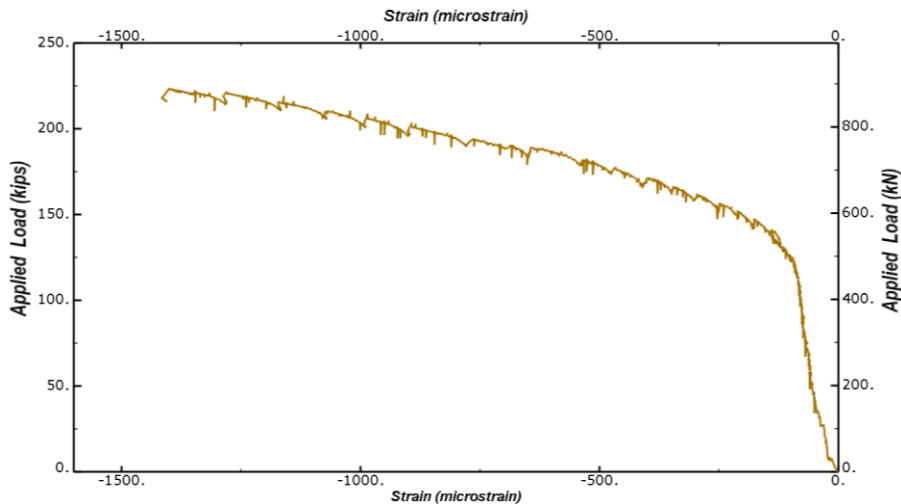


Figure 6-28 Variation of strain with applied load at the extreme concrete compression fiber for Girder-2



Strain data were also taken at different locations on the concrete surface of the bottom of the flange as shown in Figure 6-29. In bending test, it is a common phenomenon to observe flexural cracks originating from the bottom flange. Once cracks are initiated, strain gauges installed on the bottom flange read either small or large value which are not representative of the test. If the strain gauges are sandwiched in between cracks like G2-12, the values of the strain will be very small. If the strain gauges are crossed by a crack like G2-15 and G2-18, the value of the strain will be very high. As it can be observed from the figure, there is an inconsistent distribution of strain along the girder length once the cracking load is exceeded.

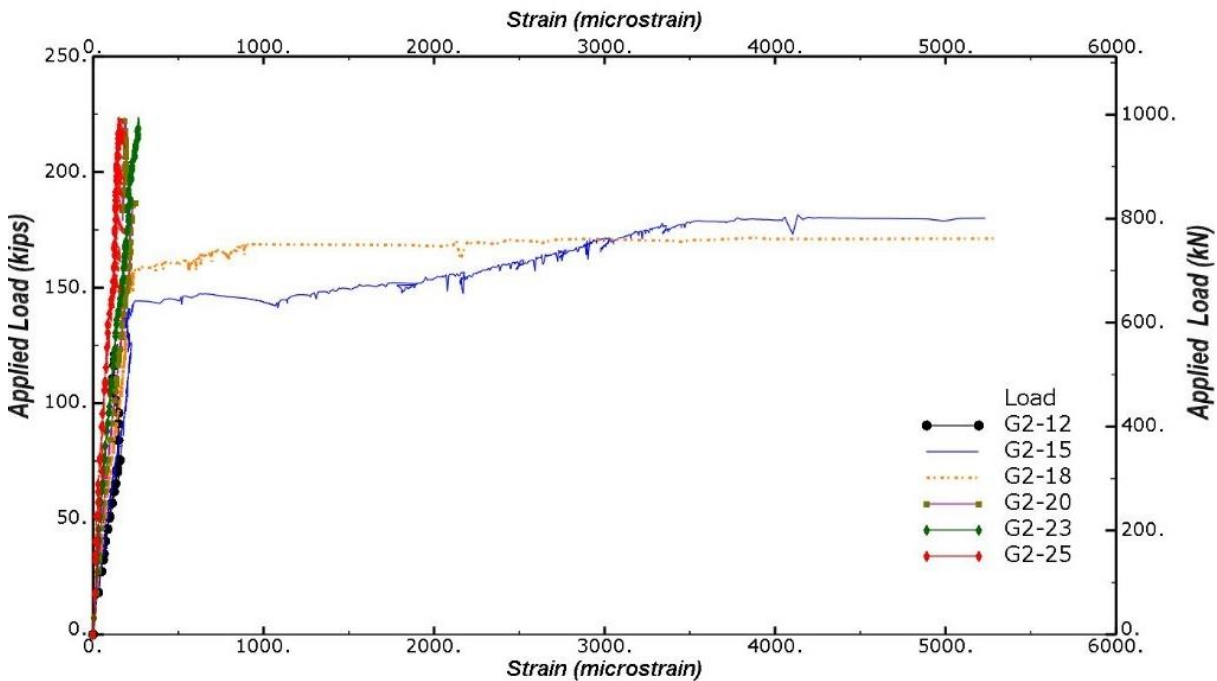


Figure 6-29 Load versus strain at various location on the concrete surface of the bottom flange

None of the prestressing strands were broken during the test. Figure 6-30 shows the strain measured in the exposed strands. It is observed that the strain profiles from the four strain gauges are approximately identical. From this, it can be concluded that all the strands sustained the same level of fire exposure. The maximum strain reading out of the four gauges was 1390  $\mu\epsilon$ . These strain gauges were installed away from the mid-span, which contributed to the lower strain readings.

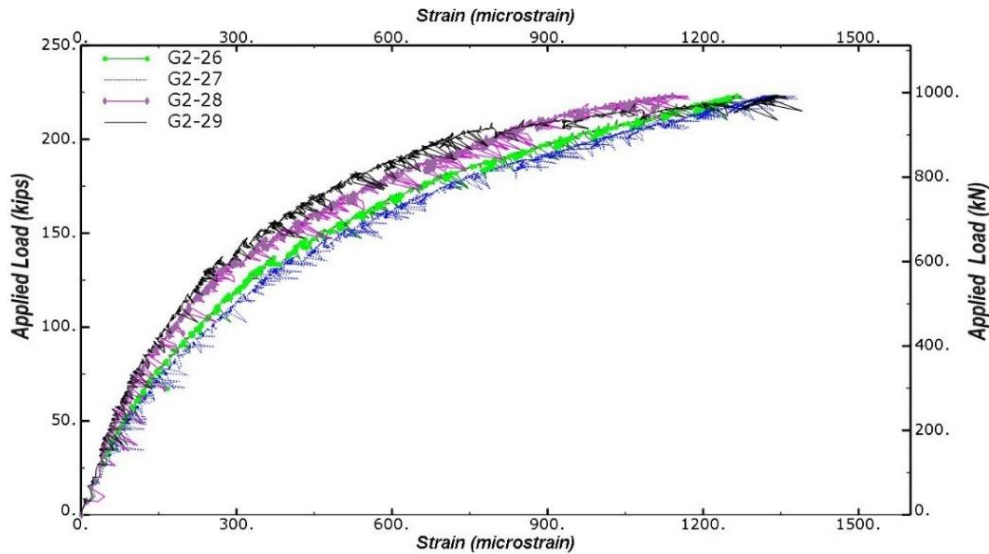


Figure 6-30 Strain on exposed prestressing strands of Girder-2

The fireproofing over half of the girder span was left in place to evaluate its performance during the residual strength test. It was observed that no fireproofing was spalled off during the test. But cracks which were observed before the residual strength test increased in width and new cracks were also formed.

### 6.3.3.3 Girder-3

Figure 6-31 depicts the applied load versus deflection curve for Girder-3. The plot shows a linear behavior approximately up to a load of 447.8 kN (100.7 kips). It then displayed a decrease in stiffness. The first visible crack was observed at a load of 467.1 kN (105 kips). The girder failed at a load of 804.80 kN (180.8 kips) when the mid-span deflection was 58.53 mm (2.30 inches). This corresponds to an applied moment of 1930.4 kN-m (1423.8 kip-ft). One of the prestressing strands was broken after the fire test. The calculated nominal flexural capacity according to the provision of AASHTO (2014), considering the remaining strands, was 1875.95 kN-m (1383.6 kip-ft). The theoretically predicted capacity deviated from the actual test result by 2.8 %. Figure 6-32 shows the deflected shape profile of the girder at different load increments. Before cracking, a large increase in applied load didn't cause a significant increase in the deflection. But once the

cracking load is exceeded, a relatively small increase in the load caused a notable difference in deflection.

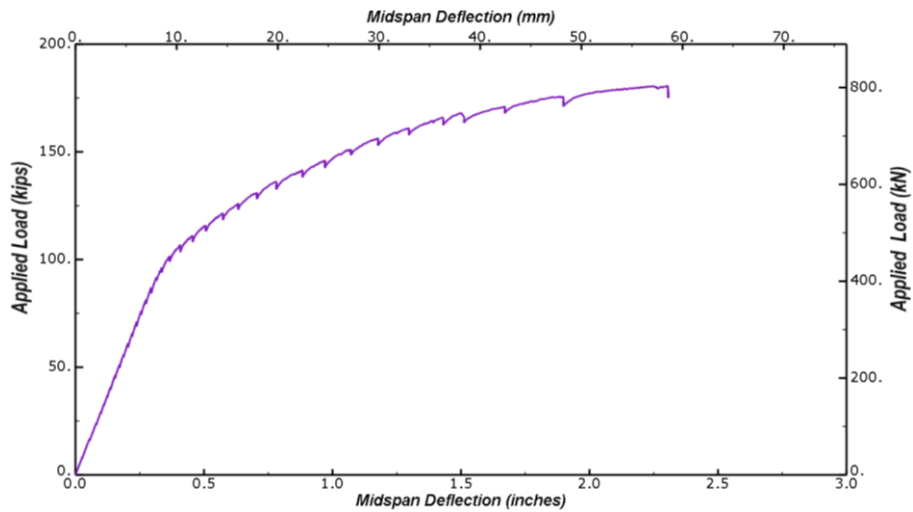


Figure 6-31 Applied load vs mid-span deflection of Girder-3

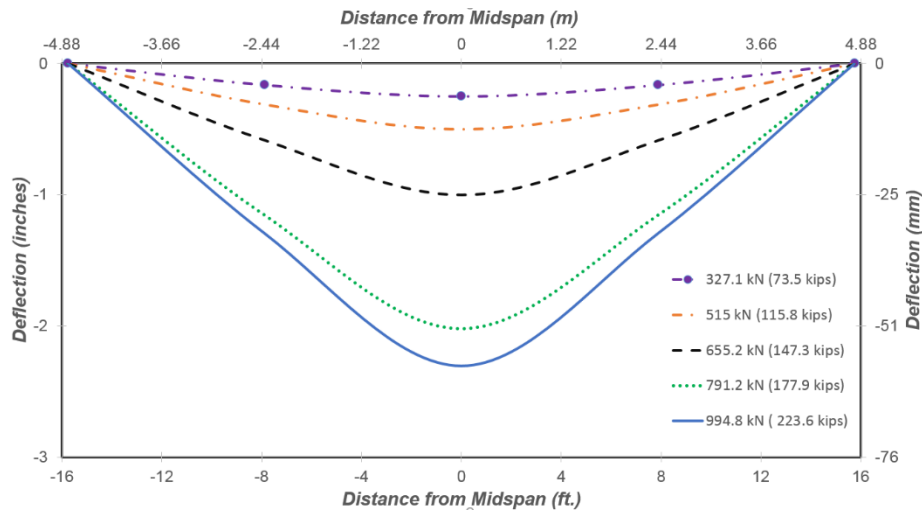


Figure 6-32 Deflection along girder length for various load increments of Girder-3

Girder-3 was exposed to the least amount of fire compared to the other two girders. Thus, most of the exterior surface finish was intact to mark the cracks formed both during the fire and the residual strength test as shown in Figure 6-33. All the cracks marked in red color were the result of the fire test; whereas those marked in dark-blue were from the residual strength test. As it can be observed from the figure, the cracks from the fire test were horizontal which were created

due thermal gradient. The cracks from the residual strength test were diagonal/vertical as expected.



Figure 6-33 Cracks formed during fire and residual strength test

Figure 6-34 shows the strain reading for the bottom flange at different locations. The reading shows a consistent increase going from the mid-span to the end of the girder until the concrete cracks. Once the concrete cracks, the strain gauges show inconsistent trend due to either the strain gauge being sandwiched between cracks or crossed by a crack/cracks (Figure 6-35).

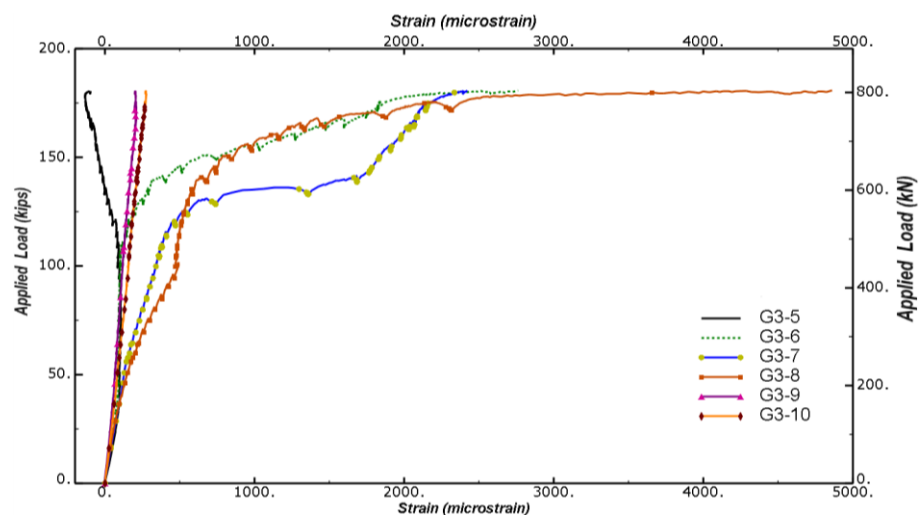


Figure 6-34 Applied load versus strain at the bottom of Girder-3



Figure 6-35 Cracks underneath the strain gauge

Figure 6-36 shows the variation of strain measured in the extreme concrete compression fiber with the applied load. The maximum measured strain was 1015  $\mu\epsilon$ .

Like the strain gauges installed on the bottom flange; G3-2, G3-3, and G3-4 didn't give a consistent reading.

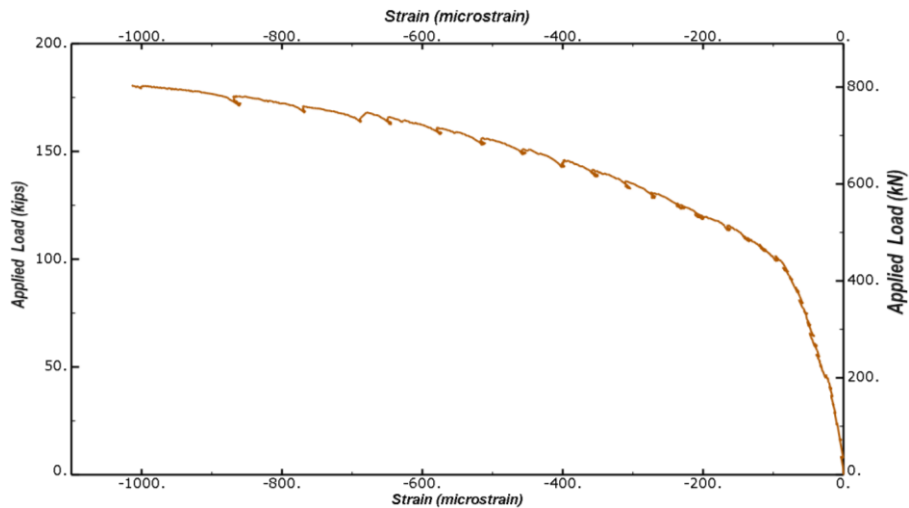


Figure 6-36 Variation of strain with applied load at the extreme concrete compression fiber for Girder-3

#### 6.3.3.4 Control Girder

Like the previous three girders, the control girder was also tested under the same setup. Figure 6-37 depicts its mid-span deflection responses for monotonically increasing applied loads. An elastic behavior is observed up to a load of 400 kN (90 kips) with corresponding deflection of

3.8 mm (0.15 inches). It then shows a decrease in stiffness. The first crack was observed at an applied load of 378.1 kN (85 kips). The calculated cracking moment as per AASHTO's (2014) guideline is 1125.9 kN-m (830.4 kip-ft), which corresponds to an applied load of 467.1 kN (105.4 kips). The theoretically predicted cracking load deviated from the test result by 23.5%. The girder failed at a load of 756.50 kN (170.1 kips) when the mid-span deflection was 71.25 mm (2.81 inches). This corresponds to an applied moment of 1816.2 kN-m (1339.5 kip-ft). Its calculated nominal flexural capacity using the provision of AASHTO (2014) is 1929.3 kN-m (1423 kip-ft). The theoretical calculation over-predicted by 6.2 %. Figure 6-38 shows the deflected shape profile of the girder at different load increments.

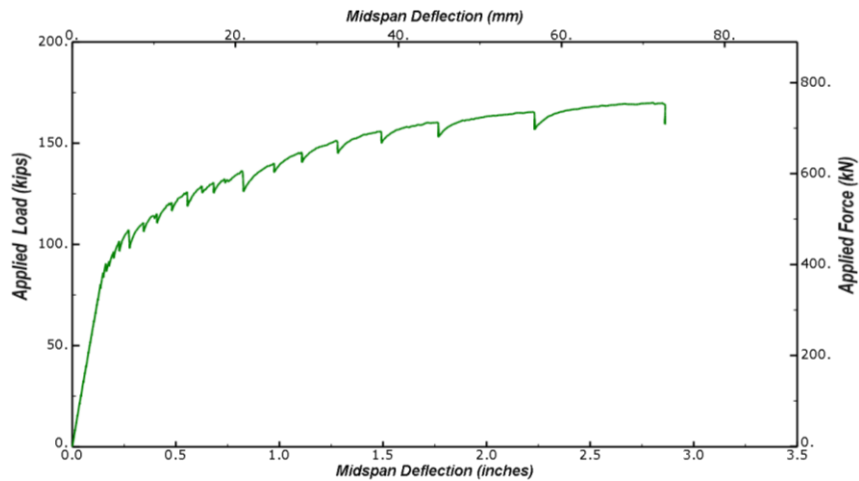


Figure 6-37 Applied load vs mid-span deflection of the control girder

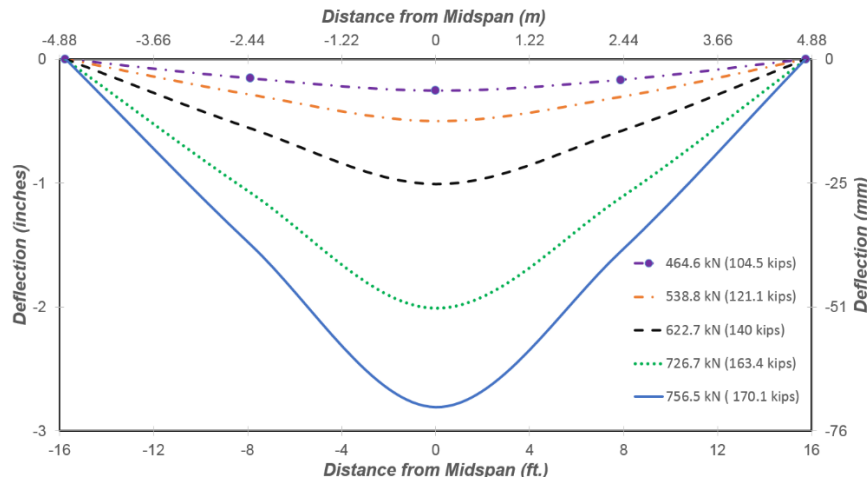


Figure 6-38 Deflection along girder length for various load increments of the control girder

The approximate variation of the depth of the neutral axis with the applied load is also plotted as shown in Figure 6-39. Strain values from strain gauges GC-6, GC-7, and GC-8 is used in calculating the depth. As it can be observed from the figure, the neutral axis stays approximately at the same depth till the girder cracks. After cracking, it moves up and stabilizes at a constant value before continuing to move up again.

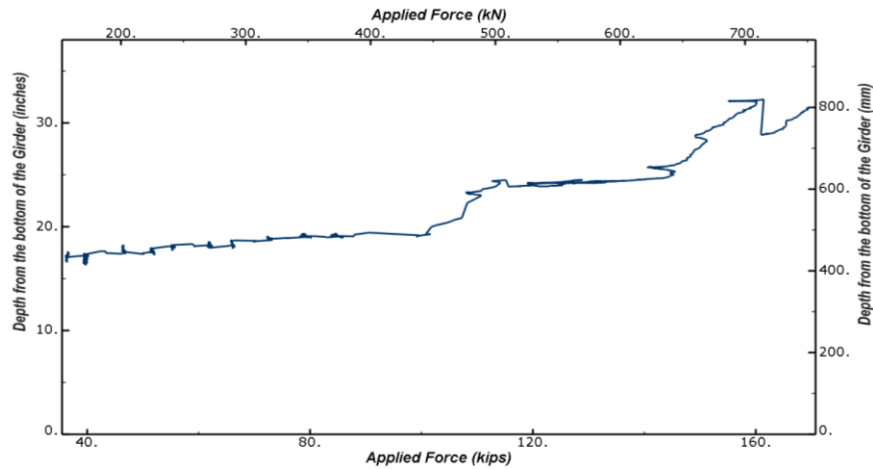


Figure 6-39 Variation of neutral axis depth with load for the control girder

Figure 6-40 shows the variation of strain measured at the extreme concrete compression fiber with the applied load. The maximum measured strain was 1887  $\mu\epsilon$ . Figure 6-41 shows the crack pattern of the control girder at the end of the test.

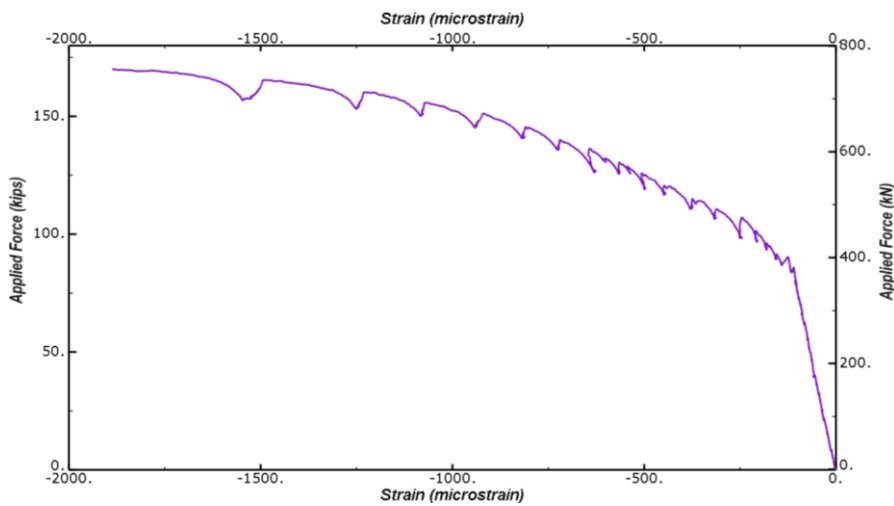


Figure 6-40 Strain versus applied load at the extreme concrete compression fiber for the control girder



Figure 6-41 Crack pattern of control girder

Figure 6-42 shows the strain reading at various locations on the bottom the control girder. GC-13, GC-14, and GC-15 were operational until the end of the test. Whereas GC-10, GC-11, and GC-12 exhibited a consistent reading up to a load of 355.4 kN (79.9 kips), 598.7 kN (134.6 kips) and 693 kN (155.8 kips), respectively. As it can be observed from the plot, the strain values displayed a decreasing trend going from the mid-span to the end of the girder as expected.

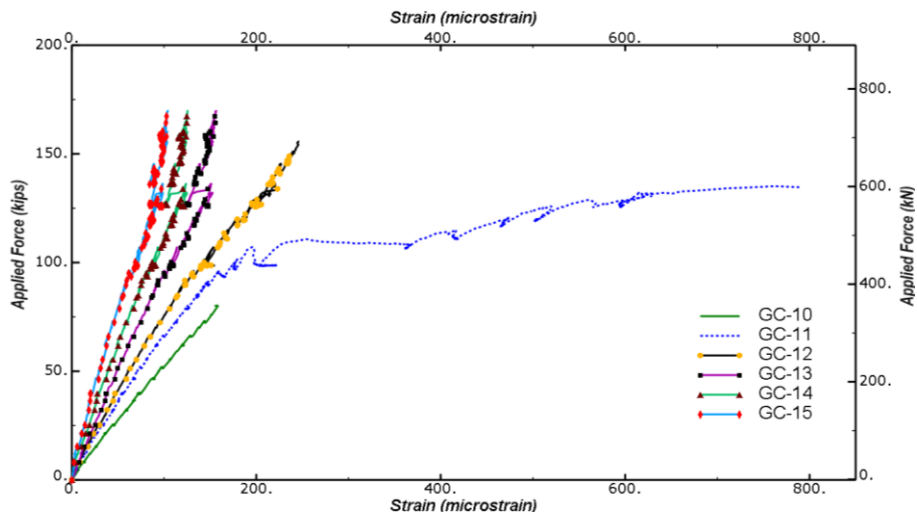


Figure 6-42 Applied load versus strain at various location on the bottom of control girder



### 6.3.3.5 Combined Results

Table 6-5 summarize the results of the residual strength tests. There is a long-standing belief among engineers that fire don't have a pronounced effect on the load carrying capacity of concrete structure. However, the results of the residual strength test of Girder-1 is a contrary to this assumption. The ultimate load attained by Girder-1 is 59.9 %, 50.4 % and 47.3 % less than that of Girder-2, Girder-3 and the control girder, respectively. The fire caused a significant reduction in the flexural capacity of Girder-1.

The ultimate load sustained by the control girder is less than Girder-3. Since its topping was poured 38 days after the test bridge deck. Table 6-2 shows the difference in the compressive strength of the two at the time of the residual strength test. Girder-3 was exposed to the least amount of fire compared to Girder-1 and Girder-2. It only lost one strand and a section of concrete on the bottom flange. Thus, the fire has caused the least amount of effect on its ultimate flexural capacity.

The ultimate load carrying capacity of Girder-2 is 23.7 % and 31.5 % more than Girder-3 and the control girder. Looking at this values and the fire test results, it can be deduced that the fireproofing was successful in protecting the FRP, the concrete, the prestressing strands and the reinforcements.

The maximum compressive strain in the extreme compression fiber of girders is observed in the control girder. This could be due to the lower compressive strength of the concrete used for the topping.

Figure 6-43 shows the load versus deflection diagram of all the girders. Girder-2 and the control girder have approximately the same stiffness before cracking. However, Girder-2 is stiffer after cracking (post cracking). As a matter of fact, Girder-2 has the highest cracking load and post-cracking stiffness compared to all the girders. It can also be clearly observed from the plot that

the fire had caused a significant reduction in stiffness and ultimate load carrying capacity of Girder-1 compared to the other girders.

Table 6-5 Summarized results of residual strength tests

Parameter	Girder-1	Girder-2	Girder-3	Control Girder
Maximum compressive strain in concrete, $\mu\epsilon$	1199	1514	1015	1887
Maximum tensile strain in CFRP, $\mu\epsilon$	-	8100	-	-
Measured Load at first observed crack, kN (kips)	333.62 (75)	489.3 (110)	467.1 (105)	378.1 (85)
Measured ultimate load, kN (kips)	399.10 (89.70)	994.80 (223.63)	804.80(180.8)	756.50(170.1)
Deflection at Ultimate load, mm (in.)	66.04(2.6)	60.45(2.38)	58.53 (2.30)	71.25 (2.81)

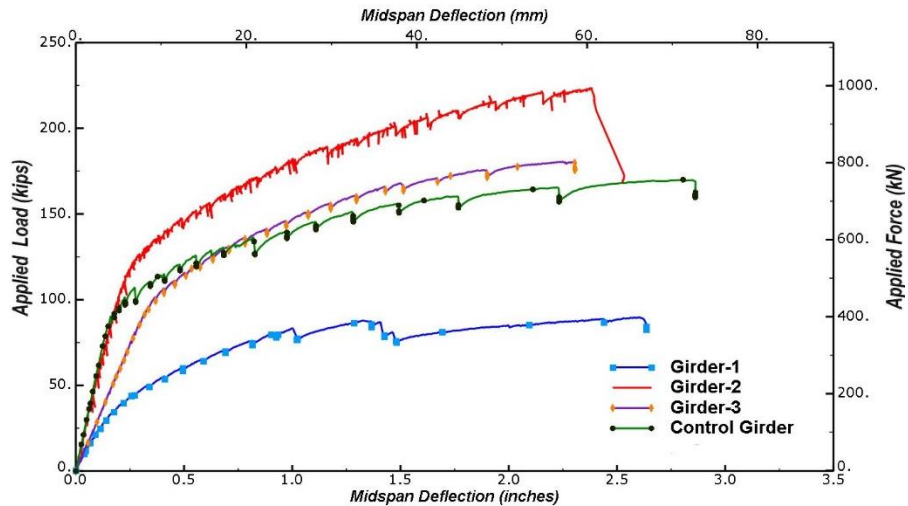


Figure 6-43 Applied load versus midspan deflection for all the tested girders

A comparison was also made among the girder in terms of their ductility. Structural ductility is the ability to sustain an applied load beyond the elastic limit without significant loss of load carrying capacity until failure (Grace et al. 1998). The ductile behavior of a beam can be quantified

in terms of displacement ductility, curvature ductility, energy ductility and deformability factor. AASHTO (2014), which is used in the current study, defines ductility as the ratio of deformation at ultimate load to the deformation at yield as expressed in equation 6-2.

$$\mu = \frac{\Delta_u}{\Delta_y} \quad 6-2$$

Where:  $\mu$  is the ductility factor,  $\Delta_u$  is the deformation at ultimate load and  $\Delta_y$  is the deformation at yield.

The deformation at yield is determined using the method suggested by Park (1988). As shown in Figure 6-44, the yield displacement is defined as the point of intersection of the horizontal line that passes through the ultimate load and the secant stiffness line that passes through at 75 % of the ultimate load.

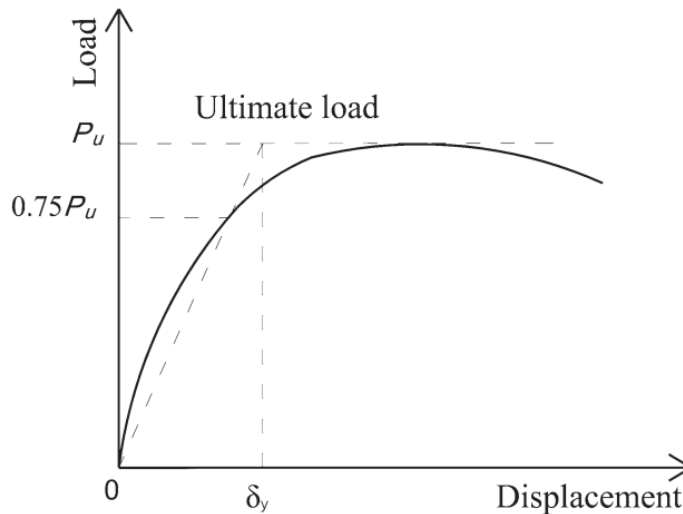


Figure 6-44 Definition of yield displacement (Park, 1988)

Table 2-1 shows the ductility factor for each girder. The control girder has the highest ductility factor compared to all the girders. Out of all the fire tested girders, Girder-1 has the highest ductility factor. This is due to increase in ductility of concrete and prestressing strand with an increase in temperature. Girder-3 has the least ductility factor.

Table 6-6 Ductility factor for each girder

<b>Girder</b>	$\Delta_y$ , mm (inches)	$\Delta_u$ , mm (inches)	$\mu$
Girder-1	21.44 (0.84)	66.04 (2.60)	3.10
Girder-2	26.42 (1.04)	2.38 (60.45)	2.29
Girder-3	26.97 (1.06)	58.53 (2.30)	2.17
Control Girder	86.87 (3.42)	71.25 (2.81)	3.42

## Chapter 7

### NUMERICAL MODELING

The numerical modeling scheme is developed with the goal of verifying the capability of currently used software to model the response of bridges to a pool fire. It also aimed in setting up a prototype numerical scheme that can be used in forensic investigation of similar bridge fire incidents. The numerical analysis consists of three modeling steps: fire analysis, heat transfer analysis, and thermo-mechanical analysis. The fire is simulated using Pyrosim (2016) which is the graphical user interface of NIST (National Institute of Standard and Technology) developed CFD based fire dynamics simulator (FDS) software (NIST 2014). Pyrosim is used to predict the boundary fire temperature. The fire temperature from Pyrosim is then applied in ABAQUS (2014) to perform sequentially coupled thermo-mechanical analysis. The thermo-mechanical procedure involves first conducting the heat transfer analysis to determine the transient nodal temperatures with respect to time followed by stress analysis.

#### 7.1 Analysis procedure

##### 7.1.1 Fire Model

Developing a fire model in Pyrosim requires defining a control volume with its boundary condition, meshing of the control volume, the geometry of the structure subjected to the fire, material properties, fire source and sensors for recording the fire temperature (Figure 7-1).

Defining the fire source requires specifying the heat release rate and the combustion reaction. The heat release rate is calculated using Equation 5-1. The author contacted several sources including the manufacturer to get the parameters needed to define the fire from the E-III fuel, but it was unsuccessful. Because of this, the temperature readings from the installed thermocouples as well as the temperature derived by correlating the surface hardness of fire tested girder and control girder were used as a fire temperature.

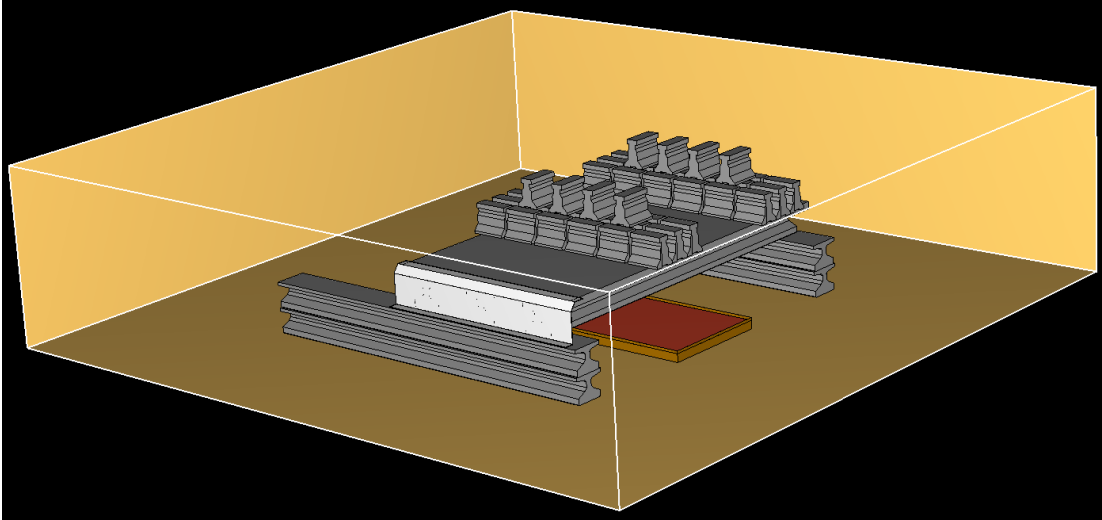


Figure 7-1 Fire tested bridge Pyrosim model

Out of the three fire tested girders, Girder-2 was considered for modeling. Only half of the section shown in Figure 7-2 is modeled to take advantage of symmetry. This helps to save computation time and resources.

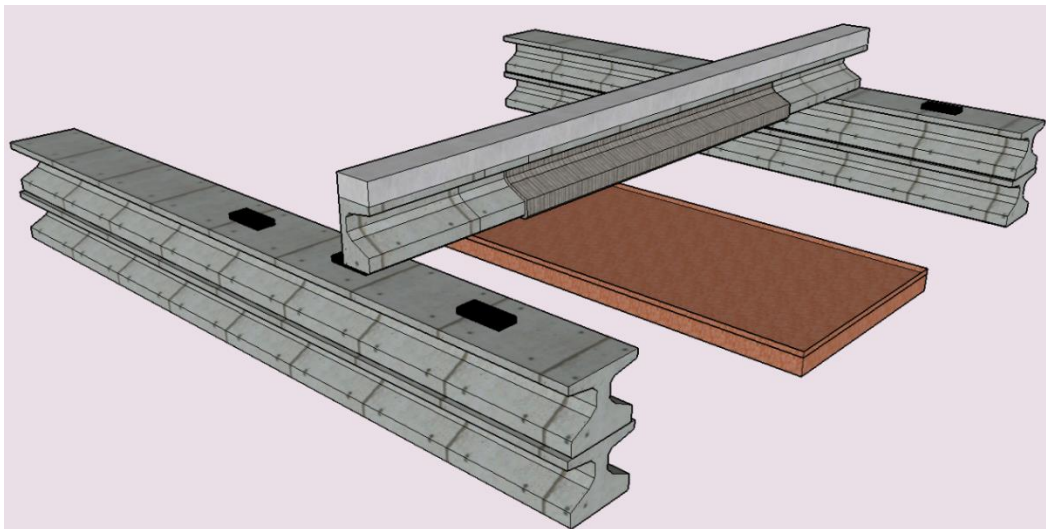


Figure 7-2 Half section of Girder-2 considered for modeling

The mid-section of the girder, where there is fire proofing, was subjected to the largest intensity of the fire. The reading from thermocouple-1BO is used for this section as a fire temperature. To facilitate merging with Abaqus, the temperature curve T-6 is created taking the average of the temperature readings from this thermocouple (Figure 7-3).

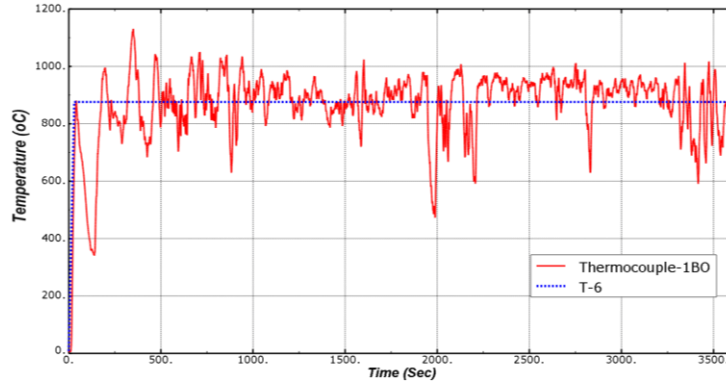


Figure 7-3 Temperature curve T-6

The readings from thermocouple B-3 was used as fire temperature on the ends of the girder. The temperature readings from thermocouple B-2 was applied on the bottom flange for a span of 1.52m (5 ft) from each end. To facilitate merging with Abaqus, temperature curve T-4 and T-5 are created from thermocouple B-2 and B-3 respectively by taking the average of the readings as shown in Figure 7-4 and Figure 7-5.

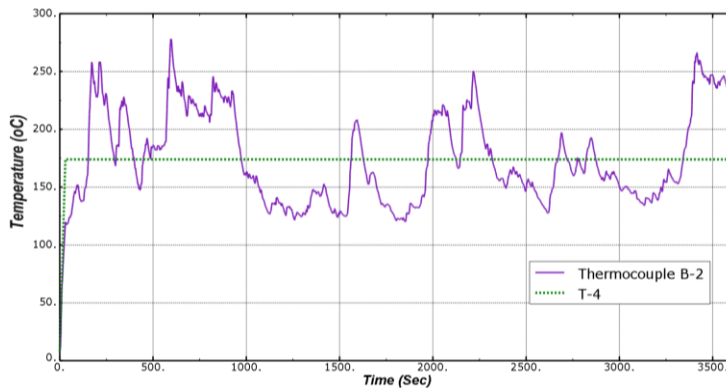


Figure 7-4 Temperature versus time curve T-4

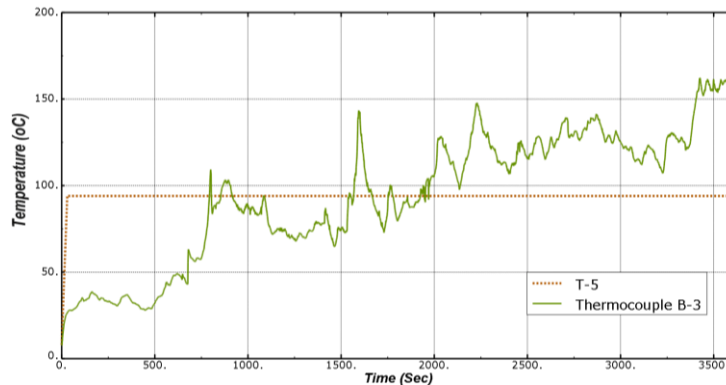


Figure 7-5 Temperature versus time curve T-5

For other sections of the girder, where there was no thermocouple reading in the vicinity, an approximate fire curve was created by correlating their surface hardness with the surface hardness of the control girder. The surface hardness of Girder-2 is shown in Figure 5-52. The average surface hardness of the control girder is 62.1 MPa (9000 psi).

Taking the ratio of the surface hardness of Girder-2 to the surface hardness of the control girder yielded a reduction factor, which could be correlated to the maximum temperature the surface is exposed as per Table 7-1. Table 7-1 shows reduction factor for compressive strength of concrete as a function of temperature according to Eurocode 2 (2005b).

Table 7-1 Reduction factor for compressive strength of concrete (Eurocode 2, 2005b)

<b>Concrete Temperature, <math>\Theta</math> (°C)</b>	<b>Reduction Factor (<math>f_{c,\Theta}/f_c</math>)</b>
20	1.00
100	1.00
200	0.95
300	0.85
400	0.75
500	0.60
600	0.45
700	0.30
800	0.15
900	0.08
1000	0.04
1100	0.01
1200	0.00

*Note:  $f_{c,\Theta}$ : is the compressive strength after exposure to a temperature  $\Theta$ ;  $f_c$  is the compressive strength at room temperature.*

The surface hardness of the north elevation and the south elevation are different. To take advantage of the symmetry geometry of the girder, the average value of the two is calculated and depicted as shown in Figure 7-6(A). Because of the prevalent wind during the fire test, the surface hardness of the girder section on the side of support-2 has lower value compared to that of the



side by support-1. To reduce variability, the same values of surface hardness were used on both sides (taking the smallest value). The strength reduction was then calculated for each section by dividing the surface hardness of that particular section to the surface hardness of the control girder, which is 62.1 MPa (9000 psi). The calculated reduction factors are shown in Figure 7-6(B) are correlated to temperature using Table 7-1, which was then used to develop a temperature versus time curve for each section. Each curve starts at ambient temperature then goes up linearly to the maximum temperature obtained using Table 7-1 in 30 secs and remained constant for the duration of the fire test. The same procedure was also followed for the bottom flange. The temperature versus time curve for each section are shown in Figure 7-8.

The top of the deck was assumed to be exposed to 100°C ambient temperature. On the other hand, the section of the deck on the side was assumed to be perfectly insulated by the adjoining slab. Figure 7-7 shows the name of temperature versus time curve assigned to different sections of the girder.

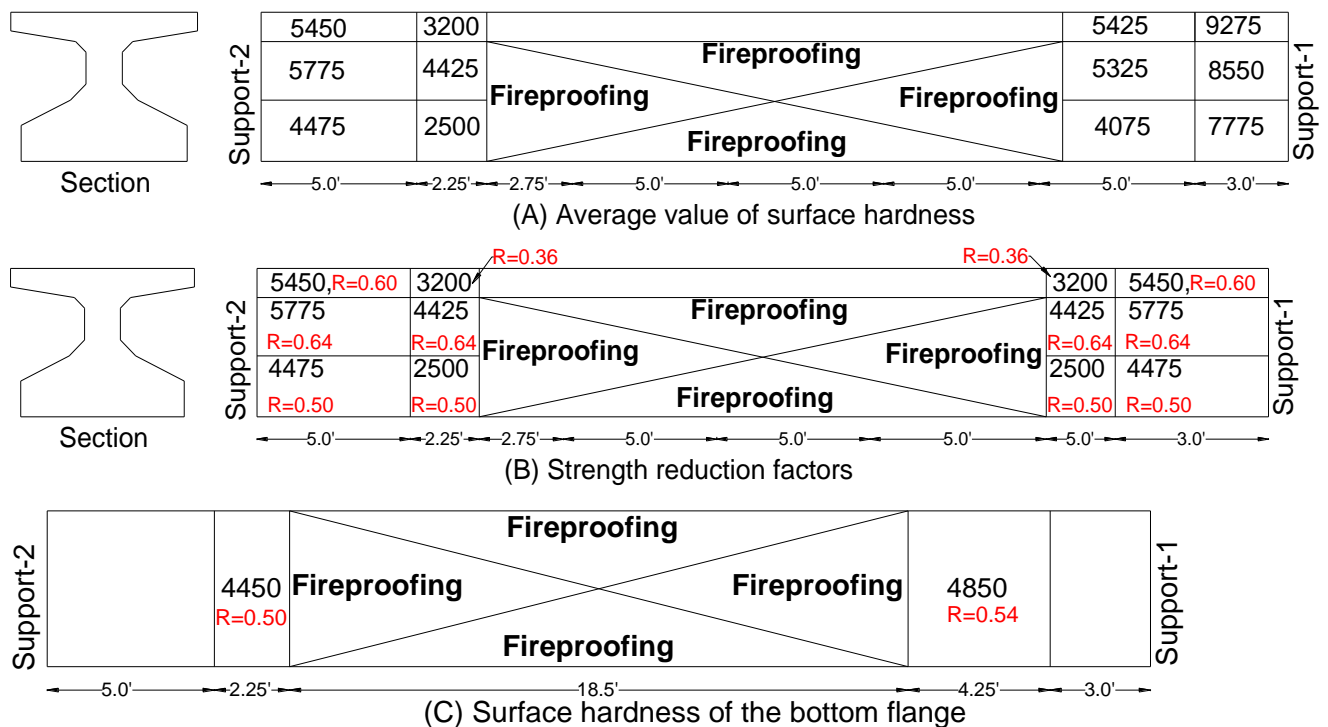
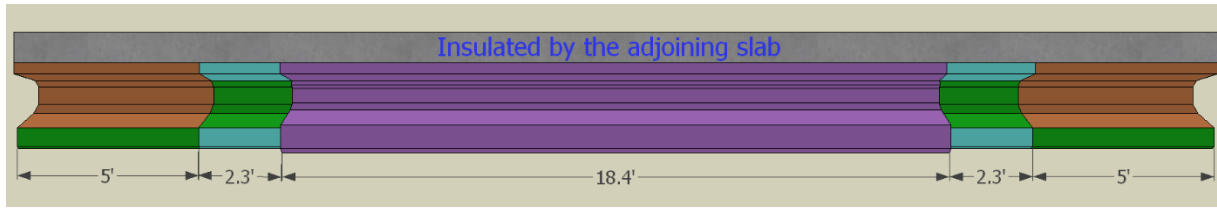
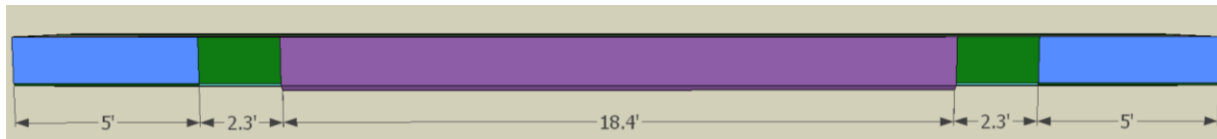


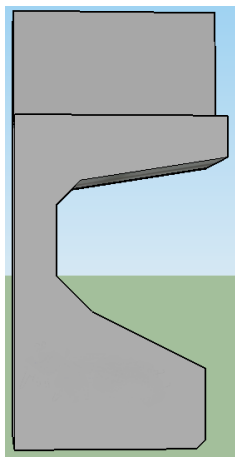
Figure 7-6 Strength reduction factors



(a) Elevation



(b) Bottom flange



(c) End of the girder and the deck

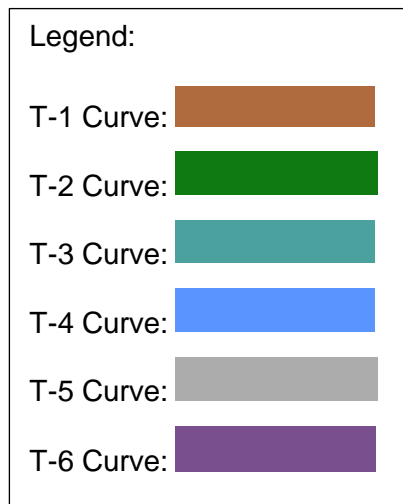


Figure 7-7 Assignment of temperature curves

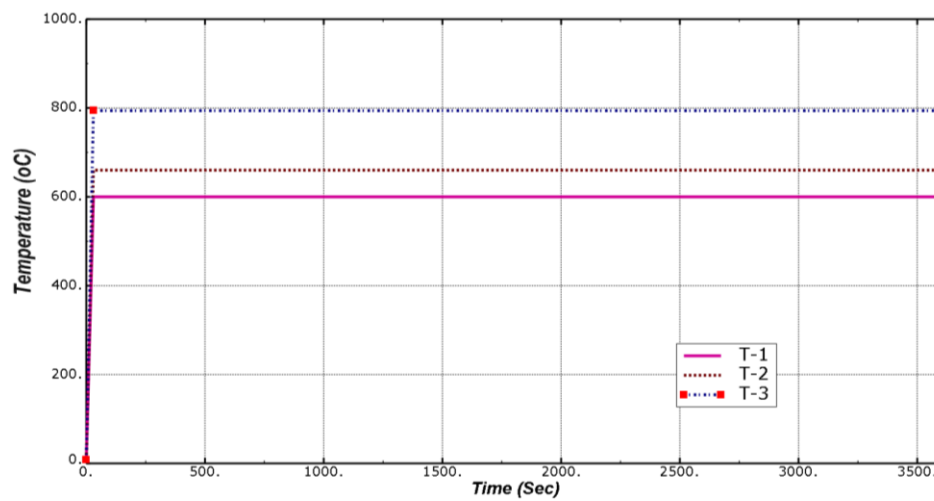


Figure 7-8 Temperature versus time curve T-1, T-2 and T-3

### 7.1.2 Heat Transfer and Mechanical Analysis

Conduction, convection, and radiation are the three basic mechanisms of heat transfer that needs to be considered to solve the transient nodal temperatures. In a hydrocarbon pool fire, the heat fluxes from the fire were exchanged with the surface of the girder through convection and radiation. On the other hand, the heat transfer inside the girder was through conduction. The governing equation for transient heat conduction is given by (SFPE 2016):

$$\rho c \frac{\partial T}{\partial t} = \frac{\partial}{\partial x} \left( k \frac{\partial T}{\partial x} \right) + \frac{\partial}{\partial y} \left( k \frac{\partial T}{\partial y} \right) + \frac{\partial}{\partial z} \left( k \frac{\partial T}{\partial z} \right) + \dot{Q}_v''' \quad 7-1$$

where  $k$ ,  $\rho$  and  $c$  denote the temperature-dependent thermal conductivity, density and specific heat capacity, respectively;  $\dot{Q}_v'''$  is the inherently generated heat; and  $t$  is the time variable.

To solve the governing differential equation initial condition and boundary condition needs to be specified. The initial condition is given by:

$$T(x, y, z, t)|_t = T_o(x, y, z) \quad 7-2$$

Where:  $T_o(x, y, z)$  is the ambient temperature of the test specimen.

The bottom flange and the sides of the girder were directly exposed to the pool fire. Thus, heat is exchanged between the fire and these surfaces through convection and radiation, which can be expressed using Robin boundary condition (Purkiss 2007):

$$\dot{h}_{net} = \alpha_c(\theta_g - \theta_m) + \varepsilon_m \varepsilon_f \sigma [(\theta_g + 273)^4 - (\theta_m + 273)^4] \quad 7-3$$

Where:  $\dot{h}_{net}$  is the net heat flux;  $\alpha_c$  is the convective heat transfer coefficient. Its value is 50 W/(m<sup>2</sup>. K) for hydrocarbon fire and 9 W/(m<sup>2</sup>. K) for unexposed surface (EN 1992-1-2 2002);  $\theta_g$  is the fire temperature;  $\theta_m$  is the surface temperature of the structural member;  $\sigma$  is the Stefan–Boltzmann constant and is equal to 5.67x10<sup>-8</sup> W/(m<sup>2</sup>. K<sup>4</sup>);  $\varepsilon_m$  and  $\varepsilon_f$  are the emissivity of the

exposed surfaces and the fire, respectively. As per the provision of EN 1992-1-2 2002),  $\varepsilon_m = 0.8$  and  $\varepsilon_f = 1.0$ .

The modeling involved defining the geometry, boundary condition, temperature dependent material properties, analysis methods and contact. The defined geometry is discretized into elements. Abaqus (2014) has an array of element types for modeling the heat transfer analysis. The concrete and the insulation were modeled using DC3D8 (eight-node solid) element. The mild reinforcements and the prestressing strands were modeled using DC1D2 (two-node link) element. The longitudinal and the transverse FRP were modeled using DS4 (shell) element. A tie constraint was used to tie the nodes of the reinforcement/prestressing strand to the nearby node of the concrete as well as to create the interaction between the FRP, girders and the fireproofing.

After completing the heat transfer analysis, the thermal elements were switched into stress element to conduct the mechanical analysis. All of the defined components were kept during the stress analysis except the insulation. The concrete was modeled using C3D8R (eight-node continuum element with reduced integration) element. The mild reinforcements and the prestressing strands were modeled using T3D2 (two-node link) element. The longitudinal and the transverse FRP were modeled using S4R (reduced integration shell) element.

The stress analysis considered both geometric and material nonlinearity. It was carried out in two steps. The first step involved applying the prestressing force of the strand, the self-weight of the girder and the HL-93 simulated live load at ambient temperature and let the deflection stabilize. In the second step, the nodal temperatures from the heat transfer analysis were imposed while keeping the load applied on the first step throughout the duration of the simulation.

A perfect bond between the FRP and the concrete as well as between the prestressing strand (also the reinforcement) and the concrete was assumed.

## 7.2 Material properties at elevated temperature

The FEM analysis requires providing the thermal and mechanical properties of the material as input data. The thermal properties include thermal conductivity and specific heat capacity. On the other hand, the mechanical properties include density, modulus of elasticity, Poisson's ratio, stress-strain relationships and thermal expansion. The material properties of concrete, prestressing strands and mild reinforcement were provided as per the provision of Eurocode 2 (2004) and Eurocode 3 (2005). Temperature-dependent properties of the FRP and the insulation were used from published literature.

The specific heat capacity and the thermal conductivity for the girder and the deck concrete are defined per Eurocode 2 (2004) as shown in Figure 7-9. The spike in the specific heat capacity between 100°C to 115°C is to take into account the evaporation of free water in the concrete. For the current study, the peak value of 2020KJ/(kg.K) was used assuming 3% moisture in the concrete. The density of concrete was provided as a constant value of 2400 kg/m<sup>3</sup>(150 pcf).

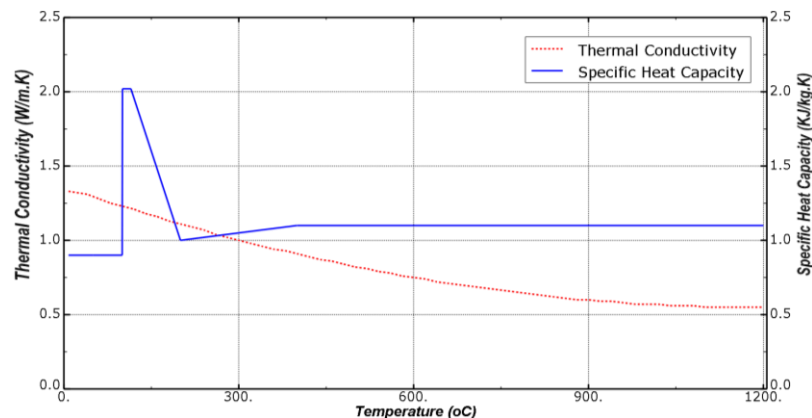


Figure 7-9 Specific heat capacity and thermal conductivity for concrete

The mechanical behavior of the concrete is modeled using the damage plasticity constitutive model available in Abaqus (2014). The model requires defining the parameters for yield surface, plastic flow rule and uniaxial stress-strain relationships. The yield function proposed by Lubliner et al. (1989) and later modified by Lee and Fenves (1998) was used by the software to define the behavior of concrete in multiaxial state of stress. The Drucker-Prager hyperbolic function is

employed to define the plastic flow rule. The constitutive model assumes tensile cracking and compressive crushing of concrete as a failure mechanism. The stress-strain diagram defined according to Eurocode 2(2004) is shown in Figure 7-10 and Figure 7-11 for the girder and the deck, respectively. The response is assumed to be linearly elastic until the compressive stress reaches its proportional limit, which is  $0.4f'_c$ . This is followed by strain hardening up to the peak compressive strength. The curve then descends which represents the softening behavior of concrete.

The tensile failure stress for the concrete was taken as 10% of the compressive strength. The tensile behavior of the concrete was represented using the tension-stiffening model proposed by Wahalathantri et al. (2011). The reduction in tensile strength at elevated temperature was determined using the relationship proposed by Eurocode 2 (2004). The variation of the tensile stress-strain for the girder and the deck concrete with temperature are shown in Figure 7-12 and Figure 7-13, respectively.

The Poisson's ratio of concrete was defined according to Gao et al. (2013). Its value was taken as 0.20 at 20°C and remained constant until 150°C. It then decreased linearly to 0.1 at 400°C and further decreased linearly down to zero at 1200°C.

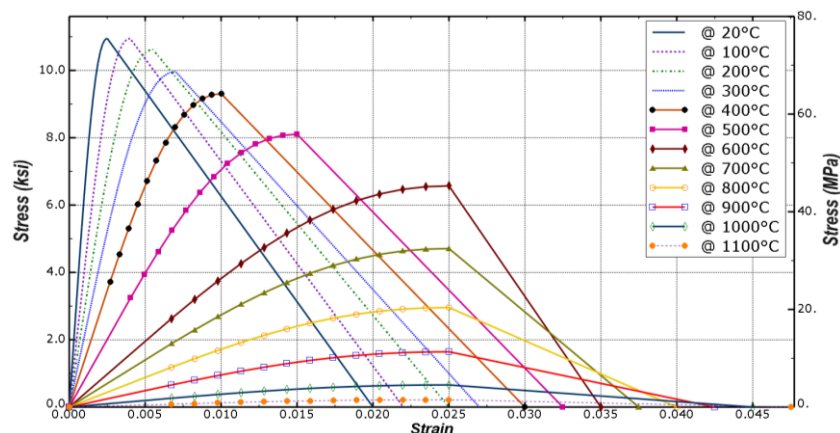


Figure 7-10 Variation of compressive stress-strain diagram with temperature for the girder concrete

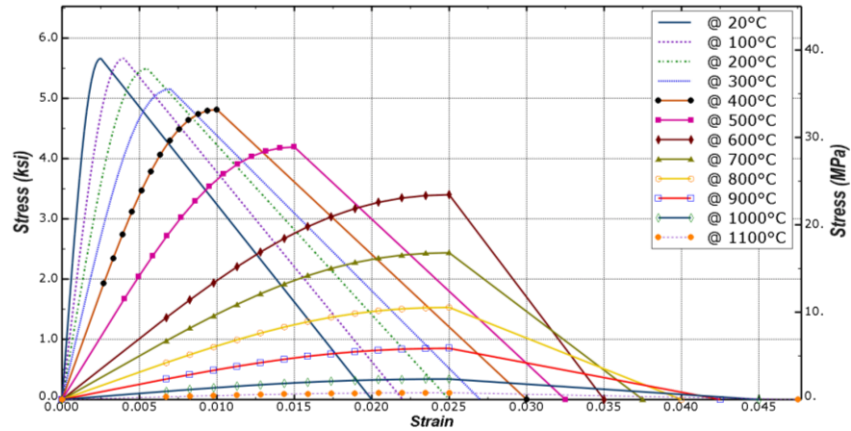


Figure 7-11 Variation of compressive stress-strain diagram with temperature for the deck concrete

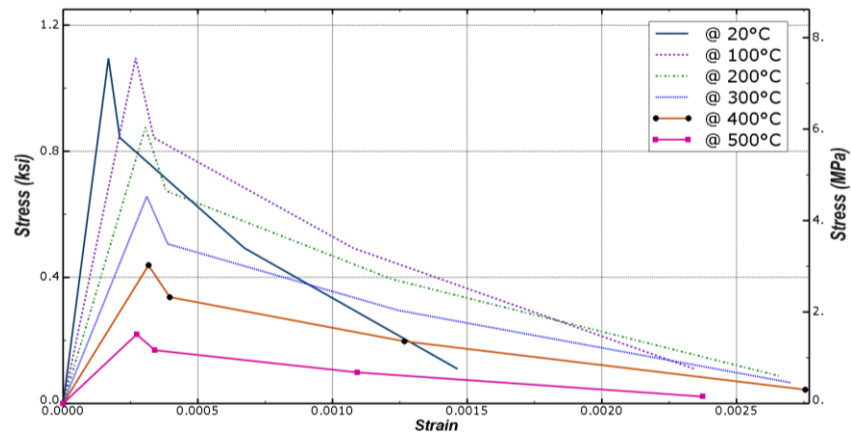


Figure 7-12 Variation of tensile stress-strain diagram with temperature for the girder concrete

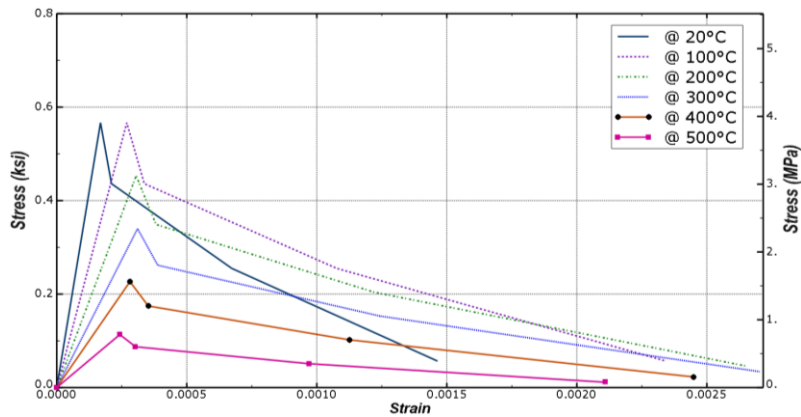


Figure 7-13 Variation of tensile stress-strain diagram with temperature for the deck concrete

The coefficient of thermal expansion of concrete was defined per the provision of Eurocode 2 (2004) as shown in Figure 2-19. The current model did not take into consideration concrete spalling since there is no clear modeling guideline.

The thermal conductivity, specific heat capacity, and coefficient of thermal expansion for the prestressing steel and mild reinforcement were defined according to the provision shown in Figure 2-22, Figure 2-23 and Figure 2-29, respectively. The tensile stress-strain variation of prestressing strands and mild reinforcements with temperature defined according to the provision outlined in Eurocode 2 (2004) are shown in Figure 7-14 and Figure 7-15. It is observed from both figures that the curves are linear-elastic up to the proportional limit, followed by a non-linear trend till yielding which is followed by yield plateau (Eurocode ignores strain hardening) and finally a softening branch.

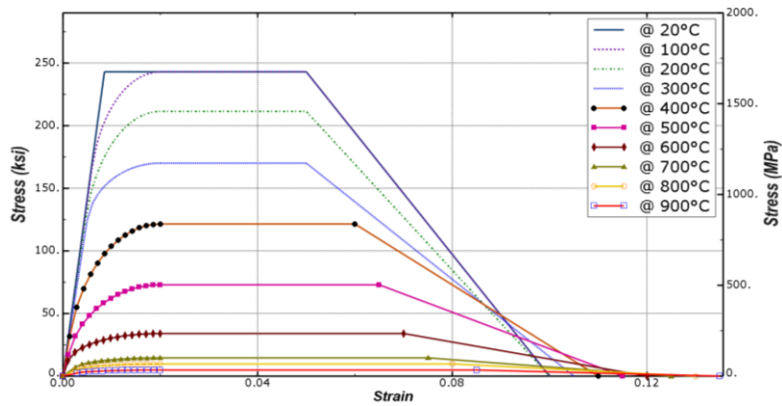


Figure 7-14 Variation of tensile stress-strain diagram with temperature for prestressing steel

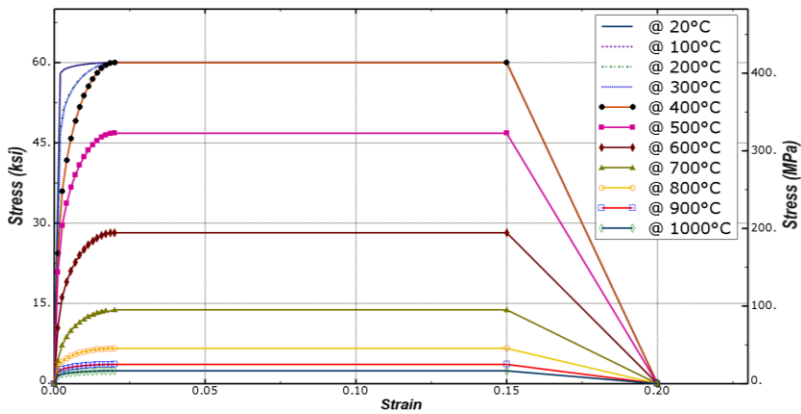


Figure 7-15 Variation of tensile stress-strain diagram with temperature for mild reinforcement

There is no reliable temperature dependent thermal properties for Sikacrete-213F. Similar numerical studies on the performance of Sikacrete-213F insulated RC members used the



properties of Tyfo VG insulation (Cree et al. 2012). Since both are known to have similar material composition. The results of their research depicted a good agreement between the numerical model prediction and the experiment. Thus, the specific heat capacity and thermal conductivity of VG insulation shown Figure 7-16 is also used for the current study.

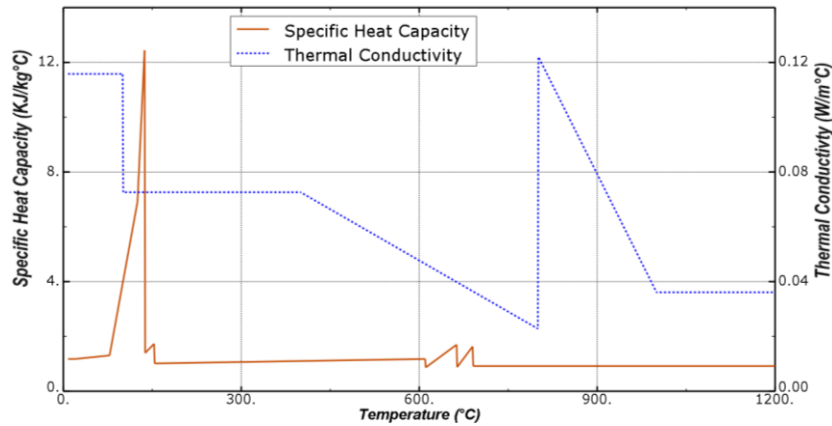


Figure 7-16 Thermal Properties of VG insulation (Bisby 2003)

The thermal conductivity and the specific heat capacity of the FRP is defined using the relationship developed by Griffis et al. (1981) as shown in Figure 2-8. Its variation of modulus of elasticity with temperature is defined using the relationship developed by Bisby (2003). The coefficient of thermal expansion is defined as  $0.3 \times 10^{-6} / ^\circ\text{C}$  (Klamer 2006).

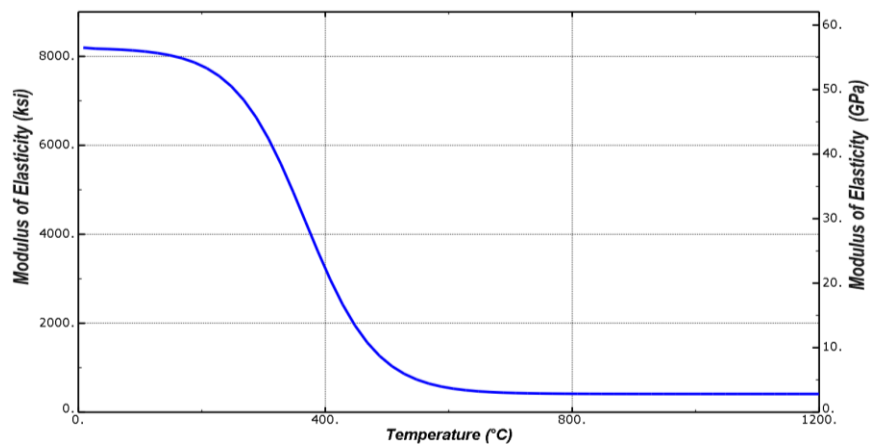


Figure 7-17 Variation of modulus of elasticity of FRP with temperature

### 7.3 Results and discussion

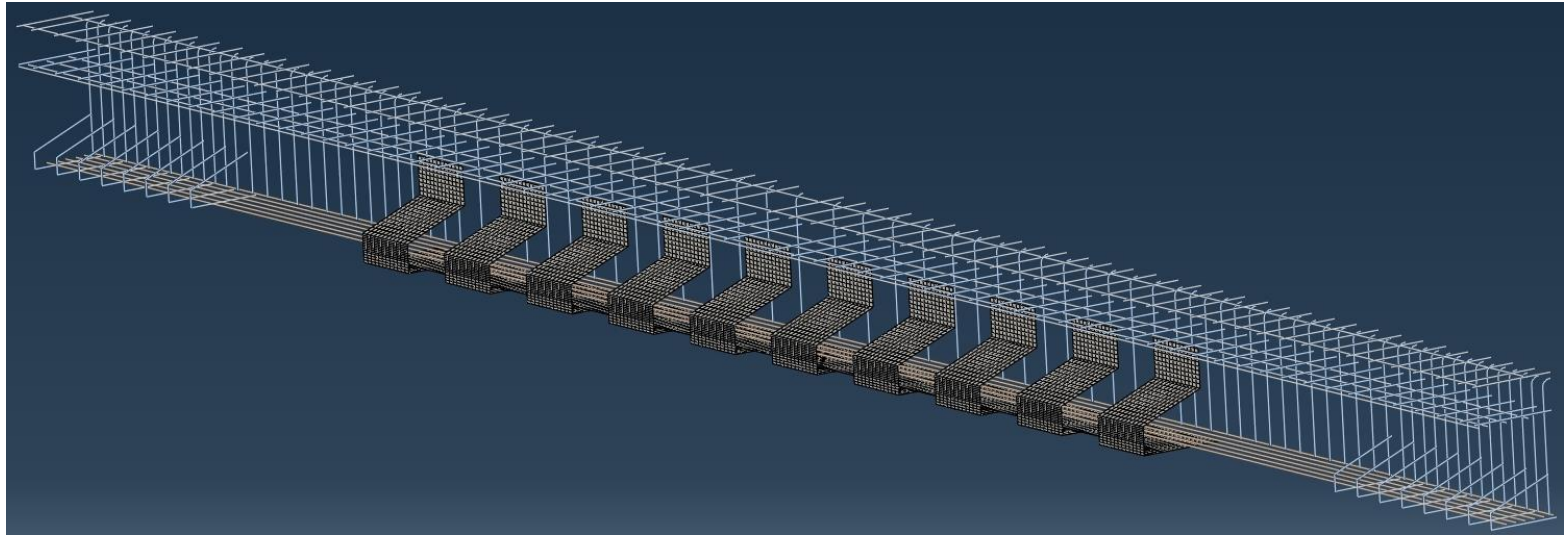
Figure 7-18 shows the FEM model that incorporate concrete, FRP, mild reinforcement, prestressing strand and insulation material.

As it can be observed from Figure 7-19; with increase in fire exposure time, the temperature progressed through the cross-section. Figure 7-20 compare the experimental result and the numerical prediction at different locations in the cross-sections of the girder. All the curves from the numerical prediction are smooth, unlike the curves from the fire experiment. This is attributed to the simplified and averaged temperature versus time curve applied as a boundary condition for the numerical model.

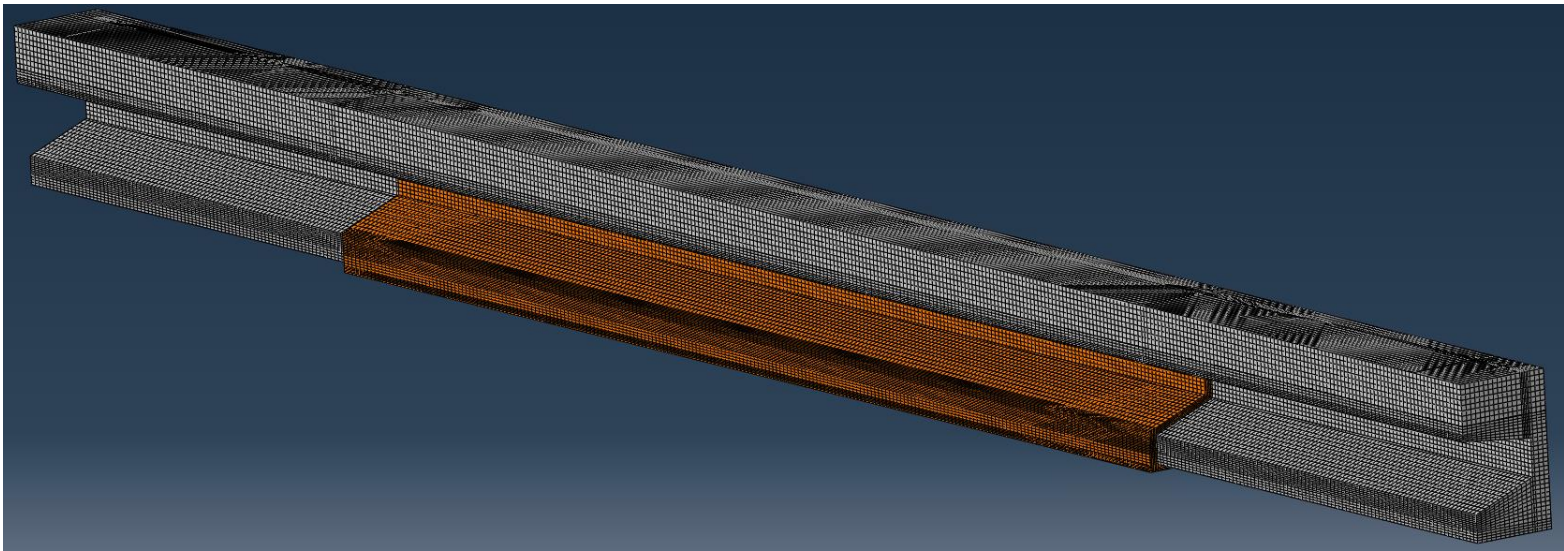
Figure 7-20 (a) shows the temperature at the FRP-concrete interface. As it was observed from the result of the fire experiment, the numerical model also predicted that the glass transition temperature is not exceeded during fire exposure. It is also seen that the measured and the predicted temperature are fairly in close agreement.

The temperature comparison at the insulation-FRP interface is shown in Figure 7-20 (b). Both the measured temperature and the numerical prediction were in good agreement for the first 4 minutes only. After that the measured temperature spikes due to the ingress of smoke through the cracks of the insulation (Figure 5-27). Similar kind of trend is also observed on the temperature of the prestressing strand shown in Figure 7-20 (c), which could also be attributed to the same reason.

Figure 7-20 (d) and (e) depicts the temperature at mid-height of the web and the deck-girder interface, respectively. Both plots show a close agreement between the measured and the numerically predicted temperature. As it is observed from the fire test result, the numerically predicted temperature at the deck-girder interface is also very low to compromise the composite action between the two.

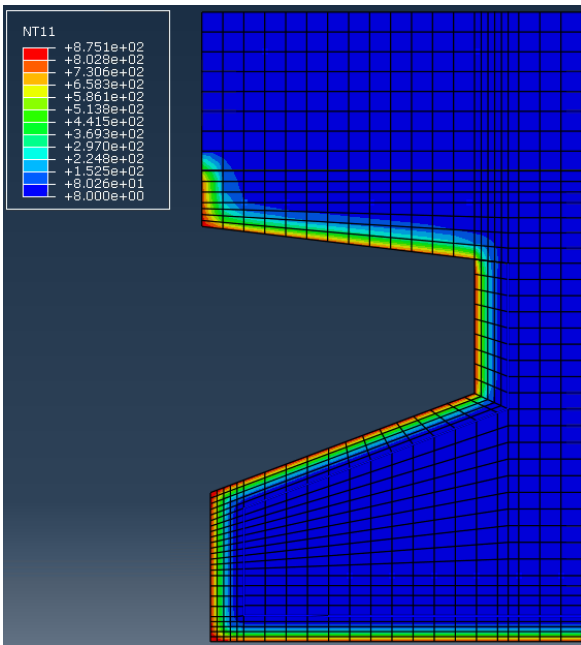


(a) Reinforcements cage and CFRP

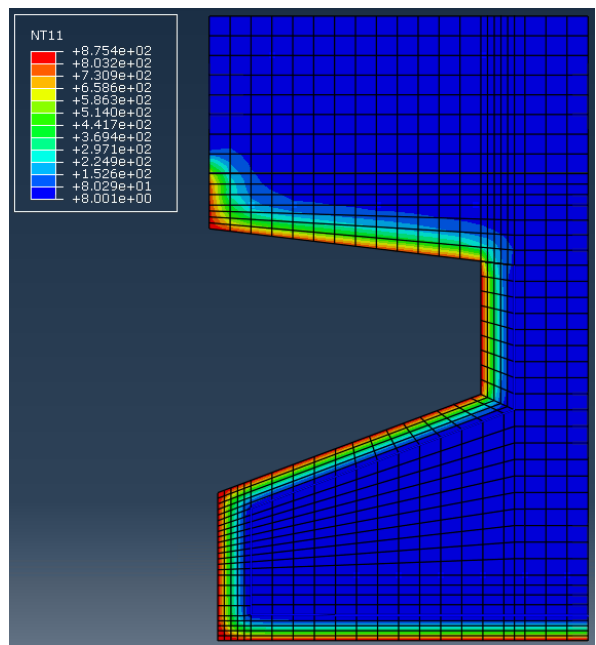


(b) Insulation, deck and girder

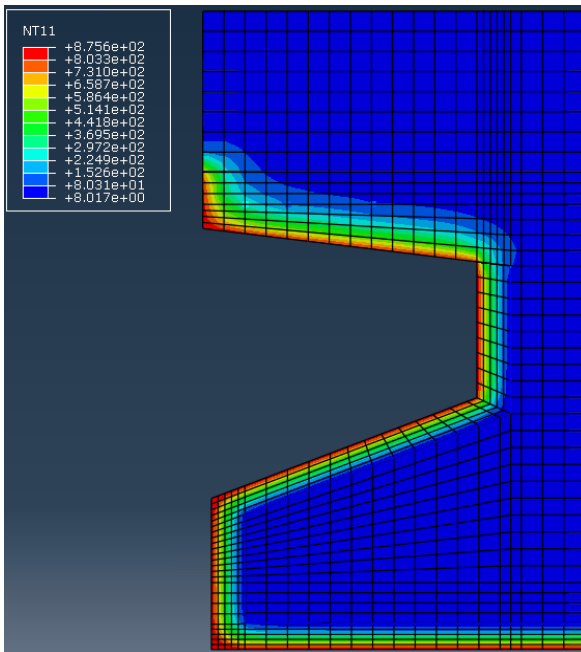
Figure 7-18 FEM Model



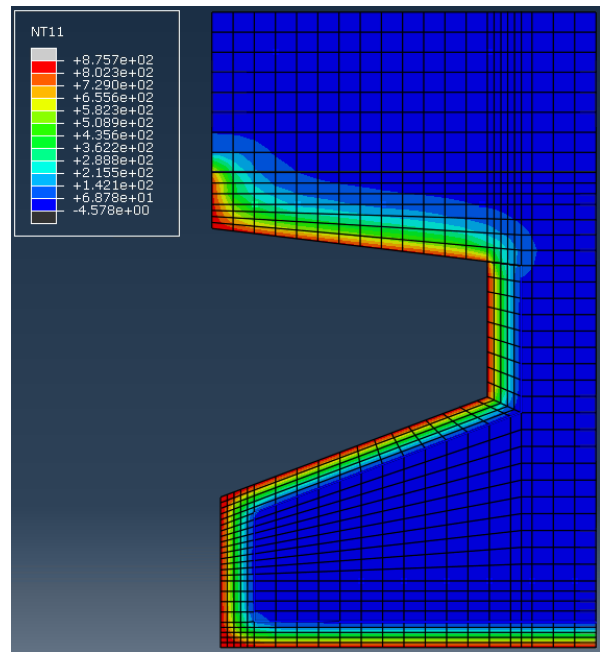
(a)



(b)

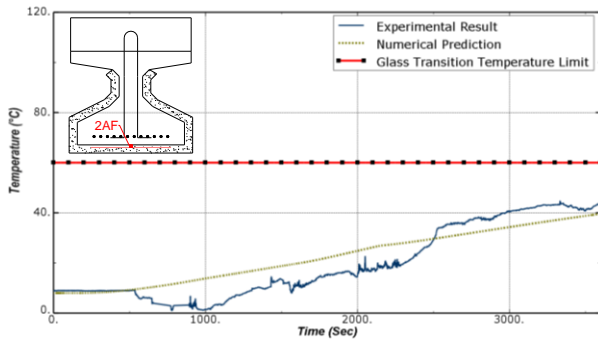


(c)

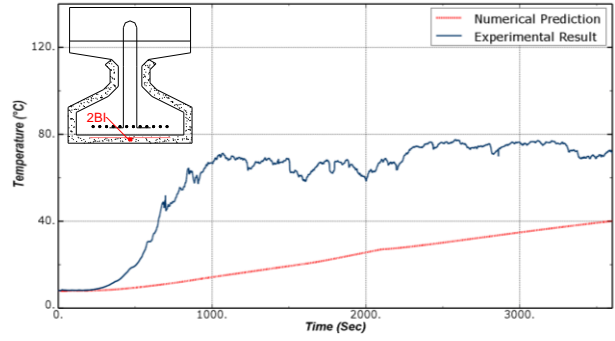


(d)

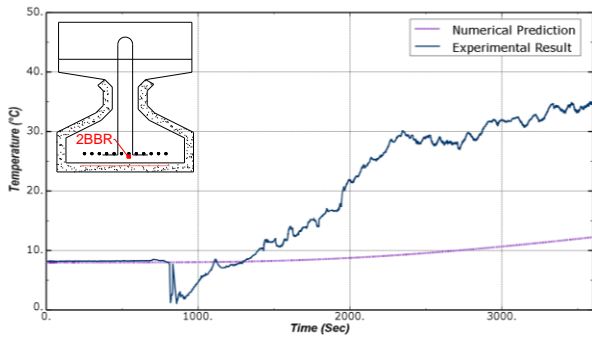
Figure 7-19 Temperature distributions over the mid-span cross-section: a)  $t=15$  min, (b)  $t=30$  min, (c)  $t=45$  min, (d)  $t=60$  min



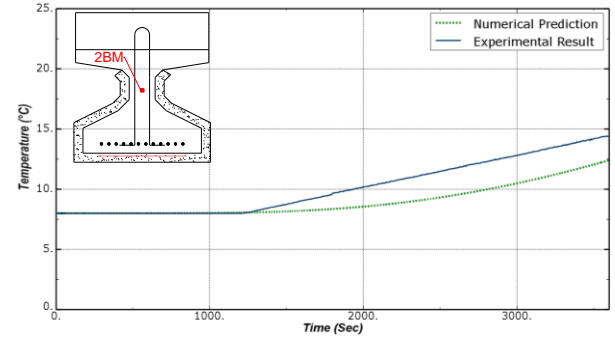
(a)



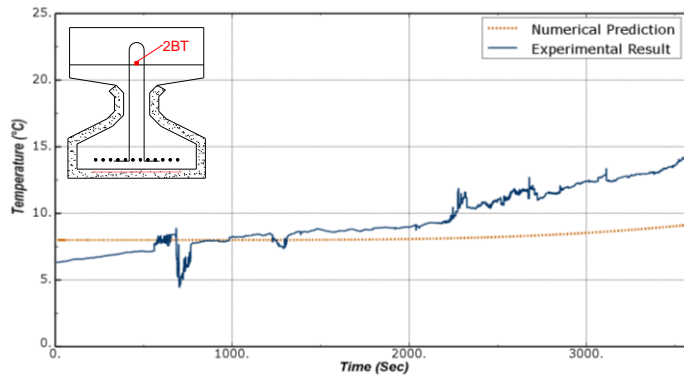
(b)



(c)



(d)



(e)

Figure 7-20 Numerical prediction versus experimental result for Girder-2: (a)FRP-concrete interface; (b) Insulation-FRP interface; (c) prestressing strand; (d) mid-height of the web of the girder; (e) deck-girder interface.

## Chapter 8

### CONCLUSIONS AND RECOMMENDATIONS

Fire is the least studied extreme load hazard on bridges compared to earthquake, flood, blast and collision. The current study is conducted with the aim of bridging this knowledge gap on the study of bridges in general and FRP- strengthened bridge girders in particular against fire hazard. To accomplish this; the research was conducted in three different phases. The first phase involved building a full-scale bridge and subjecting it to combined hydrocarbon pool fire and simulated AASHTO HL-93 live load. The superstructure of the tested bridge comprised of three Texas standard girders, precast deck panels, and cast-in-place deck. One girder was wrapped with carbon fiber reinforced polymer (CFRP), another with CFRP and sprayed with fire proofing and the third was a control girder without CFRP or fire proofing. In the second phase, the girders were saw-cut, transported to CELAB and tested for flexure using three-point loading protocol to determine their residual strength. In the third phase, a numerical scheme was developed to verify the results of the fire experiment. In the following subsections, the summary of the findings of the current research and recommendations for future studies are presented.

#### 8.1 Summary of Findings and Conclusions

One of the challenges of conducting open-pool fire experiment is the lack of specifications and standard. The current study was instrumental in setting benchmarks on the various consideration while conducting similar studies. These include but not limited to member size determination, fire load determination, live load protocol of the test bridge, determination of safe standing distance and data collection. As a pioneer study, the current research paved the way in understanding the response of bridges to hydrocarbon pool fire.

During the first phase of the research study, the test bridge was subjected to fire from 1140 gallons of E-III fuel. The fire generated a temperature as high as 1131°C. A continuous popcorn like explosion and an intermittent loud explosion were heard throughout the test from the spalling

of concrete. The prevalent wind caused most of the fire to be concentrated on Girder-1 and Girder-2.

Girder-1 was the most severely damaged girder compared to Girder-2 and Girder-3. It lost approximately 25 % its concrete. The degree of spalling was high since the girders were made of high strength concrete. It is known that high strength concrete is more prone to spalling compared to normal strength concrete due to their low permeability and low water-cement ratio. Visual color inspection of the spalled big chunks of concrete revealed that the most severe spalling occurred at the beginning of the test. This could be attributed to thermal shock. The spalling of the concrete resulted in exposing the prestressing strand and the mild reinforcements. This in turn caused the breaking of two of the strands and the weakening in the strength of the remaining prestressing steel and mild reinforcement. The glass transition temperature of the CFRP was exceeded early on the test, at a time of 41 seconds after the start of the fire. The CFRP was then observed debonding from the concrete surface and falling on the ground at approximately 6 minutes into the test.

Even though Girder-2 experienced the same intensity of fire as Girder-1, it sustained less damage. This is mainly attributed to the protection provided by the proposed insulation system. The insulation covered 42 % of the fire-exposed surface area of the girder. The temperature at the FRP-concrete interface was well below the glass transition temperature during and after the fire test, which indicated an intact bond between the two. The insulation not only protected the FRP system but it also provided protection for the concrete, prestressing strand and mild reinforcement. Outside the area where there was no insulation, moderate level of spalling and six exposed prestressing strands were observed. No spalled or separated insulation were seen. However, small cracks which were observed before the fire showed an increase in length and width after the fire. This was due to thermally induced shrinkage.

Girder-3 was subjected to the least amount of fire compared to Girder-1 and Girder-2. This is mainly attributed to the prevalent wind during the fire test. Minor spalling, breaking of one prestressing strand and exposing of the top mild reinforcements were observed.

The structural response of each girder was also evaluated by comparing their displacement response. The deflection was calculated for each girder by taking the difference in elevation before and after the fire. The largest mid-span deflection was observed in Girder-1 as expected. Even though Girder-2 was subjected to the same intensity of fire as Girder-1, it experienced less deflection compared to Girder-1. This is mainly due to the beneficial effect of the insulation material in protecting the FRP from debonding, the concrete from spalling and in slowing down the rise in temperature of prestressing strands. The deflection of Girder-3 is the smallest.

Visual inspection and rebound hammer test were employed to understand the extent of the fire sustained by each girder in areas where there were no thermocouples in the vicinity. The results from the both non-destructive evaluation method showed a good agreement. Both techniques can be effectively employed in the forensic investigation of similar fire incidents.

The precast deck panels sustained the most severe spalling compared to cast-in-place deck. This was attributed to the fact that the former was made from high strength concrete, whereas the latter from normal strength concrete. Despite the damage on the bottom, the top of the deck didn't show any sign of distress or crack. It is also observed that the temperature at the deck-girder interface was very low to adversely affect the composite action between the two.

During the second phase of the research, the girders were tested for flexure to determine their residual strength. The test revealed that the ultimate load carried by Girder-1 was 399.10 kN (89.70 kips). The fire caused a 60 % reduction in ultimate capacity. This is a significant loss in strength, which defied the myth fire don't cause severe damage to concrete bridges.

Girder-2 failed at an ultimate load of 994.80 kN (223.63 kips), which corresponds to an applied moment of 2387.7 kN-m (1761.1 kip-ft). It's calculated nominal flexural capacity per the



provision of ACI440 (2008) was 2412.7 kN-m (1779.5 kip-ft). Comparing the theoretically predicted and the actual test value, it is observed that the fire didn't cause any reduction in capacity due to the presence of the insulation material. From these observations, it can be concluded that with properly designed insulation system the full contribution of the FRP towards the flexural strength of girders can be considered. It is also recommended to use insulation material over the FRP on bridges which are deemed to be at high risk of fire.

Girder-3 reached an ultimate load of 804.8 kN (180.8 kips), which corresponds to an applied moment of 1930.4 kN-m (1423.8 kip-ft). The calculated nominal flexural capacity per the provision of AASHTO (2014), considering the remaining strands, was 1875.95 kN-m (1383.6 kip-ft). There is only a 2.8% deviation between the theoretically predicted and the actual test result, which confirms the severity of the fire was less on Girder- 3.

A numerical modeling scheme was also developed with the goal of verifying the capability of currently used numerical method to model the response of bridges to a pool fire. The scheme proposed using the relationship between compressive strength reductions factors and temperature to develop the temperature versus time curve for the fire boundary condition. The numerically predicted response agreed well with the experimental result. The proposed method can be used in forensic investigation of similar bridge fire incidents.

## 8.2 Future Research

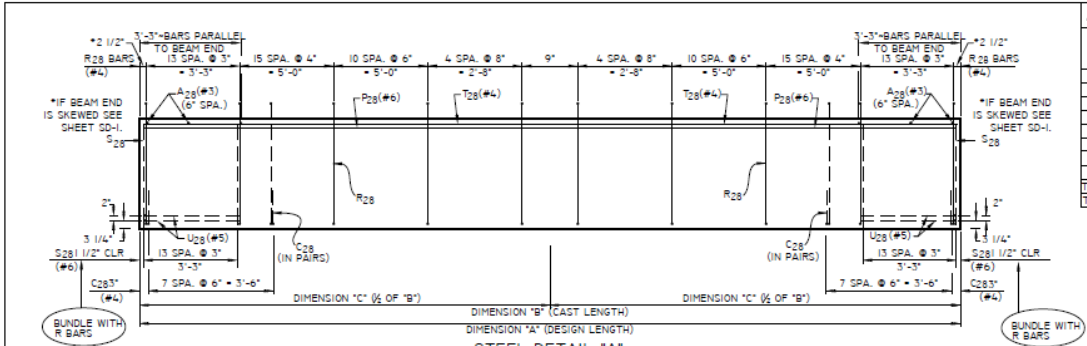
The following are the recommendations for future research work:

- The long-term performance of the insulation material used in the current study is unknown. Thus, its durability needs to be investigated by employing methods like accelerated aging.
- Cracks were observed on the surface of the insulation few days after installation. This was due to a lack of proper curing guidelines. Hence, it is recommended to

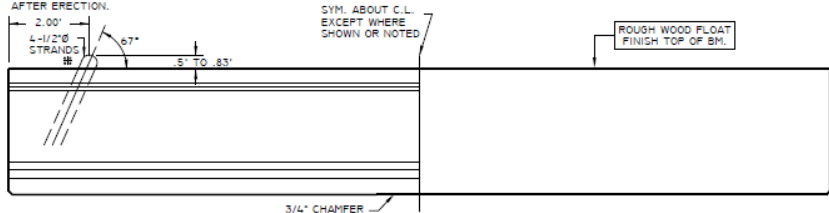
develop a curing guideline that applies to outdoor structures and various weather conditions.

- The numerical model developed in the current study didn't incorporate a fire model. This was due to the lack of fuel properties. It is suggested to determine the fuel parameters and verify the results of the experiment. Once the results are verified, a parametric study can be carried out to investigate the various factors that affect the performance of FRP-strengthened bridge girders. These parameters include fire size, fire location, types of fuels, vertical clearance above the fire, the size of bridge, insulation thickness, insulation layout, etc.
- The current numerical model didn't incorporate spalling of concrete since there is no specific guideline. It is suggested to develop a more robust numerical scheme that considers spalling.
- It is observed from the current research that prestressed concrete girders and precast prestressed concrete deck panels are prone to a high degree of spalling. It is suggested to find ways to mitigate this serious problem.
- One of the challenges conducting hydrocarbon pool fire experiment is a lack of a standard. It is suggested to develop one that can be used for further studies.
- One of the concerns of industry practitioners on applying insulation over the FRP is access for periodic inspection. To curb this challenge, it is recommended to develop a non-destructive testing protocol to evaluate the CFRP-concrete bond without removing the fireproofing.
- It is evident that all bridges don't have the same level of risk for hydrocarbon pool fire. Thus, all of them may not need to be equipped with some form of fire protection. It is suggested to conduct a statistical study that categorizes bridges into different risk level and recommended level of fire protection.

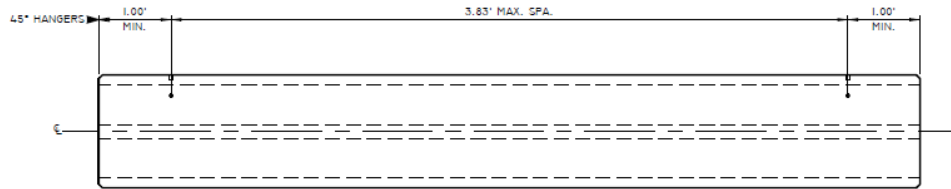
**Appendix A:**  
**Shop drawings for girders**



# LIFT DETAILS SHOWN ARE USUAL, BUT MAY BE CHANGED BY FABRICATOR TO FIT JOB REQUIREMENT. CUT TO 1/2" AFTER ERECTION.



**BEAM ELEVATION**  
(NOT TO SCALE)



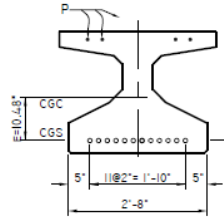
**PLAN DETAIL**  
(NOT TO SCALE)

MARKED END

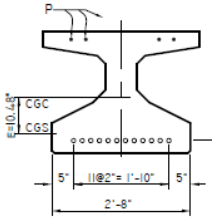
- GENERAL NOTES:**
- FOR DETAILS OF EMBEDDED ITEMS SEE SHEET H-1.
  - FABRICATOR REQUEST TO USE WELDED WIRE FABRIC TO REPLACE ALL OR SOME OF BARS A,C,R (EXCLUDING ADDITIONAL "R" BARS) AND ANY COMBINATION OF W.W.F. DETAILS, REF. TO SHT. WWF-1 & WWF-3.
  - FOR REINFORCING SEE STEEL DETAIL "A" THIS SHEET AND STANDARD END DETAIL SHEET SD-1.

△ BEAM SCHEDULE & DIMENSIONS				OPTIONAL DESIGN SHEET NO.	
BEAM MARK	NO. REQ'D	BEAM LENGTHS (ALONG CENTERLINE OF BM.)			
		A	B	C	
TGI-1	1	33.00'	33.03'	16.515'	1
TOT. BMC	1				
TOT. LINEAR FT.		33.00'			

△ REINFORCING STEEL SCHEDULE					
BAR	QUANTITY PER GIRDER	TOTAL QUANTITY	SKEW ANGLE	SIZE	LENGTH
A28	67	67		#3	2'-9"
C28	32	32		#4	3'-10"
R28	92	92		#4	6'-2"
S28	52	52		#6	2'-0 1/2"
T28	4	4		#6	32'-9"
U28	4	4		#6	8'-1"
P28	4	4		#6	32'-0"
A28	X	X	X*	#3	SEE SHT. S-1
U28	X	X	X*	#3	SEE SHT. S-1
A28	X	X	X*	#3	SEE SHT. S-1
U28	X	X	X*	#3	SEE SHT. S-1
A28	X	X	X*	#3	SEE SHT. S-1



**C.L. SECTION VIEW**



**END VIEW**

**TX28 I2-0 LO-LAX**

STRAND PATTERN (LO-LAX STRANDS)	
NUMBER OF STRANDS:	I2 1/2" @ 270k @ 31.0k EA.
NUMBER OF STRAIGHT STRANDS:	I2
NUMBER OF DEFLECTED STRANDS:	N/A
INITIAL LOAD STRAIGHT STRANDS:	2000 LBS.
INITIAL LOAD DEFLECTED STRANDS:	2000 LBS.
CLASS OF CONCRETE:	H + 25% FLY ASH
CONCRETE RELEASE STRENGTH:	4000 PSI
CONCRETE DESIGN STRENGTH:	5000 PSI
UPLIFT AT HOLD-DOWN POINT:	N/A K

REV.	DATE	BY	DESCRIPTION
△	12-22-14	D.L.	PER REVIEWER'S COMMENTS

FOR ERECTION PLANS SEE SHEET #E-1  
**"TX28" EXTERIOR BEAM DETAIL**  
 △ TGI-1

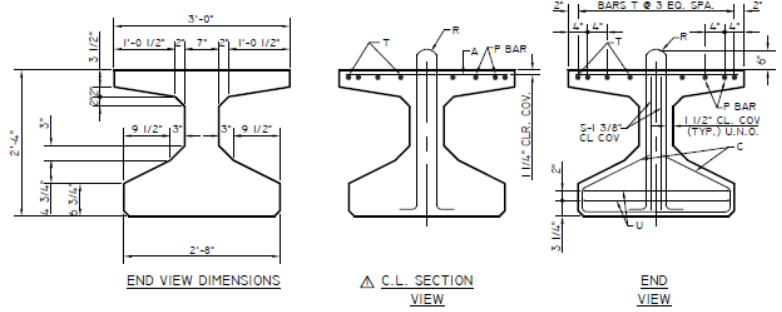
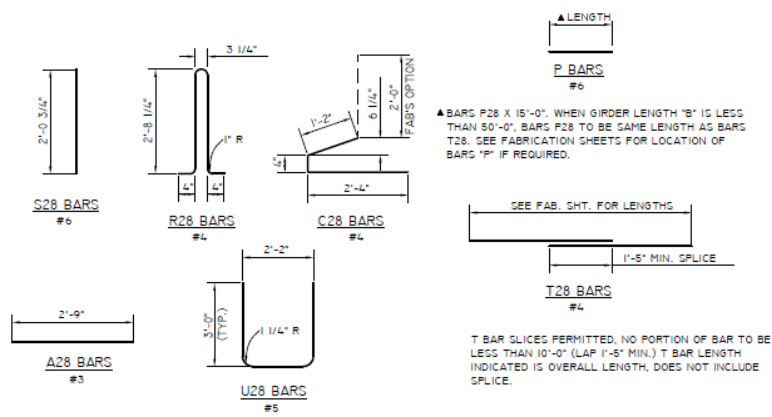
**TEXAS CONCRETE PARTNERS, L.P.**

VICTORIA, TEXAS P.O. BOX 1870 VICTORIA, TX 77902  
 361-873-9943 FAX 361-873-9889

ELM HOLT, TEXAS P.O. BOX 338 ELM HOLT, TX 76640  
 817-822-5331 FAX 817-822-1023

CUSTOMER UNIVERSITY OF TEXAS AT ARLINGTON  
 OWNER UNIVERSITY OF TEXAS AT ARLINGTON  
 ENGINEER UNIVERSITY OF TEXAS AT ARLINGTON  
 STRUCTURE UNIVERSITY OF TEXAS AT ARLINGTON  
 LOCATION UNIVERSITY OF TEXAS AT ARLINGTON  
 PROJECT N/A

DWG. D.L.  
 CHD B.C.  
 DATE 10/20/14  
 SHEET  
 JOB NO. 14-757



**GENERAL NOTES**

1. DIMENSIONS RELATING TO STRANDS ARE CENTER TO CENTER.
2. STRANDS MAY BE RECESSED 1/2" MAX. INTO END OF GIRDER.
3. GIRDER ENDS MAY BE FORMED WITH WOOD.
4. BOTTOM CORNERS OF ALL GIRDER FLANGES AND OUTSIDE CORNERS OF EXTERIOR GIRDER ENDS SHALL BE CHAMFERED 3/4" OR ROUNDED TO A 3/4" RADIUS. ALL VERTICAL EDGES ON ALL GIRDERS SHALL BE CHAMFERED 3/4".
5. GIRDER MARKS TO BE PLACED AS NOTED.
6. ALL DIMENSIONS MEASURED ALONG BOTTOM OF GIRDER AT C.L. UNLESS NOTED OTHERWISE.
7. USE CLASS H CONCRETE. CONCRETE TO HAVE A MINIMUM 25% FLY ASH.

**REINFORCING STEEL NOTES**

1. ALL DIMENSIONS ARE CENTER TO CENTER.
2. ALL STEEL TO BE A.S.T.M. A-615, GR. 60.
3. BARS A AND C MAY BE SUBSTITUTED WITH WWF AS SHOWN ON SHEETS WWF(1)-TX28 AND WWF(2)-TX28. BARS R MAY BE SUBSTITUTED WITH WWF SHOWN ON SHEETS WWF(1)-TX28, WWF(2)-TX28 AND WWF(3)-TX28. ALL OTHER REINFORCING BARS ARE TO BE CONVENTIONAL REINFORCING AS SHOWN. CONVENTIONAL REINFORCING AND WWF MAY BE USED IN ANY COMBINATION.

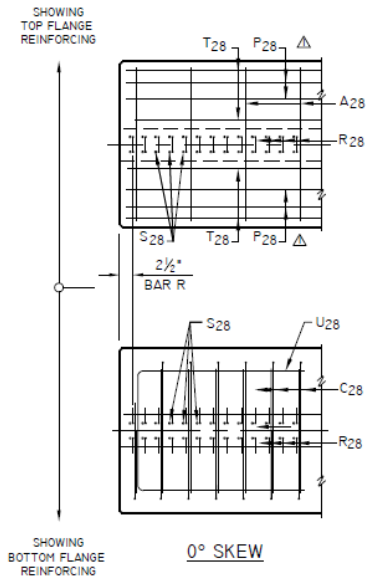
REV.	DATE	BY	DESCRIPTION
▲	12-22-14	D.L.	PER REVIEWER'S COMMENTS

**STANDARD SHEET**  
Tx28

**TEXAS CONCRETE PARTNERS, L.P.**

VICTORIA, TEXAS P.O. DRAWER 0176 VICTORIA, TX 77902 EL PASO, TEXAS P.O. BOX 308 EL PASO, TX 79960  
361-873-9148 FAX 361-878-8889 284-822-0351 FAX 284-822-0228

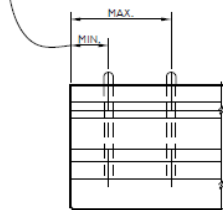
CUSTOMER	UNIVERSITY OF TEXAS AT ARLINGTON	DWL	D.L.
OWNER	UNIVERSITY OF TEXAS AT ARLINGTON	CHD	B.C.
ENGINEER	UNIVERSITY OF TEXAS AT ARLINGTON		DATE 10/05/2016
STRUCTURE	UNIVERSITY OF TEXAS AT ARLINGTON		SHEET
LOCATION	UNIVERSITY OF TEXAS AT ARLINGTON		JOB NO. 14-757
PROJECT	N/A		



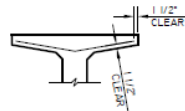
**TYPICAL GIRDER END REINFORCING DETAILS**

1. THE REINFORCING PATTERN SHOWN IS A GUIDE TO THE PLACEMENT OF REINFORCING AT GIRDER END. SEE FABRICATION SHEETS FOR ACTUAL GIRDER SKEW.
2. PLACE BARS S AS CLOSE TO GIRDER END AS COVER REQUIREMENTS PERMIT, WHICH MAY PREVENT THEM TO BE BUNDLED WITH BARS R.

**GIRDER ERECTION NOTE:**  
 LIFTING LOOP(S) MAY BE LOCATED ANYWHERE WITHIN THE MINIMUM AND MAXIMUM DISTANCE FROM THE END OF THE GIRDER AS DETAILED. THE USE OF ONE OR MORE LIFTING LOOPS WITHIN THE AREA MAY BE USED AT FABRICATOR'S OPTION.



**GIRDER ERECTION - LIFTING LOOPS**



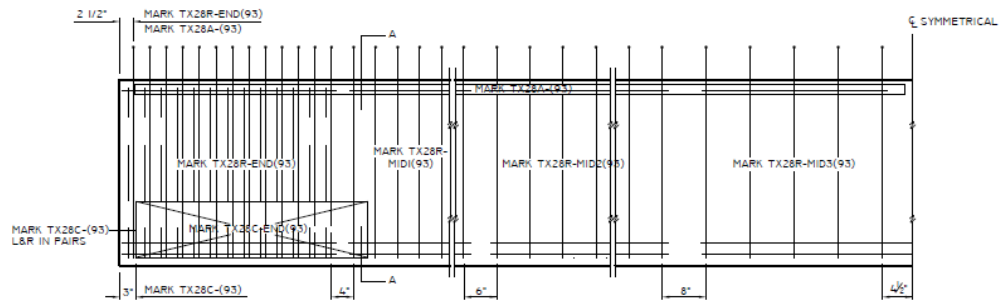
**OPTIONAL TOP FLANGE REINFORCING DETAIL**

TO CONTROL TOP FLANGE CRACKING THAT MAY OCCUR DURING FORM REMOVAL, ADDITIONAL TOP FLANGE REINFORCING MAY BE PLACED AS SHOWN IN GIRDER ENDS AT THE FABRICATOR'S OPTION.

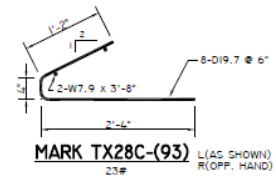
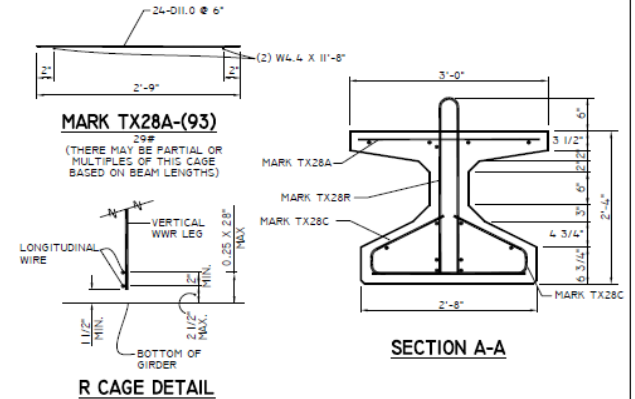
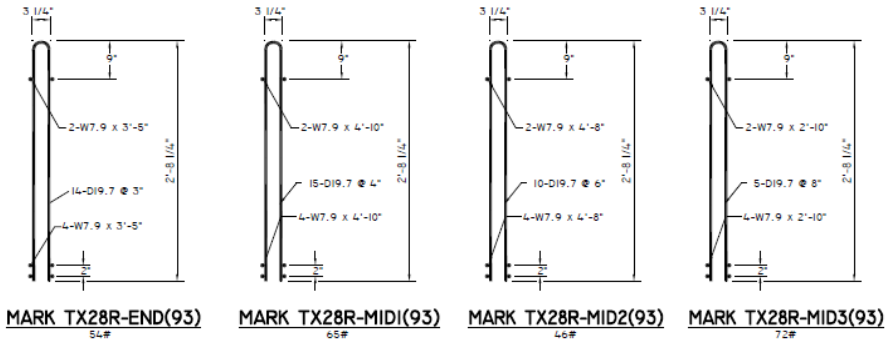
REV.	DATE	BY	DESCRIPTION
Δ	12-22-14	D.L.	PER REVIEWER'S COMMENTS

<b>STANDARD DETAIL SHEET</b>	
Tx28	
<small>           VICTORIA, TEXAS      EL PASO, TEXAS            P.O. DRAWING 010    VICTORIA, TX 77902    P.O. BOX 308    EL PASO, TX 79640            361-873-9145    FAX 361-878-8889    284-822-0281    FAX 284-822-0288         </small>	
<b>CUSTOMER</b>	UNIVERSITY OF TEXAS AT ARLINGTON <b>DBL</b> D.L.
<b>OWNER</b>	UNIVERSITY OF TEXAS AT ARLINGTON <b>DND</b> B.C.
<b>ENGINEER</b>	UNIVERSITY OF TEXAS AT ARLINGTON
<b>STRUCTURE</b>	UNIVERSITY OF TEXAS AT ARLINGTON
<b>LOCATION</b>	UNIVERSITY OF TEXAS AT ARLINGTON
<b>PROJECT</b>	N/A
	<small>           DATE 10/05/2014            SHEET 001            JOB NO. 14-757         </small>



**△ TYPICAL BEAM ELEVATION-WWF PLACEMENT**  
(EXTERIOR BEAM ONLY)



EQUAL AREA & STRENGTH WWR REPLACEMENT FOR "R", "C" & "A" BARS  
**GENERAL NOTES**

- DIMENSIONS RELATING TO WELDED WIRE FABRIC ARE CENTER TO CENTER OF WIRES. (U.N.O.)
- TYING OF WELDED WIRE FABRIC ASSEMBLY WILL BE SUFFICIENT TO PROVIDE RIGID CAGE ONLY. TYING OF ALL STRAND AND WIRE INTERSECTIONS NOT REQUIRED.
- LONGITUDINAL SPLICE IS NOT REQUIRED FOR WELDED WIRE FABRIC. DO NOT EXCEED TYPICAL SPACINGS OF TRANSVERSE WIRES.
- WELDED WIRE FABRIC CONFORMS TO ASTM A 185 OR A 497, 70 KSI WIRE.
- THE WWF SHOWN MAY BE USED IN LIEU OF THE CONVENTIONAL REINFORCING BARS A,C, OR R.
- W7.9 WIRES ON TX28C CAGE MAY BE CUT AND CAGE REARRANGED TO MISS ANCHOR OR DIAPHRAGM HOLES IF REQUIRED.
- BOTTOM W7.9 WIRES ON TX28R CAGES ARE NOT TO BE CUT, THEY REPLACE THE BENT LEGG OF STANDARD "R" BARS.
- NO CUTTING OF D11.0 OR D19.7 ALLOWED ON ANY CAGE.
- S28 TO BE INSTALLED IN ALL END CONDITIONS PER CONTRACT DRAWINGS.

REV.	DATE	BY	DESCRIPTION
△	12-22-14	D.L.	PER REVIEWER'S COMMENTS

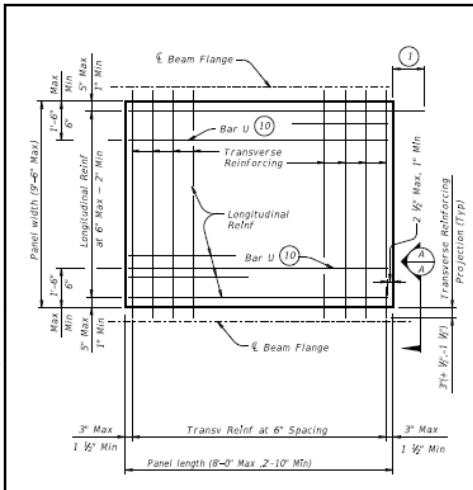
**"TX28" BEAMS-(ENGLISH)--HL93 LOADING**  
**WELDED WIRE FABRIC**  
**(EXTERIOR BEAMS)**

<b>TEXAS CONCRETE PARTNERS, L.P.</b>	
VICTORIA, TEXAS P.O. DRAWER 1819 VICTORIA, TX 77902 361-973-9143 FAX 361-978-5889	ELM HOUT, TEXAS P.O. BOX 338 ELM HOUT, TX 76640 254-822-0291 FAX 254-822-1028
CUSTOMER UNIVERSITY OF TEXAS AT ARLINGTON	DRN D.L.
OWNER UNIVERSITY OF TEXAS AT ARLINGTON	CHD B.C.
ENGINEER UNIVERSITY OF TEXAS AT ARLINGTON	DATE 12/16/2014
STRUCTURE UNIVERSITY OF TEXAS AT ARLINGTON	SHEET
LOCATION UNIVERSITY OF TEXAS AT ARLINGTON	WFF-1
PROJECT N/A	JOB NO. 14-757

**Appendix B:**

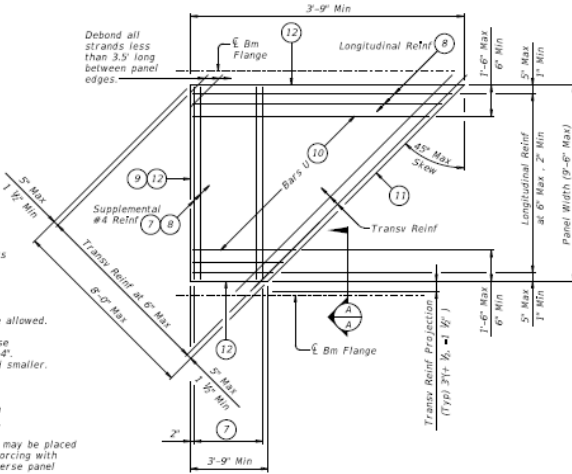
**Prestressed concrete panel fabrication details**



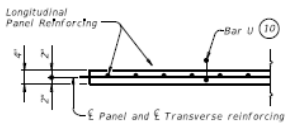


**TYPICAL NON-SKEWED PANEL PLAN**

- 1 At connection with cast-in-place slab, extend longitudinal panel reinforcement 1'-0" (+2'-0") past panel end. Alternatively, provide (#3) x 2'-0" dowels at 6" Max Spacing and extend dowels 1'-0" past panel end.
- 2 Four loops required per panel.  $\frac{3}{8}$ " or  $\frac{1}{2}$ " strands may be used.
- 3 Normal dimensions must be used on spans with parallel beams. Maximum and Minimum dimensions apply only to spans with flared beams.
- 4 See Normal Grading Detail on PCP standard for lap requirements and bedding strip dimensions. Some laps shown in tables cannot utilize all bedding strip widths.
- 5 One Splice allowed per panel. No more than two sheets of WWR are allowed.
- 6 Provide (#4) bars under transverse reinforcing, 10 Spacing at 4" = 2'-4". Omit for 5 degree (1:12) skew and smaller.
- 7 End Cover 2  $\frac{1}{2}$ " Max, 1" Min.
- 8 Recess strands on indicated panel edge in accordance with Item 424.
- 9 At the fabricator's option, Bars U may be placed parallel to transverse panel reinforcing with horizontal legs in plane of transverse panel reinforcing.
- 10 Use length of indicated panel edge as panel width for purpose of determining type of transverse reinforcing.
- 11 Timber form work permissible this edge.

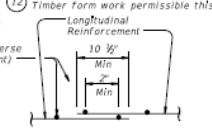


**TYPICAL SKEWED END PANEL PLAN**  
(Only to be used with details shown elsewhere in the plans.)

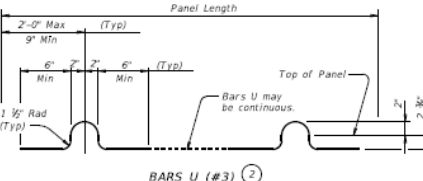


**SECTION A-A**

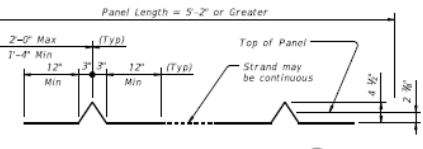
(Not Showing supplemental #4 bars for Skewed End Panels.)



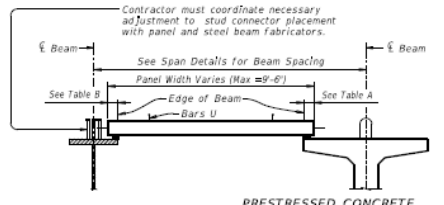
**WELDED WIRE REINFORCEMENT (WWR) SPLICE DETAIL**



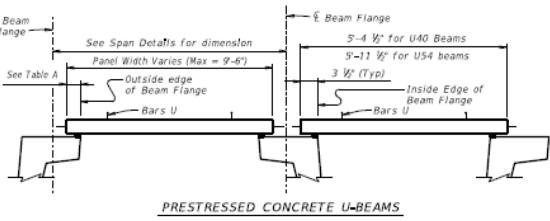
**BARS U (#3)**



**OPTIONAL STRAND FOR BARS U**



**STEEL BEAMS**  
**PRESTRESSED CONCRETE BEAMS OR GIRDERS**



**PRESTRESSED CONCRETE U-BEAMS**

**TYPICAL SECTIONS FOR DETERMINING PANEL WIDTH**

TABLE A (4)				TABLE B (4)			
Beam Type	Normal (In.)	Min (In.)	Max (In.)	Top Flange Width	Normal (In.)	Min (In.)	Max (In.)
A	3	2 1/2	3 1/2	11" to 12"	2 1/2	2 1/2	2 1/2
B	3	2 1/2	3 1/2	Over 12" to 15"	3 1/2	3	3 1/2
C	4	3	4 1/2	Over 15" to 18"	4	3	4 1/2
IV	6	4	7 1/2	Over 18"	5	3 1/2	6 1/2
VI	6 1/2	4 1/2	8 1/2				
U40 - 54	5 1/2	5 1/2	7				
TX28-70	6	4	7 1/2				
XB20 - 40	4	3	4 1/2				
YSB12 - 15	4	3	4 1/2				

**GENERAL NOTES:**  
Provide Class H concrete for panels. Release strength  $f'c = 3500$  psi. Minimum 28 day strength  $f'c = 5000$  psi.  
Do not use epoxy-coated reinforcing steel bar or strand in panels. Remove lube from top panel surface. Finish top of panel to a roughness between a No.6 and No.9 concrete surface profile, inclusive, as specified by the International Concrete Repair Institute (ICRI).  
Shop drawings for the fabrication of panels will not require the Engineer's approval if fabrication is in accordance with the details shown on this standard.  
A panel layout which identifies location of each panel must be developed by the Fabricator. Permanently mark each panel in accordance with the panel layout. A copy of the layout is to be provided to the Engineer.

**TRANSVERSE PANEL REINFORCEMENT:**  
For panel widths over 3', use  $\frac{3}{8}$ " or  $\frac{1}{2}$ " Dia (270k) prestressing strands with a tension of 14.4 kips per strand.  
For panel widths over 3'-6" up to and including 5', use  $\frac{3}{8}$ " or  $\frac{1}{2}$ " Dia (270k) prestressing strands with a tension of 14.4 kip per strand. Optionally, #4 Grade 60 reinforcing bars may be used in lieu of prestressed strands.  
For panel widths up to 3'-6", use #4 grade 60 reinforcing bars (prestressed strands alone are not allowed).  
Place transverse panel reinforcement at panel centerline and space at 6" Max.

**LONGITUDINAL PANEL REINFORCEMENT:**  
Any of the following options may be used for longitudinal panel reinforcement:  
1. (#3) Grade 60 reinforcing steel at 6" Max Spacing. No splices allowed.  
2.  $\frac{3}{8}$ " Dia prestressing strands at 4  $\frac{1}{2}$ " Max Spacing (unstressed). No splices allowed.  
3.  $\frac{3}{8}$ " Dia prestressing strands at 6" Max Spacing (unstressed). No splices allowed.  
4. Deformed Welded Wire Reinforcement (WWR) (ASTM A1064) providing 0.22 sq in per foot of panel width. Wires larger than D11 not permitted. Provide transverse wires to ensure proper handling of reinforcing. One splice per panel is allowed. See WWR Splice Detail.  
No combination of longitudinal reinforcing options in a panel is allowed. Place longitudinal panel reinforcement above or below transverse panel reinforcement. Must be placed above transverse panel reinforcement for skewed end panels with supplemental #4 reinforcement.

HL93 LOADING

Bridge Division Standard

**PRESTRESSED CONCRETE PANEL FABRICATION DETAILS**

**PCP-FAB**

PLAN	pcp3092.dgn	DATE	1/2007	BY	JFR	CHK	ALS
REV	1	DATE	January 2015	DATE		BY	
DESCRIPTION		DATE		COUNT		SHEET NO.	

**Appendix C:**  
**Material Properties at Elevated Temperature**

## High Temperature Properties of Normal Strength Concrete Per Eurocode 2 (2004)

*Specific heat (J/kg°C)*

$$c = 900, \quad \text{for } 20^\circ\text{C} \leq T \leq 100^\circ\text{C}$$

$$c = 900 + (T - 100), \quad \text{for } 100^\circ\text{C} \leq T \leq 200^\circ\text{C}$$

$$c = 1000 + (T - 200) / 2, \quad \text{for } 200^\circ\text{C} \leq T \leq 400^\circ\text{C}$$

$$c = 1100, \quad \text{for } 400^\circ\text{C} \leq T \leq 1200^\circ\text{C}$$

*Density (kg/m<sup>3</sup>)*

$$\rho = \rho(20^\circ\text{C}), \quad \text{for } 20^\circ\text{C} \leq T \leq 100^\circ\text{C}$$

$$\rho = \rho(20^\circ\text{C}) \left( 1 - \frac{0.02(T-115)}{85} \right), \quad \text{for } 115^\circ\text{C} \leq T \leq 200^\circ\text{C}$$

$$\rho = \rho(20^\circ\text{C}) \left( 0.98 - \frac{0.03(T-200)}{200} \right), \quad \text{for } 200^\circ\text{C} \leq T \leq 400^\circ\text{C}$$

$$\rho = \rho(20^\circ\text{C}) \left( 0.95 - \frac{0.07(T-400)}{800} \right), \quad \text{for } 400^\circ\text{C} \leq T \leq 1200^\circ\text{C}$$

*Volumetric specific heat =  $\rho c$*

*Thermal conductivity (W/m°C)*

*All types*

*Upper limit*

$$K_C = 2 - 0.2451(T/100) + 0.0107(T/100)^2, \quad \text{for } 20^\circ\text{C} \leq T \leq 1200^\circ\text{C}$$

*Lower limit*

$$K_C = 1.36 - 0.136(T/100) + 0.0057(T/100)^2, \quad \text{for } 20^\circ\text{C} \leq T \leq 1200^\circ\text{C}$$

*Thermal strain*

Carbonate Aggregates:

$$\varepsilon_{th} = -1.2 \times 10^{-4} + 6 \times 10^{-6}T + 2.3 \times 10^{-11}T^3, \quad \text{for } 20^\circ\text{C} \leq T \leq 700^\circ\text{C}$$

$$\varepsilon_{th} = 14 \times 10^{-3}, \quad \text{for } 700^\circ\text{C} \leq T \leq 1200^\circ\text{C}$$

Siliceous Aggregates:

$$\varepsilon_{th} = -1.2 \times 10^{-4} + 6 \times 10^{-6}T + 1.4 \times 10^{-11}T^3, \quad \text{for } 20^\circ\text{C} \leq T \leq 805^\circ\text{C}$$

$$\varepsilon_{th} = 12 \times 10^{-3}, \quad \text{for } 805^\circ\text{C} \leq T \leq 1200^\circ\text{C}$$

Stress-strain relationships (MPa):

$$\sigma_c(\theta) = \frac{3\varepsilon f'_{c,\theta}}{\varepsilon_{c1,\theta} \left( 2 + \left( \frac{\varepsilon}{\varepsilon_{c1,\theta}} \right)^3 \right)} \quad \text{for } \varepsilon \leq \varepsilon_{c1,\theta}$$

for numerical purposes a descending branch for  $\varepsilon_{c1,\theta} \leq \varepsilon \leq \varepsilon_{cu1,\theta}$

should be adopted. Linear or non linear models are

permitted. For the variables in this equation refer to the following table.

Temperature, °C	Siliceous			Carbonate		
	$\frac{f'_{c,\theta}}{f'_{c,20}}$	$\varepsilon_{c1,\theta}$	$\varepsilon_{cu1,\theta}$	$\frac{f'_{c,\theta}}{f'_{c,20}}$	$\varepsilon_{c1,\theta}$	$\varepsilon_{cu1,\theta}$
20	1.00	0.0025	0.0200	1.00	0.0025	0.0200
100	1.00	0.004	0.0225	1.00	0.0040	0.0225
200	0.95	0.0055	0.0250	0.97	0.0055	0.0250
300	0.85	0.0070	0.0275	0.91	0.0070	0.0275
400	0.75	0.0100	0.0300	0.85	0.0100	0.0300
500	0.60	0.0150	0.0325	0.74	0.0150	0.0325
600	0.45	0.0250	0.0350	0.60	0.0250	0.0350
700	0.30	0.0250	0.0375	0.43	0.0250	0.0375
800	0.15	0.0250	0.0400	0.27	0.0250	0.0400
900	0.08	0.0250	0.0425	0.15	0.0250	0.0425
1000	0.04	0.0250	0.0450	0.06	0.0250	0.0450
1100	0.01	0.0250	0.0475	0.02	0.0250	0.0475
1200	0.00	-	-	0.00	-	-

## **High Temperature Properties of Normal Strength Concrete Per ASCE MANNUAL (1992):**

*Volumetric specific heat (J/m°C)*

Carbonate Aggregates:

$$\rho_c = 2.566, \quad \text{for } 20^\circ \leq T \leq 400^\circ\text{C}$$

$$\rho_c = 0.1765T - 68.034, \quad \text{for } 400^\circ < T \leq 410^\circ\text{C}$$

$$\rho_c = 25.00671 - 0.05043T, \quad \text{for } 410^\circ < T \leq 445^\circ\text{C}$$

$$\rho_c = 2.566, \quad \text{for } 445^\circ\text{C} < T \leq 500^\circ\text{C}$$

$$\rho_c = 0.01603T - 5.44881, \quad \text{for } 500^\circ < T \leq 635^\circ\text{C}$$

$$\rho_c = 0.16635T - 100.90225, \quad \text{for } 635^\circ < T \leq 715^\circ\text{C}$$

$$\rho_c = 176.07343 - 0.22103T, \quad \text{for } 715^\circ < T \leq 785^\circ\text{C}$$

$$\rho_c = 2.566, \quad \text{for } T > 785^\circ\text{C}$$

Siliceous Aggregates:

$$\rho_c = 0.005T + 1.7, \quad \text{for } 20^\circ\text{C} \leq T \leq 200^\circ\text{C}$$

$$\rho_c = 2.7, \quad \text{for } 200^\circ\text{C} \leq T \leq 400^\circ\text{C}$$

$$\rho_c = 0.013T - 2.5, \quad \text{for } 400^\circ\text{C} \leq T \leq 500^\circ\text{C}$$

$$\rho_c = 10.5 - 0.013T, \quad \text{for } 500^\circ\text{C} \leq T \leq 600^\circ\text{C}$$

$$\rho_c = 2.7, \quad \text{for } T > 600^\circ\text{C}$$

*Thermal conductivity (W/m°C)*

Carbonate Aggregates:

$$k_c = 1.355 \text{ for } 20^\circ\text{C} \leq T \leq 293^\circ\text{C}$$

$$k_c = -0.001241T + 1.7162 \text{ for } T > 293^\circ\text{C}$$

Siliceous Aggregates:

$$k_c = -0.000625T + 1.5, \quad \text{for } 20^\circ\text{C} \leq T \leq 800^\circ\text{C}$$

$$k_c = 1.0, \quad \text{for } T > 800^\circ\text{C}$$

*Pure Quartz Aggregates*

$$k_c = -0.00085T + 1.9, \quad \text{for } 0^\circ\text{C} \leq T \leq 800^\circ\text{C}$$

$$k_c = 1.22, \quad \text{for } T > 800^\circ\text{C}$$

### Expanded Shale Aggregates

$$k_c = -0.00039583T + 0.925, \quad \text{for } 20^\circ\text{C} \leq T \leq 600^\circ\text{C}$$

$$k_c = 1.0, \quad \text{for } T > 600^\circ\text{C}$$

### Thermal Strain

#### All Types

$$\varepsilon_{th} = (0.008T + 6), \quad \text{for } 20^\circ\text{C} \leq T \leq 1200^\circ\text{C}$$

### Stress-strain relationships (MPa) for All Types of Aggregate:

#### Stress

$$\sigma_c = f'_{c,T} \left[ 1 - \left( \frac{\varepsilon - \varepsilon_{max,T}}{\varepsilon_{max,T}} \right)^2 \right] \quad \text{for } \varepsilon \leq \varepsilon_{max,T}$$

$$\sigma_c = f'_{c,T} \left[ 1 - \left( \frac{\varepsilon_{max,T} - \varepsilon}{3\varepsilon_{max,T}} \right)^2 \right] \quad \text{for } \varepsilon > \varepsilon_{max,T}$$

#### Compressive Strength (MPa)

$$f'_{c,T} = f'_c, \quad \text{for } 20^\circ\text{C} < T \leq 450^\circ\text{C}$$

$$f'_{c,T} = \left[ 2.011 - 2.353 \left( \frac{T - 20}{1000} \right) \right], \quad \text{for } 450^\circ\text{C} < T \leq 874^\circ\text{C}$$

$$f'_{c,T} = 0, \quad \text{for } T > 874^\circ\text{C}$$

### **Constitutive Relationships for High Temperature Properties of Prestressing Steel Per Eurocode 2 (2004)**

#### Thermal Strain

$$\varepsilon_{th} = -2.016 \times 10^{-4} + 1.0 \times 10^{-5}T + 0.4 \times 10^{-8}T^2, \quad \text{for } 20^\circ\text{C} \leq T \leq 1200^\circ\text{C}$$

#### Stress-strain relationships (MPa)

#### Stress

$$\sigma_p = \varepsilon_p E_{p,\theta} \quad \text{for } \varepsilon_p \leq \varepsilon_{pp,\theta}$$

$$\sigma_p = f_{pp,\theta} - c + \left( \frac{b}{a} \right) \left[ a^2 - (\varepsilon_{py,\theta} - \varepsilon_p)^2 \right]^{0.5} \quad \text{for } \varepsilon_{pp,\theta} < \varepsilon_p \leq \varepsilon_{py,\theta}$$

$$\sigma_p = f_{py,\theta} \quad \text{for } \varepsilon_{py,\theta} < \varepsilon_p \leq \varepsilon_{pt,\theta}$$

$$\sigma_p = f_{py,\theta} \left[ 1 - \frac{(\varepsilon_p - \varepsilon_{pt,\theta})}{(\varepsilon_{pu,\theta} - \varepsilon_{pt,\theta})} \right] \text{ for } \varepsilon_{pt,\theta} < \varepsilon_p \leq \varepsilon_{pu,\theta}$$

$$\sigma_p = 0.0 \text{ for } \varepsilon_p = \varepsilon_{pu,\theta}$$

### Parameters

$$\varepsilon_{pp,\theta} = f_{pp,\theta}/E_{p,\theta} \quad \varepsilon_{py,\theta} = 0.02$$

### Functions

$$a^2 = (\varepsilon_{py,\theta} - \varepsilon_{pp,\theta})\varepsilon_{py,\theta} - \varepsilon_{pp,\theta} + \frac{c}{E_{p,\theta}}$$

$$b^2 = c(\varepsilon_{py,\theta} - \varepsilon_{pp,\theta})E_{p,\theta} + c^2$$

$$c = \frac{(f_{py,\theta} - f_{pp,\theta})^2}{(\varepsilon_{py,\theta} - \varepsilon_{pp,\theta})E_{p,\theta} - 2(f_{py,\theta} - f_{pp,\theta})}$$

(Values for  $f_{py,\theta}$ ,  $f_{pp,\theta}$ ,  $E_{p,\theta}$ ,  $\varepsilon_{pt,\theta}$  and  $\varepsilon_{pu,\theta}$  can be found from the following table.)

Values for Main Parameters of Stress-strain Relationships of Prestressing Steel Reinforcement at Elevated Temperatures (Eurocode 2, 2004)

Temperature, °C	$\frac{f_{py,\theta}}{\beta f_{yk}}$	$\frac{f_{pp,\theta}}{\beta f_{yk}}$	$\frac{E_{p,\theta}}{E_p}$	$\varepsilon_{pt,\theta}$	$\varepsilon_{pu,\theta}$
20	1.00	1.00	1.00	0.050	0.100
100	0.99	0.68	0.98	0.050	0.100
200	0.87	0.51	0.95	0.050	0.100
300	0.72	0.32	0.88	0.055	0.105
400	0.46	0.13	0.81	0.060	0.110
500	0.22	0.07	0.54	0.065	0.115
600	0.10	0.05	0.41	0.070	0.120
700	0.08	0.03	0.10	0.075	0.125
800	0.05	0.02	0.07	0.080	0.130
900	0.03	0.01	0.03	0.085	0.135
1000	0.00	0.00	0.00	0.090	0.140
1100	0.00	0.00	0.00	0.095	0.145
1200	0.00	0.00	0.00	0.100	0.150

Values for Ultimate Strength of Prestressing Steel at Elevated Temperatures  
(PCI, 2004)

Temperature, °C	Strength Loss
20	1.00
93	1.00
149	0.98
238	0.90
260	0.86
304	0.78
371	0.64
460	0.42
582	0.20
627	0.14
716	0.06
749	0.04

**Constitutive Relationships for High Temperature Properties of Reinforcing Steel Eurocode 2 (2004)**

*Thermal Strain*

$$\varepsilon_{th} = -2.416 \times 10^{-4} + 1.2 \times 10^{-5} T + 0.4 \times 10^{-8} T^2, \quad \text{for } 20^\circ\text{C} < T \leq 750^\circ\text{C}$$

$$\varepsilon_{th} = 11 \times 10^{-3}, \quad \text{for } 750^\circ\text{C} < T \leq 860^\circ\text{C}$$

$$\varepsilon_{th} = -6.2 \times 10^{-3} + 2 \times 10^{-5} T, \quad \text{for } 860^\circ\text{C} < T \leq 1200^\circ\text{C}$$

*Stress*

$$\sigma_s = \varepsilon_s E_{s,\theta} \text{ for } \varepsilon_s \leq \varepsilon_{sp,\theta}$$

$$\sigma_s = f_{sp,\theta} - c + \left(\frac{b}{a}\right) \left[ a^2 - (\varepsilon_{sy,\theta} - \varepsilon_s)^2 \right]^{0.5} \text{ for } \varepsilon_{sp,\theta} < \varepsilon_s \leq \varepsilon_{sy,\theta}$$

$$\sigma_s = f_{sy,\theta} \text{ for } \varepsilon_{sy,\theta} < \varepsilon_s \leq \varepsilon_{st,\theta}$$

$$\sigma_s = f_{sy,\theta} \left[ 1 - \frac{(\varepsilon_s - \varepsilon_{st,\theta})}{(\varepsilon_{su,\theta} - \varepsilon_{st,\theta})} \right] \text{ for } \varepsilon_{st,\theta} < \varepsilon_s \leq \varepsilon_{su,\theta}$$

$$\sigma_s = 0.0 \text{ for } \varepsilon_s = \varepsilon_{su,\theta}$$

*Parameters*

$$\varepsilon_{sp,\theta} = f_{sp,\theta} / E_{s,\theta} \quad \varepsilon_{sy,\theta} = 0.02 \quad \varepsilon_{st,\theta} = 0.15 \quad \varepsilon_{su,\theta} = 0.20$$



## Functions

$$a^2 = (\varepsilon_{sy,\theta} - \varepsilon_{sp,\theta})\varepsilon_{sy,\theta} - \varepsilon_{sp,\theta} + \frac{c}{E_{s,\theta}}$$

$$b^2 = c(\varepsilon_{sy,\theta} - \varepsilon_{sp,\theta})E_{s,\theta} + c^2$$

$$c = \frac{(f_{sy,\theta} - f_{sp,\theta})^2}{(\varepsilon_{sy,\theta} - \varepsilon_{sp,\theta})E_{s,\theta} - 2(f_{sy,\theta} - f_{sp,\theta})}$$

(Values for  $f_{sy,\theta}$ ,  $f_{sp,\theta}$  and  $E_{s,\theta}$  can be found from the following table.)

Temperature, °C	$\frac{f_{sy,\theta}}{f_{yk}}$	$\frac{f_{sp,\theta}}{f_{yk}}$	$\frac{E_{s,\theta}}{E_s}$
20	1.00	1.00	1.00
100	1.00	1.00	1.00
200	1.00	0.81	0.90
300	1.00	0.61	0.80
400	1.00	0.42	0.70
500	0.78	0.36	0.60
600	0.47	0.18	0.31
700	0.23	0.05	0.13
800	0.11	0.04	0.09
900	0.06	0.02	0.07
1000	0.04	0.01	0.04
1100	0.02	0.00	0.02
1200	0.00	0.00	0.00

**Constitutive Relationships for High Temperature Properties of Reinforcing Steel according to ASCE Manual (1992)**

*Thermal Strain*

$$\varepsilon_{th} = [0.004(T^2 - 400) + 12(T - 20)] \times 10^{-6} \text{ for } T < 1000^\circ\text{C}$$

$$\varepsilon_{th} = [16 - (T - 20) \times 10^{-6}] \text{ for } T \geq 1000^\circ\text{C}$$

*Stress*

$$f_s = \frac{f(T, 0.001)}{0.001} \varepsilon_p \text{ for } \varepsilon_s \leq \varepsilon_p$$

$$f_s = \frac{f(T, 0.001)}{0.001} \varepsilon_p + f[T, (\varepsilon_s - \varepsilon_p + 0.001)] - f(T, 0.001) \text{ for } \varepsilon_s \geq \varepsilon_p$$

*Functions*

$$f(T, 0.001) = (50 - 0.04T)x \left\{ 1 - \exp \left[ (30 + 0.03T)\sqrt{(0.001)} \right] \right\} \times 6.9$$

$$\varepsilon_p = 4 \times 10^{-6} f_{yo}$$

$$f[T, (\varepsilon_s - \varepsilon_p + 0.001)] = (50 - 0.04T)x$$

$$\left\{ 1 - \exp \left[ (-30 + 0.03T)\sqrt{(\varepsilon_s - \varepsilon_p + 0.001)} \right] \right\} \times 6.9$$

**Constitutive Relationships for High Temperature Properties of FRP**

*Specific Heat,  $C_{w,T}$*

In the following equations  $C_{w,T}$  has units of (KJ/Kg °C) and  $T_w$  in °C

$$0 \leq T_w \leq 325 : \quad C_{w,T} = 1.25 + \frac{0.953}{325} (T_w)$$

$$325 \leq T_w \leq 343 : \quad C_{w,T} = 2.2 + \frac{2.8}{18} (T_w - 325)$$

$$343 \leq T_w \leq 510 : \quad C_{w,T} = 5.0 + \frac{-0.15}{167} (T_w - 343)$$

$$510 \leq T_w \leq 538 : \quad C_{w,T} = 4.85 + \frac{-3.59}{28} (T_w - 510)$$

$$538 \leq T_w \leq 3316 : \quad C_{w,T} = 1.265 + \frac{1.385}{2778} (T_w - 538)$$

$$T_w \geq 3316 : \quad C_{w,T} = 0$$

*Density,  $\rho_{w,T}$*

In the following equations  $\rho_{w,T}$  has units of  $g/cm^3$  and  $T_w$  in  $^{\circ}C$ .

$$0 \leq T_w \leq 510 : \quad \rho_{w,T} = 1.6$$

$$510 \leq T_w \leq 538: \quad \rho_{w,T} = 1.6 + \frac{-0.35}{28}(T_w - 510)$$

$$538 \leq T_w \leq 1200: \quad \rho_{w,T} = 1.25$$

*Thermal Conductivity,  $K_{w,T}$*

In the following equations  $k_{w,T}$  has units of  $W/m \cdot ^{\circ}C$  and  $T_w$  in  $^{\circ}C$ .

$$0 \leq T_w \leq 500 : \quad k_{w,T} = 1.14 + \frac{1.1}{500} \cdot T_w$$

$$500 \leq T_w \leq 650: \quad k_{w,T} = 1.4 + \frac{-0.1}{150}(T_w - 500)$$

$$T_w \geq 650: \quad k_{w,T} = 0.2$$

*Strength,  $f_{com,T}$ , and Elastic Modulus  $E_{com,T}$*

For a CFRP wrap:

$$a_{\sigma} = 0.1$$

$$b_{\sigma} = 5.83e-3$$

$$c_{\sigma} = 339.54$$

$$a_E = 0.05$$

$$b_E = 8.68e-3$$

$$c_E = 367.41$$

For a GFRP Wrap:

$$a_{\sigma} = 0.1$$

$$b_{\sigma} = 8.10e-3$$

$$c_{\sigma} = 289.14$$

$$a_E = 0.05$$

$$b_E = 7.91e-3$$

$$c_E = 320.35$$

For an AFRP wrap:

$$a_{\sigma} = 0.1$$

$$b_{\sigma} = 8.48e-3$$

$$c_{\sigma} = 287.65$$

$$a_E = 0.05$$

$$b_E = 7.93e-3$$

$$c_E = 290.49$$

$$f_{com,T} = f_{com} \left[ \frac{1-a_{\sigma}}{2} \tanh[-b_{\sigma}(T_w - c_{\sigma})] + \frac{1+a_{\sigma}}{2} \right]$$

$$E_{com,T} = f_{com} \left[ \frac{1-a_E}{2} \tanh[-b_E(T_w - c_E)] + \frac{1+a_E}{2} \right]$$

## References

1. AASHTO. (2004). A Policy on geometric design of highways and streets, 5th Ed., Washington, DC.
2. AASHTO (2014). "AASHTO LRFD bridge design specification." American Association of State Highway Transportation Officials.
3. ABAQUS (2014). "ABAQUS standard user's manual. Version 6.14, vol. I–III." Pawtucket(America): Hibbitt, Karlsson & Sorensen, Inc.
4. ACI 440.2R (2008). "Guide for the design and construction of externally bonded FRP systems for strengthening concrete structures." American Concrete Institute, Farmington Hills, MI.
5. Adelzadeh, Masoud (2010). "Structural and thermal behavior of insulated FRP-strengthened reinforced concrete beams and slabs in fire." Ph.D thesis, Queen's Univ., Kingston, ON, Canada
6. Ahmed, A. (2010)." Behavior of FRP-strengthened reinforced concrete beams under fire conditions." Ph.D thesis, Queen's Univ., Kingston, ON, Canada
7. Alos-Moya, j., Paya-Zaforteza, I., Garlock, M.E.M., Loma-Ossorio, E., Schiffner, D., Hospitaler, A., (2014). "Analysis of a bridge failure due to fire using computational fluid dynamics and finite element models." Engineering Structures, Volume 68, Pages 96-110.
8. Anderberg, Y. and Thelandersson, S. (1976). "Stress and deformation characteristics of concrete at high temperatures, 2-Experimental investigation and material behavior model," Bulletin 54, Lund Institute of Technology, Lund, Sweden.
9. Anderberg Y. (2008). "The Impact of Various Material Models on Structural Fire Behavior Prediction." Proceedings of Fifth International Conference on Structures in Fire, Singapore, pp. 12.
10. ASCE (1992). "Structural fire protection." Manuals and reports on engineering practice No. 78, ASCE Committee on Fire Protection, Structural Division. American Society of Civil Engineer, New York, New York.

11. Astaneh-Asl, A., Noble, C. R., Son, J., Wemhoff, A. P., Thomas, M. P., and McMichael, L. D. (2009). "Fire protection of steel bridges and the case of the MacArthur Maze fire collapse." Proc., ASCE TCLEE Conf., ASCE, Reston, VA, 1–12.
12. ASTM C39/C39M (2014). "Standard Test Method for Compressive Strength of Cylindrical Concrete Specimens," Annual Book of ASTM Standards, ASTM International, Vol. 04. 02, West Conshohocken, PA.
13. ASTM A615/A615M (2014). "Standard Specification for Deformed and Plain Carbon Steel Bars for Concrete Reinforcement," Annual Book of ASTM Standards, ASTM International, Vol. 01. 04, West Conshohocken, PA.
14. ASTM A416/A416M (2014). "Standard Specification for Steel Strand, Uncoated Seven Wire for Prestressed Concrete," Annual Book of ASTM Standards, ASTM International, Vol. 01. 04, West Conshohocken, PA.
15. Bajwa, C., Easton, E., Adkins, H., Cuta, J., Klymyshyn, N., and Suffield, S. (2012). "The MacArthur Maze fire and roadway collapse: a 'worst case scenario' for spent nuclear fuel transportation." Proceedings of the ASME 2012 Pressure Vessel & Piping Division Conference, Toronto, Ontario, Canada, 2012.
16. Barnes, R. and Fidell, J. (2006). "Performance in fire of small-scale CFRP strengthened concrete Beams." J. Compos. Constr., 10.1061/(ASCE)1090-0268(2006)10:6(503), 503-508.
17. Bažant, P., Z. and Kaplan, F., M. (1996). "Concrete at high temperatures: material properties and mathematical models." Longman Group Limited, Essex, UK, 1996.
18. Behnood, A. and Ghandehari, M. (2009). "Comparison of compressive and splitting tensile strength of high-strength concrete with and without polypropylene fibers heated to high temperatures." Fire Safety Journal, vol. 44, no. 8, pp. 1015–1022.
19. Belarbi, A., Bae, S-W, Ayoub, A., Kuchma, D., Mirmiran, A., and Okeil, A. Design of FRP Systems for Strengthening Concrete Girders in Shear, NCHRP Report 678, Transportation Research Board, Washington, D.C., 2011.
20. Bennetts, I., Moinuddin, K. (2009). "Evaluation of the impact of potential fire scenarios on structural elements of a cable-stayed bridge." J. Fire Prot. Eng. 19(2009) 85–106.

21. Bisby, L. A. (2003). "Fire behavior of fibre-reinforced polymer (FRP) reinforced or confined concrete," PhD Thesis, Queen's University, Kingston, Canada.
22. Bisby, L.A., Kodur, V.K.R., Green, M.F. (2005). "Fire endurance of fiber-reinforced polymer confined concrete columns." *ACI Structural Journal*, 102(6): 883-891.
23. Blontrock, H., Taerwe, L., and Matthys, S. (1999). "Properties of fiber reinforced plastics at elevated temperatures with regard to fire resistance of reinforced concrete members." 188, 43-54.
24. Blontrock, H., Taerwe, L., and Vandeveld, P. (2000). "Fire tests on concrete beams strengthened with fiber composite laminates." *Proc., 3rd Ph.D. Symp. in Civil Engineering, Institute of Structural Engineering, Univ. of Agricultural Sciences, Vienna, Austria*, 151–161.
25. Blontrock, H., Taerwe, L., and Vandeveld, P. (2000). "Fire testing of concrete slabs strengthened with fiber composite laminates." *Fifth Annual Symposium on Fiber-Reinforced Plastic Reinforcement for Concrete Structures (FRPRCS-5)*. C. Burgoyne, ed., Thomas Telford, London, pp. 547-556.
26. Bourbigot, S., and Flambard, X. (2002). "Heat resistance and flammability of high-performance fibers: A review." *Fire and Materials*, 26(4-5), 155-168.
27. Carolin, A. (2003). "Carbon Fiber Reinforced Polymers for Strengthening of Structural Elements", Doctoral Thesis, Luleå University of Technology.
28. Carette, G., G., Painter, E., K. and Malhotra, M., V. (1982). "Sustained high-temperature effect on concretes made with normal portland cement, normal portland cement, and slag, or normal portland cement and fly ash." *Concrete International*, vol. 4, no. 7, pp. 41–51, 1982.
29. Castillo, C. and Durrani, J., A. (1990). "Effect of transient high temperature on high-strength concrete." *ACI Materials Journal*, vol. 87, no. 1, pp. 47–53.
30. CBC news (2016). "RCMP not Laying Charges after Massive Train Bridge Fire in Porcupine Plain, Sask."  
<<<http://www.cbc.ca/news/canada/saskatoon/no-charges-porcupine-plain-1.3516419?cmp=rss>>> Last accessed June 22, 2016.

31. CEN, Eurocode 1: Actions on Structures, Part 1–2 – General Actions on Structures Exposed to Fire, European Committee for Standardization, Brussels, Belgium, 2002.
32. Choi, J. (2008). "Concurrent Fire Dynamics Models and Thermomechanical Analysis of Steel and Concrete Structures." Ph.D. dissertation, Georgia Institute of Technology, Atlanta, GA.
33. Chowdhury, E. (2009). "Behavior of fiber reinforced polymer confined reinforced concrete columns under fire conditions." Ph.D thesis, Queen's Univ., Kingston, ON, Canada.
34. Chung P, Wolfe RW, Ostrom T & Hida, S. (2008). "Accelerated bridge construction applications in California—lessons learned report." report issued by the California Department of Transportation.
35. Committee for European Normalisation (CEN). EN 1991-1-2: 2002 "Eurocode 1: Actions on structures. Part 1–2: General actions –Actions on structures exposed to fire." Brussels (Belgium): European Committee for Standardization; 2002.
36. Committee for European Normalisation (CEN). EN 1991-1-2:2004 "Eurocode 2: design of concrete Structures-Part 1-2: general rules – structural fire design." Brussels, Belgium.
37. Committee of European Normalisation (CEN) (1993–2005b), EN 1993-1-2-2005, Eurocode 3: Design of Steel Structures, Part 1-2: Structural Fire Design, CEN, Brussels.
38. Dai, J., Gao, W., and Teng, J. (2014). "Finite element modeling of insulated FRP-strengthened RC beams exposed to fire." J. Compos. Constr., 10.1061/(ASCE)CC.1943-5614.0000509, 04014046.
39. Davidson, M. (2012). "Assessment of Passive Fire Protection on Steel-Girder Bridges." Masters Theses, Western Kentucky University.
40. Davis, M and Tremel, P. (2007). "Bill Williams River Bridge Fire Damage Assessment and Repair." <[ftp://ftp.wsdot.wa.gov/public/Bridge/WBES2007/assets/tuesday/8A/Martha\\_Davis\\_8A.pdf](ftp://ftp.wsdot.wa.gov/public/Bridge/WBES2007/assets/tuesday/8A/Martha_Davis_8A.pdf)> Last accessed June 20, 2016.
41. Deuring, M. (1994). "Fire tests on strengthened reinforced concrete beams." Research Rep. No. 148'795, Swiss Federal Laboratories for Materials Testing and Research, Dubendorf, Switzerland.

42. Dotreppe, J., Majkut, S., and Franssen, J. (2005). "Failure of a tied-arch bridge subjected to a severe localized fire." Proceedings of the 2005 IABSE Symposium, Lisbon, Portugal.
43. Dwaikat, M. and Kodur, V. (2009). "Response of restrained concrete beams under design fire exposure." J. Struct. Eng., Volume 135, Issue 11, Pages 1408-1417.
44. Dwaikat, M., B. (2009). "Flexural response of reinforced concrete beams exposed to fire," PhD Thesis, Michigan State University, East Lansing, Michigan, USA.
45. Elghazouli, A.Y., Cashell, K.A., and Izzuddin, B.A. (2009). "Experimental evaluation of the mechanical properties of steel reinforcement at elevated temperature." Fire Safety Journal, 44, pp. 909-919.
46. Felicetti, R., Gambarova, G., P., Rosati, P., G., Corsi, F., and Giannuzzi, G. (1996). "Residual mechanical properties of high-strength concretes subjected to high-temperature cycles." in Proceedings of the International Symposium on Utilization of High-Strength/High-Performance Concrete, pp. 579–588, Paris, France.
47. GangaRao, H. and Vijay, P. (2010). "Feasibility review of FRP materials for structural applications. "Constructed facilities center, College of Engineering and Mineral Resources, West Virginia University, Morgantown, WV-26506.
48. Gao, W. Y., Hu, K. X., and Lu, Z. D. (2010). "Fire resistance experiments of insulated CFRP strengthened reinforced concrete beams." Chin. Civ. Eng. J., 43(3), 15–23.
49. Gibson, F. R. (1994). "Principles of composite material mechanics." McGrawhill, Inc,
50. Gong, X. and Agrawal, A. (2014). "Numerical simulation of fire damage to a long-span truss bridge." J. Bridge Eng., Volume 20, Issue 10, Pages.
51. Grace, N. F., Soliman, A. K., Abdel-Sayed, G., and Saleh, K. R. (1998). "Behavior and ductility of simple and continuous FRP reinforced beams." J. Compos. Constr., 2(4), 186–194.
52. Harada, T., Takeda, J., Yamane, S., and Furumura, F. (1972). "Strength, elasticity and thermal properties of concrete subjected to elevated temperatures." ACI Concrete for Nuclear Reactor SP, vol. 34, no. 2, pp. 377–406.



53. Harmathy T.Z. (1967), "A Comprehensive Creep Model." *Journal of Basic Engineering Transaction of the ASME*, (89), pp. 496-502.
54. Harmathy, Z., T. and Allen, L.,W. (1973) "Thermal properties of selected masonry unit concretes," *Journal American Concrete Institution*, vol. 70, no. 2, pp. 132–142.
55. Harries, K.A., Porter, M.L., and Busel, J, P. (2003). "FRP materials and concrete research need." *Concrete International*, Vol. 25, No. 10, pp. 69-74.
56. Hatinger, R., N. (2012). "Performance-based approach for evaluating the fire response of prestressed concrete double T-beams." MSc Thesis, Michigan State University.
57. Hawileh, R. A., Naser, M., Zaidan, W., and Rasheed, H. A. (2009). "Modeling of insulated CFRP-strengthened reinforced concrete T-beam exposed to fire." *Eng. Struct.*, 31(12), 3072–3079.
58. High Steel Structures. "9-Mile Road Bridge, Hazel Park, MI." << <http://www.highsteel.com/project-gallery/emergency-replacements/9-mile-road-bridge/>>>, Last accessed June 18, 2016.
59. Hou, X., Kodur, V. and Zheng, W. (2015). "Factors governing the fire response of bonded prestressed concrete continuous beams." *Materials and Structures*, Volume 48, Issue 9, Pages 2885-2900.
60. Hurley, M. (2016). "SFPE handbook of fire protection engineering." Aon fire protection engineering, Greenbelt, MD, USA.
61. Industry Handbook Committee (2004). "PCI Design Handbook: Precast and Prestressed Concrete Institute." 6th ed., PCI MNL 120-04, Skokie, IL, USA.
62. Khabhari, V.M. and Gao, Y. (1997). "Composite jacketed concrete under axial compression – verification of simple design equations." *Journal of Materials in Civil Engineering*, 9(4): 185- 193.
63. Khaliq, W. (2012). "Performance characterization of high performance concretes under fire conditions." PhD. Thesis, Michigan State University.
64. Khoury, A., G., Grainger, N., B. and Sullivan, E., J., P. (1985). "Strain of concrete during fire heating to 600°C." *Magazine of Concrete Research*, vol. 37, no. 133, pp. 195–215.

65. Kodur, R., V. and Sultan, A., M. (1998) "Thermal properties of high strength concrete at elevated temperatures." American Concrete Institute, Special Publication, SP-179, pp. 467–480.
66. Kodur, V. (2000) "Spalling in high strength concrete exposed to fire—concerns, causes, critical parameters and cures." in Proceedings of the ASCE Structures Congress: Advanced Technology in Structural Engineering, pp. 1–9.
67. Kodur, R., V. and Sultan, A., M. (2003). "Effect of temperature on thermal properties of high-strength concrete." Journal of Materials in Civil Engineering, vol. 15, no. 2, pp. 101–107.
68. Kodur, V.K.R., Green, M.F., Bisby, L.A. and Williams, B. (2004). "Evaluating the fire performance of FRP-strengthened structures." Concrete Engineering International, Vol. 8, No. 2, pp. 48-50.
69. Kodur, V.K.R, Bisby, L.A, Green, M.F., and Chowdhury, E. (2005). "Fire endurance of insulated FRP-strengthened square concrete columns." 7th International Symposium of Fibre Reinforced Polymer Reinforcement for Concrete Structures (FRPRCS), Kansas City, U.S.A., November 6-9th.
70. Kodur, V., Dwaikat, S., M., M., and Dwaikat, B., M. (2008). "High-temperature properties of concrete for fire resistance modeling of structures." ACI Materials Journal, vol. 105, no. 5, pp. 517–527.
71. Kodur, V., Gu, L., and Garlock, M. (2010) "Review and Assessment of Fire Hazard in Bridges." Journal of the Transportation Research Board, Volume 2172, Pages 23-29.
72. Kodur, V. and Khaliq, W. (2011). "Effect of temperature on thermal properties of different types of high-strength concrete," Journal of Materials in Civil Engineering, ASCE, vol. 23, no. 6, pp. 793–801.
73. Kodur, V., Aziz, E., and Dwaikat, M. (2013). "Evaluating Fire Resistance of Steel Girders in Bridges." J. Bridge Eng., Volume 18(7), Pages 633-643
74. Kodu, V.r & Naser, M. (2013). "Importance factor for design of bridges against fire hazard." Engineering Structures. Volume 54, Pages 207-220.
75. Kodur, V. (2014). "Properties of concrete at elevated temperatures." ISRN Civil Engineering, Volume 2014, 1-15.

76. Lee, J., and Fenves, G. (1998). "Plastic damage model for cyclic loading of concrete structures." *J. Eng. Mech.*, 10.1061/(ASCE)0733-9399(1998)124:8(892), 892–900.
77. Lie, T., T. and Kodur, V. (1996). "Thermal and mechanical properties of steel-fibre-reinforced concrete at elevated temperatures." *Canadian Journal of Civil Engineering*, vol. 23, no. 2, pp. 511–517.
78. Lillistone, D and Jolly, C.K. (2000). "An innovative form of reinforcement for concrete columns using advanced composites." *The Structural Engineer*, 78 (23): 20-28.
79. Liu, F. T., Wu, B., and Wei, D. M. (2009). "Failure modes of reinforced concrete beams strengthened with carbon fiber sheet in fire." *Fire Saf. J.*, 44(7), 941–950.
80. Liu, Y., Guangyuan, W. and Yansheng, S. (2012). "Finite element analysis of fire behavior of steel girders in bridges." *Adv.Mater.Res.*594–597(2012)2296–2300.
81. Lubliner, J., Oliver, J., Oller, S., and Onate, E. (1989). "A plastic-damage model for concrete." *Int. J. Solids Struct.*, 25(3), 299–326.
82. Mallik, P. K. (1988). "Fiber-reinforced Composites: Materials, manufacturing, and design." Marcel Dekker Inc., New York.
83. Meier, U., and Kaiser, H. "Strengthening of Structures with CFRP Laminates," *Advanced Composite Materials in Civil Engineering Structures*, ASCE Specialty Conference, pp. 224-232, 1991.
84. Mohanamurthy, M. and Yazdani, N. (2015). "Flexural strength prediction in FRP strengthened concrete bridge girders." *European J. of Adv. In Eng. And Tech.*, 2(3), 59-68.
85. Mueller, K. (2015). "Protecting our infrastructure from hydrocarbon fires." [http://hce.com/blog/index.php/article/view/protecting\\_our\\_infrastructure\\_from\\_hydrocarbon\\_fires](http://hce.com/blog/index.php/article/view/protecting_our_infrastructure_from_hydrocarbon_fires)>> accessed on May 19, 2015.
86. NFPA (2008). "NFPA 502 Standard for road, tunnels, bridges, and other limited access highways." National Fire Protection Association. Quincy, MA.
87. New York Times (2007). "Tanker Truck Fire Collapses Bay Area Overpass." <<[http://www.nytimes.com/2007/04/30/us/30collapse.html?\\_r=0](http://www.nytimes.com/2007/04/30/us/30collapse.html?_r=0)>> Last accessed June 18, 2016.

88. Park, R. (1988). "State-of-the-art report ductility evaluation from laboratory and analytical testing." Proceedings of ninth world conference on earthquake engineering, August 2-9, 1988. Tokyo-Kyoto, Japan.
89. Payá-Zaforteza, I., and Garlock, M.E.M (2012). "A numerical investigation of the fire response of a steel girder bridge." Journal of Constructional Steel Research, Volume 75, Pages 93-103
90. PCI (1989). "Design for fire resistance of precast prestressed concrete." Prestressed Concrete Institute.
91. Pessiki, S., Harries, K.A., Kestner, J.T., Sause, R., and Ricles, J.M. (2001). "Axial behavior of reinforced concrete columns confined with FRP jackets." Journal of Composites for Construction, 5(4): 237-245.
92. Phan, L.T. (1996). "Fire performance of high-strength concrete: a report of the state-of-the-art," Tech. Rep., National Institute of Standards and Technology, Gaithersburg, Md, USA.
93. Purkiss, J., A. (2007). "Fire safety engineering design of structures." Butterworth-Heinemann, Elsevier, Oxford, UK, 2007.
94. Quiel, S., Yokoyama, T., Bergman, L., Mueller, K and Marjanishvili, S. (2015) "A Streamlined Framework for Calculating the Response of Steel-supported Bridges to Open -air Tanker Truck Fires." Fire Safety Journal. Volume 73, Pages 63-75.
95. Purkiss, J., A. (2007). "Fire safety engineering design of structures." 2nd ed. Oxford: Butterworth-Heineman.
96. Raut, N. (2011). "Response of high strength concrete columns under fire-induced biaxial bending." Ph.D. thesis, Michigan State University, East Lansing, Mich, USA.
97. Rein, G., Abecassis Empis, C., and Carvel, R. (2007). "The Dalmarnock fire tests: experiments & modeling." School of Engineering and Electronics, The University of Edinburgh, Edinburgh, UK
98. Ritchie, P.; Thomas, D.; Lu, L.; and Conneley, G., "External Reinforcement of Concrete Beams Using Fiber Reinforced Plastics," ACI Structural Journal, V. 88, No. 4, July-Aug., pp. 490-500, 1991.
99. ROSTASY, F., HANKERS, C. and RANISCH, E., 1992. "Strengthening of RC and PC structures with bonded FRP plates." Advanced Composite Materials in Bridge and Structures, pp. 253-263.

100. Saafi, M., Toutanji, H.A. and Li, Z. (1999). "Behavior of concrete columns confined with fiber reinforced polymer tubes." *ACI Material Journal*, 96(4): 500-509.
101. Samaan, M., Mirmiran, A. and Shahawy, M. (1998). "Model of concrete confined by fiber composite." *Journal of Structural Engineering*, 124(9): 1025-1031.
102. Schneider, U. (1988). "Concrete at high temperatures—a general review." *Fire Safety Journal*, vol. 13, no. 1, pp. 55–68.
103. SFGATE (2007). "The Maze meltdown." <http://www.sfgate.com/bayarea/article/THE-MAZE-MELTDOWN-Eyewitness-sees-driver-2597951.php>, Accessed on 07/09/15.
104. SFPE (2016). "SFPE Handbook of fire protection engineering." 5th Ed., SFPE, Quincy, Massachusetts.
105. Sharif, A.; Al-Sulaimani, G.; Basunbul, I.; Baluch, M.; and Ghaleb, B. (1994) "Strengthening of initially loaded reinforced concrete beams using FRP plates." *ACI Structural Journal*, V. 91, No. 2, Mar.-Apr., pp. 160-168.
106. Shin, K., Y., Kim, S., B., Kim, H., J., Chung, M., and Jung, S., P. (2002) "Thermo-physical properties and transient heat transfer of concrete at elevated temperatures." *Nuclear Engineering and Design*, vol. 212, no. 1–3, pp. 233–241.
107. Sika Corporation (2006). "State highway 183 MacArthur Boulevard overpass emergency repair" *ICRI Concrete Repair Bulletin*.
108. Spoelstra, M.R. and Monti, G. (1999). "FRP-confined concrete model." *Journal of Composites for Construction*, 3(3): 143-150
109. Stein, W. and Neumna, T. (2007). "Mitigation Strategies for Design Exceptions." U.S. Department of Transportation, Federal Highway Administration, Office of Safety, Washington, D.C.
110. Stoddard, R. (2004). "Inspection and repair of a fire damaged prestressed girder bridge." *International Bridge Conference*, Pittsburgh.
111. Stratford, T.J., Gillie, M., Chen, J.F. and Usmani A.S. (2009). "Bonded fiber reinforced polymer strengthening in a real fire." *Adv Struct Eng* 12(6):867–877

112. Sudheera, S., Kumarb, L., Manjunathb, B., Pasic, A., Meenakshic, G. and Prabhu, S. (2013). "Fire safety distances for open pool fires." *Infrared physics and technology*, 61,265-273
113. Tan, K. and Zhou, Y. (2011). "Performance of FRP-strengthened beams subjected to elevated temperatures." *J. Compos. Constr.*, 10.1061/(ASCE)CC.1943-5614.0000154, 304-311
114. Tonicello, E., Desanghere, S. Vassart, O. and Franssen, J. (2012). "Fire analysis of a new steel bridge." *Proceedings of the 7th International Conference on Structures in Fire, Zurich, Switzerland.*
115. Toutanji, H.A. (1999). "Stress-strain characteristics of concrete column externally confined with advanced composites." *ACI Materials Journal*, 96(3): 397-404.
116. TxDOT (2013). "Bridge Design Manual-LRFD." Texas Department of Transportation.
117. TxDOT (2014). "Standard Specifications for Construction and Maintenance of Highways, Streets, and Bridges." Texas Department of Transportation.
118. TxDOT (2015). "Externally bonded fiber reinforced polymer (FRP) system for repairing and strengthening concrete structure members." Texas Department of Transportation.
119. TxDOT (2015). "Prestressed member fabrication plants (multi-project)." Texas Department of Transportation.
120. TxDOT (2016). "Fiber reinforced polymer (FRP) material/producer list." Texas Department of Transportation.
121. Vives, R., Serna, J. and Mather, K. (2014). "Bridge Fire Leaves Hesperia Plan for Economic Boost in Ashes." << <http://www.latimes.com/local/la-me-bridge-fire-20140507-story.html>>> Last accessed June 22, 2016.
122. Wang, Y., Burgess, I., Wald, F., and Gillie, M. (2013). "Performance-based fire engineering of structures." CRC Press, 6000 Broken Sound Parkway NW, Suite 300 Boca Raton, FL 33487-2742.
123. Williams, B. (2004). "Fire performance of FRP-strengthened reinforced concrete flexural members." Ph.D. thesis, Queen's Univ., Kingston, ON, Canada.

124. Williams, B., Kodur, V. K. R., Green, M. F., and Bisby, L. A. (2008). "Fire endurance of fiber-reinforced polymer strengthened concrete T-beams." *ACI Structural Journal*, 105(1), 60–67.
125. Wojdyla, B (2009). "Detroit I-75 Bridge Collapse Mega-Gallery." <<<http://jalopnik.com/5316090/detroit-i-75-bridge-collapse-mega-gallery>>> Last accessed June 18,2016.
126. Woodworth, M. (2013). "Fire Hazard Assessment for Highway Bridges with Thermal Mechanical Modeling." PhD dissertation, Virginia Polytechnic Institute and State University.
127. Wright, W., Lattimer, B., Woodworth, M., Nahid, M., and Sotelino, E. (2013), NCHRP 12-85. "Highway bridge fire hazard assessment." Transportation Research Board, Blacksburg, VA.
128. Wu, B. and Wan, Z.J. (2009). "Experimental investigation into fire resistance of reinforced concrete beams strengthened in flexure with carbon fiber sheets." *Journal of South China University of Technology*, Vol. 40, No. 6, pp. 26-41.
129. Xiao, Y. and Wu, H., (2000). "Compressive behavior of concrete confined by carbon fiber composite jackets." *Journal of Material in Civil Engineering*, 12(2): 139-146.
130. Yang, D., Merrill, B. D. and Bradberry, T. E. (2011). "Texas use of CFRP to repair concrete bridges." *Int. Concr. Abstr. Portal*, 277, 39–57.
131. Zarate, L., Arnaldos, J. and Casal, J. (2008). "Establishing safety distances for wildland fires." *Fire Safety Journal*, 43, 565–575.
132. Zureick, A-H, Ellingwood, B., Nowak, A., Mertz, D., and Triantafillou, T., "Recommended Guide Specification for the Design of Externally Bonded FRP Systems for Repair Strengthening of Concrete Bridge Elements," NCHRP Report 655, Transportation Research Board, Washington, D.C., 2010

### **Biographical Information**

Eyosias Beneberu received his Bachelor of Science degree in civil engineering from Bahirdar University, Ethiopia in 2007 and Master's degree in Structural Engineering from Oklahoma state university in 2010. He has worked as a structural engineering for a design firm in Ethiopia and as an engineering specialist for Texas Department of Transportation (TxDOT). He is a licensed professional engineer in the states of California and Texas. His research interest includes structural fire engineering, repair and rehabilitation of structures and structural health monitoring of bridges.